

DISSERTATION

Development of Large Area CsI Photocathodes for the ALICE/HMPID RICH Detector

ausgeführt zum Zwecke der Erlangung des akademischen Grades eines Doktors der
technischen Naturwissenschaften unter der Leitung von

Univ.Prof. Dr. Dipl.-Ing. Christian W. Fabjan

E141

Atominstitut der Österreichischen Universitäten

eingereicht an der Technischen Universität Wien
Fakultät fuer Physik

von

Dipl.-Ing. Herbert Hödlmoser

Matrikel Nr. 9525780

Ramsau 57
5351 Aigen-Voglhub

Diese Arbeit wurde unterstützt vom Österreichischen Bundesministerium für Bildung,
Wissenschaft und Kultur.

Genf, am 18 März 2005

H. Hödlmoser

Kurzfassung

Im Rahmen dieser Doktorarbeit wurden die photoelektrischen Eigenschaften von großflächigen Cesiumjodid (CsI) Photokathoden untersucht. Diese Photokathoden sollen in einem sogenannten RICH (Ring Imaging CHerenkov) Detektor zur Abbildung der von geleadenen Teilchen erzeugten Cherenkov Lichtringe verwendet werden. Ein derartiges System ist im ALICE Experiment am CERN/LHC zur Identifizierung von Teilchen im Hochimpulsbereich vorgesehen. Die Aufgabe dieser Arbeit war zuerst die Kommissionierung einer Meßanlage (VUV-Scanner) zur orts aufgelösten Messung des Photonenstroms der CsI Kathoden unmittelbar nach dem Beschichtungsprozess. In weiterer Folge sollte dieses System zur Untersuchung verschiedener charakteristischer Eigenschaften dieser Photonendetektoren verwendet werden. Im Vorfeld dieser Arbeit sowie vor der Festlegung des Detektordesigns für die Anwendung in ALICE, wurden die Photokathoden im Rahmen von Forschungs- und Entwicklungsprojekten sowohl am CERN als auch an anderen Laboratorien untersucht. Diese Studien wurden vornehmlich an kleinen Musterkathoden unter Verwendung verschiedener Substrate und Prozeduren durchgeführt mit teilweise sehr unterschiedlichen Resultaten. Daher war es notwendig, bestimmte für die Qualität der Kathoden ausschlaggebende Eigenschaften und Prozeduren für die spezielle Anwendung mit großflächigen, industriell hergestellten Substraten weiter zu analysieren. Die wichtigsten der untersuchten Phänomene waren:

- *Wärmebehandlung der Kathoden nach der Beschichtung:* Aus den vorangegangenen Forschungsarbeiten war bekannt, daß die Effizienz der Photokathoden nach der Beschichtung durch vorübergehende Temperaturerhöhung gesteigert werden kann. Im Rahmen dieser Arbeit wurde dieser Effekt sowohl an großflächigen Testkathoden als auch mit den für den endgültigen Detektor konzipierten Kathoden untersucht. Es wurde gezeigt, daß zum Erreichen der für den Detektor erforderlichen Quanten Effizienz die Wirksamkeit dieses Effekts unbedingt erforderlich ist. Ausserdem konnte nachgewiesen werden, daß Variationen in der endgültigen Effizienz der Kathoden ausschließlich auf unterschiedliche Effektivität der Wärmebehandlung zurückzuführen sind. Die Ergebnisse dieser Studie wurden zur ständigen Anpassung und Verbesserung des Beschichtungs- und Nachbehandlungsprozesses verwendet.
- *Effizienzmindernde Effekte:* Die Qualität von CsI Photokathoden nimmt sowohl durch Exposition an Luftfeuchtigkeit aufgrund der Hygroskopie des CsI, sowie unter hohen Photonen- und Ionenflußdichten ab. Alle drei Effekte wurden mithilfe der neu aufgebauten Meßanlage untersucht. Der erste Effekt erfordert einen sorgsamen Umgang mit den CsI

Kathoden um jeglichen Kontakt mit Luftfeuchtigkeit zu vermeiden. Es konnte gezeigt werden, dass dieser Effekt reversibel ist, wenn die Kathode geheizt wird. Hohe Photonenflüsse sind für die Anwendung in einem Cherenkov Detektor irrelevant, da der Detektor zum Nachweis von Einzelphotonen verwendet wird. Es war jedoch erforderlich dieses Problem im Hinblick auf den Meßprozess selbst zu untersuchen, da in der Meßanlage ein wesentlich höherer Photonenfluß zur Erzeugung eines Photostroms verwendet wird. Der dritte qualitätsmindernde Mechanismus ist wichtig für den Betrieb des Detektors in einem Hochenergiephysik-Experiment, da hier durch das Strahlungsumfeld ständig Ionenströme in der Kammer erzeugt werden, die über die Kathode fließen. Mithilfe einer radioaktiven Quelle wurde ein beschleunigter Bestrahlungstest an einem Detektor-Prototyp durchgeführt. Im Rahmen einer ersten Testserie mit hohen Dosen (und Dosisraten) wurde für eine Dosis entsprechend der Belastung während 20 Jahren im ALICE Experiment, ein bis zu 40 prozentiger Effizienzverlust festgestellt. Ausserdem wurde festgestellt, daß sich der Schädigungsmechanismus im Anschluß an die Bestrahlungsphase weiter fortsetzt. Die Resultate zeigen, daß weitere Messungen mit niedrigen Dosen und Dosisraten erforderlich sind, um endgültige Schlußfolgerungen bezüglich der Lebensdauer der Kathoden in ALICE zu ziehen.

Mit den Resultaten dieser Studien wurden die Produktionsprozeduren für die 42 Photokathoden für den ALICE/RICH Detektor optimiert sowie die ersten 17 Kathoden hergestellt und in der Meßanlage analysiert. Die Kathoden wurden in die entsprechenden Detektormodule eingebaut, die anschließend in Pionenstrahlen getestet wurden. Der Vergleich dieser Daten aus den Tests der Detektormodule mit den Meßergebnissen des VUV-Scanners zeigte die Verlässlichkeit der Meßanlage sowie die Vergleichbarkeit des Einzelphotonennachweises im Detektor mit Photostrom Messungen im Vakuum unter Verwendung hoher Photonenflußdichten.

Acknowledgements

Regarding my work here at CERN I am indebted to Christian Fabjan. First he provided me with an opportunity to get to know this research center as a summer student, later he supported my application within the Austrian doctoral student program and finally he supervised my PhD thesis for the Technical University of Vienna. Of all the people involved in the HMPID project at CERN I am very grateful to my local supervisor Emile Schyns. I very much appreciated his talent to explain everything from the physics concerning photocathodes and detectors to the used hardware. I also have to thank him for his patience, when I was distracted by snow or mountains. (I remember it was particularly hard for him, when I continued to find snow in the mountains, long after the winter was gone...). Furthermore I am grateful to Andre Braem, for his help with the VUV-scanner and for offering his good ideas concerning both the experimental setup and theory. I am also indebted to Paolo Martinengo – besides discussing my work with me and helping with the corrections of the thesis, he never failed to encourage me. This was very important. Also thank you to Antonello DiMauro, Francois Piuze, Abraham Gallas and Martyn Davenport for the good teamwork. Many thanks to Antonello for his patience at the group meetings, when I was usually late, picking up the final results from the scanner just minutes before the presentation. I am especially grateful to the technicians Miranda van Stenis, Jacob Bastiaan van Beelen, Pieter Ijzermans, Xavier Pons and Claude David – without their help the scanner would have never worked. Finally here is the place to express my gratitude to several people in more private matters. First of all I would like to thank my parents for encouraging me in my decision to study abroad and for their unquestioned support. I would also like to thank the large community of Austrians here at CERN for the warm welcome and the nice company. Last but not least I want to thank Thomas Steiner, Bernhard Auchmann, Peter Urschuetz and Thomas Meinschad. I would not be who I am now, if they had not taught me to laugh about myself. Our mountaineering, skiing and climbing tours were adventures which I will never forget. Sometimes our undertakings have earned us wry looks from other people when we were pushing our “philosophy” too far (“In winter we don’t need to rappel because we have skis...”). But I am convinced, there is no other place better suited to learn about responsibility and team spirit than on an exposed ridge, where the only safety is the rope that attaches you to your partners. Thanks for sharing that rope with me.

Abstract

The work carried out within the framework of this PhD deals with the measurement of the photoelectric properties of large area thin film Cesium Iodide (CsI) photocathodes (PCs) which are to be used as a photon converter in a proximity focusing RICH detector for High Momentum Particle Identification (HMPID) in the ALICE experiment at the LHC. The objective was to commission a VUV-scanner setup for in-situ measurements of the photoelectric response of the CsI PCs immediately after the thin film coating process and the use of this system to investigate the properties of these photon detectors. Prior to this work and prior to the finalization of the ALICE/HMPID detector design, R&D work investigating the properties of CsI PCs had been performed at CERN and at other laboratories in order to determine possible substrates and optimized thin film coating procedures. These R&D studies were usually carried out with small samples on different substrates and with various procedures with sometimes ambiguous results. Consequently it was necessary to further analyze various properties and procedures using the final large area substrates and production facilities. Among the investigated phenomena the most important ones were:

- Post deposition treatment: from the R&D studies it was known, that the PC response can be increased by heating the PC after the coating process. Within this thesis this effect was investigated both with large area test PCs and with the final PCs for the detector. It could be shown that the enhancement effect is mandatory to achieve the photon conversion efficiency required by the detector design. Furthermore it could be shown that any difference in PC quality is due to differences in this enhancement effect. The results of these measurements were and are continuously used to refine and optimize the production procedure.*
- Ageing effects: CsI PCs age under exposure to humidity due to the hygroscopicity of CsI and under high photon flux and ion bombardement inside the Multi Wire Proportional Chamber (MWPC) of the detector. All three effects have been investigated with the VUV scanner. The first effect requires a careful treatment of the CsI PCs to avoid exposure to humid air. Furthermore this effect was found to be reversible if the PC is heated. High photon fluxes are irrelevant in a Cherenkov detector dealing with single photons, however the problem needed to be investigated to verify that the measurement process itself does not damage the PCs. The third mechanism is very important as it occurs during normal detector operation and depends only on the radiation environment of the experiment. An accelerated test was carried out by irradiating a detector with a radioactive source. For high doses corresponding to 20 years of operation inside ALICE (and much higher dose rates) a clear degradation of up to 40 % of the PC response was observed. The results show that low dose and low dose rate measurements are still required to draw a conclusion on the projected lifetime of the PCs inside ALICE.*

With the results of these studies the production procedure for the 42 PCs for the ALICE/HMPID was optimized and the first 17 PCs have been produced and analyzed by means of the VUV-scanner. The results were compared with an evaluation of the PCs inside the final detector modules using charged particle beams. The comparison of scanner and test beam results showed the reliability of the VUV-scanner system and the comparability of a high photon flux photocurrent measurement under vacuum with the single photon counting process in the detector.

This thesis is structured in the following way: Chapter 1 provides an introduction to the ALICE experiment at LHC. Chapter 2 outlines the concept of particle identification with Cherenkov detectors and describes the ALICE/HMPID detector. In the Chapter 3 the properties of CsI photocathodes are summarized and the thin film coating setup for production and VUV-scanner setup for evaluation are introduced. Chapter 4 elaborates on the various commissioning tests carried out to clarify the influence of various measurement parameters and setup conditions on the measurement process. In Chapter 5 the results of the investigation of the post deposition heat enhancement phase of CsI PCs are given. Chapter 6 treats ageing of CsI by exposure to humidity. Chapter 7 summarizes the results obtained during the production of the first 17 PCs for the detector and compares the VUV scanner measurements and the beam tests. Finally, in Chapter 8 the ageing of CsI under ion bombardement is discussed, followed by the final conclusions in Chapter 9.

Contents

1	ALICE and the LHC project	13
1.1	The LHC.....	13
1.1.1	The particle accelerator.....	13
1.1.2	The experiments	14
1.2	ALICE (A Large Ion Collider Experiment).....	15
1.2.1	Observables	17
1.2.2	The ALICE detector.....	19
2	Cherenkov detectors and the ALICE/HMPID project	25
2.1	The Cherenkov effect.....	25
2.2	Particle identification by means of the Cherenkov effect.....	28
2.3	Cherenkov detector concepts	32
2.3.1	Detector components and materials	32
2.3.2	Threshold counters	34
2.3.3	Differential counters	35
2.3.4	RICH detectors	36
2.4	The ALICE/HMPID RICH.....	37
3	The CsI photocathodes	43
3.1	Properties of CsI photocathodes.....	43
3.2	ASSET	48
3.3	The Substrate.....	50
3.4	The CsI deposition facility.....	54
3.4.1	Source preparation	54
3.4.2	Control of the CsI layer thickness	56
3.4.3	The CsI deposition process	57
3.5	Quality control: the VUV Scanner	60
3.5.1	Characteristics of the UV beam.....	62
3.5.2	Photocurrent measurement	63
4	Commissioning of the VUV Scanner System.....	67
4.1	Sensitivity of the photoelectron measurement to measurement parameters	67
4.1.1	Sensitivity to pressure and pressure gauges	67
4.1.2	Sensitivity to temperature.....	68
4.1.3	Operational voltages for photocurrent measurements	68
4.1.4	Sensitivity to anode position.....	70
4.2	Source stability and reference measurement.....	71
4.3	Decreased effective QE in interpad zones.....	71
4.3.1	Interpad effect in the VUV-scanner.....	72
4.3.2	Calculation of the effective QE in the interpad zones	74
4.3.3	Wavelength dependent measurements on test samples in ASSET	75

4.3.4	Choice of a spot size in the VUV scanner to minimize interpad effect	77
4.4	Sensitivity to stray light from the UV source	78
4.5	Alignment, form and size of the UV spot	78
4.5.1	Alignment of the entrance pinhole and influence on measurement	78
4.5.2	Grazing incidence reflections inside the UV beam pipe.....	79
4.5.3	Form of the UV spot in the final measurement configuration	83
4.6	Inhomogeneous PC response: exclusion of systematic effects	84
4.7	Influence of the photon flux.....	85
4.7.1	Identification of effects in the VUV-scanner	86
4.7.2	High flux illumination tests.....	88
4.7.3	Negligible effect in a standard scanning procedure.....	93
5	Post deposition enhancement	95
5.1	Introduction and motivation.....	95
5.2	QE enhancement of large area test PCs.....	96
5.2.1	Experimental procedures	96
5.2.2	Summary of tests	97
5.2.3	Wavelength dependent enhancement effect.....	98
5.2.4	Influence of substrate temperature during evaporation	99
5.2.5	Influence of pressure and temperature during the enhancement phase.....	101
5.2.6	Definition of a standard procedure for the series production of the PCs	104
5.3	QE enhancement of standard PCs in the HMPID series production.....	104
5.3.1	Summary of the results of the series production	104
5.3.2	Analysis of the enhancement behavior of the standard PCs	105
5.4	QE enhancement of small samples.....	108
5.5	Summary and discussion	109
6	Ageing due to exposure to humidity and recovery.....	111
6.1	Exposure and recovery tests with a test PC in the VUV-scanner.....	111
6.1.1	Increased spatial inhomogeneity of the CsI response after recovery	112
6.2	Exposure and recovery tests with small samples in ASSET	114
6.3	SEM analysis of small samples before and after exposure	115
6.4	Conclusions and suggestions for further tests.....	117
7	Quality evaluation in the PC production.....	119
7.1	Quality evaluation scans during production	119
7.2	Summary of production in 2004	120
7.3	Comparison of VUV-scanner and test beam results.....	123
7.3.1	Inhomogeneities in the PC response	126
8	Ageing due to ion bombardement.....	127
8.1	Introduction	127
8.2	Experimental layout	127
8.3	Doses and dose rates.....	129

8.4	Effects measured with the VUV-scanner.....	130
8.4.1	QE decrease.....	130
8.4.2	Time-dependent self-ageing.....	131
8.4.3	Stability of the PC performance in the reference areas	134
8.4.4	Negative result for recovery by annealing	134
8.4.5	Negative result for wavelength dependency of the effects	135
8.5	Effects measured in test beam	135
8.6	Dose-effect relationship.....	137
8.7	Discussion.....	141
9	Summary and conclusions.....	143
	Literature	145
	Glossary	149
	Curriculum Vitae	151

1 ALICE and the LHC project

1.1 The LHC

In 2007 the Large Hadron Collider (LHC) at CERN will become operational and start a new phase in the exploration of the most fundamental laws of physics. During the last few decades there has been enormous progress in our understanding of the basic composition of matter. The theory of fundamental particles and their interactions, the Standard Model, describes all matter by means of its six types of quarks, six leptons, and the four forces with their respective force carriers. In this mathematical formulation of the basic laws governing the universe the concept of mass is introduced via a symmetry breaking mechanism associated with the Higgs particle. This particle has not yet been observed experimentally. The search for the Higgs particle provides the main motivation for the construction of the LHC. At the LHC the energies achieved in proton – proton collisions will be considerably higher than in any previous high energy physics experiment which would allow the discovery of the Higgs particle. However, the experiments at the LHC will also pursue different physics goals such as the search for heavy W- and Z-like objects, supersymmetric particles, compositeness of the fundamental fermions, CP violation in B-decays and studies of the top quark. Some of these investigations address physics concepts that go beyond the Standard Model such as Supersymmetry. Last but not least the accelerator will also be used to study the physics of strongly interacting matter at extreme energy densities in ultra-relativistic heavy ion collisions in a dedicated experiment. These collisions hope to achieve and analyze a phase transition from the confined state of quarks and gluons inside the hadrons to a Quark Gluon Plasma (QGP).

1.1.1 The particle accelerator

The LHC is being built reusing the existing infrastructure of its predecessor LEP. Fig. 1 a) shows the different stages of the accelerator system at CERN. The machine will accelerate protons and heavy ions with the objectives of very high center of mass energies of up to 14 [TeV] and luminosities of 10^{34} [$\text{cm}^{-2}\cdot\text{s}^{-1}$] in p-p runs. In order to deliver the maximum centre-of-mass energy within the confines of the existing LEP tunnel (circumference 27 kilometers), the machine features a magnetic system of 1232 dipole magnets with a strength of 8.4 [T] employing superconducting coils operating with of 11.2 [kA]. To achieve superconductivity at these strong B-fields the magnets must operate cooled with superfluid helium at temperatures below 2 [K]. Contrary to the case of the LEP in which electrons and positrons were circling in the same beam pipe the LHC requires two beam pipes in which protons circle in opposite directions. Beam pipes and super conducting coils are arranged inside an iron yoke confining the magnetic flux – cross section in Fig. 1 c).

The above quoted values for the center of mass energy and luminosity are given for the p-p runs for the high luminosity experiments. In heavy ion runs the respective values will be different. For Pb-Pb collisions the maximum center of mass energy per participating

nucleon will be 5.5 [TeV]. The achievable luminosity for these runs is determined by accelerator- and detector limitations¹ and will be $L = 10^{27}$ [cm⁻²·s⁻¹] - Fig. 1 b).

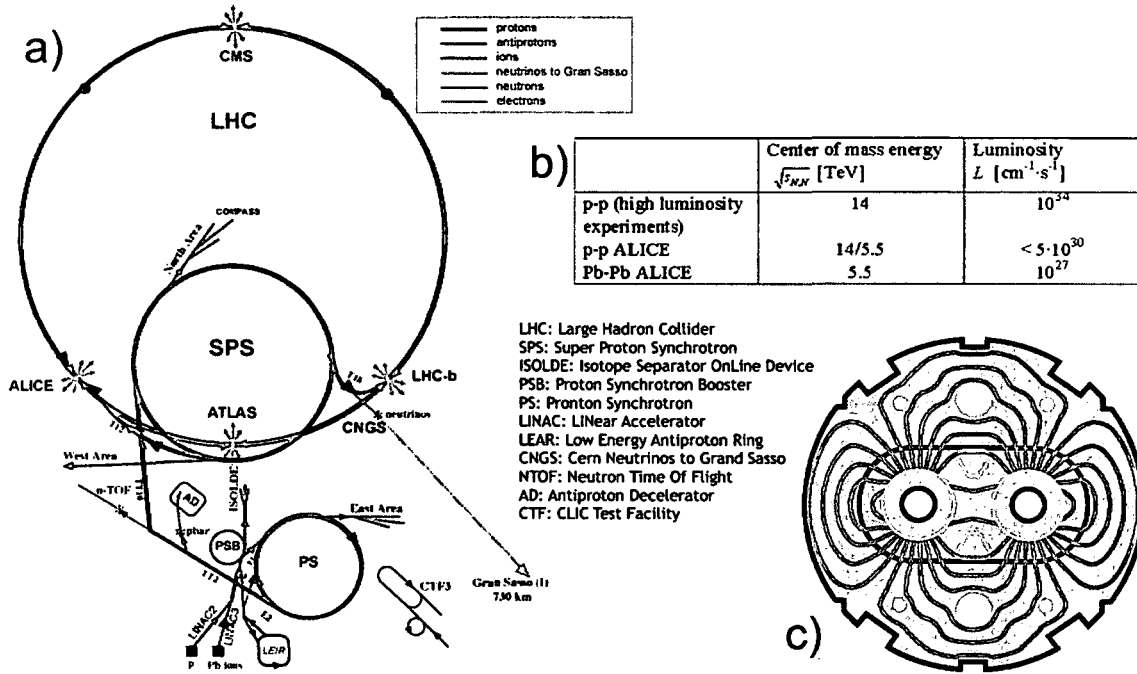


Fig. 1 Layout of the accelerator system at CERN (a) with the different acceleration stages and experimental sites. Energies and luminosities in p-p and Pb-Pb runs (b). Cross-section of the yoke of an LHC dipole containing beam-pipes and superconducting coils (c).

1.1.2 The experiments

At the four collision points at the LHC (see Fig. 1) four large experiments are being installed. The two largest, CMS (Compact Muon Solenoid, [3]) and ATLAS (A Toroidal LHC ApparatuS, [1]), are general-purpose experiments optimized for the discovery of the Higgs boson. They take different approaches, in particular, to the detection of muons. CMS is built around a very high field solenoid magnet; its relative compactness derives from the fact that there is a massive iron yoke so that the muons are detected by their bending over a relatively short distance in a very high magnetic field (4 [T]). By contrast, the ATLAS experiment is substantially larger and essentially relies upon an air cored toroidal magnet system for the measurement of the muons. A more specialized experiment is the LHCb [2] experiment which employs a forward collider detector dedicated to the study of CP violation and other rare phenomena in the decays of Beauty particles. The fourth of the large experiments is ALICE (A Large Ion Collider Experiment, [4]), which is dedicated to heavy ion physics. In the following section a more detailed description of ALICE will be given.

¹ From the accelerator side the luminosity is limited due to a higher beam divergence due to the high charge of the ions (Pb⁸²⁺).

1.2 ALICE (A Large Ion Collider Experiment)

ALICE studies nuclear matter under conditions of extreme density and temperature in ultra-relativistic heavy ion collisions. These studies are not only of great interest in particle physics to test the predictions of the Standard Model about the fundamental constituents of matter, but they are also of high importance for our current understanding of the evolution of the early Universe immediately after the Big Bang. According to Big-Bang cosmology, the Universe evolved from an initial state of extreme energy density to its present state through rapid expansion and cooling thereby traversing a series of phase transitions of matter predicted by the Standard Model. Global features of our Universe, like baryon asymmetry or the large scale structure, are believed to be linked to characteristic properties of these phase transitions. The phase transitions are connected to the intrinsic symmetries of the theory, which are valid at high-energy densities, and broken below certain critical energy densities. Particle content and particle masses originate as a direct consequence of the symmetry-breaking mechanism. Most of the predicted transitions occur at energy densities which are not accessible by the experiment. An exception is the transition from ordinary hadronic matter to the Quark Gluon Plasma (QGP). Quantum Chromo Dynamics (QCD) predicts that this transition takes place at a critical temperature of ~ 170 [MeV], corresponding to an energy density of $\epsilon_c \sim 1$ [GeV fm $^{-3}$]. In the QGP quarks and gluons are no longer confined to hadrons, chiral symmetry is approximately restored and quark masses are reduced from their large effective values in hadronic matter to their small bare ones. In ultra-relativistic heavy-ion collisions, one expects to attain energy densities which reach and exceed the critical energy density ϵ_c , thus making the QCD phase transition possible. The objective of heavy-ion physics is to explore the phase diagram of strongly interacting matter, to study the QCD phase transition and the physics of the QGP state. Heavy ion collisions at CERN-SPS and BNL-RHIC have reported evidence for the QGP. Fig. 2 shows the phase diagram of strongly interacting matter as a function of baryo-chemical potential (baryon number density) and temperature. In the above mentioned experiments the phases of hadronic matter are studied at extremely high temperatures and low net baryon densities, where the number of particles and anti-particles are approximately equal. This region of the phase diagram, which corresponds to the conditions in the early universe, is characterized by small values of the baryo-chemical potential. The same region will be explored by collisions in ALICE however the achieved temperature range will be significantly higher. The highest QGP temperatures will be far enough from the phase transition region to guarantee greatly increased lifetime of the state. Fig. 3 shows the energy density (ϵ) as a function of temperature. The crossover takes place in a narrow temperature interval and is characterized by a rapid rise of energy density in the vicinity of the crossover temperature.

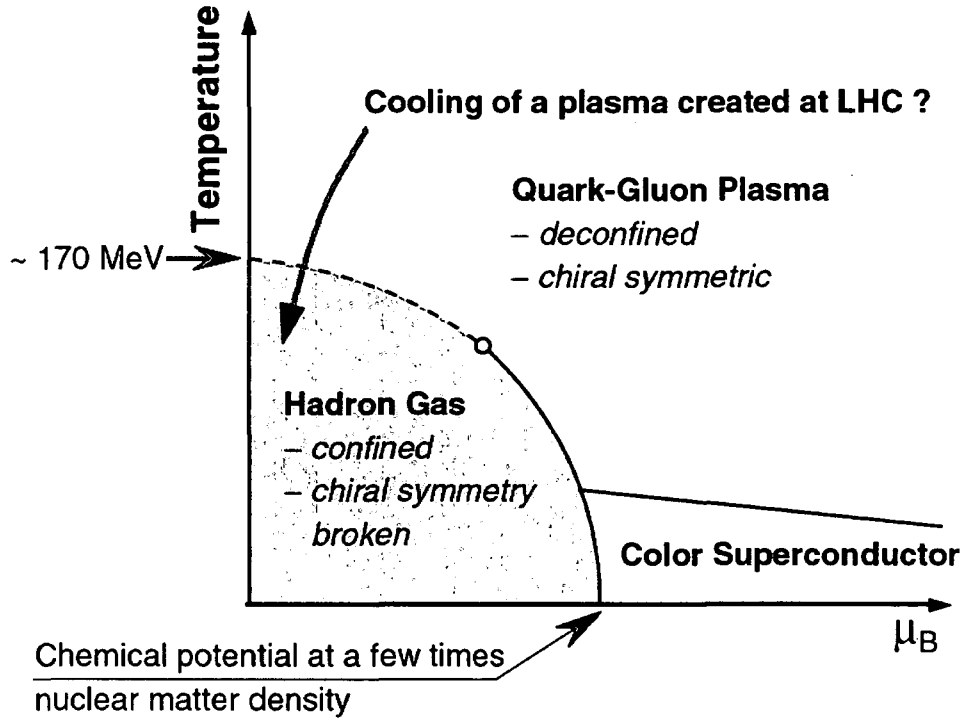


Fig. 2 The phase diagram of strongly interacting matter plotted as a function of temperature and baryo-chemical potential. The solid lines indicate likely first-order transitions. The dashed line indicates a possible region of a continuous but rapid crossover transition. The open circle gives the possible position of a second-order critical endpoint of a line of first-order transitions.

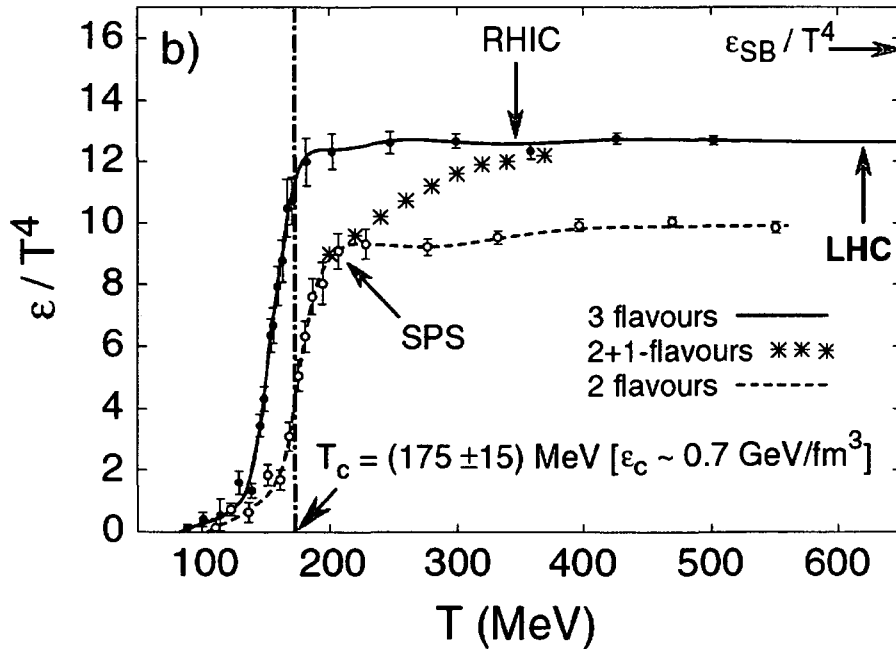


Fig. 3 Energy density as a function of temperature in the medium produced in heavy ion collisions. The phase transition to the QGP state is characterized by a drastic increase in energy density. The theoretical curves depend on how many quark flavours are taken into account. 3 flavour QCD delivers the most realistic description for the LHC temperatures, as only up, down, and strange quarks contribute to the thermodynamics at these energies [1].

1.2.1 Observables

Due to the small timescales and spatial extensions the QGP cannot be observed directly therefore probes or observables are needed which convey information about the state of the medium during the early stage of the collision. Possible probes are for example particles which are produced during the earliest stages of the collision and which do not interact strongly with the QGP after their production, e.g. photons or leptons which are not affected by the strong force. If the production rates of such probes can be derived from theory, e.g. perturbative QCD, the analysis of these probes allows a direct verification of the theoretical models. Another type of observables are probes, which are ordinarily produced in nucleus-nucleus (e.g. p-p) collisions and which are suppressed or modified due to the presence of QGP, e.g. jets or heavy quark states. For these observables the analysis largely relies on a comparison of the A-A data to a reference obtained from p-p collisions and p-A collisions. Therefore not only Pb-Pb collisions, but also p-p and p-A type collisions have to be studied in ALICE. Some of the most important observables will be mentioned in the list below. For details the reader is referred to [5].

Particle multiplicities

The average charged-particle multiplicity per rapidity unit is one of the most fundamental observables. On the theoretical side, it fixes a global property of the medium produced in the collision. Since it is related to the attained energy density, it enters the calculation of most other observables. Another important ‘day-one’ observable is the total transverse energy, per rapidity unit at mid-rapidity. It determines how much of the total initial longitudinal energy is converted to transverse debris of QGP matter. On the experimental side, the particle multiplicity fixes the main unknown in the detector performance; the charged-particle multiplicity per unit rapidity largely determines the accuracy with which many observables can be measured. Despite their fundamental theoretical and experimental importance, there is no first principles calculation of these observables starting from the QCD Lagrangian. Attempts to calculate values for the charged particle multiplicity at mid rapidity have usually overestimated the values actually found in heavy ion collisions, e.g. at RHIC. Taking these comparisons with actual data into account, the estimates for the multiplicity at mid rapidity in ALICE for central Pb – Pb collisions at a center of mass energy of $\sqrt{s_{NN}} = 5.5$ [TeV] range from 2000 to 5000. The detector has been designed to cope with multiplicities up to 8000 which gives a comfortable safety margin.

Direct photons

Photons are produced during all stages of the heavy ion collision. There are photons produced in the initial hard parton scattering with energies of up to several hundred [GeV], followed by those radiated from the QGP with energies up to several [GeV] and even later by photons emitted during scatter processes and decays during and after freeze out. Due to the fact that they do not interact strongly they are not affected by the medium and convey information about the state at the time of their production. The production of the prompt photons from the initial parton scattering can be calculated by means of perturbative QCD; consequently these photons test the validity of the theory.

Dileptons

Dileptons are lepton – antilepton pairs (e/e^+ , μ/μ^+) emitted throughout the evolution of the system much as in the case of direct photons. Again the leptons are efficient probes as

they do not interact strongly and the rate of prompt leptons from the hard scattering can be calculated with pQCD.

Jets

Jets originate from hard scattering processes, in which the partons (quarks, gluons) interact directly. By definition, hard collisions involve very large momentum transfers, and probe the structure of the hadrons at short distances. The incident hadrons break apart and many new particles are created. The outgoing partons from the hard sub process fragment into jets of particles. The rest of the particles in the event are rather soft particles, which mostly arise due to the break up of the remnants of the incident hadrons. They form the underlying event. The hard-scattering component of the event consists of the outgoing two energetic coloured partons which form two jets: they undergo a cascade of branchings thus degrading their energies and momenta, as they escape from each other. Finally, the end points of this branching process fragment into a number of colourless hadrons during the so-called hadronization stage. The hard scatter process can be described in the framework of perturbative QCD. Thus, the measurement of inclusive jet and dijet cross sections, as well as various other jet properties can be used to test the predictions of perturbative QCD. In ultra relativistic ion collisions jets can be modified due to the presence of the QGP. The strong interaction of the escaping partons from the hard scatter process with the free partons in the QGP leads to an energy loss of the scattered particles mainly due to gluon emission. The energy loss depends on the path length inside the QGP and can lead to a complete suppression of a jet. This effect is called jet “quenching”. This suppression of large E_T jets naturally leads to the suppression of large p_T particles. Therefore, the measurement of the momentum spectra of identified particles at large momenta allows the study of the effect of jet quenching. The comparison of the high- p_T spectra of identified particles measured in Pb–Pb collisions with the calculated curves, and with the spectra obtained from p-p data, will be very sensitive to the medium-induced energy loss of high-energy partons. This already stresses the importance of the high momentum PID in ALICE. Fig. 4 shows the influence of jet quenching on the ratio of proton spectra between Pb-Pb and p-p collisions.

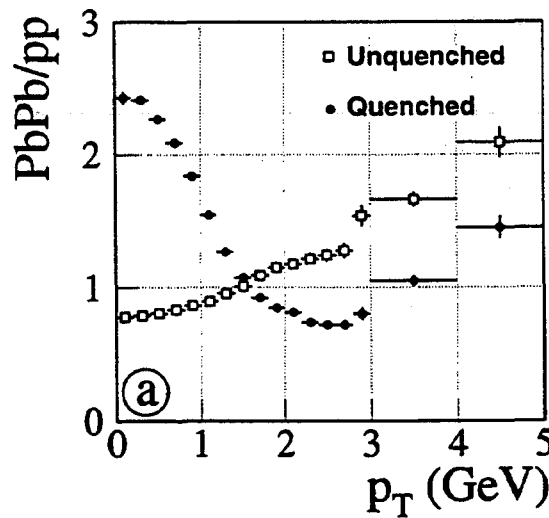


Fig. 4 Influence of jet quenching on the ratio of Pb-Pb proton spectra against p-p proton spectra in the high p_T range. The curves are normalized to a spectrum from a p-p collision.

Heavy quarks and quarkonium states

Heavy quarks (charm, bottom) will be produced in the ion collisions as the collision energies are far above the production threshold. The production can be described within pQCD and the long lifetime of charm and bottom quarks will allow them to live through the thermalization phase of the plasma and be affected by its presence. Heavy quark – antiquark pairs can form bound quarkonium states with binding energies in the range of the thermal energies of the plasma. Therefore there is a high break-up probability for these states and quarkonium suppression should be observed due to the presence of the QGP.

1.2.2 The ALICE detector

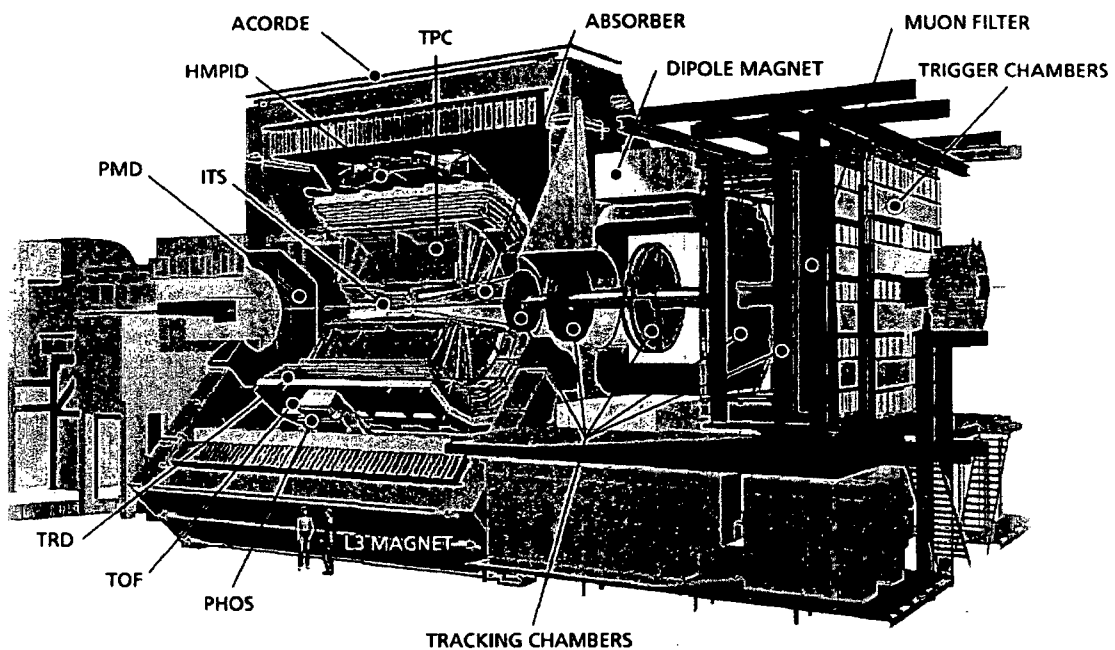


Fig. 5 Layout of the ALICE detector.

The ALICE experiment, illustrated in Fig. 5, consists of a central detector system, covering mid-pseudorapidity ($|\eta| \leq 0.9$) over the full azimuth, and several forward systems. The central system is installed inside the large solenoidal magnet from the LEP/L3 experiment, which generates a magnetic field of 0.5 [T]. The central system includes, from the interaction vertex to the outside, six layers of high-resolution silicon detectors (Inner Tracking System—ITS), the main tracking system of the experiment (Time-Projection Chamber—TPC), a transition radiation detector for electron identification (Transition-Radiation Detector—TRD), and a particle identification array (Time-Of-Flight—TOF). The central system is complemented by two small-area detectors: an array of ring-imaging Cherenkov detectors ($|\eta| \leq 0.6$, 57.6° azimuthal coverage) for the identification of high-momentum particles (High-Momentum Particle Identification Detector—HMPID), and an electromagnetic calorimeter ($|\eta| \leq 0.12$, 100° azimuthal coverage) consisting of arrays of high-density crystals (PHOTon Spectrometer—PHOS). The large rapidity systems include a muon spectrometer ($-4.0 \leq \eta \leq -2.4$), a photon counting detector (Photon Multiplicity Detector—PMD), an ensemble of multiplicity detectors (Forward Multiplicity Detector—

FMD) covering the large pseudo-rapidity region (up to $\eta = 5.1$). A system of scintillators and quartz counters (T0 and V0) will provide fast trigger signals, and two sets of neutron and hadron calorimeters, located at 0° and about 115 [m] away from the interaction vertex, will measure the impact parameter (Zero-Degree Calorimeter—ZDC). An absorber positioned very close to the vertex shields the muon spectrometer. The spectrometer consists of a dipole magnet, five tracking stations, an iron wall (muon filter) to absorb remaining hadrons, and two trigger stations behind the muon filter.

The large particle multiplicities in Pb-Pb collisions in combination with the luminosities lead to a huge amount of data from the detectors, which has to be handled by the Data Acquisition system (DAQ). The resulting requirements are an aggregate event building bandwidth of up to 2.5 [GByte/s] and a storage capability of up to 1.25 [GByte/s], giving a total of more than 1 [Pbyte] of data every year. A short description for the detectors is given below. Detailed descriptions can be found in the Technical Design Reports [6]-[17] and in [5].

Inner Tracking System (ITS)

The ITS consists of six cylindrical layers of silicon detectors, located at radii, $r = 4, 7, 15, 24, 39$ and 44 [cm] from the interaction point. It covers the pseudo-rapidity range of $|\eta| < 0.9$ for all vertices located within the length of the interaction diamond, i.e. 10.6 [cm] along the beam direction. The number, position and segmentation of the layers are optimized for efficient track finding and high impact-parameter resolution. In particular, the outer radius is determined by the necessity to match tracks with those from the TPC, and the inner radius is the minimum allowed by the radius of the beam pipe (3 [cm]). Because of the high particle density, up to 80 particles [cm^{-2}], pixel detectors have been chosen for the innermost two layers, and silicon drift detectors for the following two layers. The outer two layers, where the track densities are below 1 particle [cm^{-2}], will be equipped with double-sided silicon micro-strip detectors. With the exception of the two innermost pixel planes, all layers will have analogue readout for particle identification via dE/dx measurement. This will give the ITS a stand-alone capability as a low- p_T particle spectrometer. The most important objectives of the ITS are:

- high resolution primary vertex localisation
- recording vertices from decays of hyperons and D and B mesons
- low momentum particle tracking and identification (>100 [MeV])

Time Projection Chamber (TPC)

The TPC is the main detector for tracking inside the central barrel contained within the large L3 magnet. It has to provide charged particle momentum measurements with good two-track separation and particle identification. The phase space covered by the TPC ranges in pseudo-rapidity $|\eta| < 0.9$ (up to $|\eta| \sim 1.5$ for tracks with reduced track length and momentum resolution) and in p_T up to 100 [GeV/c] with good momentum resolution. The TPC consists of a large gas filled cylindrical field cage (length ~ 5 [m]) divided in two halves by a high voltage membrane (~ 100 [kV]) in the interaction plane and terminated at both ends with Multi Wire Proportional Chambers (MWPC). Between the HV plane and the readout chambers a highly uniform electrostatic field causes the electrons produced in the gas by traversing charged particles to drift towards the readout chambers. In the MWPC the electrons are amplified by an avalanche process and the signal is read out from the segmented cathode-plane. Together with the measurement of the drift time of the electrons this readout provides full 3 dimensional coordinates for a track. By measuring the

amount of charge collected on the cathode pads of the chamber and taking into account the gain, the charge deposited by the primary particle and thus the energy loss per unit length dE/dx can be obtained and used to identify the primary particle.

Transition Radiation Detector (TRD)

The main goal of the TRD is to provide electron identification in the central barrel for momenta greater than 1 [GeV/c], e.g. to measure dileptons. It consists of a radiator coupled with a multi wire proportional chamber. All charged particles are registered in the wire chamber, however only the ultrarelativistic electrons emit transition radiation in the radiator which is in the X-ray range. Due to the high sensitivity of the chamber gas to X-rays (Xenon mixture) an electron accompanied by transition radiation from the radiator leads to a much higher signal than other charged particles. The TRD fills the radial space between the TPC and the TOF detectors and covers the same pseudo-rapidity range. It consists of six individual layers. To match the azimuthal segmentation of the TPC, there are 18 sectors. There is a 6-fold segmentation along beam direction. In total there are $18 \times 5 \times 6 = 540$ detector modules. Each module consists of a radiator of 4.8 cm thickness, a multi-wire proportional readout chamber, and the front-end electronics for this chamber. The signal induced on the cathode pads is read out. The pads have a typical area of 6–7 [cm²] and cover a total active area of about 736 [m²] with 1.16×10^6 readout channels.

Time Of Flight (TOF)

The TOF detector is the outermost detector in the central barrel, covering the same pseudo-rapidity region as TPC and TRD. It consists of a large array of Multi-gap Resistive-Plate Chambers (MRPC), a type of gaseous detector which records charged particles by gas amplification in high fields. This detector array is used for particle identification in the intermediate momentum range from 0.2 to 4.5 [GeV/c] by the measurement of the TOF from the interaction point. The TOF, coupled with the ITS and TPC for track and vertex reconstruction and for dE/dx measurements, will provide event-by event identification of large samples of pions, kaons, and protons. The TOF-identified particles will be used to study relevant hadronic observables on a single-event basis.

PHOton Spectrometer (PHOS)

PHOS is a single-arm high-resolution high-granularity electromagnetic spectrometer including a highly segmented ElectroMagnetic CALorimeter (EMCA) and a Charged-particle Veto (CPV) detector. PHOS is used to identify photons against the background of charged particles and measure their energy with high resolution over a large dynamical range. Photons and charged particles are detected in the scintillating crystals of the EMCA. One unit is segmented into 3584 detection channels arranged in 56 rows of 64 channels. The detection channel consists of a $22 \times 22 \times 180$ [mm³] lead-tungstate crystal, PbWO₄ (PWO), coupled to a Avalanche Photo-Diode (APD). The CPV detector on top of each PHOS module is a Multi-Wire Proportional Chamber (MWPC) with cathode-pad readout which identifies only the charged particles and thus provides a veto for signals in the EMCA not originating from photons. PHOS is subdivided into five independent EMCA+CPV units, named PHOS modules, positioned on the bottom of the ALICE setup at a distance of 460 cm from the interaction point. It will cover approximately a quarter of a unit in pseudo-rapidity, $-0.12 \leq \eta \leq 0.12$, and 100° in azimuthal angle. Its total area will be 8 [m²].

High Momentum Particle Identification Detector (HMPID)

The HMPID, is dedicated to inclusive measurements of identified hadrons for $p_T > 1$ [GeV/c]. The HMPID was designed as a single-arm array with an acceptance of 5 % of the central barrel phase space. HMPID will enhance the PID capability of ALICE by enabling identification of particles beyond the momentum interval attainable through energy loss (in ITS and TPC) and time-of-flight measurements (in TOF). The detector was optimized to extend the useful range for π/K and K/p discrimination, on a track-by-track basis, up to 3 and 5 [GeV/c] respectively. The detector will be described in detail in the following Chapter.

Muon spectrometer

The measurement of muons is essential for the analysis of hard penetrating probes such as quarkonia states. The complete spectrum of heavy quark vector mesons (i.e. J/ψ , ψ' , Υ , Υ' and Υ''), as well as the φ meson, will be measured in the $\mu^+\mu^-$ decay channel by the ALICE muon spectrometer. The spectrometer is designed to detect muons in the pseudo-rapidity range of $-4.0 \leq \eta \leq -2.5$, i.e. in the forward direction. The spectrometer consists of the following components:

- a passive front absorber within the L3 magnet made from concrete, carbon and steel to absorb hadrons and photons from the interaction vertex and a beam shield; due to the absorber the minimum momentum of the muons is 4 [GeV/c].
- a large dipole magnet with resistive coils producing a bending field of 0.7 [T] placed outside the L3 magnet 7 [m] from the interaction point.
- a high-granularity tracking system of 10 detection planes consisting of cathode pad chambers with a spatial resolution of 100 [μm]. The planes are arranged in 5 stations, 2 before, one inside and 2 after the dipole magnet.
- a passive muon filter wall, followed by four planes of trigger chambers (resistive plate chambers).

Zero Degree Calorimeter (ZDC)

The ZDC serves to measure the impact parameter of a collision which is related to the number of participating nucleons, by measuring the amount of energy carried in forward direction, i.e. zero degrees relative to the beam direction. With increasing centrality of a collision more energy is transferred in the transversal plane and the number of passive spectator nucleons continuing in the beam direction decreases. In ALICE the spectator nucleons will be measured with a hadronic and an electromagnetic calorimeter 116 [m] from the interaction point, where the distance between beam pipes (~ 8 [cm]) allows insertion of a detector (see figure 3.25). At this distance, spectator protons are spatially separated from neutrons due to the bending magnets at the LHC beam line. Therefore two distinct detectors will be used: one for spectator neutrons, placed at zero degrees relative to the LHC axis, and one for spectator protons, placed externally to the outgoing beam pipe on the side where positive particles are deflected. The calorimeters consist of dense passive absorbers in which the incident particle creates a shower. The shower particles in turn produce Cherenkov radiation in quartz fibres interspersed in the absorber. This technique allows a very compact design with a dense absorber due to the limited space and is insensitive to the background radiation environment due to the threshold effect in the Cherenkov counters.

Photon Multiplicity Detector (PMD)

The PMD is a pre-shower detector to measure multiplicity and spatial distribution of photons event-by-event, which will be installed at 360 [cm] from the interaction point, on the opposite side of the forward muon spectrometer, covering the pseudo-rapidity range $2.3 \leq \eta \leq 3.5$. It consists of two identical detector planes (gas proportional counters with wire readout) separated by a Pb converter plane. The first detector plane is used to veto charged particles while the second plane detects showers both from photons and charged particles.

Forward Multiplicity Detector (FMD)

The FMD is a silicon strip detector, located on both sides of the central barrel, providing (offline) charged-particle multiplicity information in the pseudo-rapidity range $-3.4 < \eta < -1.7$ and $1.7 < \eta < 5.1$. It consists of 51 200 silicon strip channels distributed over five ring counters of two types with each 20 or 40 sectors in azimuthal angle, respectively.

V0

The V0 detector, which provides minimum bias and centrality triggers, consists of two arrays located asymmetrically on each side of the interaction point. The V0 detector units are scintillators combined with wavelength shifting fibers. The light is collected and transported by clear fibers and recorded by means of PMs installed at 3–5 [m] from the detectors, inside the L3 magnet. The time resolution of each individual counter will be better than 1 [ns].

T0

The main objective of the T0 detector are the generation of a T0 signal for the TOF detector with a precision of about 50 [ps] (r.m.s.), the measurement of the vertex position with a precision ± 1.5 [cm] for each interaction and to provide the earliest L0 trigger when the position is within the preset values. The detector consists of two arrays of Cherenkov counters, covering the pseudo-rapidity range $2.9 < \eta < 3.3$ on the side of the muon arm and $-5 < \eta < -4.5$. In the radial (transverse) direction both T0 arrays are placed as close to the beam pipe as possible to maximize triggering efficiency.

2 Cherenkov detectors and the ALICE/HMPID project

This chapter contains an introduction to particle identification (PID) by means of Cherenkov detectors. In the first section the physical effect is illustrated and the most important formulas for the mathematical description are summarized. The second section explains, how the Cherenkov effect can be used for particle identification and shows some practical detector concepts with the main focus on the Ring Imaging CHerenkov (RICH) technology. The last section in this chapter focuses on the RICH detector for the ALICE experiment and outlines the detector design and the status of the ALICE/HMPID project. The material presented in this chapter has been compiled from references [6] and [22] to [30]. For additional detailed information the reader can refer to the extensive collection of publications on Cherenkov detectors in the proceedings of the 5 International RICH Workshops [31].

2.1 The Cherenkov effect

In a medium with refractive index n a charged particle moving with a velocity $c\beta$ can exceed the velocity of light c/n inside the medium. In this case the particle emits characteristic electromagnetic radiation, the Cherenkov radiation.

Historically the observation of blue light in concentrated radium solutions by Mme. Curie in 1910 preceded the understanding of this effect. In the exhaustive experimental work of Cherenkov [22] between 1934 and 1944 he characterized this radiation and he was able to observe the angular distribution of the radiation, a threshold effect, its dependence on n and β . Furthermore he was able to measure its spectral distribution and total intensity as discussed in the text below. He demonstrated that the light intensity was proportional to the electron path length and that the radiation was polarized. A classical electromagnetic theory of this effect was developed by Frank and Tamm [23] in 1937. They had to overcome the then commonly held assumption that only accelerated charges radiate (this is true only in vacuum), and a general hesitancy to investigate faster than light particles. A quantum calculation of this effect by Ginsburg [24] in 1940 resulted in only minor modifications to the Frank-Tamm theory. Together with Frank and Tamm, Cherenkov was awarded the Nobel Prize in 1958.

The Cherenkov effect can be understood from the fact, that the charged particle locally polarizes atoms or molecules in the medium and creates a time-dependent dipole field resulting in an emission of electromagnetic radiation. If the particle is slower than the local velocity of light, the dipoles are arranged symmetrically around the particle track and the resulting integrated dipole field is zero. Only if $v > c/n$ or

$$\beta > \frac{1}{n}$$

Equation 1

the symmetry is broken and there is a net dipolefield resulting in the emission of electromagnetic radiation – compare Fig. 6.

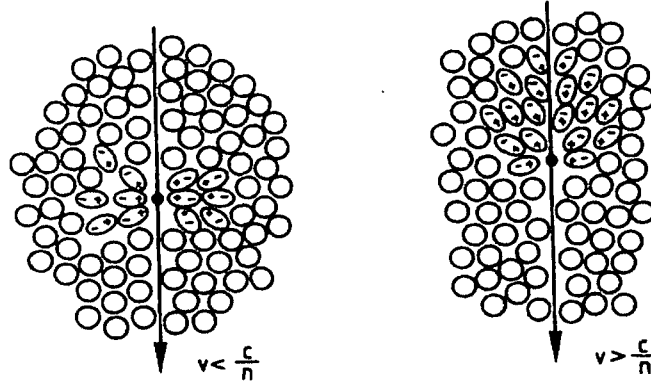


Fig. 6 Illustration of the polarization of a medium due to a charged particle traveling above or below the speed of light in this medium [25].

The emission angle θ_c of the Cherenkov light with respect to the direction of the particle track can be derived from a simple consideration of the positive interference of photons in the direction of θ_c following from Fig. 7. While the particle travels the distance $AB = t\beta c$, the photon covers the distance $AC = tc/n$ and the relation for the emission direction becomes²

$$\cos \theta_c = \frac{1}{n\beta}$$

Equation 2

With the polar emission angle θ_c fixed by Equation 2 the Cherenkov photons are emitted isotropically in azimuthal direction. Consequently they propagate on a cone around the direction of the particle with an included angle θ_c . A further property of Cherenkov photons is their polarization with the electric field vector in the plane defined by photon and particle direction. This can be understood from the orientation of the dipoles illustrated in Fig. 6.

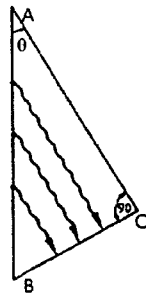


Fig. 7 Derivation of the emission angle θ_c [25].

The threshold already stated in Equation 1 also follows from Equation 2. At the threshold $\beta_{th} = 1/n$ or expressed with the Lorentz factor γ :

² By taking into account the quantum theory of Cherenkov effect, the recoil of the charged particle of momentum p slightly modifies the classical Cherenkov equation by providing an additive term that is completely negligible for any practical application.

$$\gamma_{TH} = \left(1 - \frac{1}{n^2}\right)^{\frac{1}{2}}$$

Equation 3

At the threshold the radiation is emitted in forward direction and the emission angle increases with the speed of the particle. The emission angle takes its maximum for $\beta = 1$:

$$\theta_{c,MAX} = \arccos \frac{1}{n}$$

Equation 4

Both the threshold effect and the dependence of the emission angle of the Cherenkov light on the particle velocity can be used to identify a particle of a known momentum $p = m_0 \gamma v \beta$.

The spectral dependence of the radiation can be taken into account by means of Frank and Tamm's equation, which describes the energy radiated in the frequency interval $d\omega$ and per unit length dx by a particle of charge Ze :

$$\frac{d^2W}{dx d\omega} = \frac{Z^2 e^2 \omega}{c^2} \left(1 - \frac{1}{\beta^2 n^2(\omega)}\right)$$

Equation 5

Due to the chromatic dispersion of the optical medium, n is a function of the radiation frequency. Integrated over the radiating path length L the energy radiated in the frequency interval $d\omega$ is:

$$\frac{dW}{d\omega} = \frac{LZ^2 e^2 \omega}{c^2} \left(1 - \frac{1}{\beta^2 n^2(\omega)}\right)$$

Equation 6

Compared to the energy loss due to ionization and excitation, the energy loss due to the emission of Cherenkov light is small, even in the case of minimum ionizing particles. E.g. for gases with $Z > 6$ it is less than 1 % of the energy loss due to ionization and excitation.

The most important quantity for the design of a Cherenkov detector is the emitted number N of Cherenkov photons, which is easily obtained from Equation 6:

$$N = \frac{LZ^2 \alpha}{c} \int \left(1 - \frac{1}{\beta^2 n^2(\omega)}\right) d\omega$$

$$N = 2\pi LZ^2 \alpha \int \left(1 - \frac{\beta_{TH}^2}{\beta^2}\right) \frac{d\lambda}{\lambda^2}$$

Equation 7

where α is the fine structure constant. It follows that in 1 [cm] of material with a refractive index n , the number of photons emitted in the spectral range of 1 [eV] by a particle of charge Z and $\beta \sim 1$ is given by

$$N[cm^{-1}eV^{-1}] = 370Z^2 \left(1 - \frac{1}{n^2}\right)$$

Equation 8

The total number of photons emitted can be obtained by integrating over the energy interval that is used, however the number of photons emitted per unit length and per unit energy is a constant. From the $d\lambda/\lambda^2$ dependence of the number of photons already follows that most of the photons are emitted in the UV range. From Equation 8 it also follows that the number of emitted photons is rather small and very efficient photon detectors are required to measure Cherenkov light.

2.2 Particle identification by means of the Cherenkov effect

A particle can be identified by its mass and electrical charge. If the momentum and charge sign of the particle can be obtained from the measurement of its trajectory in a magnetic field, it is necessary to measure either its velocity or its kinetic energy in order to determine the mass. From the relativistic relationship between momentum, velocity and mass

$$p = m\gamma \cdot c\beta$$

Equation 9

follows how accurately the mass can be resolved depending on the velocity and momentum resolution:

$$\left(\frac{dm}{m}\right)^2 = \left(\gamma^2 \frac{d\beta}{\beta}\right)^2 + \left(\frac{dp}{p}\right)^2$$

Equation 10

For two relativistic particles with masses m_1 and m_2 and a given momentum p a separation becomes more and more difficult with increasing momentum. As the velocity approaches the speed of light with increasing p , the difference in velocity decreases and consequently the velocity resolution $\Delta\beta/\beta$ must improve. From a calculation of $m_1^2 - m_2^2$ with Equation 9 follows the approximation

$$\frac{\Delta\beta}{\beta} \cong \frac{m_1^2 - m_2^2}{2p^2}$$

Equation 11

for the velocity resolution as a function of the momentum. Fig. 8 shows the required resolution for the separation of pions and kaons or protons and kaons as a function of the momentum.

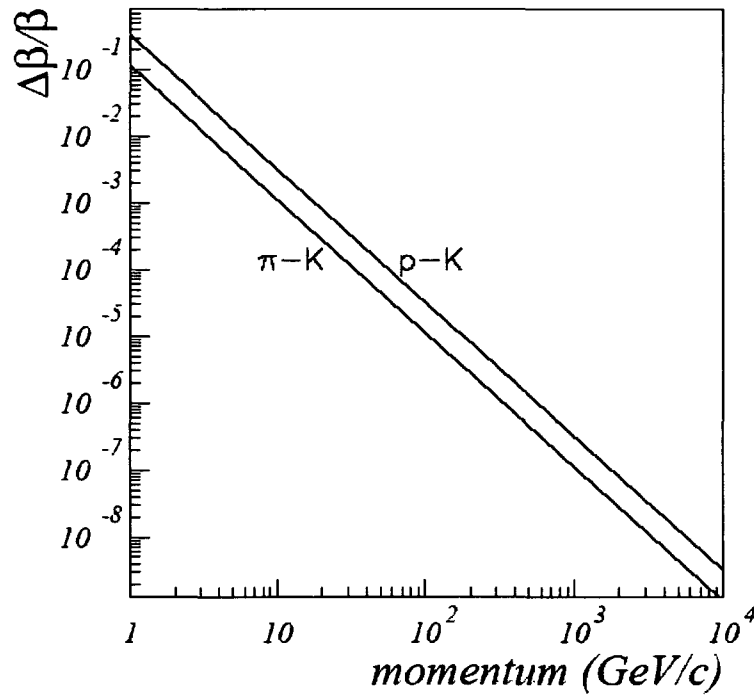


Fig. 8 Required velocity resolution for the separation of pions and kaons or protons and kaons as a function of the momentum.

The velocity of the particle can be derived from energy loss or time of flight (TOF) measurements or from the detection of Cherenkov or transition radiation. While PID by TOF is limited to the range of low momenta (<1.5 [GeV/c] for 1 [m] distance and 50 [ps] time resolution) the detection of Cherenkov light makes a separation of particles with higher momenta (e.g. proton identification up to 30 [GeV/c] with a CF_4 radiator) possible.

Cherenkov detectors use either the threshold effect to discriminate between particles above and below threshold, or they determine the velocity of the particle by a measurement of the emission angle:

$$m = \frac{p}{c} \sqrt{n^2 \cos^2 \theta_c - 1}$$

Equation 12

Fig. 9 shows the variation of the Cherenkov angle as a function of β . The highest sensitivity for a measurement of θ_c is given close to the threshold where the variation of the angle with β is largest. However from Equation 7 follows that the number of photons emitted close to the threshold is very small. In order to obtain a good velocity resolution Cherenkov detectors have to be designed to operate close to the threshold and consequently the main concern in the detector design is to optimize the detection efficiency for single Cherenkov photons.

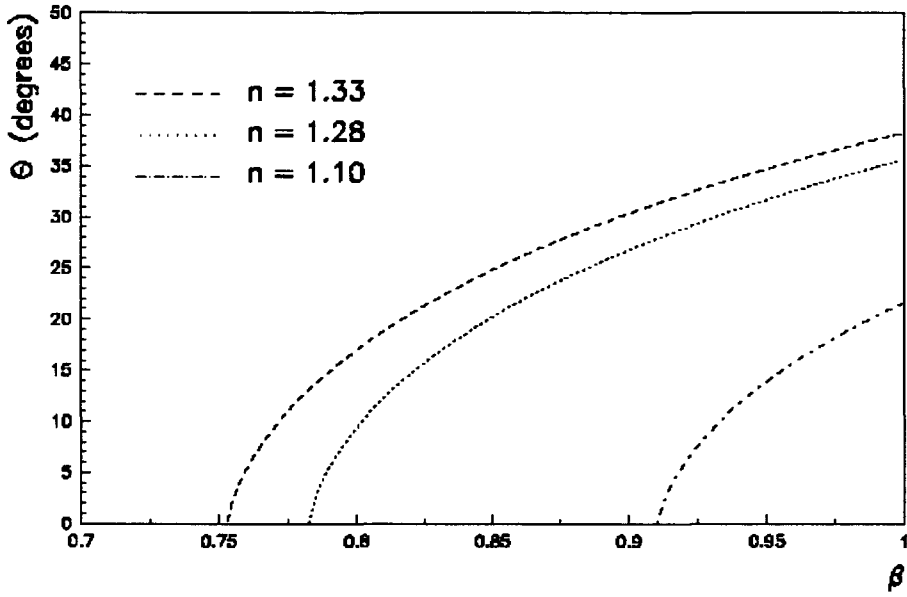


Fig. 9 Variation of the Cherenkov angle with β .

In its basic form any Cherenkov detector has to combine a radiating medium of a suitable refractive index n with a photon detector. The photoelectrons have to propagate the radiator and some optical elements, e.g. a window before they reach the photon detector. The absorption of photons inside the radiator and windows has to be accounted for by means of the transmittance $T(\omega)$ of the system. If a mirror is used to focus the light onto the photon detector, the reflectivity $R(\omega)$ has to be taken into account. Inside a photon converter the photons create charges, i.e. a photoelectron, with a certain quantum efficiency $QE(\omega)$. The quantum efficiency specifies how many electrons are created per incident photon and depends on the type of photon detector which is used. The photoelectron itself has to be detected and amplified to create a readable signal, which is again performed with a certain efficiency depending on the specific method, e.g. a phototube or multi wire proportional chamber (MWPC) as in the case of the ALICE/HMPID detector. This efficiency is referred to as the single electron detection efficiency ϵ . If the electron is detected by means of gas ionization followed by an avalanche process in a MWPC, the electron produces a charge pulse which is recorded by the readout electronics. At moderate gains up to $5 \cdot 10^5$ the pulse height distribution is exponential

$$P(q) = \frac{e^{-q/\langle q \rangle}}{\langle q \rangle}$$

Equation 13

$P(q)$ is the probability that an avalanche has a charge q and $\langle q \rangle$ is the mean charge of the avalanche. The single electron detection efficiency is then given by

$$\epsilon = \int_{q_{TH}}^{\infty} P(q) dq = e^{-q_{TH}/\langle q \rangle}$$

Equation 14

where q_{TH} is the detector noise threshold.

A given photon finally leads to a signal with a probability $\varepsilon \cdot QE(\omega) \cdot T(\omega) \cdot R(\omega)$. These parameters are used to define the so called figure of merit N_0 which is used to characterize Cherenkov detector:

$$N_0 = \frac{\alpha}{c} \int \varepsilon \cdot QE(\omega) T(\omega) R(\omega) d\omega$$

Equation 15

The integration limits are given by the photo ionization threshold of the photon converter at the low energy boarder and by the system transparency cutoff at the high energy boarder. This number is a measure for the quality of the detector. If the wavelength dependency of the refractive index can be neglected within the wavelength range defined by transparency and photo-conversion threshold, the number of detected photons can be written as

$$N = N_0 L \cdot \sin^2 \theta_C$$

Equation 16

by means of Equation 7 and Equation 15. Due to the inherently statistical processes of photon emission, conversion and detection the quantity given by Equation 16 is the mean or expected value of a Poisson distribution.

For β approaching 1 the Cherenkov angle assumes its asymptotic value $\theta_{C,MAX}$ related to threshold Lorentz factor γ_{TH} (see Equation 3 and Equation 4):

$$\sin^2 \theta_{C,MAX} = \frac{1}{\gamma_{TH}^2}$$

Equation 17

At the maximum emission angle also the number of Cherenkov photons is maximized:

$$N_{MAX} = \frac{N_0 L}{\gamma_{TH}^2}$$

Equation 18

The number of detected Cherenkov photons is very important for the velocity resolution of the detector. From Equation 2 follows:

$$\left(\frac{\sigma_\beta}{\beta} \right)^2 = (\tan(\theta) \cdot \sigma_\theta)^2 + \left(\frac{\sigma_n}{n} \right)^2$$

Equation 19

The chromatic aberration of the radiating medium, σ_n , is usually the dominant contribution to the detector precision, especially if the RICH detector is designed to be operated in the ultraviolet region, as the dispersion is usually much higher in the UV region. The spread in particle direction due to multiple scattering in the radiator, the finite spatial resolution of the photon detector and the aberration of the optics lead to an uncertainty σ_θ . Since each

detected photoelectron gives a separate measurement, for N photoelectrons, the Cherenkov angle resolution is improved:

$$\sigma_{\theta_c} = \frac{\sigma_{\theta}}{\sqrt{N}}$$

Equation 20

2.3 Cherenkov detector concepts

The capability of using the Cherenkov radiation for PID, was already suggested by Cherenkov himself. A major breakthrough in this technique was achieved in the 1940s with the availability of photomultipliers capable of detecting feeble light with high efficiency and fast response. Since then detectors have been designed and built for nuclear and particle physics experiments as well as for astrophysics applications. Cherenkov detectors played a fundamental role in important high energy physics achievements, for example in the discovery of the antiproton. The idea to discriminate particles by differentiating between different values of the emission angle was conceived by A. Roberts in 1960. T. Ypsilantis and J. Seguinot demonstrated the applicability of this method in 1977 by imaging Cherenkov photons directly in a gaseous photo-detector. The technique was named Ring Imaging Cherenkov (RICH). More references to the historical development of Cherenkov detectors can be found for example in [27].

2.3.1 Detector components and materials

Radiators

The momentum range in which PID has to be performed determines the choice of the radiator. The small amount of Cherenkov photons emitted from a charged particle limits the choice of radiator materials, which should neither scintillate nor have absorption bands in the interesting wavelength range, which is usually in the UV or far UV range due to the $1/\lambda^2$ dependence of the Cherenkov spectrum. Solid materials, liquids and gases are used as radiators in Cherenkov detectors. Gaseous radiators allow to adjust the refractive index continuously by varying the pressure. The gap in the range of refractive indices between gases (e.g. pentan $n = 1.0017$) and liquids (e.g. C_6F_{14} $n = 1.28$) can be filled with aerogels. Aerogels are SiO_2 materials with a very porous structure containing air bubbles. The size of these structures is in the range of 1-10 [nm] and therefore much smaller than the wavelength of the Cherenkov photons. Consequently the photons “see” a mean refractive index which is related to the density of the aerogel. Table 1 lists different radiator materials with their refractive indices. The values cited in this table should only illustrate the range of materials and refractive indices, however it has to be kept in mind that n can vary strongly in the UV and for practical purposes the dispersion $n(\lambda)$ has to be taken into account. The radiator is separated from the photon detector and the windows have to be optimized for transmission in the low wavelength region. Calcium fluoride, magnesium fluoride, lithium fluoride, quartz and fused silica are suitable materials. If mirrors are used, the reflectivity has to be optimized for the wavelength as well. Due to the fact that Cherenkov light is

linearly polarized, all materials have to be fully isotropic and reflection losses at the material interfaces have to be carefully analyzed.

Material	n	$\pi_{thr}(GeV/c)$	$K_{thr}(GeV/c)$	$P_{thr}(GeV/c)$	$\theta_{max}(\beta=1)$
Diamond	2.417	0.06	0.25	0.42	65°
Plexiglas	1.488	0.13	0.45	0.85	48°
Vodka	1.363	0.15	0.53	1.01	43°
Water	1.332	0.16	0.56	1.07	41°
C_6F_{14}	1.29	0.17	0.60	1.13	39°
CF_4 (liquid)	1.226	0.19	0.7	1.32	35°
Aerogel	1.05-1.01	0.4-1	1.5-3.5	3-7	18° - 8°
C_4F_{10}	1.00140	2.6	9	17	3°
Isobutane	1.00127	3	10	18	2.9°
Argon	1.00059	4	14	27	2°
CF_4 (gas)	1.00050	5	16	30	1.8°
Methane	1.00051	5	16	30	1.8°
Air	1.00029	6	20	39	1.4°
Helium	1.000033	17	60	115	0.5°

Table 1 List of radiator materials with refractive indices and threshold momenta for pions, kaons and protons.

Photon detectors

Due to the low energy of Cherenkov photons only the photoelectric effect³ can be used to detect Cherenkov light, either in gases or in solid materials, e.g. thin layers of photoelectric substances, allowing to extract the photoelectrons. The photoelectrons have to be detected with high efficiency due to the small number of primary Cherenkov photons. There are basically two categories of photon detectors: gaseous or vacuum based devices. This terminology refers to the electron amplification process rather than to the photosensitive material.

In gaseous photon detectors the photoelectrons are amplified by gas multiplication e.g. in a MWPC. The photoelectrons themselves are either created in a photosensitive vapor, which is added to the chamber gas, or in a solid photocathode. Examples for photosensitive gases are triethylamine (TEA) or tetrakis(dimethylamine)ethylene (TMAE), which has been used in the DELPHI/RICH detector. An example for a solid photon converter is CsI. The signal produced in the MWPC can be read out from a segmented pad cathode, allowing spatial sensitivity of the detector. However the de-excitation of avalanche ions can lead to feedback photons which produce new electrons in the photosensitive material. This photon feedback limits the chamber gain. A relatively new development in gaseous photon detectors are Gas Electron Multipliers (GEMs) [28], which consist of thin metal-insulator-metal foil composites with small holes (50-100 μm). The electrons, which are released in the gas above the foil or in a thin photocathode layer on top of the foil, are amplified in

³ The two other interaction mechanisms of photons with matter, Compton effect and pair production, require much higher photon energies.

avalanches in the high field in these channels and localized and detected on a segmented readout board. This technology allows reducing both photon- and ion⁴-feedback.

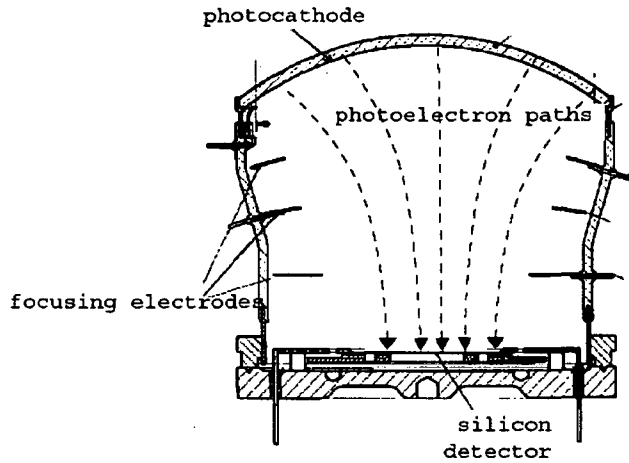


Fig. 10 Layout of a HPD photon detector.

Vacuum based photon detectors are for example standard photomultiplier tubes (PMTs) and hybrid photodevices (HPD). PMTs feature low noise, high gains and high rate capabilities and a high single electron detection efficiency. However this technology is sensitive to magnetic fields and the cost per channel is relatively high. Fig. 10 shows the layout of another vacuum based photon detector, the HPD. These devices consist of a transmissive photocathode. In an electric field the photoelectrons released from the photocathode are accelerated and focused onto an array of silicon diodes where they create a signal by electron-hole production. The HPDs are also sensitive to magnetic fields. Large area HPDs have been developed at CERN for the LHCb/RICH detector.

2.3.2 Threshold counters

Cherenkov threshold detectors use a specific radiator medium whose refractive index n is chosen in such a way that different particle species with different masses can be discriminated, as only the lighter particles are fast enough to be above the threshold for the emission of Cherenkov photons. A modern version of the Threshold Cherenkov detector was proposed [29] in 1995 for performing the hadron identification in the 3-8 [GeV/c] momentum range in the CERN-NA44 heavy ion experiment. The device, called TIC (Threshold Imaging Cherenkov) is shown in Fig. 11. It exploits the property of a gaseous wire chamber equipped with a UV sensitive pad-segmented cathode to localize with high spatial accuracy Cherenkov photons. Contrary to the traditional threshold counters, TIC can be employed in experiments with several particles in the detector acceptance.

⁴ Ion backflow to the photocathode material can cause ageing problems as discussed in Chapter 8.

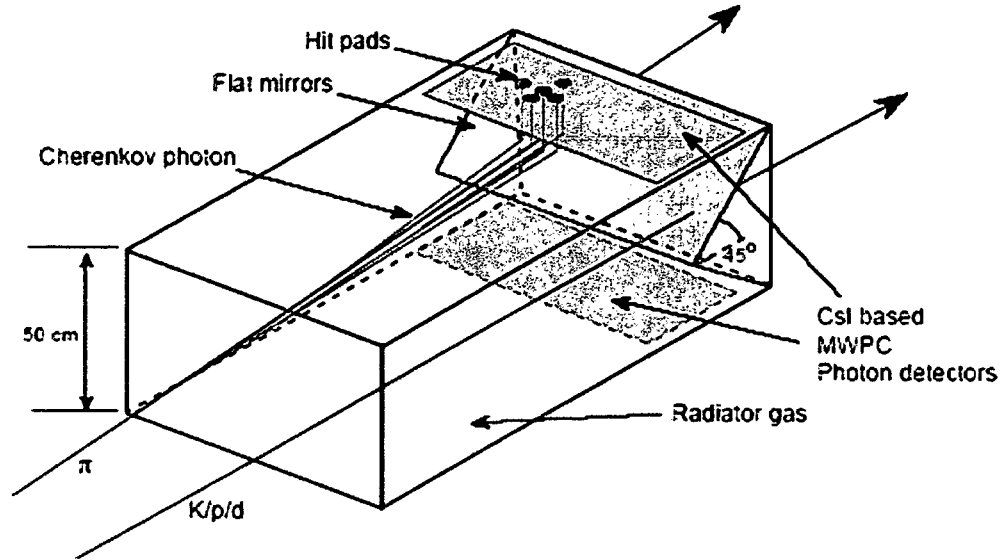


Fig. 11 Schematic layout of a TIC detector. Two particles are traversing the gas radiator, one of them emits Cherenkov photons since it is above the Cherenkov threshold.

For many applications a combination of several radiators is used to achieve a high momentum range of the detector. For the discrimination between pions, kaons and protons for example, a combination of 3 threshold counters with different radiators is conceivable in which the light pions give a signal in all 3 counters, the kaons in 2 of 3, whereas the heaviest protons only emit radiation in one radiator. With such a combination PID can be extended up to momenta of a few 10 [GeV/c].

2.3.3 Differential counters

In contrast to a threshold counter, which allows only the distinction above or below threshold, differential counters also allow measuring β by limiting the acceptance of the photon detector for a certain θ_c . Fig. 12 shows the Cherenkov counter used in the antiproton discovery experiment by Segre, Chamberlain, Wiegand and Ypsilantis [30]. It consisted of a quartz cylinder radiator, a cylindrical reflecting mirror and three PMs. The device achieved its β selectivity due to the limited axial length of the cylindrical mirror. The β range was varied by moving the cylindrical mirror relative to the radiator. The

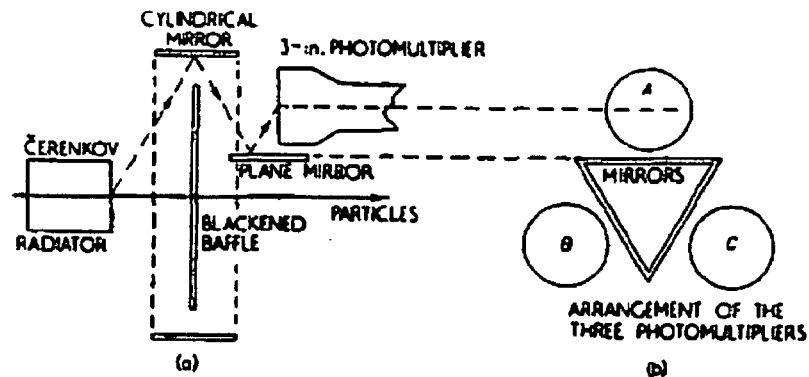


Fig. 12 The differential Cherenkov counter used in the antiproton discovery experiment: (a) side view; (b) end view.

Differential counters are characterized by an excellent velocity resolution, however their drawback is the limited detector acceptance, for both particle velocity and angle.

2.3.4 RICH detectors

In a Ring Imaging Cherenkov (RICH) detector the cone of Cherenkov light produced in a suitable radiator is detected on a position sensitive planar photon detector. The position sensitivity allows reconstructing a ring or disc, the radius of which is a measure for the Cherenkov emission angle. These detectors have a large acceptance and allow the simultaneous detection of several particles from one event due to a high spatial and time resolution of the photon detectors. Both focusing and proximity-focusing detector layouts are used as shown in Fig. 13. In the focusing layout the photons are collected by a mirror of focal length f and focused onto the photon detector placed at the focal plane. The result is a circle of radius $r = f \tan \theta_c$, independent of the emission point along the particle track. This scheme is suitable for low refractive index radiators, i.e. gases, due to the larger radiator length needed to create enough photons. In the more compact proximity-focusing design a thin radiator volume emits a cone of Cherenkov light which traverses the proximity gap and is detected on the photon detector plane. The image is a ring of light the radius of which is defined by the Cherenkov emission angle θ_c and the proximity gap. The ring thickness is determined by the thickness of the radiator.

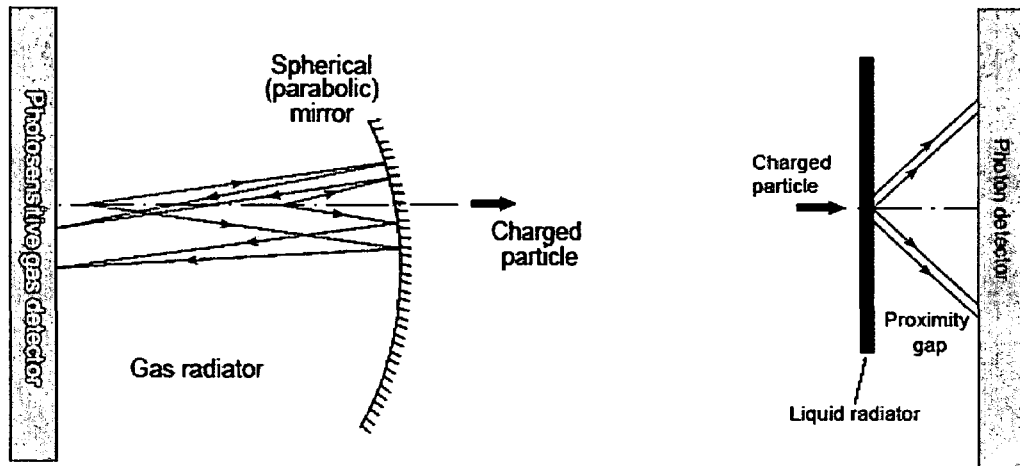


Fig. 13 Focusing (left) and proximity-focusing (right) layouts for a RICH detector.

If a CsI photocathode in combination with a MWPC or GEM foil is used as a photon detector, the proximity-focusing layout allows covering large areas, which makes this technology very attractive for HEP experiments requiring a large acceptance. Table 2 lists several experiments using a CsI based RICH detector for PID.

EXPERIMENT	DETECTOR	RADIATOR	AREA CsI-PC m ²
<i>NA44-SPS completed</i>	MWPC	ISOBUTAN	2 PCs of 78x19 cm ² 0.3 m ²
<i>STAR-RHIC completed</i>	MWPC	C6F14	4 PCs of 64x40 cm ² 1 m ²
<i>HADES-GSI running</i>	MWPC	C4F10	6 PCs of 0.25 m ² 1.5 m ²
<i>COMPASS-CERN running</i>	MWPC	C4F10	16 PCs of 58x58 cm ² 6 m ²
<i>ALICE-HMPID In preparation</i>	MWPC	C6F14	42 PCs of 64X40 cm ² 11 m ²
<i>HALLI-JLAB running</i>	MWPC	C6F14	3 PCs of 64x40 cm ² 0.7 m ²
<i>PHENIX In preparation</i>	GEM		20 PCs of 30X30 cm ² 1.8 m ²

Table 2 List of CsI based RICH detectors in operation or preparation.

2.4 The ALICE/HMPID RICH

The ALICE/HMPID system consists of an array of seven identical RICH detector modules of 1.5×1.5 [m²], arranged in a cupola-like structure and located at a radial distance of 4.7 [m] from the interaction point (Fig. 14). A detailed description of the detector can be found in [1] and [6]. The most recent publications covering the current status of the HMPID project are [18]-[21].

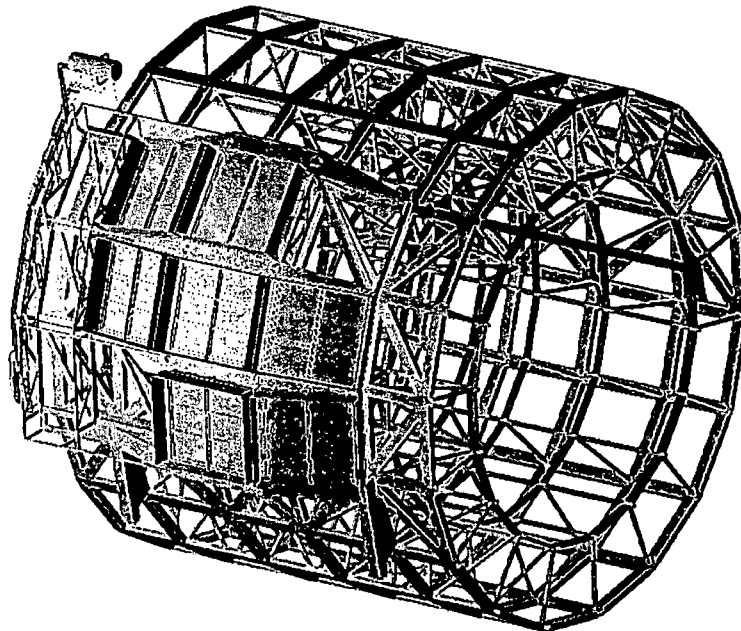


Fig. 14 The seven modules of the ALICE/RICH on the spaceframe.

Detector layout

charged particle

15 mm

Neoceram
C₆F₁₄ liquid radiator
fused silica

CH₄

collection electrode

80 mm

pad cathode coated with CsI film

MWPC

Front-end electronics

100 μm Cu-Be₂ wires

20 μm W-Re₃ wires

4 mm

4.2 mm

8x8.4 mm pads

+ 2.05 kV

Fig. 15 Schematic layout of the ALICE/RICH.

The readout of the HMPID modules for the total of 161280 cathode pads is organized according to a parallel/serial architecture and is based on two ASICs: the GASSIPLEX chip, a 16-channels charge sensitive pre-amplifier and shaper, enabling the determination of the hit coordinates by centroid measurement, and the DILOGIC chip, a digital processor for zero suppression, specifically developed for this application.

⁵ NEOCERAM® is a glass material having thermal coefficient very close to the fused silica plates used as UV-transparent windows.

Gas system

High gas purity (5 [ppm] of O_2 and H_2O , total absence of silicon or other outgassing organic compounds from any system component) is required for the stability of the MWPC efficiency and even more so due to the large CsI hygroscopicity (any exposure to moisture will result in a QE deterioration). The chamber deformation induced by the gas pressure has to be minimized to keep the parallelism of radiator vessels and photocathodes within 100 [μm] and avoid the breaking of the fragile radiator vessels resulting from the deflection of the supporting composite panel. A module has a total volume of 200 [l] and can be flushed up to 100 [l/h] with Ar, during stand-by, or CH_4 , during operation. The gas pressure will be kept at 2-3 [mbar].

Liquid system

The liquid circulation system has to fill and drain the radiator vessels (8 [l] volume each) independently, remotely and safely, at a constant flow of 4 [l/h]. Due to its intrinsic high degree of safety, gravity flow has been adopted to prevent accidental large hydrostatic loads in the fragile radiator vessels. In addition, C_6F_{14} has a high affinity for O_2 and H_2O resulting in a decrease of the transparency in the VUV region, the Cherenkov photons spectral range where CsI is sensitive. Therefore, a dedicated filtering station, with 13X molecular sieves, will be implemented.

Detector performance

The HMPID modules were commissioned in beam tests, in which the MWPC is studied with respect to operational stability (HV, rate, noise...) and gain uniformity. Furthermore the quality of the CsI photocathodes can be checked in terms of an evaluation of the number of resolved clusters per track. By means of a Monte Carlo simulation [44] QE data can be extracted from the test beam measurements. Fig. 16 shows an event display on one of the CsI PCs tested in 2004. So far, five modules have been tested in the CERN/SPS-X5 area with a 120 [GeV/c] pion beam.

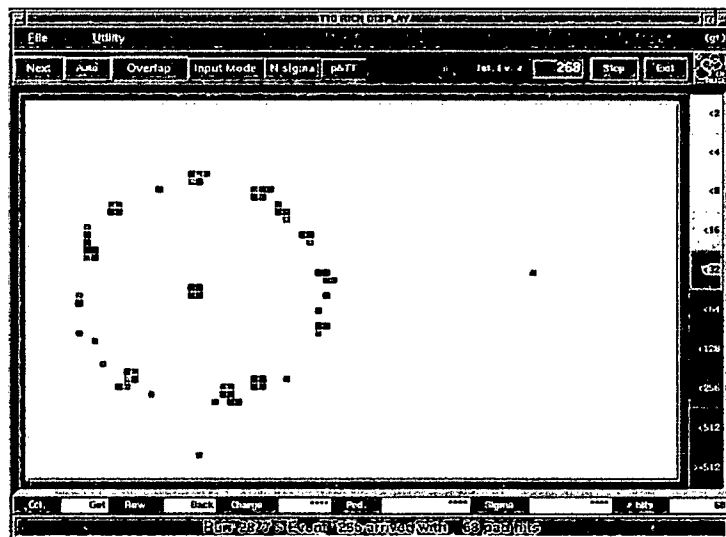


Fig. 16 Event display during a beam test of PC⁶ 41.

⁶ PC numbering system: PCs are referred to as PCxx where xx is the number of the PC. PCs 1-40 are prototypes and test PCs, from PC41 on they were produced for use in the detector.

Fig. 17 shows the variation of the Cherenkov angle resolution from single photon up to 25 detected photons, measured in beam tests of the HMPID modules produced in 2004. The fitting curve corresponds, as expected (see Equation 20), to a scaling of the angular resolution with the square root of the number of detected photons. Studies of the analytical relation between the Cherenkov angle resolution and the corresponding momentum limit, set the resolution needed for 3σ π -K separation at 5 [mrad]. The experimental resolution shown in Fig. 17 refers to single particle events, where 3 [mrad] can be obtained with 15 detected photons. More details on the performance of the modules and especially the CsI PCs can be found in Chapter 7, as well as in the publications [18]-[21].

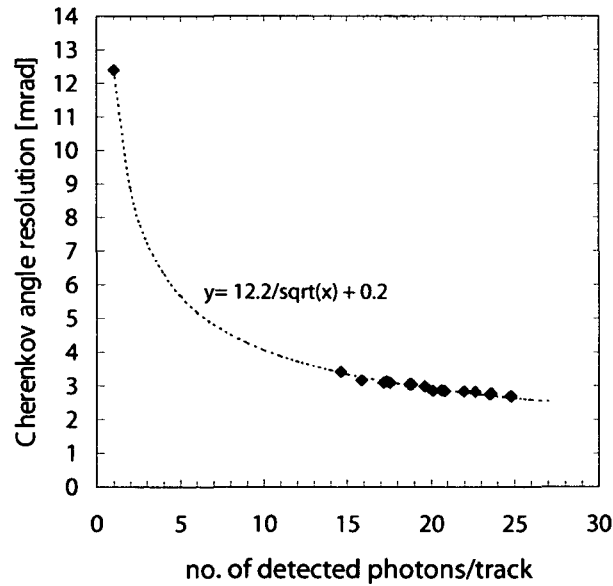


Fig. 17 Cherenkov angle resolution as a function of the number of detected photons per track.

Photon losses in the detector

As can be seen in the detector layout in Fig. 15 the Cherenkov photons produced in the radiator can be lost due to absorption or reflection in the detector materials or due to the QE and single electron detection efficiency. Table 3 lists the relative contributions in per cent of the various loss mechanisms in our detector geometry. From this comparison of the loss mechanisms follows the importance of the CsI QE for the detector performance. Most of the photons are lost due to the photon conversion and photoelectron emission process from the PC due to its QE. This result highlights the importance of the goal of this thesis to investigate and optimize the CsI photoemission properties. The second important loss mechanism is the absorption of photons in the radiator due to O_2 and H_2O contaminations in the liquid, which stresses the need for highly pure radiator liquid and the importance of the liquid system.

Loss mechanism	Percentage of lost photons
Absorption radiator	22.1%
Absorption quartz	3.7%
Absorption CH ₄	0.4%
Absorption wire planes	7.8%
Reflection Csl	4.5%
Csl QE (not converted)	53.8%
Chamber + FEE	1%
Detected photons	6.6%

Table 3 Photon losses inside the detector.

3 The CsI photocathodes

In this chapter a brief description of CsI photocathodes, their most important properties and the process of CsI deposition onto a suitable substrate will be given. The CsI deposition plant at CERN will be introduced as well as a VUV-scanner system to measure the quality of the PCs after production. This information was collected from a wealth of publications on CsI photocathodes listed in the literature section. It was the aim of this thesis to investigate the properties of CsI photocathodes described in the following section. Properties, obtained from R&D studies, which were performed mostly with small samples and often involving exposure of the samples to air, had to be re-measured for the case of the large area PCs in order to define an optimized procedure for the series production of PCs for the ALICE/HMPID detector and increase the understanding of the basic phenomena. A further aim of this thesis was to complete the VUV-scanner system (Section 3.5) and perform all the commissioning tests to derive reliable measurement procedures (Chapter 4).

3.1 Properties of CsI photocathodes

CsI films are used as photon converters in the UV range due to their excellent photoelectron yield over a relatively large spectral range. In order to create a photoelectron the photon needs sufficient energy to overcome both the bandgap E_g and the electron affinity E_a of the photoconverter:

$$h\nu = \frac{hc}{\lambda} \geq E_g + E_a$$

Equation 21

Therefore there exists a threshold for the photoemission. For CsI the bandgap is $E_g \cong 6$ [eV] and the electron affinity $E_a \cong 0.1-0.2$ [eV]. Consequently the threshold for photo emission is approximately $\lambda = 210$ [nm]. The QE increases from zero to values up to 0.35 - 0.4 at 160 [nm]. Examples for QE curves are given in Fig. 20 and Fig. 40. Towards the short wavelength end the use of CsI as a photo-converter is usually limited by absorption in gas or in other optical materials, like windows. Compared to other alkali halides and all other known solid photo-converters ([32], [33]), CsI has the largest QE, which is a consequence of both the low electron affinity and the relatively large electron escape length – compare Fig. 19. In comparison to gaseous photo-converters like TMAE [tetraakis (dimethylamine) ethylene] the QE is comparable in the short wavelength range but lower above 190 [nm].

Film deposition

Although different methods like electron beam evaporation [50] or sputtering were tested and used, resistive evaporation under vacuum (10^{-8} to 10^{-5} [mbar]) is normally used to deposit CsI layers onto metallic substrates. Several substrates, like Au, Ni, Al, or metals coated with thin films of these elements are in use. Copper substrates should be avoided because Cu interacts with CsI to form CuI. The raw material is a powder of very small CsI crystallites from varying suppliers. Details about the preparation of the CsI sources and the CsI deposition process established for the ALICE/HMPID PCs are given in Sections 3.4.1 and 3.4.3.

Layer thickness

A UV photon incident on a CsI layer is absorbed in the layer with a certain probability and can create photoelectrons. The photoelectrons are emitted isotropically and many of them will be lost due to collision processes inside the CsI. Depending on their initial energy and direction of movement only some of the electrons will reach and leave the surface – compare Fig. 18. The UV photons have an absorption length in the range of 10 [nm] to 20 [nm] [43] and can penetrate the CsI layer up to a depth of 50 - 90 [nm] at which 99% of the photons are absorbed.

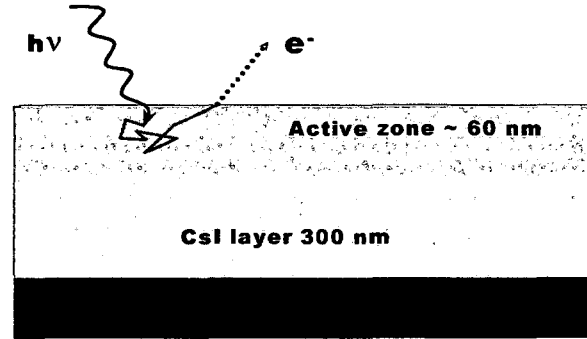


Fig. 18 Illustration of the photo electron creation process.

As shown in Fig. 19 from [42] the escape probability of the photoelectrons is the quantity determining the thickness of the active zone, which is relevant for creation of photoelectrons, which can actually leave the CsI layer and be measured. For a depth of < 60 [nm] the escape probability is almost zero and therefore only the first 60 [nm] of the layer contribute and the QE of CsI should be independent of the layer thickness of the CsI layer for more than 60 [nm]. For our PCs a thickness of approximately 300 [nm] was chosen in order to provide additional stability against moisture, which can destroy a thin layer much faster than a thick one, and to minimize any influence of the substrate.

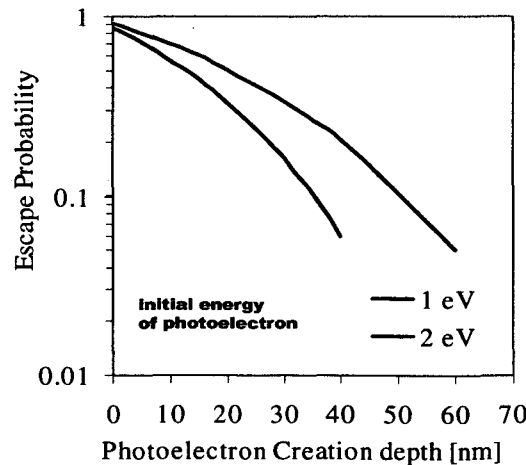


Fig. 19 Escape probability for photoelectrons from CsI published in [42].

Post deposition treatment

The quality of a CsI PC is known [45], [46], [6], [38] to depend on the treatment after coating. Initially the QE is rather low but it increases if the PC is heated or if the deposition is already performed on a hot substrate. The conditioning, initially described by Anderson

[45], consists of heating the photocathode under vacuum after the evaporation to 50 – 60[°C] for 4 – 6 hours. In addition, different configurations were tested such as flushing the vessel with CH₄ or C₂H₆ during the heating, varying the substrate temperature or the duration of the process. In Fig. 20, the enhancement of the QE with time is illustrated by a measurement made in the Weizmann set-up using a PCB substrate. A drastic increase in the QE was observed, mainly in the long wavelength range (> 190 [nm]), after heating the film to 60 [°C] for 5 hours compared with measurements taken just after the evaporation. In addition, the films appear to have a better stability following exposure to air after conditioning. Such an effect was systematically reproduced by Breskin on a large number of different substrates, PCB included [46].

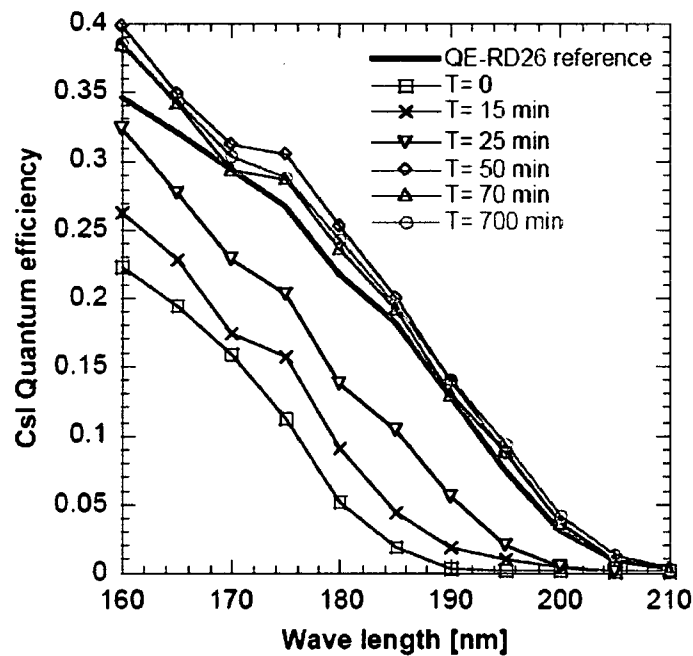


Fig. 20 Development of the QE during the heat enhancement phase after CsI deposition [46].

It should be mentioned that the positive influence of the post treatment was not observed by some authors [47]. Others [6], [38] tried to explain this with the fact, that different substrates were used, such as aluminum, known for their peculiar surface structure usually porous and oxidized. It was among the objectives of this thesis to further investigate the post deposition heat enhancement of the QE by means of photocurrent measurements on the large area PCs for the ALICE/RICH detector in order to increase the understanding of the effect and most of all to optimize the production procedure. The results of these tests, which are discussed in detail in Chapter 5, seem to indicate, that the quality enhancement of the CsI PCs is an effect that can take place with varying speed and increased temperature only accelerates a process, which can also happen without heating the PC.

Microanalysis studies of the CsI layers

In addition to measurements of photocurrents due to UV-induced photoemission, CsI photocathodes have also been characterized by means of surface analytical methods in order to make an effort to understand the surface properties of the films. The aim of the work carried out by several groups has been to find correlations between the

photoemission ability of CsI and other properties of the coatings, like structure, morphology and if possible relate them to the method of film preparation or the substrates used. The most significant work in this field has been described in [48]. Several experimental techniques were employed in this work, the most important being a laterally resolved electron spectroscopy for chemical analysis (ESCA) and photoemission electron microscopy (PEEM), which permit correlation of photoemission with I or Cs species at the surface. Other complementary techniques such as SEM and STM provide the gross structure of the surface. AFM measurements resolve even the atomic structure of CsI, indicating that the polycrystalline surface has indeed a very regular structure like that of the CsI crystal [48]. X-ray diffraction studies provide a good way for studying the chemical composition of the surface, and confirm the crystalline CsI structure. The most significant revelations of the microanalysis studies of thin CsI films are the confirmation of the role of the substrate material on the photoemission yield and the inhomogeneity of the photoemission correlated with the chemical composition, on a micrometer scale. It has been shown that very regular polycrystalline structures are contained on inert substrates (Au), with a grain size varying from a fraction of a micron to a few microns, depending on the substrate surface quality. The latter could be modified for example by vacuum coating of the sample metal surface with thin Al or C films. Films deposited on Cu substrates present very strong surface inhomogeneity, reflected by cracks and very irregular crystalline structures [48]. This is due to a chemical reaction between CsI and Cu, followed by surface decomposition into Cs and I species [48]. Thin Au coating of the Cu surface does not prevent this chemical reaction, while thicker Ni, Ni/Au and Sn/Pb coatings of Cu provide very smooth CsI films [49], [48]. These substrates, important for the preparation of pad readout electrodes for UV detectors, have very homogenous photoemission properties compared to that of Cu, as reflected by VUV-ESCA studies [48]. The substrates chosen for the PCs of the ALICE/HMPID detector are described in Section 3.3. Laterally resolved UV and X-ray induced photoemission and secondary electron emission studies indicate that on a microscopic scale (3-30 μm) the emission from CsI films is highly inhomogeneous. This is true not only for Cu but also for other substrates investigated [48]. The local variations reach factors up to 2-3 and are correlated with the chemical composition of the irradiated area. The enhanced emission is usually correlated with an excess of Iodine atoms.

Ageing due to exposure to humidity

CsI is a very hygroscopic compound and the hydration of the CsI surface is known to decrease the QE of the photocathode. Consequently all exposure of the CsI films to humid air should be avoided. An overview of the published literature is given in [38] and some results are also quoted in [6]. Heat enhanced photocathodes are reported to be more stable to exposure and a recovery of the decreased QE can be observed if the PC is heated under vacuum. The hydration of the CsI film affects the surface morphology. In Fig. 21, the texture of the non-exposed film is compared to the one observed after controlled exposures to a moist inert gas in the SEM chamber. Initially, the size of the grain is small, of the order of several hundred nanometers and increases significantly after a short exposure to moisture. The grains are also more faceted. After a longer exposure, the film becomes discontinuous and is composed of very large isolated grains [6].

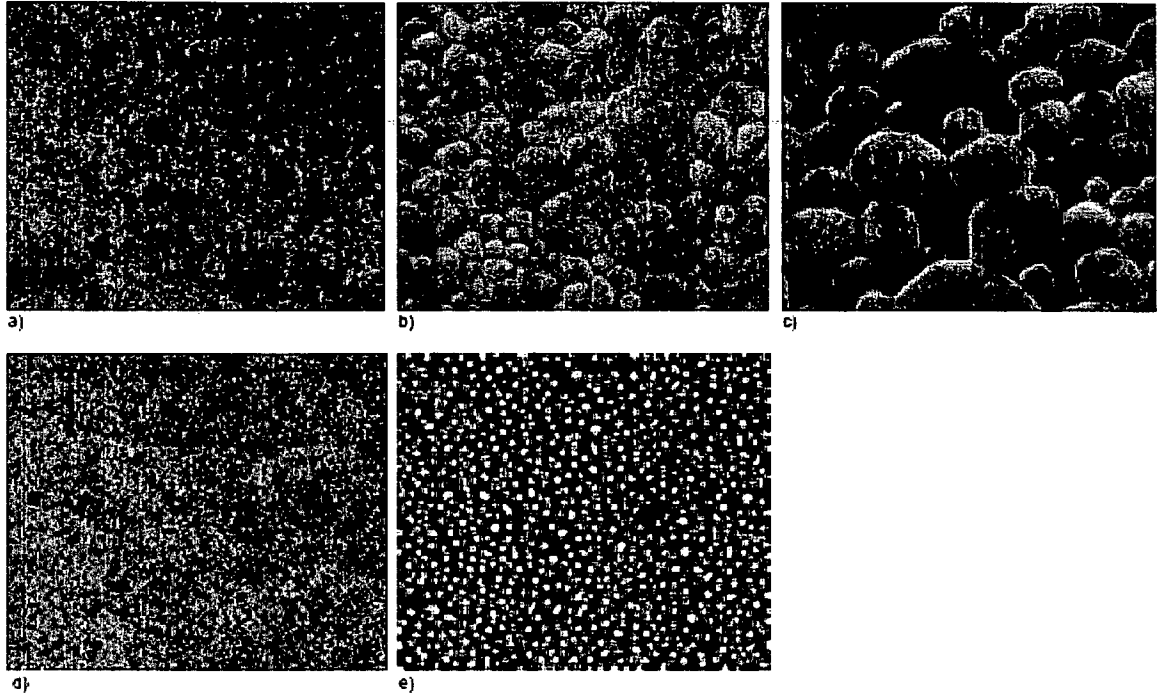
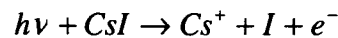


Fig. 21 SEM images: $\times 10\,000$. Influence on the morphology of a CsI film of an exposure to argon at a relative humidity of 80% during a time T . Substrate: G10/Cu/Ni/Au. Series a, b, c: thickness 400 [nm]. a) $T = 0$, b) $T = 3$ [min], c) $T = 5$ [min]. Series d, e: thickness 20 [nm]. d) $T = 0$, e) $T = 1$ [min] [6].

As a consequence to the sensibility of the PCs to humidity, strict procedures of storage and operation of the PCs under dry gas with levels of $\text{H}_2\text{O} < 10$ [ppm] are applied for the PCs of the ALICE/RICH detector. The mounting of the PCs on the detector is carried out in a custom made glove box. The effectiveness of these procedures is described in [35]. Within the framework of this thesis further investigations of the ageing of the ALICE/RICH PCs due to exposure to humid air were carried out. By means of photocurrent measurements before and after exposure the quality decrease of exposed PCs could be measured. The recovery of the exposed PCs due to annealing could also be observed. The measurements and results are described in Chapter 6.

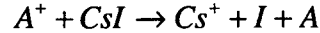
Ageing due to irradiation with UV and due to ion bombardement

Both irradiation with high fluxes of UV photons and the bombardement of the CsI layer with ions inside a detector are known to decrease the QE of CsI. Both processes are believed to cause a dissociation of the CsI molecules leading to an enrichment of the surface with Cs. In the case of irradiation with high intensity UV photons the reaction is



Equation 22

A similar process occurs, if the PC is mounted inside a MWPC where it is bombarded with ions originating from the avalanche processes in the chamber:



Equation 23

Due to the desorption of the iodine atoms the surface is enriched in Cs, which increases the electron affinity and consequently decreases the QE. An overview of existing literature can be found in [38], [51], [52].

Ageing due to irradiation with UV is of no relevance for the ALICE/HMPID detector, as the fluxes of Cherenkov photons inside the detector will be negligible. However higher photon fluxes are used in the quality evaluation photocurrent measurements described in Section 3.5. Therefore the ageing of large area PCs has been addressed in the commissioning tests of the photocurrent measurement system. PCs were irradiated with low fluxes ($2 \cdot 10^{10}$ [photons \cdot s $^{-1}$ \cdot cm $^{-2}$]) comparable to a standard measurement and with much higher fluxes ($6.2 \cdot 10^{14}$ [photons \cdot s $^{-1}$ \cdot cm $^{-2}$]) in order to produce a measurable effect. The results and a comparison to the effects reported in the literature are given in Section 4.7. The outcome of these tests was that the photocurrent measurements in our evaluation system do not damage the PCs due to the comparatively low fluxes. In addition to that, a full recovery of the irradiated positions was observed under vacuum after irradiation.

Ageing due to ion bombardement is more important for the ALICE/HMPID detector, as it will be exposed to high levels of ionizing radiation inside the ALICE experiment. The ionizing particles will continuously cause avalanche processes inside the MWPC chamber, producing ions which hit the CsI layer. To find out how much the detector suffers from this effect, an ageing test was carried out with a detector prototype, in which a standard large area PC was irradiated with a radioactive source. Details about this test, references to the relevant literature and a discussion of the results are given in Chapter 8. The most important result from the first test series was the discovery of a possible self-ageing effect which decreases the QE even after the irradiation is finished, probably due to interaction of the Cs enriched irradiated zones with contaminations in the gas (Ar, CH $_4$) used during operation or storage.

3.2 ASSET

ASSET is a laboratory set-up to characterize small samples of CsI film (1–10 [cm 2]) by performing evaporation, conditioning, QE evaluation, and storage in a container inside a vacuum vessel. The samples can be enclosed under vacuum which allows a transfer to any external measuring device, e.g. SEM, X-ray, without exposure to air. As seen in Fig. 22, the set-up is composed of two vessels, one used for film processing, the other for QE evaluation. They are separated by a vacuum valve to isolate one vessel from the other. An arm makes a linear transfer of the sample from one vessel to another and can also be rotated to vary the orientation of the substrate with respect to normal incidence. Fig. 23 shows the sample holder together with the lid, which allows to enclose the samples in vacuum for a transfer to SEM or any other analysis system without exposure to air. The system has been used to perform a relative comparison between different substrates, or for morphology studies similar to the ones presented in Fig. 21. Recently it was attempted to upgrade the system with a monochromator recuperated from a previous experiment. The UV source and the interference filters were removed from the measurement chamber and replaced by a 45° mirror. The monochromator and D $_2$ light source were placed inside a

box with a CaF_2 window, as shown in Fig. 24. The box can be purged with high purity argon in order to avoid any absorption of the short wavelength part of the UV spectrum due to water or oxygen. The monochromator box is attached to the measurement chamber via an extension of the measurement chamber, containing a lens and a diaphragm. Unfortunately the monochromator proved to be inadequate for use in vacuum. We observed instabilities in the measurements which we believe are due to outgassing of water and oxygen from some of the materials inside the monochromator and lamp housing. The outgassing occurs, as the lamp is heating up inside the box during operation. Nevertheless the system could be used to obtain some measurements with small samples within the framework of this thesis. These tests were carried out in order to reproduce effects measured on the large PCs for the detector and will be presented in the relevant chapters.

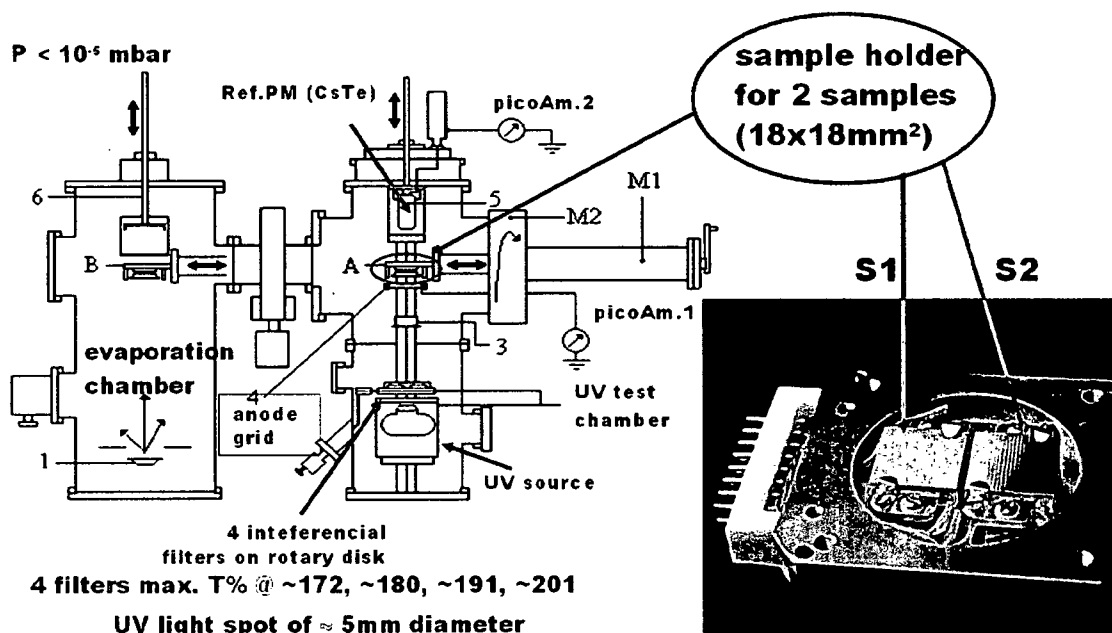


Fig. 22 Layout of the ASSET evaporation and measurement system for small samples and photo of the sampleholder.

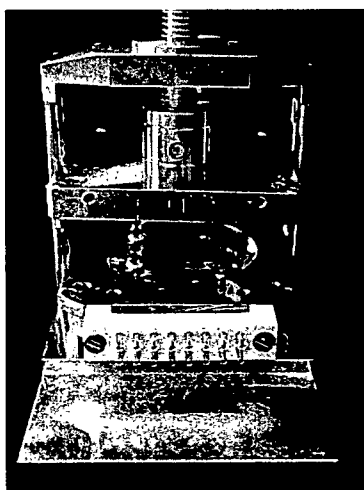


Fig. 23 Photo of the ASSET sampleholder and the lid which allows enclosure of the samples under vacuum and transfer without exposure.

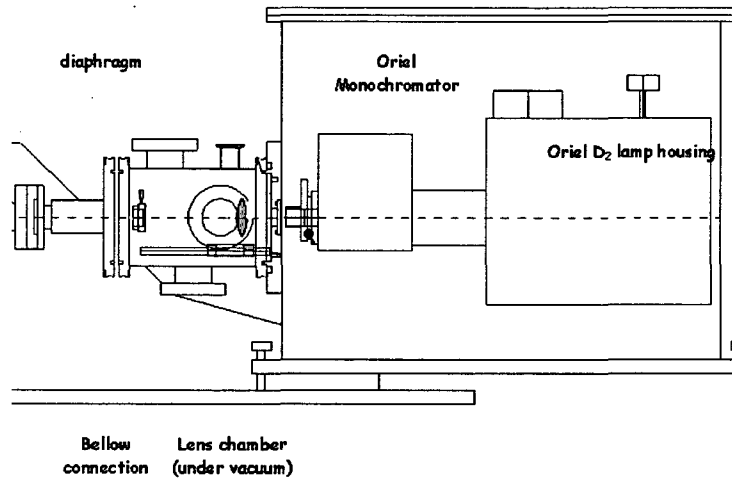


Fig. 24 Monochromator box for the ASSET system.

3.3 The Substrate

The substrate for the ALICE/HMPID PCs [6], [35]-[37] consists of double layer printed circuit boards (PCBs). There are two 40×30 [cm²] PCBs per PC, which are segmented into 8×8.4 [mm²] copper pads. The copper pads are coated with gold plated nickel. The nickel layer serves to prevent a reaction between CsI and Cu which would form CuI (compare 3.1), and the gold layer is chosen as an inert substrate to ensure stability. On a microscopic scale the roughness of the substrate is in the order of 0.2 [μm] (Fig. 26). The double layer PCB structure, which is illustrated in Fig. 25, guarantees gas-tightness. The two PCBs are glued onto an aluminum frame which is in turn glued onto a grounding plate as shown in Fig. 27. The front end electronics are directly attached to the backside of the substrate by means of one connector for every 48 pads. After the gluing the overall flatness of the 60×80 [cm²] PC is ± 50 [μm] and the frame limits the deformation of the PC to roughly 5 [μm/mbar]. This results in gain variations of less than 10 % in the chamber. The CsI deposition process (3.4.3) is carried out at a pressure of 10^{-6} [mbar]. Polluted substrates would not only lead to longer vacuum cycles due to outgassing problems. A contamination of the residual gas in the chamber could also degrade the CsI QE. As some of the substrate materials (PCB, glue) are not ideal for vacuum operations, special procedures and tools had to be developed to keep the substrate clean and minimize the use of glue. Before installation into the vacuum system the substrate undergoes an elaborate cleaning procedure including ultrasonic cleaning in strong detergents, de-mineralized water and pure alcohol. The complexity of the production and cleaning procedures is illustrated in the flowchart in Fig. 29 and Fig. 28 shows a photo of the substrate prior to CsI deposition.

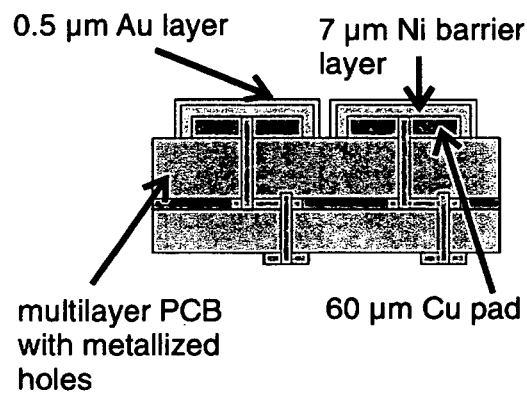


Fig. 25 Double layer PCB with copper pads. The Cu is coated with layers of Ni and Au. The double-layer structure ensures gas-tight connections between the pads and backside connectors.

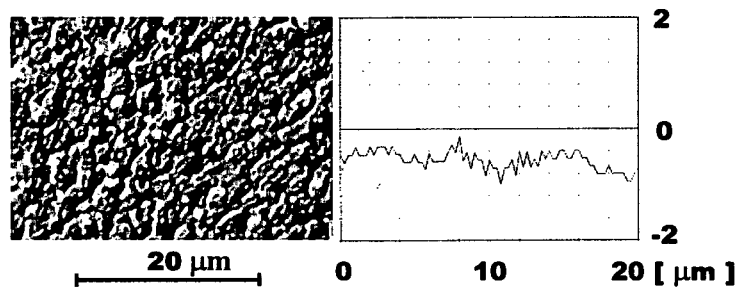


Fig. 26 Microscopic view and profilometric measurement on a typical substrate [37].

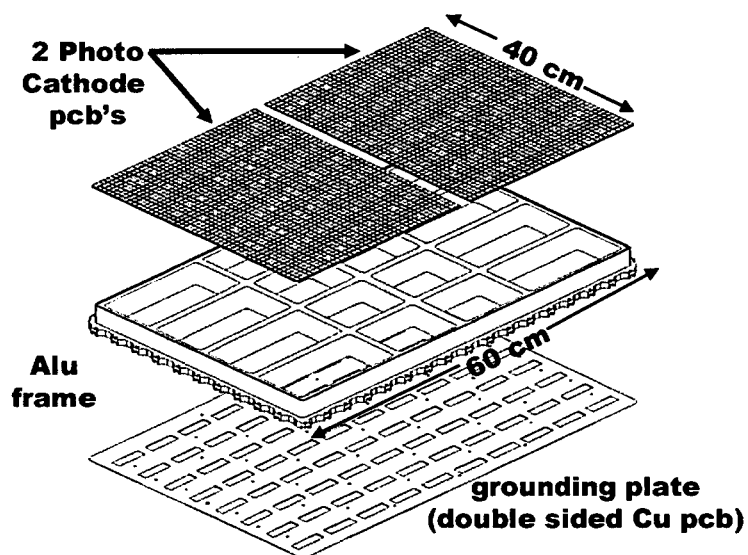


Fig. 27 The substrate consists of two engraved PCBs glued onto an aluminum frame and a grounding plate.

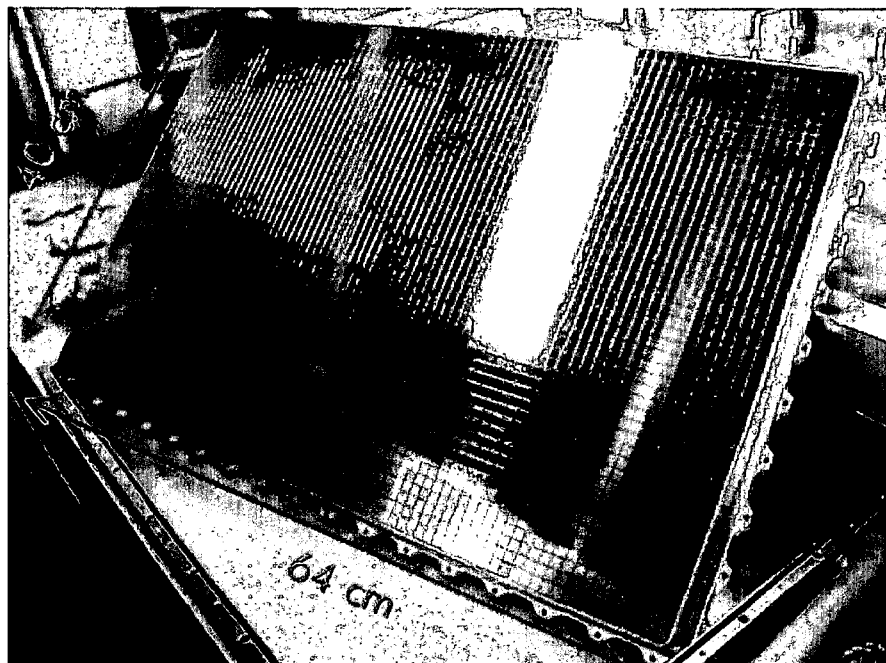


Fig. 28 Photo of a PC substrate prior to CsI coating.

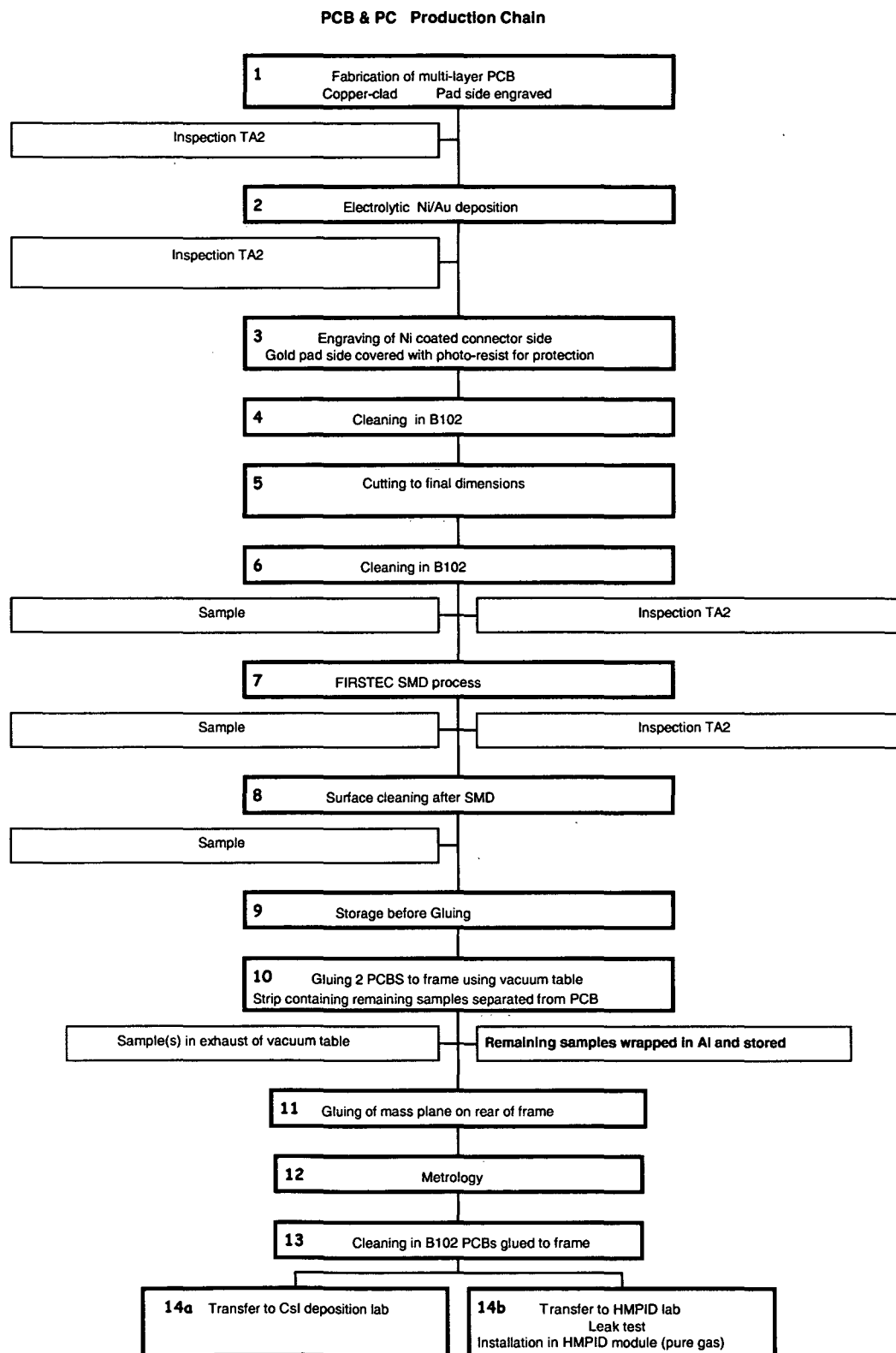


Fig. 29 Flowchart of the substrate production.

3.4 The CsI deposition facility

At CERN the large area CsI PCs are coated in the large (2000 liter) vacuum chamber shown in the drawing in Fig. 30 and on the photo Fig. 31. The system is equipped with a pre-vacuum pump and two large turbo molecular pumps and can reach a vacuum of around $10^{-8} - 10^{-7}$ [mbar]. The PC substrate is mounted in the chamber by means of an aluminum support plate which is hanging from two rails at the top of the chamber (compare Fig. 31). This backside plate also serves to close the connector side of the substrate. The backside volume can be pumped separately by means of an additional primary pump in order to separate the outgassing elements on the connector side (PCBs, glue, connectors) from the main vacuum. The CsI is deposited onto the substrate from 4 sources by resistive heating. The sources and shutters are shown in Fig. 31 and in the drawing in Fig. 30. The thickness of the CsI layer is measured during the evaporation process by means of two thickness monitors (oscillating quartz sensors) which are read out by Labview monitoring software from a computer. The evaporation chamber also contains a remotely controlled enclosure box, which is used to close the CsI PC under Argon after the production and evaluation process, as the CsI has to be protected from any exposure to humid air after production. The outside of chamber is outfitted with heating tape which allows heating the whole chamber up to 75[°C].

3.4.1 Source preparation

The CsI is evaporated by resistive heating from 4 crucibles as shown in Fig. 32. The four boats are connected in series and a current of up to 120 [A] is run through them during the evaporation process. CsI has a melting point of 621 [°C] and a relatively high vapor pressure of 0.1 [mbar] at the boiling point. If the temperature gets too high locally the CsI molecule can dissociate in the evaporation process which should be avoided. Therefore it is necessary to have a good temperature homogeneity during the process and the evaporation rate should be kept low ($1-2$ [nm·s⁻¹]) and constant. This can be achieved by premelting the raw CsI powder. This way a good thermal contact between the crucible and the CsI can be assured. In our lab the pre-melting is performed in a separate vacuum system by a stepwise increase of the current through the boats until the melting process starts. To achieve the desired thickness of the CsI layer the amount of CsI in each boat is exactly adjusted by weighing the empty and full boats and by removing any CsI in excess of the required 0.75 [g] per boat after the melting process.

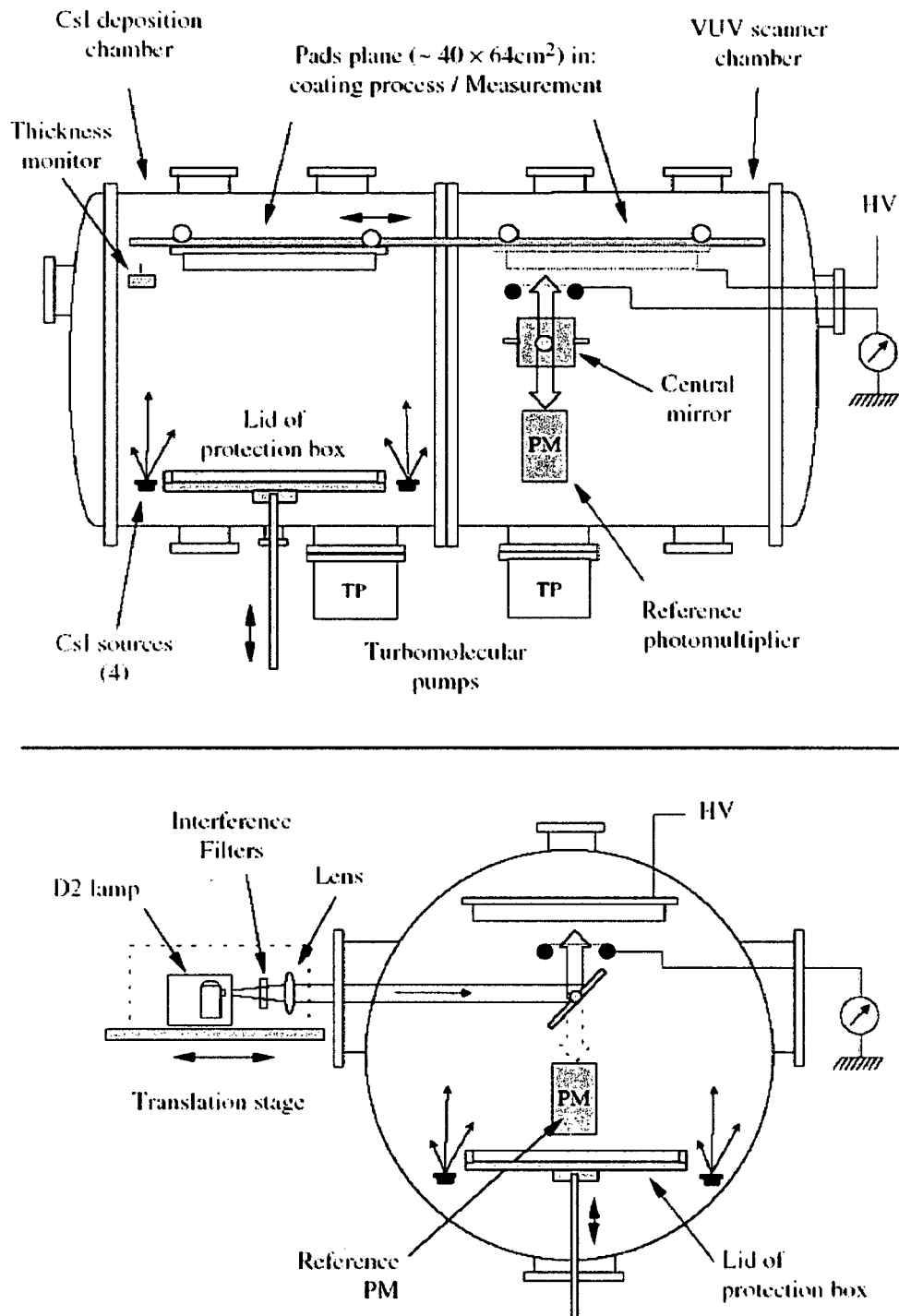


Fig. 30 Schematic side- and cross-views of the CsI evaporation system. On the top: the evaporation and the QE measurement parts are on the left and on the right side, respectively. At the bottom: principle of the QE evaluation based on the measurement of the photocurrent produced by local irradiation of the CsI PC by a monochromatic UV beam, the intensity of which is obtained from a PM.

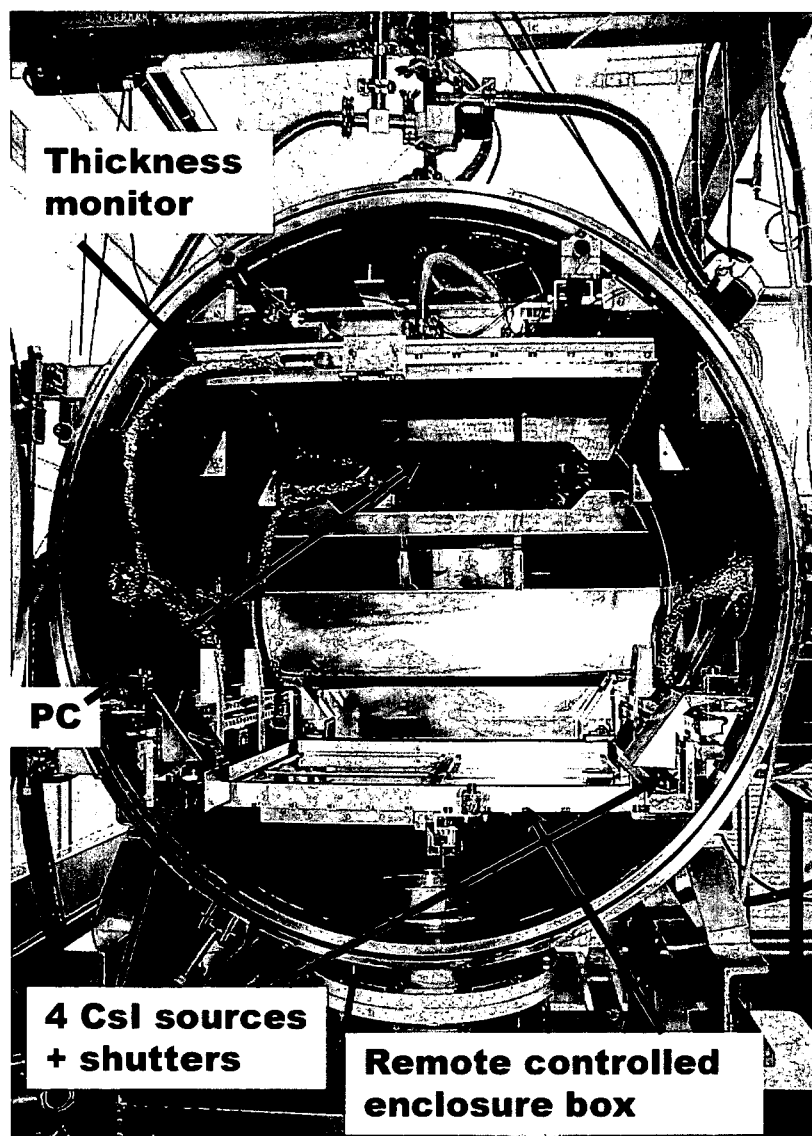


Fig. 31 Photo of the CsI deposition vacuum chamber.



Fig. 32 CsI source: Molybdenum boat filled with premelted CsI.

3.4.2 Control of the CsI layer thickness

In the CsI deposition procedure in our plant the layer thickness is controlled by carefully choosing the amount of CsI in each of the sources as mentioned above and by means of

the two oscillating quartz thickness monitors shown in Fig. 30 and Fig. 31. The thickness distribution on the PC can be calculated according to

$$e = \frac{m}{\pi \rho h^2 \left(1 + \frac{l^2}{h^2}\right)^2}$$

Equation 24

where $m = 0.75$ [g] is the mass of the source, $\rho = 4.51$ [g·cm⁻³] the density of the source, $h = 52$ [cm] the vertical distance between source and substrate plane and l is the horizontal distance between the source and a given point within the source plane. Taking the exact source positions relative to the substrate into account and summing over the contributions of the 4 boats in the configuration shown in Fig. 33, we obtain a layer thickness between 301 [nm] and 324 [nm] on the PC as shown in Fig. 34.

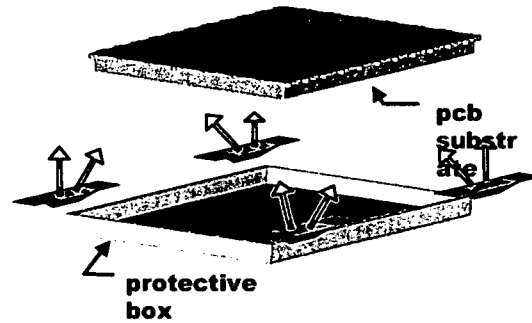


Fig. 33 Evaporation of the CsI from four sources by Joule effect.

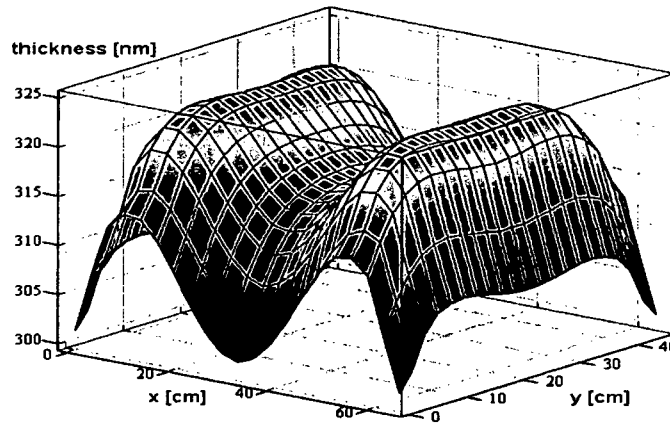


Fig. 34 Calculated thickness distribution of the CsI layer on a standard PC.

3.4.3 The CsI deposition process

In the following paragraph the standard procedure to produce a CsI PC is described which takes roughly a week. After the final cleaning of the substrate it usually arrives on a Thursday in the lab and is kept at 60 [°C] during the night before installation. The high temperature serves to outgas any residual water from the substrate. On Friday it is installed into the CsI deposition plant after a final cleaning with alcohol together with the CsI sources. All information about the substrate and the sources are noted in an Excel

datasheet. The datasheet contains identification numbers for the PC and its frame, as well as source numbers which allow to follow up the source preparation process. Any deviations from standard procedures in the cleaning or storage of the PC are noted as well as any unusual visual observations on the substrate surface. The pumping system is started at the latest on Friday evening and the chamber is heated to 60 [°C]. As soon as the pressure is low enough ($< 10^{-4}$ [mbar]) a leak detection is carried out at the chamber and the residual gas composition is checked by means of a quadrupole mass spectrometer. Pressure and temperature data as well as the results of the residual gas analysis are noted in the data sheet. A Labview monitoring program is started which records data about the pressure and temperature measured at several positions in the chamber and on the substrate. The monitoring program is equipped with an alarm system which alerts the responsible person by SMS in case the pressure or temperature leaves a pre-defined range. All the data recorded by the software is stored in the datasheet. After a weekend of pumping and outgassing of the substrate and vacuum chamber the CsI deposition is usually performed on a Monday. Before the deposition process is started, the residual gas in the chamber is analyzed again to check for any anomalies. The residual gas is by default checked for the partial pressures of the following molecules:

Ar, CO₂, H₂, H₂O, C_xH_y (hydrocarbons), N₂/CO, O₂, He

Tab. 1 shows the RGA measurements obtained before and after CsI deposition on PC53. The main constituent of the residual gas is usually water with around 70 % - 80 %. With around 10 % hydrocarbons represent also a large fraction of the residual gas. Hydrocarbons are usually outgassing from the substrate and have proved to be bad for the CsI quality. Therefore the evaporation process is usually postponed in case of hydrocarbons in excess of 15 %.

Partial pressure [mb]:

Date/time	Filename	Tot.Press. [mb]	Ar	CO ₂	H ₂	H ₂ O	C _x H _y	N ₂ /CO	O ₂	He	Temp [°C]
16/08/04 9:12	e040816a.mdc	2.45E-07	1.30E-08	1.40E-09	8.60E-10	1.60E-07	3.20E-08	6.70E-09	1.70E-08	0	64.5
17/08/04 8:52	e040817a.mdc	1.93E-07	1.00E-08	8.50E-10	7.60E-10	1.30E-07	2.10E-08	5.10E-09	1.20E-08	0	64
18/08/04 8:45	e040818a.mdc	5.58E-08	3.60E-09	0	6.20E-10	3.60E-08	6.40E-09	4.40E-09	3.80E-09	0	24
19/08/04 9:38	e040819a.mdc	4.59E-08	2.60E-09	0	4.20E-10	2.90E-08	4.20E-09	6.10E-09	2.40E-09	0	24

Concentration [%]:

Date/time	Filename	Ar	CO ₂	H ₂	H ₂ O	C _x H _y	N ₂ /CO	O ₂	He	Temp [°C]
16/08/04 9:12	e040816a.mdc	5.30%	0.57%	0.35%	65.25%	13.05%	2.73%	6.93%	0.00%	64.5
17/08/04 8:52	e040817a.mdc	5.19%	0.44%	0.39%	67.46%	10.90%	2.65%	6.23%	0.00%	64
18/08/04 8:45	e040818a.mdc	6.45%	0.00%	1.11%	64.52%	11.47%	7.89%	6.81%	0.00%	24
19/08/04 9:38	e040819a.mdc	5.67%	0.00%	0.92%	63.25%	9.16%	13.30%	5.23%	0.00%	24

Tab. 1 Composition of the residual gas before and after CsI deposition on PC 53. The deposition took place after the measurement on 17/08/2004 at 8:52.

If the residual gas is acceptable (total pressure $< 10^{-6}$ [mbar], mainly water, no indications of a leak...) the evaporation process is started. The evaporation of the CsI is performed at high temperature (60 [°C]). At first the current through the sources is increased in steps of 10 [A] every 2 [min] in order to increase the temperature of the sources gradually until the melting point is reached. The temperature must not be increased too fast, as the source material starts heating from the bottom of the crucibles and might locally already reach boiling temperature before all the material is molten. In this case the evaporation becomes very violent and source material might be expelled from the boats. When the current

reaches 70 [A] the shutters in front of the sources are opened. As soon as the thickness monitors start to indicate the start of the evaporation process, the current is regulated manually in order to achieve a CsI deposition rate of approximately $1\text{--}2\text{ [nm}\cdot\text{s}^{-1}]$.

During the deposition process a Labview monitoring program records the pressure and temperature as well as the readings from the two thickness monitors. The data is also stored in the data sheet for each PC. Fig. 30 shows an example for the data recorded during the CsI deposition on PC 53.

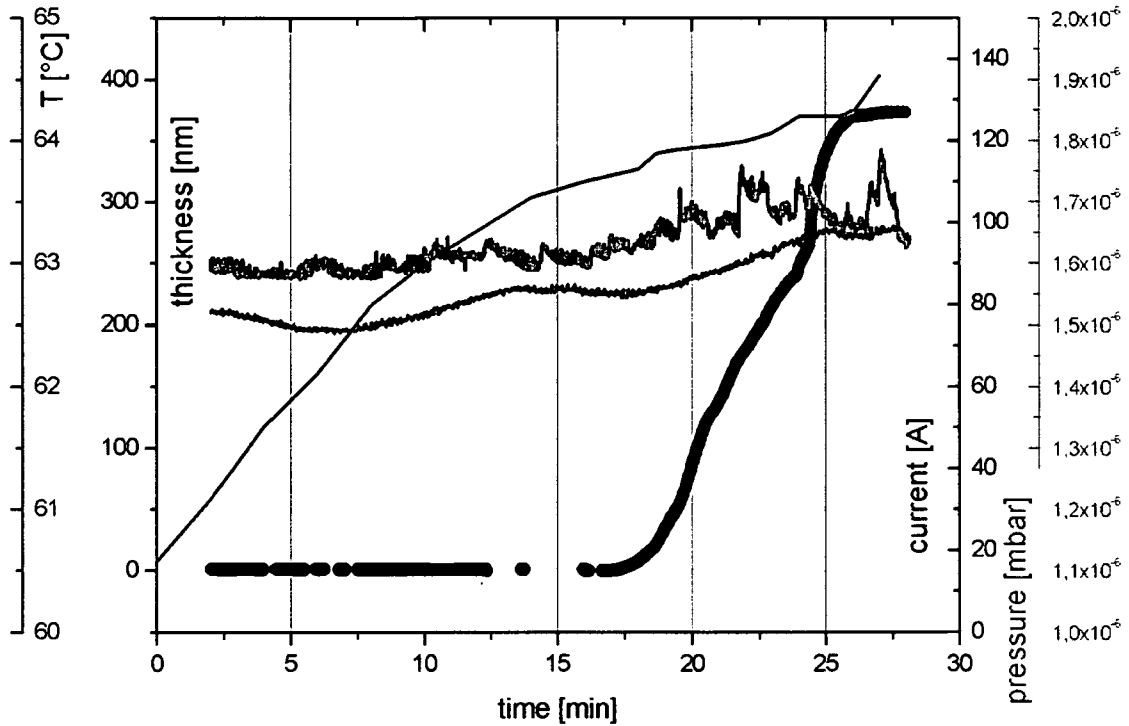


Fig. 35 Data recorded during the CsI deposition on PC53: development of current through the crucibles, layer thickness, temperature on the backside of the substrate and pressure.

As soon as the process is finished and the thickness monitors show no more change in layer thickness, the current through the boats is stopped. Following the evaporation process the PC is transported to the measurement side of the chamber where the first scans of the photocurrent from the new PC are carried out in order to record their heat enhancement behavior. The photocurrent scans and the corresponding measurement setup will be introduced in detail in the next Section 3.5. In Chapter 5 the post deposition heat enhancement of the PC quality will be discussed at length. From the results in this chapter it follows that the PC has to be kept at high temperature for 12 – 24 hours at least. Normally the heating is switched off in the morning following the evaporation. Then the PC is left to cool down to room temperature and the photocurrent measurements are carried out afterwards, as will be described in Chapter 7. All the measurement data are attached to the datasheet and when all the scans are finished the PC can be extracted from the production plant. For the extraction the plant is flooded with dry argon and the PC is closed at atmospheric pressure by means of the enclosure box. As soon as the chamber is opened, the enclosure box is fixed with a set of screws and the closed PC is then immediately connected to a gas line and purged with argon. At the output we normally measure a level of 500 [ppm O₂] which is mostly due to the connection to the gas line and

is decreasing rapidly. Later the PC is transported to another lab for storage connected to an Argon line, before it is mounted on a detector module. After the extraction from the production plant the PC is kept under a constant flow of Argon to avoid any exposure to air or humidity.

3.5 Quality control: the VUV Scanner

In the past the large area PCs have been tested together with complete detector modules and prototypes in test beam experiments. Monte Carlo analysis of the TB data allows the extraction of QE data and the assessment of the PC quality [44]. However these TB measurements are very elaborate, time consuming and dependent on beam availability. Therefore an alternative method to measure the quality of the CsI PCs during the series production for the detector had to be developed, especially due to the lack of particle beams at CERN during the main production phase in 2005. In order to provide an immediate assessment of the quality of a photocathode after the CsI evaporation process, the PC production plant has been equipped with a VUV-scanner system. This system allows scanning the large area PC with a beam of UV light and measure the resulting photocurrent from any given location on the PC. It was within the frame of this thesis that the setup was designed and put into operation. In particular the optical system had to be designed and all the commissioning tests during the installation of the system had to be carried out. The lower part of the drawing in Fig. 30 shows the basic layout of the measurement setup, which is composed of a UV source (deuterium lamp with MgF_2 window, Hamamatsu L7292) mounted on a translation stage outside the main vacuum chamber together with an optical system, and a reference photomultiplier and an anode ring to extract the photoelectrons from the PC inside the main vacuum chamber. Fig. 36 shows details of the optical system outside the main chamber. This part is usually referred to as the “scanner arm”. The scanner arm contains the source, which is kept under Argon flow and UV optics (CaF_2 lens, pinholes, diaphragm, optional quartz filter) which are kept under vacuum (10^{-6} [mbar]). This optical system is separated from the main chamber by a CaF_2 window. The Argon environment for the source and the vacuum for the rest of the optics are necessary to avoid any loss in the UV wavelength range < 180 [nm] due to absorption by O_2 and H_2O . The mechanical connection of the optical system to the main chamber is a flexible bellow, which allows moving the optics in and out of the chamber. Inside the main chamber the UV beam is directed onto the PC by means of a rotative mirror. The PC is hanging from 2 rails at the top of the chamber. The diameter of the UV beam on the PC is defined by an iris mounted in front of the mirror and is usually 16 [mm] in standard measurements. The photoelectrons produced by the UV beam are extracted from the PC by means of a bias voltage of + 100 [V] on an anode ring which is mounted approximately 5 [mm] in front of the PC. The photocurrent is measured from a PC by means of a pico-ampere meter. By means of the rotative mirror the beam can also be directed onto a CsI photomultiplier (Electron Tubes 9403B) to obtain a reference measurement. Fig. 37 is a photo of the optical system inside the main vacuum chamber.

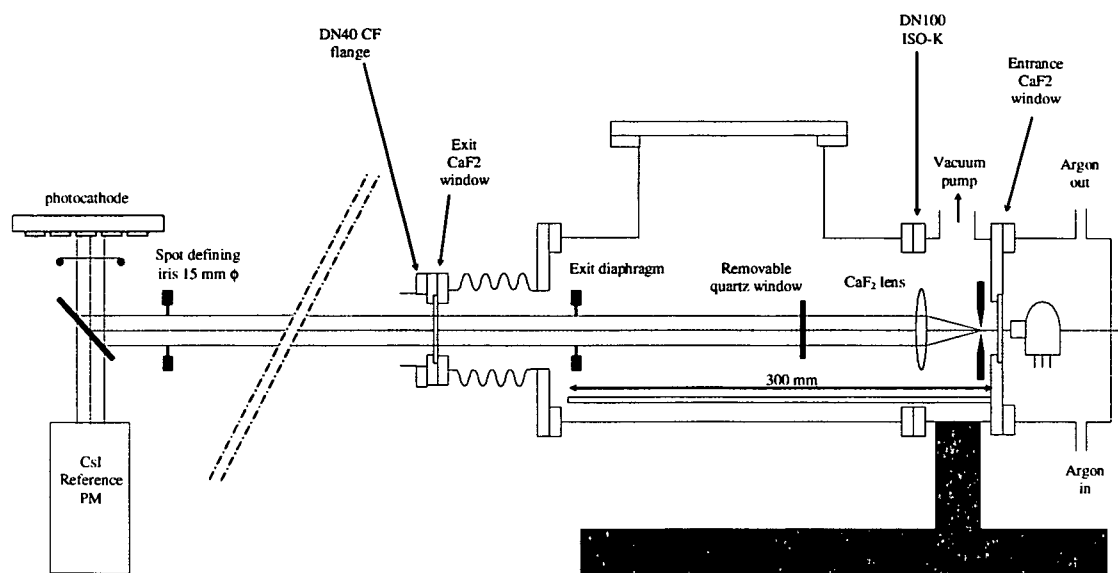


Fig. 36 Details of the optical system of the VUV scanner – scanner arm.

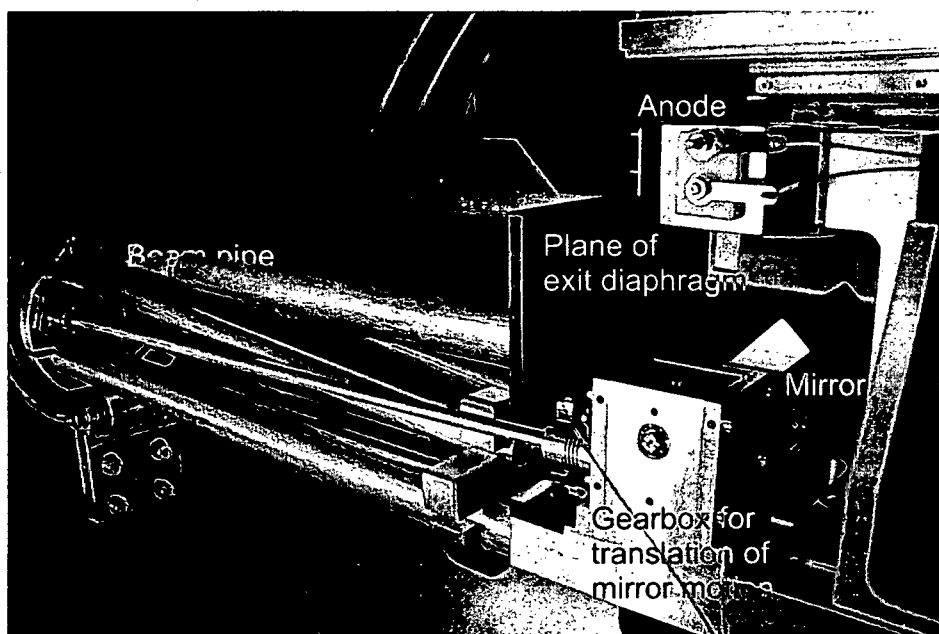


Fig. 37 Optical system inside the vacuum chamber.

Fig. 38 illustrates, how the PC can move along its support rails inside the main vacuum chamber and how the optical system moves in to and out of the chamber. Therefore it is possible to position the UV spot on any location on the PC and obtain a scan of the photocurrent over the whole PC surface. The motions are performed by stepping motors and controlled by Labview software, allowing a fully automatic positioning according to a pre-defined set of coordinates with an accuracy of 1 [mm].

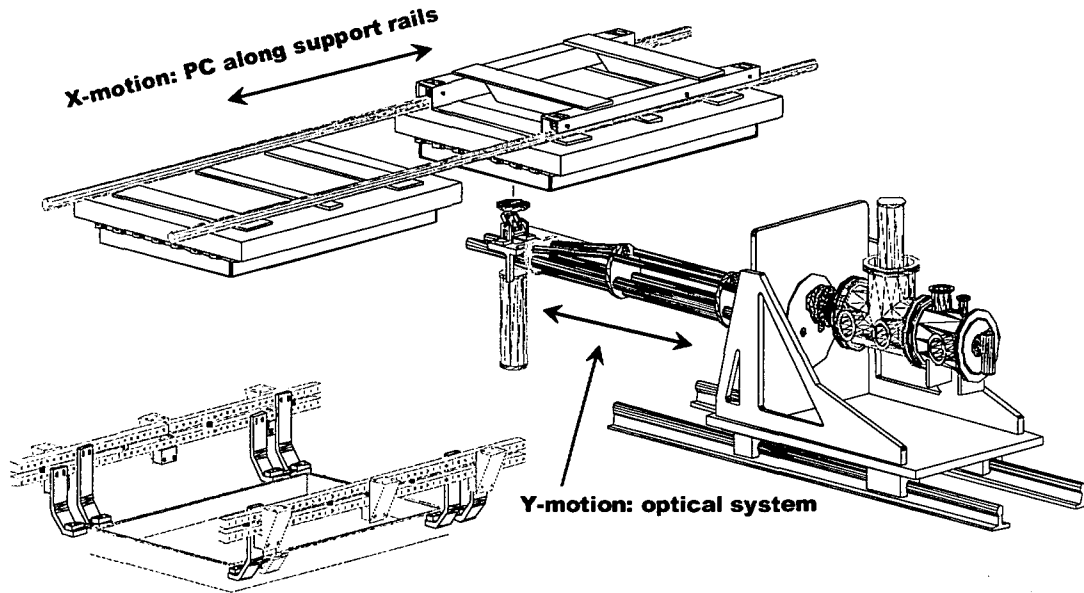


Fig. 38 Illustration of the movement of the PC along its support rails and of the scanner arm in two orthogonal directions.

3.5.1 Characteristics of the UV beam

The UV source used in our measurements is a Hamamatsu L7292 deuterium lamp with a MgF_2 window. As our system is not equipped with a monochromator, no wavelength dependent measurements can be performed and it is not possible to measure the spectral composition of the source light. From the emission spectrum of the lamp supplied by the manufacturer, we can approximately calculate the spectral composition of the UV spot on the PC in our measurement by taking into account the spectral transmittance of the various optical elements and the spectral reflectivity of the mirror. Fig. 39 shows the spectral composition of the UV beam we calculate for three different configurations in comparison to the emission spectrum of the lamp. The 3 different configurations available are:

- **Full spectrum:** in this configuration the UV light exiting from the lamp has to pass only two CaF_2 windows, the CaF_2 lens and the mirror. This is the measurement mode with the minimum loss of UV light.
- **Quartz window:** in this configuration an additional quartz window is placed into the optical path, which cuts away much of the low wavelength UV < 170 [nm]. This mode emphasizes the long wavelength part of the spectrum. By comparison between the first and second configuration we are able to detect changes in the shape of the QE curve of a PC, e.g. a shift in the photoemission threshold of the CsI in the post deposition enhancement phase (see Sections 3.1 and 5).
- **Interferential filter (170 nm):** another method to narrow the spectral range, however the intensity of the UV beam is so low that this mode is usually not used due to its poor signal to noise ratio.

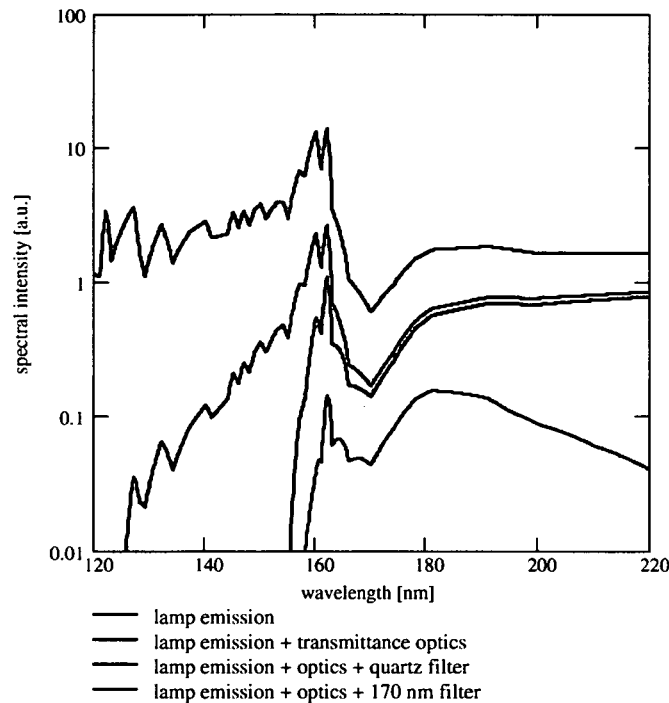


Fig. 39 Spectral composition of the UV beam for several measurement configurations.

The UV spot used in the standard measurements has a diameter of 16 [mm]. This diameter can be adjusted by placing irises of different sizes in front of the mirror inside the main chamber (compare Fig. 36). The reasons for the choice of a 16 [mm] spot are given in 4.3.4 and the homogeneity of the spot is discussed in 4.5.

3.5.2 Photocurrent measurement

For the photo-current measurement from the PC all the pads are daisy-chained and connected to a Keithley 487 Picoammeter via a multiplexer. The picoammeter is also used as a voltage source to apply + 100 [V] to the anode ring to extract the photoelectrons. The multiplexer serves to switch between the signal from the PC and from the reference PM. The PM is an Electron Tubes 9430B model with a MgF_2 window with 30 [mm] diameter. The active material in the PM is also CsI. The PM is used without amplification, i.e. there is only an extraction voltage of 100 [V] on the first dynode. Consequently the only difference between the measurement from the PC and the reference measurement is the fact that the PM uses a CsI cathode in transmissive mode as opposed to the reflective mode of the PC. Fig. 40 shows a comparison between the QE of the reference PM (supplied by the manufacturer) and the QE of a large area PC, which was obtained from the evaluation of test beam results of several large area PCs. The current measurements are automated and controlled by Labview software.

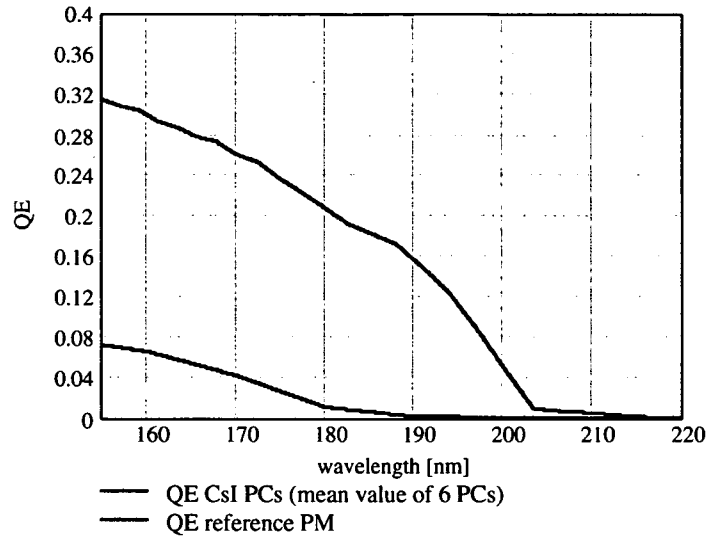


Fig. 40 QE of the reference PM compared to a standard QE obtained from the evaluation of test beam measurements of several large area prototype PCs.

For each point in a VUV-scan the photocurrent from the cathode is read as well as the reference signal from the photomultiplier. The following currents are read out:

- I_{CsI} is the current on the photocathode which is exposed to the UV beam
- I_{PM} is the reference current on the first dynode of the reference photomultiplier.
- I_{CsI_noise} is the background on the photocathode which is measured when the UV beam is on the reference photomultiplier.
- I_{PM_noise} is the background on the reference PM which is measured when the UV beam is on the photocathode.

Each of these currents is read by the pico-ampere meter with 60 [Hz] integration. The Labview control/readout software performs an averaging over 60 readings from the pico-ampere meter. The reference current on the PM is used to normalize the photocurrent on the photocathode:

$$I_{norm} = \frac{I_{CsI} - I_{CsI_noise}}{I_{PM} - I_{PM_noise}}$$

Equation 25

As the currents are measured without amplification, they are in the range of approximately 300 - 1000 [pA], whereas the background currents are usually < 1 [pA]. The normalized current usually has a value around 3-3.5 (current ratio).

In order to determine the statistical error for a standard measurement of a single spot on a PC the measurement of a chosen spot was repeated 400 times during approximately 15 hours. During this time the scanner was moving back and forth between 2 points, therefore the uncertainty related to the positioning of the scanner is included in these statistics. The

resulting distribution of measurement values for the normalized current showed a sigma of 2 % - compare Fig. 41.

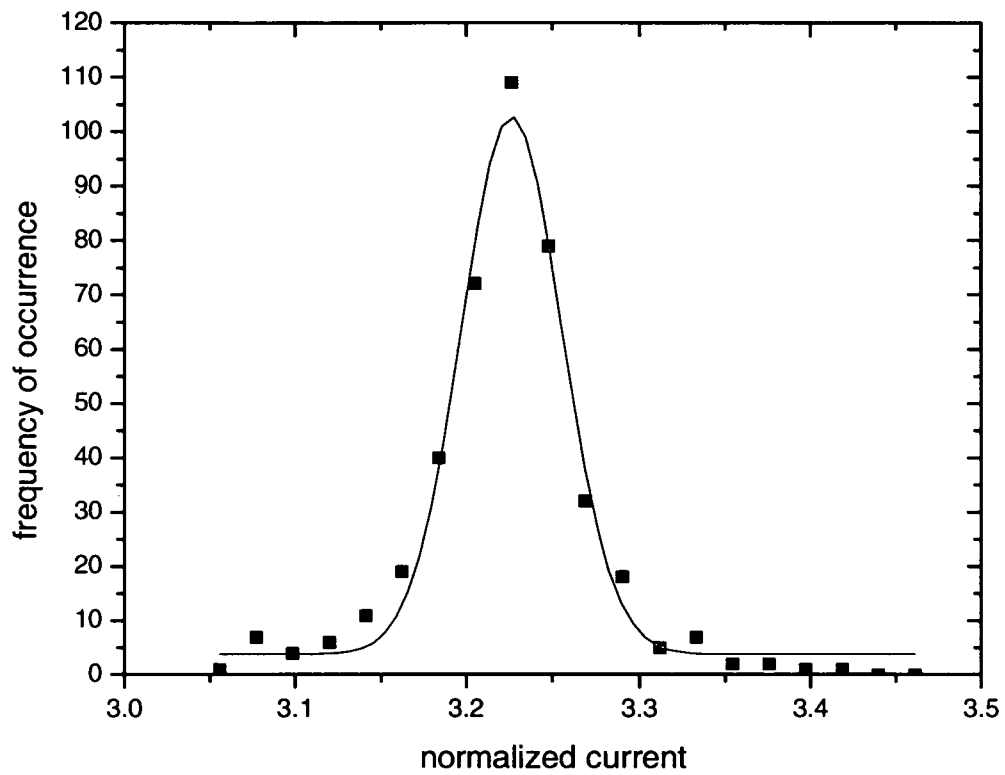


Fig. 41 Distribution of the measurement values from a repeated scan of a single position on a PC. One position was scanned 400 times, the sigma is 2 %.

4 Commissioning of the VUV Scanner System

Parallel to the final work on the construction of the VUV-Scanner system the first photocurrent measurements were obtained to provide feedback for the construction and development of the control software and to optimize the whole setup for the needs of the measurements. In the following paragraphs it will be described, which measurement parameters and other effects connected with the vacuum or measurement setup have been identified to systematically influence the measurement and how their influence has been minimized.

4.1 Sensitivity of the photoelectron measurement to basic measurement parameters

One of the first concerns when starting with the photoelectrons measurements was to find out, if the measurement is sensitive to changes of the basic parameters characterizing the environment in the vacuum chamber and to identify any systematic effects influencing the current measurements. In the following paragraphs results will be presented as to which parameters and effects influence the measurements and how their influence can be minimized.

4.1.1 Sensitivity to pressure and pressure gauges

The VUV-Scanner is normally operated at a pressure of around 10^{-7} - 10^{-6} [mbar]. By measuring the photocurrent from a PC while changing the pressure by means of a needle valve or during pumping cycles it was established that the measurement is independent of the pressure for pressures smaller than 10^{-4} [mbar] as shown in Fig. 42 and Fig. 43.

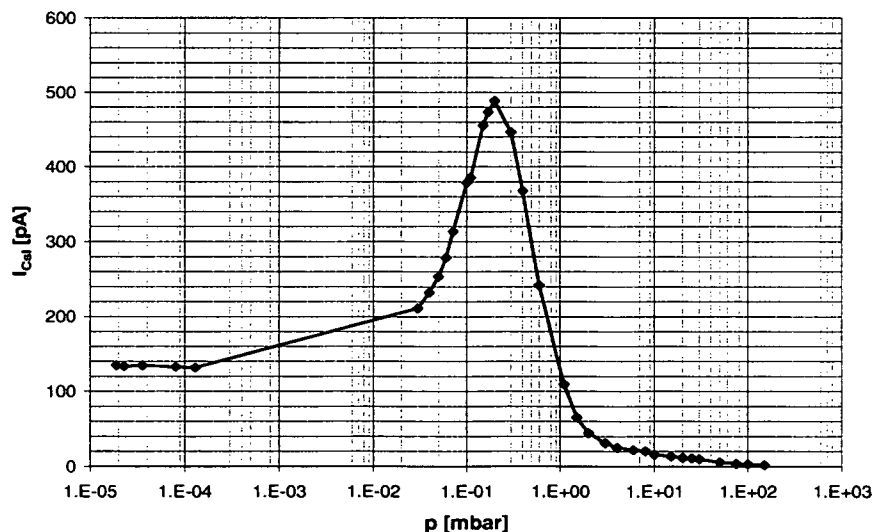


Fig. 42 Photocurrent on the CsI PC as a function of pressure inside the vacuum chamber measured during a pumping cycle.

However it turned out that the measurement is sensitive to the operation of some of our pressure gauges. Fig. 43 shows that the current read from the PC increases with increasing pressure, possibly due to collection of ions from the gauge on the large PC area. This effect

can be avoided by switching off the gauge or by means of a simple metallic shield in front of the gauge which prevents the ions from getting to the PC. A similar effect was observed when the ion gauge, was operated during a photocurrent measurement with anode readout (compare Section 4.1.3).

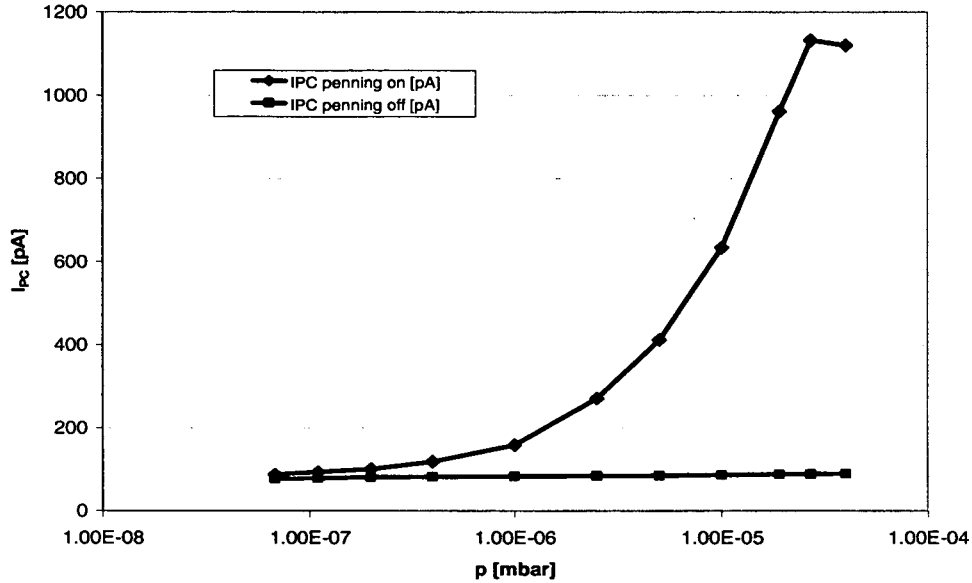


Fig. 43 Dependence of the photocurrent measurement on the CsI PC on the pressure and influence of the operation of the penning gauge on the measurement.

4.1.2 Sensitivity to temperature

As will be described in Chapter 5, temperature plays a significant role in the post deposition heat enhancement process of CsI photocathodes. In this process a temperature of approximately 60 [°C] can trigger an increase of the QE of the cathodes. However if the final level of quality is reached the photocurrents are no longer dependent on the temperature and the response of the PC is constant, even if the PC is cooled down again. On the other hand the temperature can influence the background of the photocurrent reading. While the background of reference measurement is usually independent of temperature, we observed in several cases that a temperature of 60 [°C] can increase the background measured from the CsI PC by several [pA]. This is a uniform offset of the photocurrent which is usually stable and can be easily corrected for by the subtraction of the background. Due to this increased background at higher temperatures it was chosen to do all the comparative measurements during the series production of PCs at room temperature.

4.1.3 Operational voltages for photocurrent measurements

The photoelectrons created in the CsI layer are extracted by the electrical field created by the voltage on the anode ring in front of the PC. In the case of the reference measurement the photoelectrons produced in the CsI layer inside the PM are extracted by the electrical field resulting from the voltage on the first dynode of the PM. Both for the photocurrent measurement from the PCs and for the reference measurement with the CsI

photomultiplier voltage scans were made to determine an operational voltage for which the photoelectron extraction is maximized. Fig. 44 shows the photocurrent measured on a CsI PC as a function of the voltage applied on the anode ring. Similar measurements were taken for the measurement of the reference current as a function of the voltage on the first dynode of the PM. From these measurements, which were repeated from time to time after modifications at the system, a voltage of 100 [V] on the anode ring as well as on the dynode of the PM was chosen for the standard operation of the scanner.

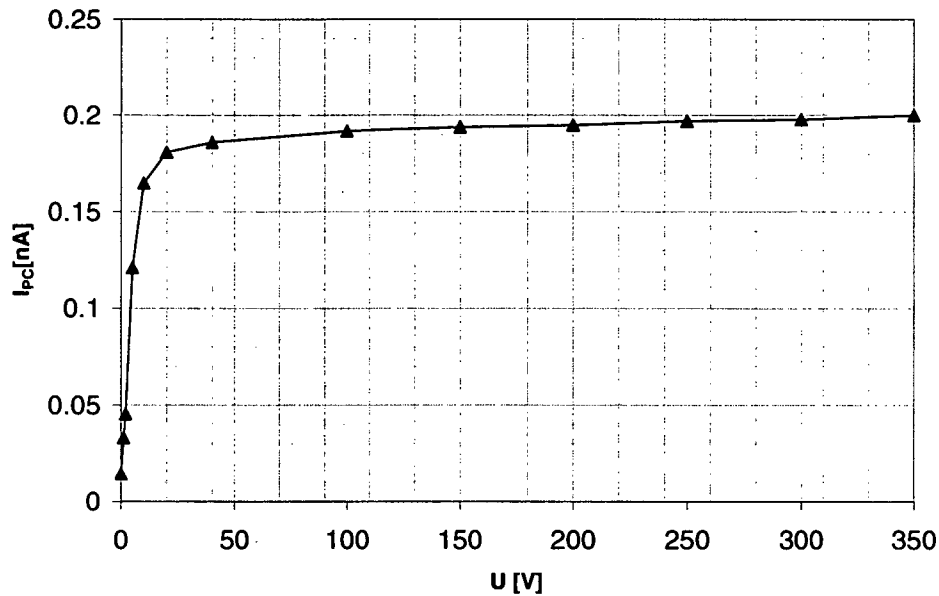


Fig. 44 Voltage scan on the CsI PC. For voltages higher than 50 [V] on the anode ring the photoelectron extraction reaches a plateau.

Anode readout

During the design phase of the VUV scanner an option to read out the photocurrent not from the PC but from the anode instead was foreseen. During the early phase of the commissioning tests this anode readout was also tested, especially to disentangle some systematic effects coming from stray light (compare 4.4) from the normal measurement. In this case a negative tension has to be applied to the PC to force the photoelectrons to leave the PC. As the anode ring can only collect part of the photoelectrons from the PC a second, smaller electrode ring was included in the design of the anode. During the standard measurement in which the photocurrent is read from the PC, both the anode ring and this second electrode are kept on the same positive potential. In the case of a current measurement from the anode the second electrode ring is also kept on a negative potential, which diverts also photoelectrons coming along a trajectory at the center of the anode towards the anode ring and therefore increases the collection efficiency of the anode. An optimized ratio between the negative tensions on the PC and second ring had to be found to maximize the collection efficiency of the anode read out. From several measurements the following optimized settings and the resulting photoelectron current were determined:

$$U_{2\text{ndring}} = -95 \text{ [V]}$$

$$U_{\text{PC}} = -50 \text{ [V]}$$

$$I_{\text{anode}} = 168 \text{ [pA]}$$

The noise level with the mirror switched down into the reference measurement position was lower than 1 [pA]. This result of a low background also helped to identify a pickup of stray light over a large area of the PC as the source for a larger background in the photocurrent readout from the PC.

Reading the signal again from the cathode the following current was measured:

$$I_{\text{cathode}} = 189 \text{ [pA]}; U_{\text{PC}} = 300 \text{ [V]}$$

If the background levels are subtracted from these measurements a collection efficiency of $\approx 90 \%$ can be calculated for the anode readout.

4.1.4 Sensitivity to anode position

One question people often raise in the discussion of the homogeneities of our scans of the photocurrent across a PC is, how well we control the distance between anode and cathode and if this affects our measurement. We have tried to measure the distance between anode and cathode which is in the order of 6 [mm] and we found a variation of this distance < 0.8 [mm] over the whole extension of the PC. In a test with our testcathode we deliberately misaligned the testcathode in y direction, causing a 2-3 [mm] variation in the distance between anode and cathode. While we were changing the alignment of the PC relative to the anode, it was exposed to air inside the lab ($T = 21.8$ [°C], $RH = 26\%$) for 15 minutes before the pumps were switched on again. The linescans obtained before and after the misalignment (see Fig. 45) show that this brief exposure has caused no visible decrease in QE as the current levels are roughly the same. Also the shape of the scans looks very similar after the misalignment and the slope of the overall line fit to the linescans is almost the same as well. The match between the scans before and after misalignment is very good, considering the exposure to air. Therefore we conclude that a variation of < 1 [mm] as is normally the case for our standard cathodes, does not influence our measurement systematically.

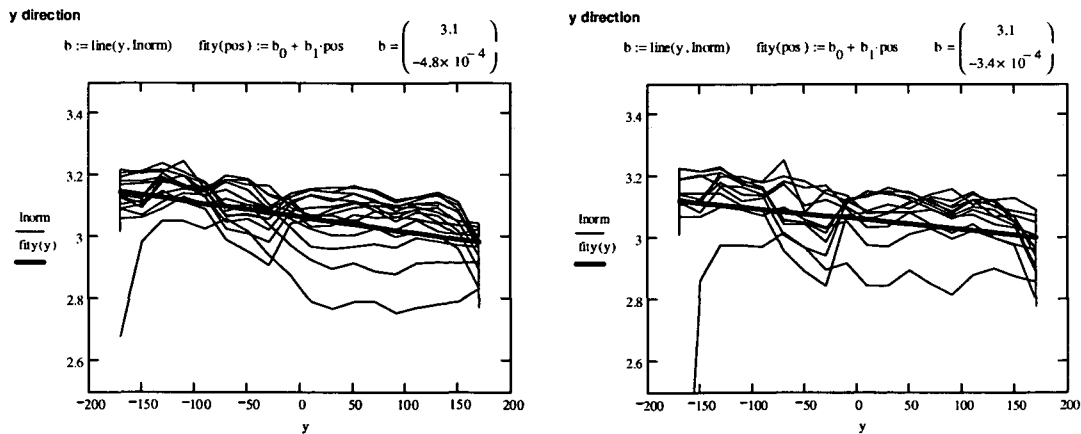


Fig. 45 Linescans across a test PC before and after a deliberate misalignment of the PC in y direction causing a variation of 2-3 [mm] in the distance between anode and cathode. Left side: before misalignment; right side: after misalignment. During the misalignment the PC was exposed to air for 15 [min] ($RH 26.3 \%$, $T = 21.8$ [°C]) before the pumps were started again.

4.2 Source stability and reference measurement

If the deuterium source is switched on and has stabilized after approximately 20 minutes of operation, the intensity of the source is very slowly decreasing. In our long duration scans e.g. during the heat enhancement process (Chapter 5), we measure a decrease of roughly 0.5 % per hour of operation on our reference measurement with the photomultiplier. However part of this decrease might also be attributed to the stability of the PM efficiency itself. Normally we measure the reference current for each point that is scanned. Due to this very slow decrease in lamp intensity it is however also possible to do quicker scans without reference measurements.

Another feature of the reference measurement itself is the stability of the PM measurement after a change in the operational voltage on the first dynode of the PM. Fig. 46 shows the behaviour of the reference current during a change of the operational voltage of the PM. After increasing the voltage a brief spike of the current is recorded. Especially when the PM is switched on and the 100 [V] tension are applied the first time it takes approximately 5 [min] until the measurement is stable. This has to be taken into account whenever a new scan is started and the voltage is applied to the PM for the first time.

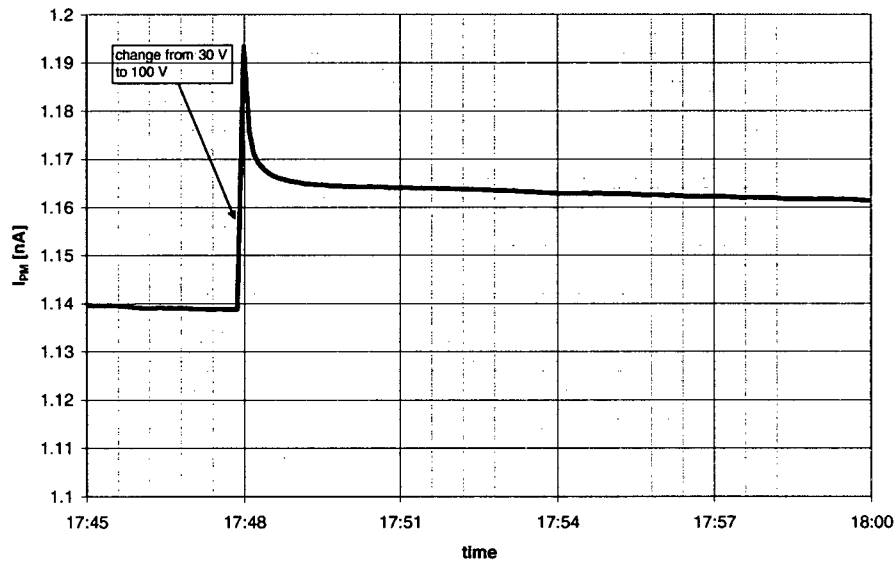


Fig. 46 Current measured on the reference PM during a change of the operational voltage it takes several minutes until the measurement becomes stable again.

4.3 Decreased effective QE in interpad zones

The pads on a standard PC are separated by an insulating zone of 0.4 [mm] width. If a UV photon extracts a photoelectron from the top of the 300 [nm] CsI layer on a pad, the charge can be replaced through the connection of the Au-Ni layer to ground (via the pico amperemeter). The electron only has to be transported through the relatively thin CsI layer, which is a semi-conductor. This situation is completely different, if the photoelectron is

created in the CsI layer on the interpad zone. As the substrate in this area is insulating the charge can only be replaced by a transport over a much larger distance through the CsI layer from the nearest pad. Therefore this much higher resistance in the current circuit will lead to a lower effective value of the QE of CsI on the interpad zones compared to the QE pad. It is reasonable to assume that this effect depends on the amount of charge that needs to be transported and therefore on the photon flux that is used in the measurement. It could be quite different for single photon counting in a Cherenkov detector than for a QE measurement with a UV source of 10^{10} [photons \cdot cm $^{-2}$ ·s $^{-1}$]. As the interpad zones account for 11 % of the total area of a PC it makes sense to take a closer look at this effect.

4.3.1 Interpad effect in the VUV-scanner

The effect is clearly visible in the measurements with the VUV-scanner. If the UV spot is scanned across the PC pads with a small step width, a clear decrease in photocurrent can be measured, when the UV spot passes over the interpad zone. Fig. 47 shows the results of a linescan with a UV spot of 2.5 [mm] diameter across several pads on PC40. The photocurrent is smaller when the spot is over the interpad zone. In Fig. 49 a 2D scan over 2 x 2 pads is shown, which visualizes the pad structure very nicely.

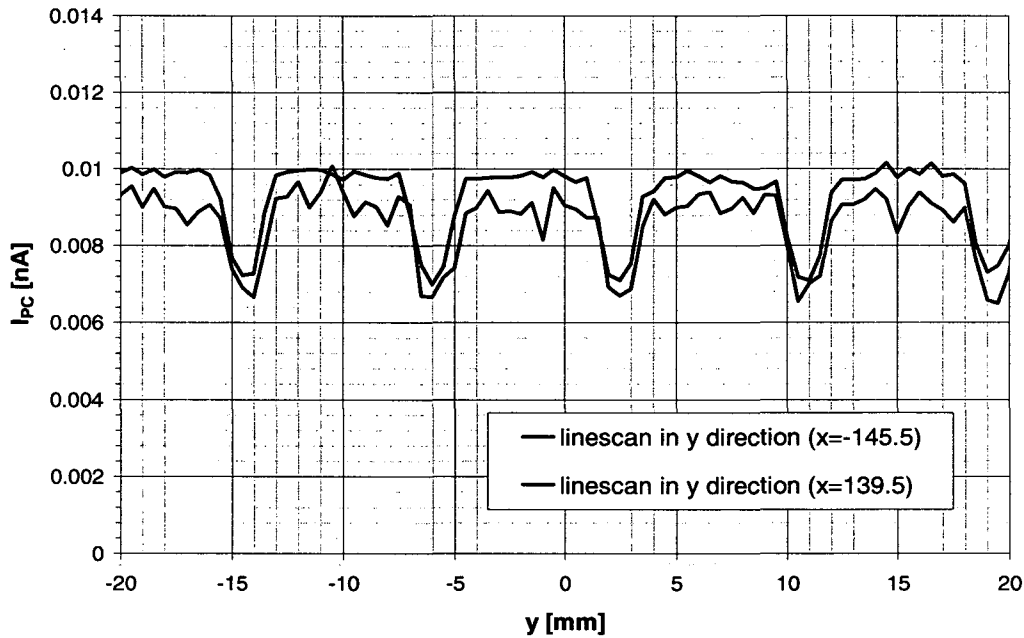


Fig. 47 Detailed linescan with a small UV spot (2.5 [mm] diameter) across the pads on PC 40. A decrease of the photocurrent can be observed, when the spot passes over the interpad zone.

A limit for the maximum possible effect can be calculated if one assumes the QE is zero in the interpad zone and the intensity distribution within the UV spot is homogenous and flat. In this case the ratio between the decreased signal (when the spot is on an interpad zone) and the maximum signal (when the spot is fully on a pad) can simply be calculated as the ratio between the active area A_{ACTIVE} inside the spot and the maximum area covered by the spot A_{SPOT} . See Fig. 48 for an illustration of these areas. A_{ACTIVE} is the area of the spot minus the “dead” area inside the spot A_{DEAD} that is taken up by the interpad zone within the spot:

$$A_{ACTIVE} = A_{SPOT} - A_{DEAD}$$

$$\text{Ratio between the decreased and the maximum current} = \frac{A_{ACTIVE}}{A_{SPOT}}$$

Equation 26

Fig. 49 shows a comparison between the calculated and measured pattern for a UV spot with 2.5 [mm] diameter. The 2D plot of the measurement data (left) shows the photocurrent scanned over 2x2 pads as a function of position. The plot of the calculation shows the ratio A_{ACTIVE} / A_{SPOT} as a function of the position of the UV spot. The match between calculation and measurement is very good⁷.

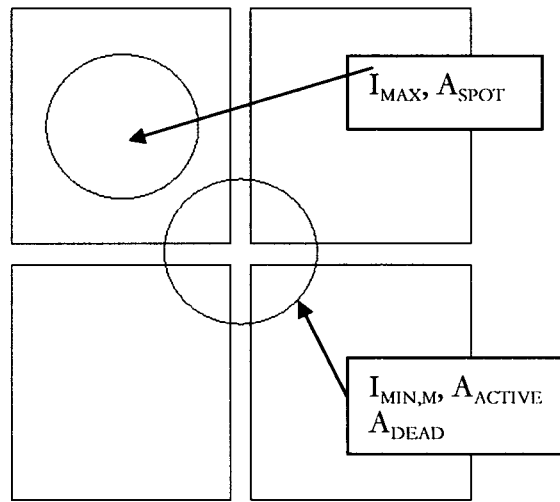


Fig. 48 Illustration of the measurement of the photocurrent from locations with and without contributions from the interpad zone. With a small UV spot diameter a measurement of the maximum current can be obtained if the spot is centered on a pad. If placed at the crossing of the interpad zones the minimum of the current can be measured due to the decreased efficiency in the “dead zones”.

If one takes a closer look on the measured currents, one finds that the ratio between the minimum current $I_{MIN,M}$ measured at a gap crossing as shown in Fig. 48 and the maximum current measured at the pad center I_{MAX} is always larger than the theoretical ratio between the active area at the pad crossing A_{ACTIVE} and the full area of the spot A_{SPOT} .

$$\frac{I_{MIN,M}}{I_{MAX}} > \frac{A_{ACTIVE}}{A_{SPOT}}$$

Equation 27

E.g. for the case of a UV spot with 2 [mm] diameter one expects to measure only 45 % of the maximum value at the pad crossing according to the calculation, but several measurements give results between 55 % and 65 %. This indicates that the QE in the

⁷ There is an additional feature visible in the plot of the measurement data which is related to a reflection problem in the UV source. This problem will be discussed in section 4.5.2.

interpad zone is actually not zero, but there are still some photoelectrons measured which are coming from this area.

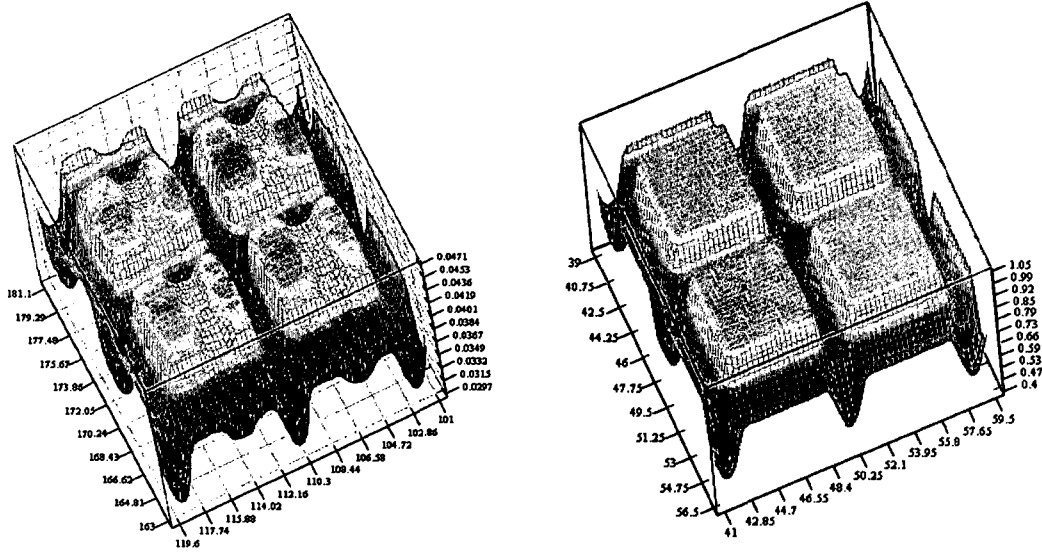


Fig. 49 Comparison between a measurement of the pad effect in the VUV scanner (left) and a calculation of the effect (right). The plot of the measurement data gives the photocurrent as a function of position scanned over 2x2 pads. The calculation plot gives the ratio between active and “dead” area within the UV spot depending on its position. The additional feature visible in the measurement is due to a reflection in the source which will be discussed in Section 4.5.2.

4.3.2 Calculation of the effective QE in the interpad zones

Theoretically it is possible to describe this fact with a decreased effective quantum efficiency QE_{DEAD} inside the interpad zones as opposed to the normal quantum efficiency on the pad QE_{ACTIVE} . The maximum current measured on the pad can then be written as

$$I_{MAX} \propto QE_{ACTIVE} \cdot \phi \cdot A_{SPOT}$$

Equation 28

where ϕ is the photon flux per second and per $[cm^2]$. The current coming from the interpad zone can be written as

$$I_{DEAD} \propto QE_{DEAD} \cdot \phi \cdot A_{DEAD}$$

Equation 29

From these expressions it follows that the ratio between the QE in the interpad zone and the QE on the pad can be written as

$$\frac{QE_{DEAD}}{QE_{ACTIVE}} = \frac{I_{DEAD}}{I_{MAX}} \cdot \frac{A_{SPOT}}{A_{DEAD}}$$

Equation 30

The current I_{DEAD} from the interpad zone can be calculated by taking the minimum current measured when the UV spot is at the intersection of the interpad zones $I_{MIN,M}$ and

subtracting the current $I_{MIN,EXP}$ that is expected to be measured at this position assuming zero QE in the dead zone.

$$I_{DEAD} = I_{MIN,M} - I_{MIN,EXP}$$

Equation 31

with the expected minimum current

$$I_{MIN,EXP} = I_{MAX} \cdot \frac{A_{ACTIVE}}{A_{SPOT}}$$

Equation 32

which can be calculated from the maximum current I_{MAX} at the pad center and the ratios between active and “dead” area.

The currents, quantum efficiencies and photon fluxes in both Equation 28 and Equation 29 are functions of the wavelength. Including the wavelength dependency the correct expressions are

$$I_{MAX} \propto \int_{\lambda} QE_{ACTIVE}(\lambda) \cdot \phi(\lambda) \cdot A_{SPOT} \cdot d\lambda$$

$$I_{DEAD} \propto \int_{\lambda} QE_{DEAD}(\lambda) \cdot \phi(\lambda) \cdot A_{DEAD} \cdot d\lambda$$

Equation 33

From these expressions it follows that Equation 30 for the ratio QE_{DEAD}/QE_{ACTIVE} only holds, if QE_{DEAD} is proportional to QE_{ACTIVE} :

$$QE_{ACTIVE}(\lambda) = k \cdot QE_{ACTIVE}(\lambda) \quad 0 < k < 1$$

Equation 34

From measurements in the VUV-scanner with several different spot diameters at different positions on and between the gaps we have calculated values for QE_{DEAD}/QE_{ACTIVE} from 0.1 up to 0.5. The large variation is possible due to the assumption of Equation 34 and maybe also due to the fact that the effective QE from the interpad zone most likely depends on the photon flux as mentioned above.

4.3.3 Wavelength dependent measurements on test samples in ASSET

In order to avoid the problem with the wavelength dependency of the various quantities we tried to measure the same effect in the ASSET system with a monochromator. Regardless of the problems with the monochromator stated above, the measurements provided us with a better estimation of the ratio QE_{DEAD}/QE_{ACTIVE} . For the tests two 16 [mm] x 16 [mm] samples cut out of a large standard substrate were used. One of the two samples was engraved with pads with the crossing of the interpad zones at the center. The second sample was not engraved (see Fig. 50). Both samples were coated simultaneously with CsI and afterwards the photocurrent was measured from them with a rectangular UV spot as indicated in Fig. 50. The total area of the UV spot was 30 mm² and the area of the “dead” zone inside the spot on sample 1 was 6.25 mm². The measurements were performed for

several wavelengths. Using Equation 30 to Equation 32 the ratio $QE_{\text{DEAD}}/QE_{\text{ACTIVE}}$ could be calculated as given in Fig. 51. This result clearly shows that the QE in the interpad zones is not zero. In all the evaluations of the QE of our PCs from test beam results it was always assumed that the full surface of the PC is active. These measurements from the scanner and from ASSET show that this way the actual QE of the CsI is underestimated due to the effect of the interpad zones. However, the reduction is less than 11 % (fraction of the total area covered by the interpad zones), due to the residual QE in the interpad zones. We also tried to measure a possible dependency of the interpad effect on the photon flux. However within the limited dynamic range for the flux of our setups we could not find any conclusive results.

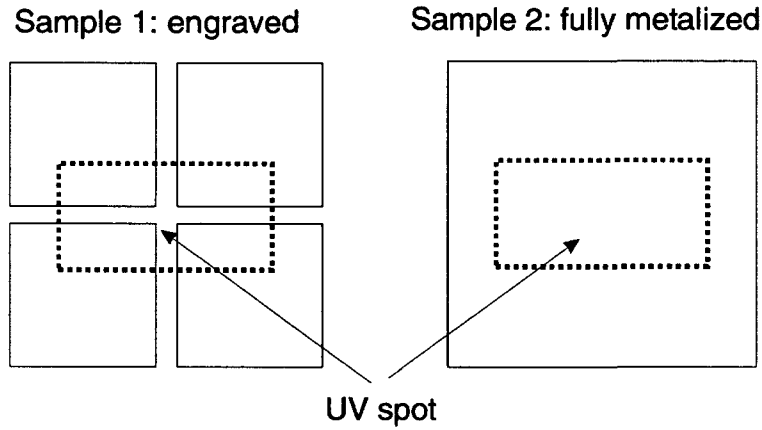


Fig. 50 Comparison of an engraved and a fully metalized sample in the ASSET setup.

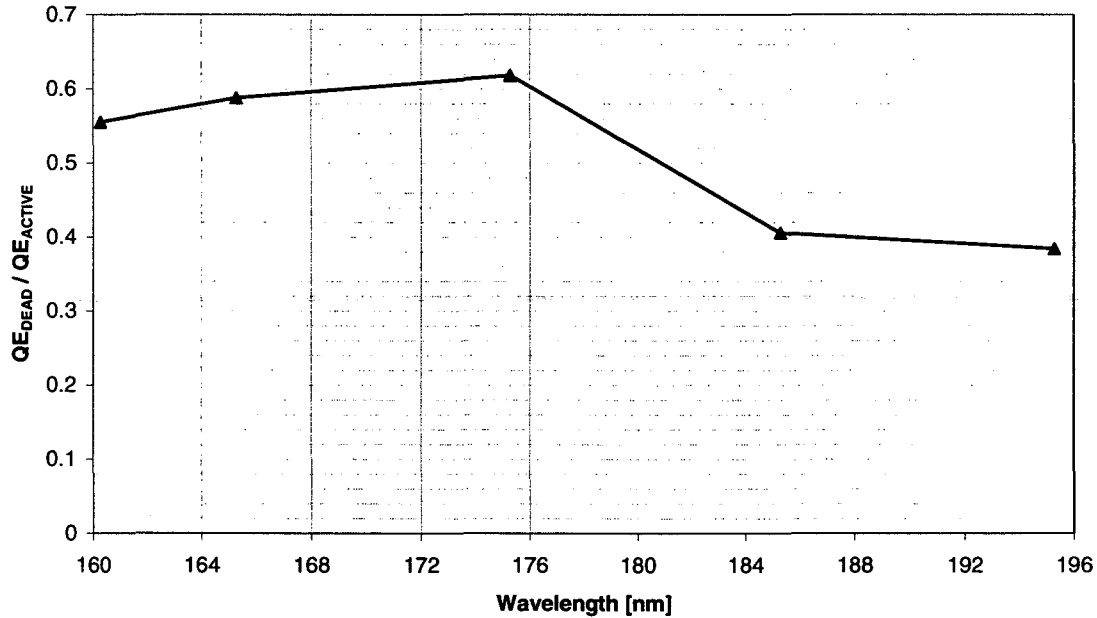


Fig. 51 Ratio between QE in the interpad zone and QE on a fully metalized sample calculated from measurements in ASSET.

4.3.4 Choice of a spot size in the VUV scanner to minimize interpad effect

For the operation of the VUV scanner it is very important to ensure that this interpad effect does not influence the measurements, as the current variations can be quite large. There are two approaches to minimize the influence of this effect on the measurements:

- Choose a UV spot which is smaller than one pad and make sure that it is always centered on the pad, so that there is no interpad zone within this spot. The positioning accuracy of the scanner (<1 [mm]) is good enough to achieve this goal, however the signal to noise ratio is degraded in the case of very small spots and as soon as the spot has almost the size of a pad, the measurement becomes very sensitive to positioning errors again.
- The second possibility is to choose a larger spot, for which the amount of interpad zones within the spot is always roughly the same and the variations due to the interpad effect are minimal. Due to concerns about the signal to noise ratio especially in the case of measurements with filters, the second possibility was chosen for the standard scans of our PCs.

Due to the need for a very good signal to noise ratio the second option was chosen for the standard scans with the VUV scanner. In these scans we are now using a UV spot with a diameter of approximately 16 [mm]. To understand the influence of the interpad zones in the measurements with a 16 [mm] UV spot, the usual calculation of the active and “inactive” surface was performed and compared to a 2D detail scan on PC 39. The results are given in Fig. 52. The agreement between calculation and measurement is good. For this large spot the maxima of the signal are on the gap crossings. Assuming zero QE within the gap, the calculations predict a difference of 7.6 % between minima and maxima. The data of the scans on PC 39 show a difference of 4 %, another confirmation of a nonzero QE in the interpad zone. A difference of the order of 5 % between maximum and minimum values is a significant improvement compared to the measurements with a very small spot presented in Fig. 49 in which the effect can be much higher (up to 45 %).

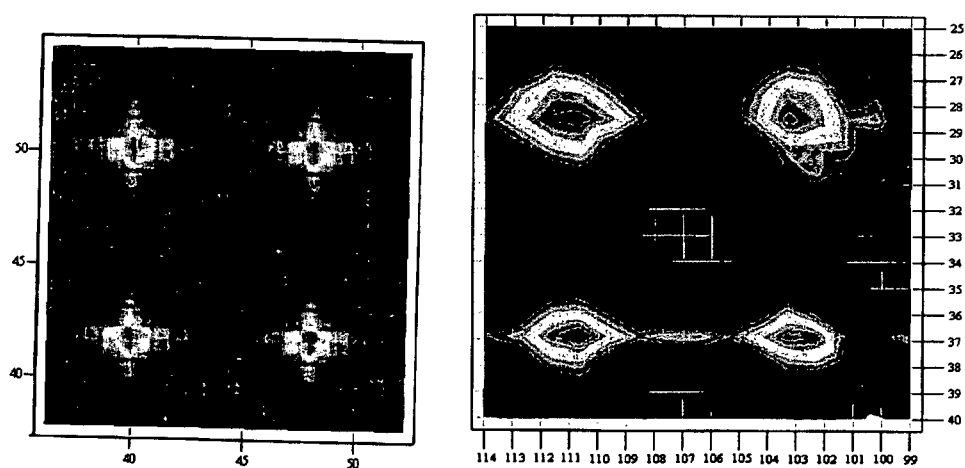


Fig. 52 Calculated (left) and measured (right) gap pattern for a 16 [mm] spot. The measurement was performed on PC 39.

4.4 Sensitivity to stray light from the UV source

In the first photocurrent measurements on a standard PC we had problems with a relatively large background measured on the PC. When the UV beam was directed onto the reference PM and away from the PC we still measured up to 100 [pA] from the PC which was more than 5 % of the signal at that time. When the source was switched off, the background dropped to < 1 [pA]. The background also was position sensitive which suggested a pickup of stray light over a large area of the PC depending on the position of the PC relative to the source. At this time the UV beam was collimated by an adjustable diaphragm just before it entered the main vacuum chamber and by a second iris just in front of the mirror (compare Fig. 36). In order to avoid the stray light problem, an aluminum pipe with a diameter of 25 [mm] was installed in which the UV beam travels up to the mirror (compare Fig. 37). The low signal linescans (with a filter and a very small UV beam diameter) given in Fig. 53 demonstrate how the stray light continued to be a problem until the beam pipe was perfected to attach directly to the entrance window of the main vacuum chamber.

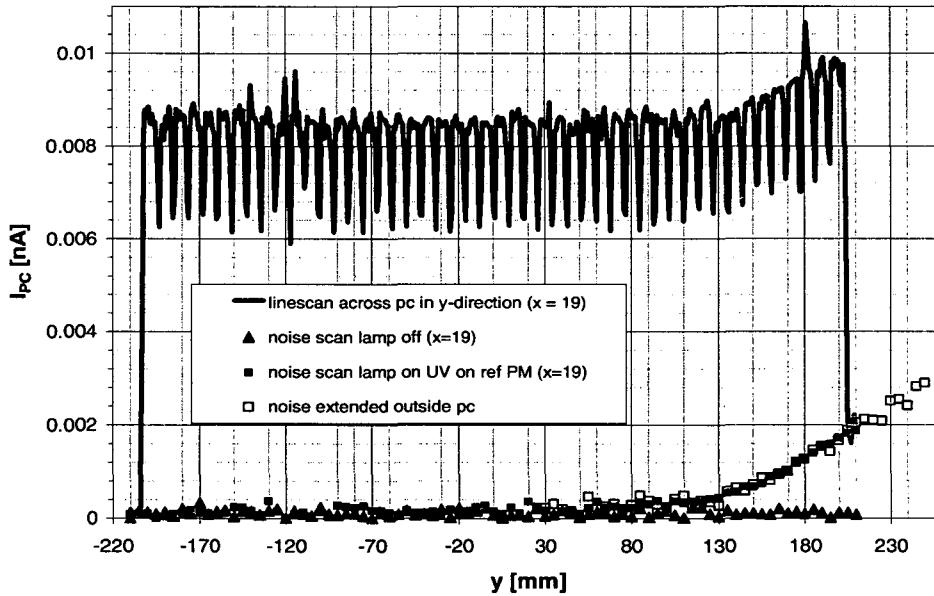


Fig. 53 Scans of the photocurrent across the width of PC 40 including details of single pads. Scans with filter and 2.5 [mm] UV beam to show details of single pads (very low signal!). As the noise scans show, the increase in photocurrent on one side of the PC is due to stray light picked up on a large area of the photocathode. The offset due to the increasing background is responsible for a slope in the signal.

4.5 Alignment, form and size of the UV spot

4.5.1 Alignment of the entrance pinhole and influence on measurement

In the alignment of the optical system the position of the 1 [mm] entrance pinhole, which is closest to the D₂ lamp, proved to be very critical for the measurement (compare Fig. 36). The easiest way to check, if the position of this pinhole is correct, is to take a photo of the UV spot by placing a camera on top of the anode ring. The photos in Fig. 54 show the UV spot before and after alignment of the pinhole. The position of the pinhole can be further optimized by maximizing the photocurrent read from the PC or the reference PM. This alignment is very crucial for the measurement due to the CaF₂ lens in the optical path. Due

to the achromatism of the lens a misaligned UV beam which is slightly off the optical axis does not only reduce the photon flux, but it also changes the spectral composition of the beam. As the QE curves for the reference PM and the CsI PCs are not completely identical (Fig. 40), a change in the spectral composition of the UV beam can change the current ratios between CsI and reference measurements, i.e. the normalized current from Equation 25. The plots in Fig. 55 show, how the photocurrent and the current ratio changes if the entrance pinhole is displaced by small distances. Consequently it is very important to keep this alignment optimized for all the measurements, as any misalignment would make a comparison of the normalized currents impossible.

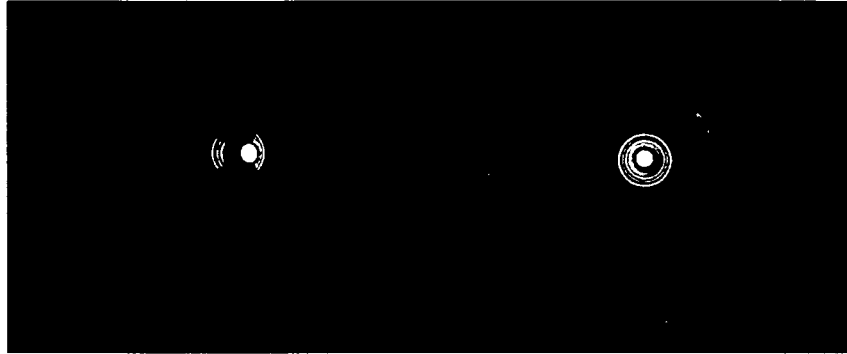


Fig. 54 Comparison of the UV spot before and after alignment of the entrance pinhole. The photos were taken with a standard digital camera. The rings around the center are reflections from the diaphragms inside the beam pipe.

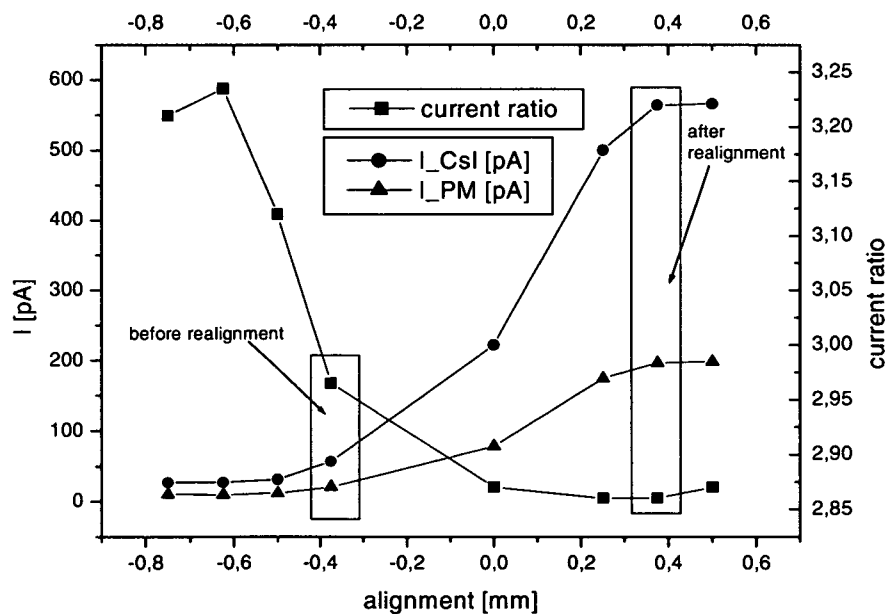


Fig. 55 High sensitivity of the measurement to the alignment of the entrance pinhole immediately after the source. The x axis gives the position of the diaphragm in [mm] to an arbitrary origin.

4.5.2 Grazing incidence reflections inside the UV beam pipe

In the investigations of the interpad effects presented in 4.3.1 the detailed 2 dimensional scans across 2×2 pads showed the striking feature of a slight current decrease (5 % effect) on every pad in x direction, which can be observed in Fig. 49. This decreased zone was

visible on every pad and the direction was following the direction of the anode wires in the detector. As the PC on which this was observed had been used in beam tests before, we were at first lead to believe the effect was somehow due to some effect in connection with the detector operation. However, when we finally measured the same feature on a freshly produced PC, we were forced to investigate a possible systematic effect in our UV source. One possible explanation for the measured effect was a second, low intensity reflection of the UV spot shifted slightly in y -direction. Therefore we tried to measure the intensity profile of the UV spot. To obtain the form of the intensity profile of the spot a standard UV photodiode (Centronic, for use from 190 [nm] to 400 [nm]) was used to scan across the UV beam. The diode was mounted on a sample holder that could be fixed on the PC rail with a 1 [mm] pinhole in front of the active area. The spot scans Fig. 56 show two reflections of the spot, one shifted in y direction and completely separate from the main spot, the other one slightly larger, shifted in x direction and not completely separate from the main spot.

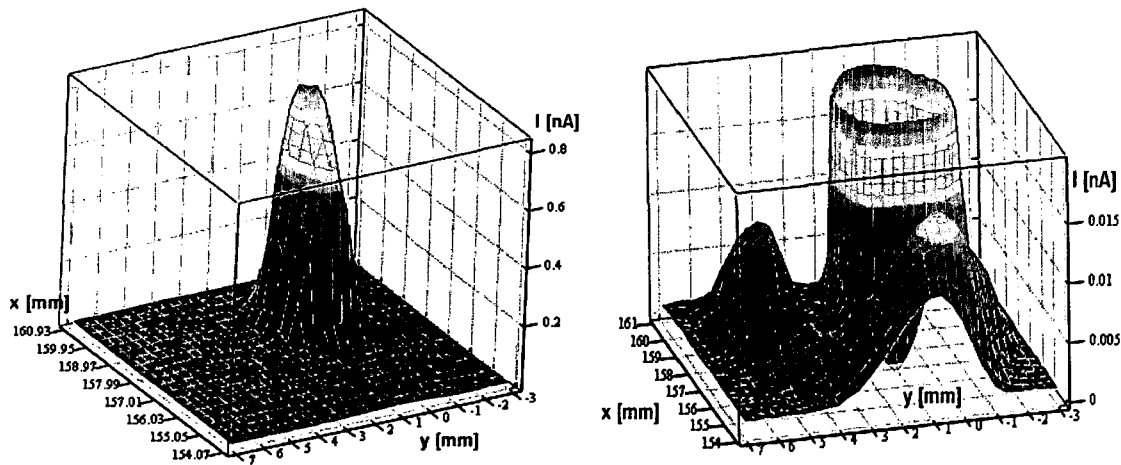


Fig. 56 Spots in vacuum: the zoom on the right side down to a few percent of the central maximum, reveals 2 reflections of the spot shifted in x and y direction.

The intensity of the reflections was about 1-2% of the intensity of the main spot. In principle this was not enough to explain the 5% effect in the measurements on the PCs. It is also not clear why the effect in the PC scans was only visible in y direction, as there was also a reflection in x direction – this might be due to the fact, that the reflection in x direction was larger and not completely separated from the main spot, thus causing only a slight inhomogeneity in x direction, whereas the smaller well separated reflection in y direction causes a distinct feature in the signal. However it should be stressed, that the sensitivity of the photodiode in the UV range below 190 [nm] is not known. Therefore it is not clear whether the reflections have the same form and intensity in the UV range relevant for the measurements on the CsI cathodes. To remove this reflections and to verify that they constituted the cause for the patterns in the scans, the 2 [mm] diaphragm at the exit of the “beam pipe” was replaced by a 6 [mm] diaphragm and an additional iris with a diameter of 2.5 [mm] was mounted on top of the anode ring, only 5 [mm] from the PC surface. In this configuration the spot was scanned again, with the result given in Fig. 57. With the iris so close to the pad plane all reflections could be blocked. Afterwards PC 38 was transferred to the evaporator and scanned again. Neither linescans in x and y direction nor a two-dimensional scan over 2x2 pads showed the pattern observed before. Fig. 58 shows the 2D

scan with the reflections blocked – the effect of a decrease at the pad center is no longer visible.

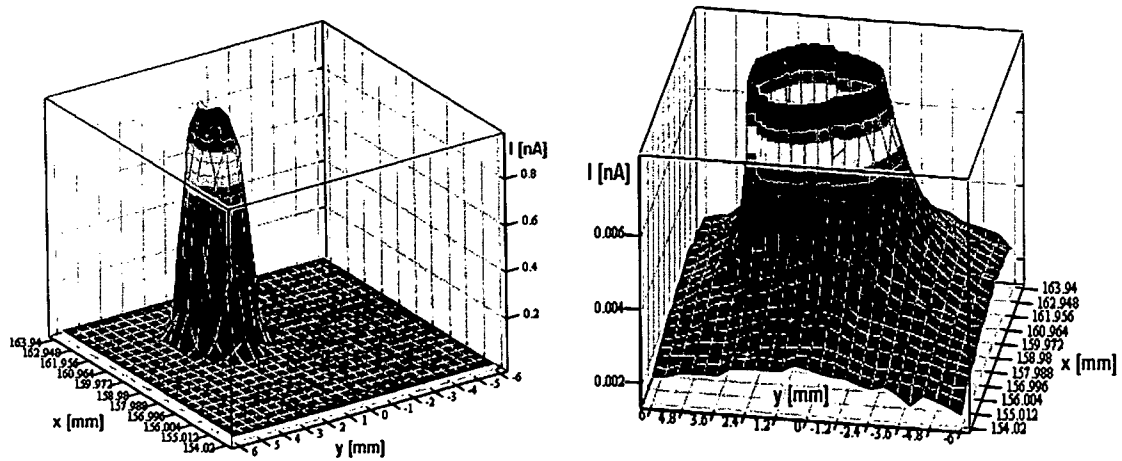
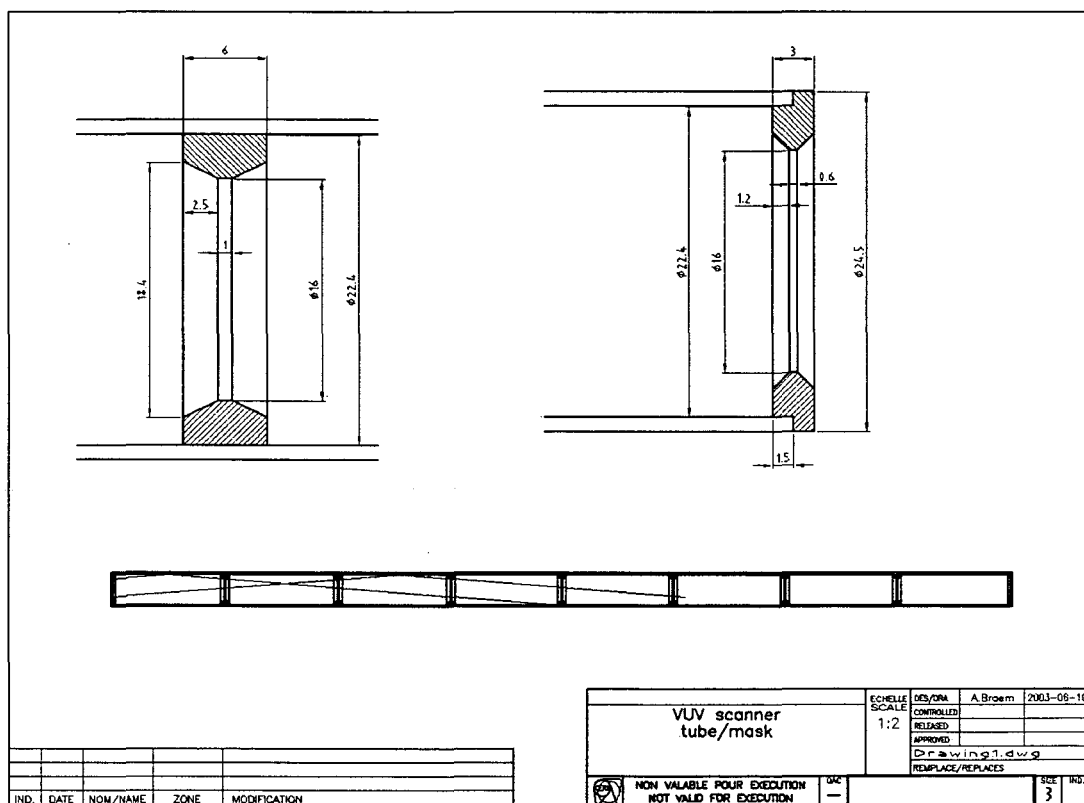
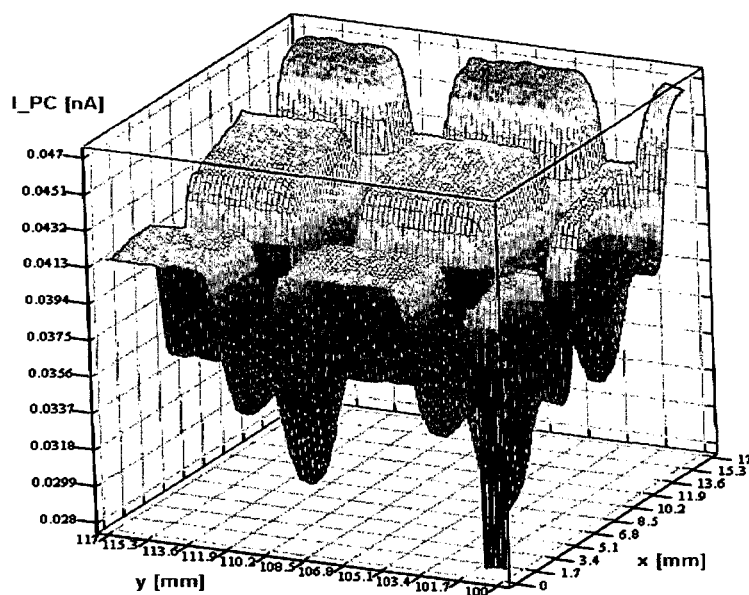


Fig. 57 Spotscans in air with an additional iris on top of the anode: no more reflections are visible even at a very small scale.

Obviously the diaphragm on top of the anode ring was no permanent solution as it makes a reference measurement impossible. Consequently the source of the reflections had to be found and removed. The fact that the reflections were very close to the main spot indicates a very small reflection angle. Therefore it was suspected that reflections at grazing angles on the inside of the aluminum beam pipe were the source of the problem. A first attempt to blacken the inside of the tube was not successful. Shutting the exit diaphragm in the external arm of the scanner to its minimal aperture on the other hand reduced the reflections considerably; however this also reduced the signal by a factor of 2. Therefore a further attempt was made to remove the reflections: As shown in Fig. 59, 7 irises with a diameter of 16 [mm] were inserted into the tube plus two similar irises on both ends of the tube. As the results of the subsequent spotscans Fig. 60 show the reflections were thus diminished to the level of the measurement noise (less than 0.2% of the maximum intensity).



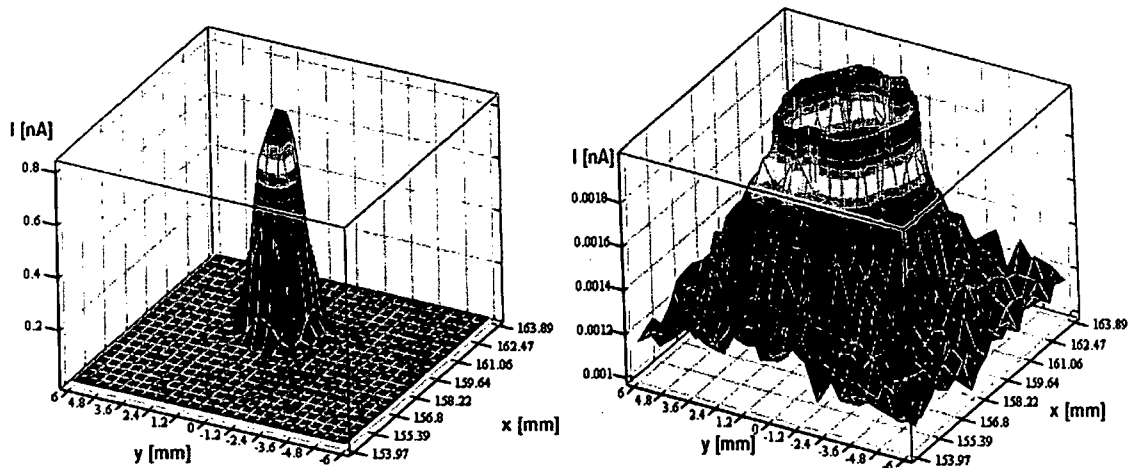


Fig. 60 Spot-scans with 9 additional 16 [mm] irises in the beam pipe to remove grazing incidence reflections. Spot defining diaphragm: 2 [mm] No reflections can be measured above noise level.

4.5.3 Form of the UV spot in the final measurement configuration

As it was foreseen to use a larger spot in the future quality monitoring measurements, spot-scans were also carried out with a spot defining diaphragm of 15 [mm] diameter. The scan in Fig. 61 shows the intensity distribution for the final spot measured after the modification of the UV beam pipe to remove the grazing incidence reflections and after the alignment of the optical system described in 4.5.1.

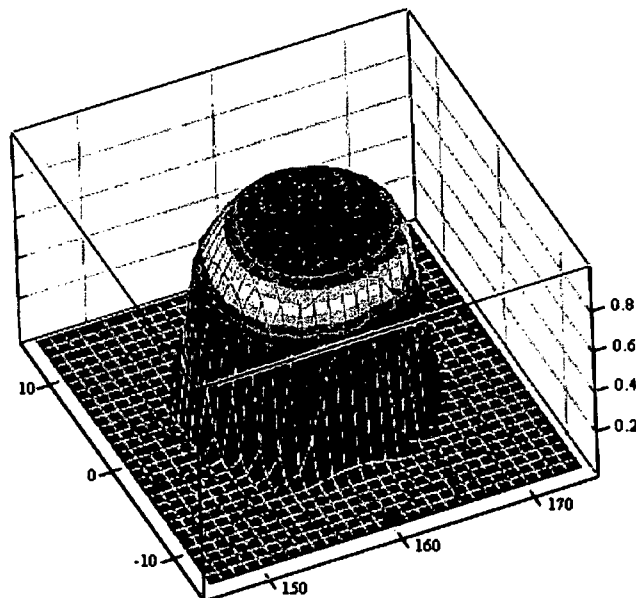


Fig. 61 Scan of the large spot after horizontal realignment of entrance diaphragm next to UV source.

4.6 Inhomogeneous PC response: exclusion of systematic effects

Already in the early tests with the VUV scanner it became obvious that the photocurrents measured from the PCs were not always homogeneous across the PC surface. There were many PCs which showed systematically higher currents on one side or on one end, i.e. linescans showed slopes across the surface. As it is not evident why a photocathode should exhibit such a behavior, quite some effort has been made to show that there are no systematic measurement effects which could cause such inhomogeneities. In the following paragraph a list of effects will be given, which could possibly result in a slope of the photocurrent in certain directions across the PC and it will be specified, how these effects were minimized to exclude their contribution to the actual quality inhomogeneity from the measurement.

- **Penning gauge operation:** as described in 4.1.1 the operation of the penning gauge can influence the photocurrent measurement from the PC possibly due to a transport from ions from the gauge to the PC. As the defect depends on the distance between the gauge and the PC it can lead to a varying response in the measurement according to the position of the PC. This effect has been minimized by placing a shield in front of the gauge, which blocks the ions from reaching the PC. Measurements with the penning gauge on or off show no difference.
- **Positioning errors in connection with the gap effect:** it was shown in 4.3 that the photocurrent depends on the position of the UV spot on the pad due to the decreased QE in the interpad zones. If the position of the UV beam relative to the center of the pad would shift by a small amount for each position in a scan due to mechanical positioning errors this could theoretically lead to an increase or decrease of the photocurrent in a scan in a given direction along the pads. However this effect can be disregarded for the following reasons:

-The gap effect was minimized to some 5% by choosing a large spot (compare Section 4.3.4). We can still measure inhomogeneities up to 10% - 15% in this configuration. The positioning of the PC can generally be reproduced with an accuracy ≤ 1 [mm].

-The inhomogeneities can also be measured on non-engraved test cathodes without pads and interpad zones.

- **Stray light pickup on the PC:** the stray light pickup on the PC depends on the position of the PC relative to the optical system and can therefore lead to a position sensitive noise signal. However this background is subtracted from the measured currents as given in Equation 25 and it was described in 4.4 how the stray light problem has been solved with the installation of a beam pipe.
- **Distance between anode and PC:** as described in Section 4.1.4 we measured that any variation of the distance between anode and PC smaller than 2-3 [mm] does not influence the measurement and in our system the variation of this distance is smaller than 1 [mm].

To remove any other doubts about possible systematic measurement errors leading to inhomogeneities in the photocurrent one of our test cathodes was rotated 180° in the chamber. During this procedure the test PC was exposed to air inside the lab briefly and consequently also the quality of the PC was degraded by approximately 10%. However we could show that the slope in photocurrent both in x and y direction had changed sign after this procedure. Later on during the measurements on standard cathodes in the series production, test beam measurements confirmed the inhomogeneities in the response of some PCs. Therefore we conclude the measured slopes and inhomogeneities are not due to systematic effects in the measurement.

4.7 Influence of the photon flux

There are a number of publications addressing the problem of the degradation of the QE of CsI under high photon flux like [6], [39] - [41]. Fig. 62, taken from [39], shows the QE decrease of CsI due to UV irradiation as a function of accumulated charge on the PC. A possible explanation [39], [38] for the QE degradation is the dissociation of the Cs and I atoms following the extraction of a photoelectron (see Section 3.1, Equation 22). Due to its vapor pressure the Iodine evaporates from the surface and leaves an excess of Cs. In addition vacancies, so called F-centers, can be created in the crystal lattice. This results in a decrease in QE in the UV range due to the smaller QE of Cs. In the visible range on the other hand, the QE can even be enhanced possibly due to lower photo-ionization threshold of both Cs and the F-centers. Fig. 63 shows the influence of UV irradiation on the QE as a function of wavelength. For lower doses there is a considerable enhancement for longer wavelength. In vacuum the Cs will also leave the surface in time, albeit slower. Therefore recovery effects, dependent on temperature can be observed.

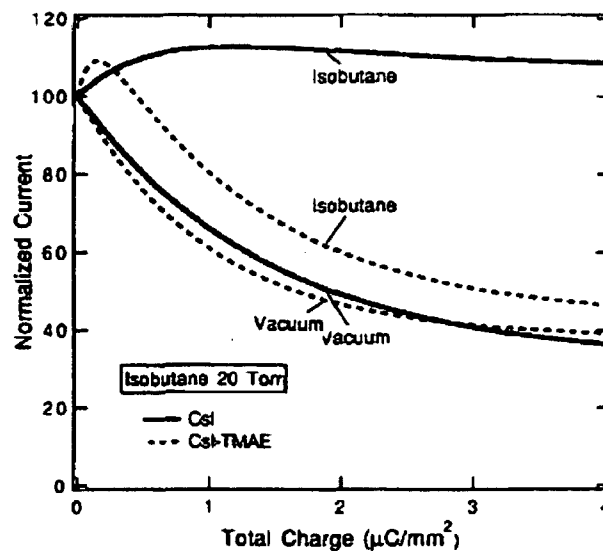


Fig. 62 Degradation of CsI (and CsI-TMAE) PCs due to irradiation with UV as a function of accumulated charge [39].

The phenomenon of ageing under high UV flux does not affect the operation of a RICH detector, as the photon rates are very low (single photon detection). During detector operation ion bombardment of the PC is the main ageing issue as discussed in Chapter 8. However, in the VUV scanner higher photon fluxes can be achieved, therefore some efforts have been made to measure these effects to understand the influence of this ageing

mechanism on our measurements and to tune the scanning procedures in order to minimize any effect on the quality control measurements.

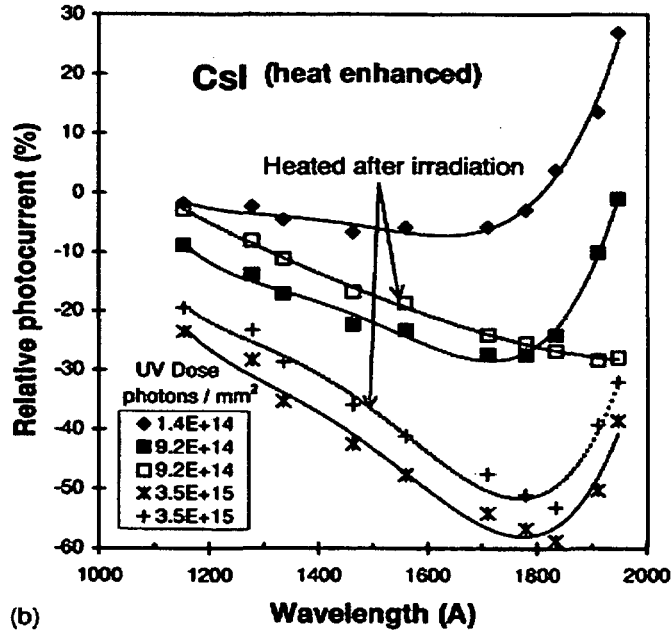


Fig. 63 Degradation of the CsI QE due to UV irradiation as a function of wavelength [40].

4.7.1 Identification of effects in the VUV-scanner

During the commissioning phase we tried to understand how the exposure of the CsI film to the UV beam affects the QE. One of the first effects we observed in measurements on PC 36 was a temporary enhancement of the photocurrent in regions that were illuminated for a longer time, e.g. in regions that were subjected to detail-scans with a very small step width (~ 1 [mm]) in order to measure the influence of the interpad zones as described above. After the detail scans, during which the UV spot (2 – 10 [mm] diameter) was illuminating a small area for a long time, an increased photocurrent was found in the scanned regions. This effect usually disappeared after a few hours.

In one measurement a 10 [mm] UV beam was left on the same spot during 12 hours. The area around and in the spot was scanned before and after this longtime exposure and during the exposure the current from the spot was continuously recorded. From the measured currents (0.5 [nA]) and the assumption of an average QE of 15% of the CsI between 160 and 200 we estimate the photon flux to be approximately $2 \cdot 10^{10}$ [photons \cdot s $^{-1}$ \cdot cm $^{-2}$] in this test. Fig. 64 shows the scans before and after the long term exposure. The scan after exposure shows a higher photocurrent at the location of the long term illumination. Fig. 65 shows the photocurrent from the illuminated spot during the long term illumination. We observed an increase in current of more than 20 % during the first 3 hours followed by a slower decrease during the remaining time.

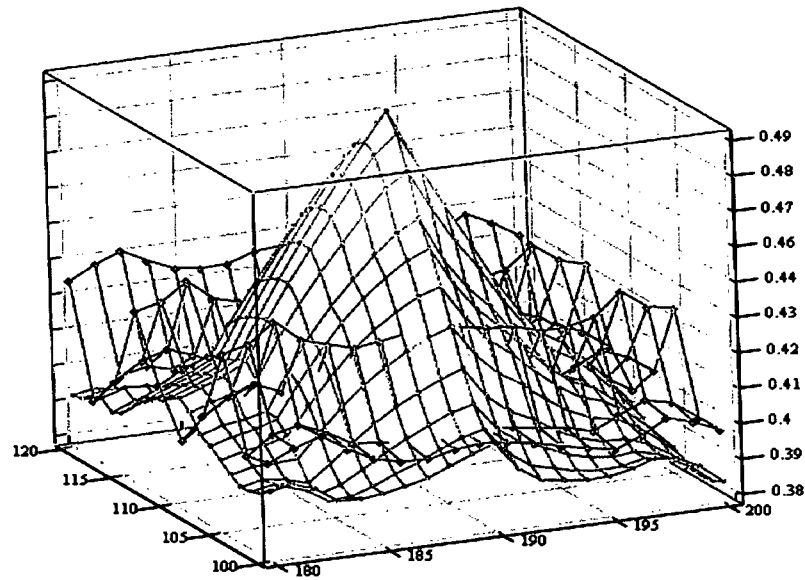


Fig. 64 Scan across an area that was exposed to a long term illumination by a 10 [mm] UV spot. The plots show the photocurrent from a spot on PC 36 in [nA] (z-axis) as a function of x-y-positions in [mm]. The black grid shows the measurement before illumination. The coloured peak in the second plot shows a higher current at the illuminated site after the long term exposure to the UV spot.

A tentative explanation for this effect can be obtained by looking at Fig. 63 which was published in [40]. From this plot it follows that for lower photon doses the enhancement in the visible range outweighs the degradation in the UV range. The low dose curve in this plot is given for a photon dose of $1.4 \cdot 10^{14}$ [photons/mm²] which is still much higher than the total dose collected in our long term illumination, for which we estimate the total dose after 12 [h] to be slightly less than 10^{12} [photons/mm²]. It is a possible explanation, that we observed only an increase in photoelectron current at these low doses, as the CsI was gradually becoming more sensitive to the visible part of the spectrum of our D₂-lamp. With more and more accumulated dose the degradation process could have gained some importance and lead to a decrease of the photocurrent with increasing dose as observed in Fig. 65. Even though the doses accumulated in the 12 [h] of our irradiation were low compared to the ones given in Fig. 63 (i.e. the dose rates were very low) this does not rule out an ageing effect, as lower dose rates can lead to a larger decrease for the same accumulated dose [40].

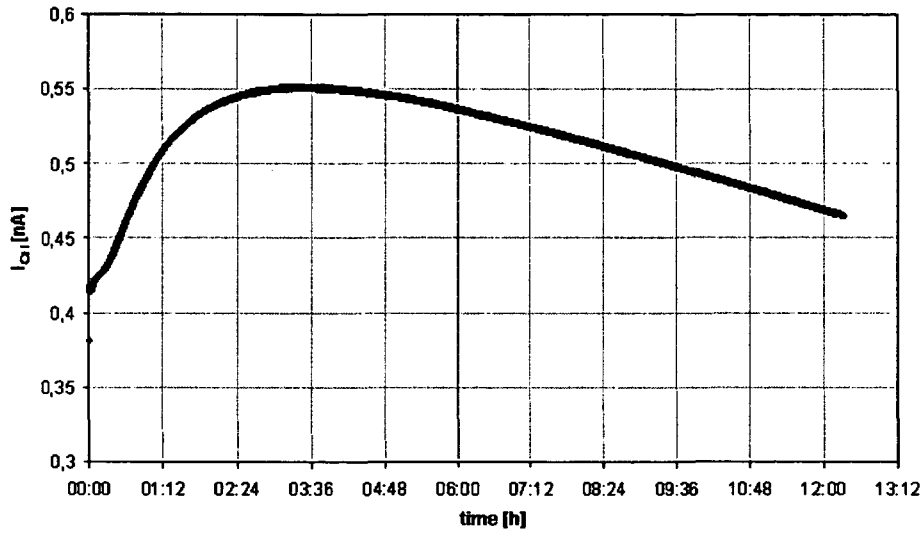


Fig. 65 Change of the photocurrent in time during a continuous illumination of a single spot on PC 36 with a 10 [mm] UV spot and a flux of approximately $2 \cdot 10^{10}$ [photons \cdot s $^{-1}$ cm $^{-2}$].

4.7.2 High flux illumination tests

Experimental setup and procedures

Following these observations of the behavior of the photocurrent under continued illumination, we tried to measure the effect of even higher photon doses in a dedicated test. For these high flux tests a 265 x 388 [mm 2] gold plated PCB-copper-nickel test substrate was used. The substrate is identical to a standard PC substrate except it is not segmented into pads. A deuterium source was mounted on the scanner arm at a distance of approximately 55 [mm] from the PC (compare Fig. 66). Two subsequent circular holes in the temporary aluminum housing were used to obtain an UV spot of approximately 20-25 [mm] diameter. Fig. 66 shows the test substrate and the UV source mounted on the scanner arm. The source housing also served to shield the PC from stray light. The source was operated at a current of 300 [mA]. From the irradiance data as a function of angle supplied by the manufacturer of the source we estimate the photon flux at the center of the illuminated area to be approximately $6.2 \cdot 10^{14}$ [photons \cdot s $^{-1}$ cm $^{-2}$] and $3.7 \cdot 10^{14}$ [photons \cdot s $^{-1}$ cm $^{-2}$] at the edges of the spot. For the photo-current measurements, a 10 [mm] spot was used to achieve a reasonable signal to noise ratio (approximately 130). The UV flux in the measurements with this spot was roughly $2 \cdot 10^{10}$ [photons \cdot s $^{-1}$ cm $^{-2}$] and could be neglected in comparison to the flux from the irradiation source. The substrate was coated with approximately 300 [nm] CsI in a standard evaporation process with 4 CsI sources. The evaporation was carried out at 60 [°C], 8 hours after the evaporation the heating was switched off and the PC cooled down to 25 [°C]. In the illumination tests the test PC was irradiated for a certain amount of time and afterwards linescans of the photo current were performed across the irradiated sites showing the response of the PC outside and inside the irradiated zones.

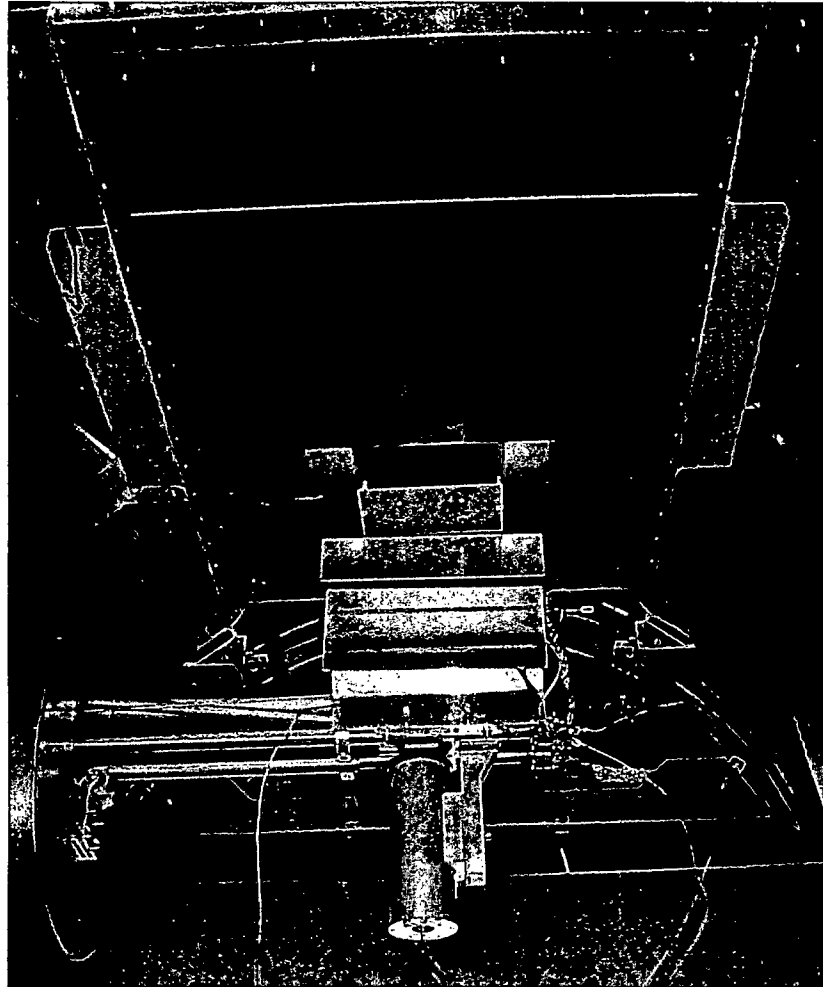


Fig. 66 Test substrate with scanning arm and aluminium shielding of the deuterium source for the high intensity illumination.

Illumination for 2 minutes

In a first test a spot near the center of the PC was illuminated for 2 minutes with the high intensity UV beam. This corresponds to an approximate dose of $7.4 \cdot 10^{16}$ [photons \cdot cm $^{-2}$] (or $7.4 \cdot 10^{13}$ [photons \cdot mm $^{-2}$]) in comparison with Fig. 63). Linescans over the investigated area were performed before illumination, immediately after illumination and several times during 112 hours after illumination. The plots are given in Fig. 67. Immediately after illumination, a clear decrease in (relative) photo-current (20 %) could be observed at the center of the illuminated area, accompanied by a smaller increase (10- 15%) near the borders of the illuminated spot. This behavior could be explained by comparing with the results in Fig. 63 from [40] again. In Fig. 63 the dose closest to our case is the one of $1.4 \cdot 10^{14}$ [photons \cdot mm $^{-2}$]. In [40] there is no reference to the recovery effect in time, however it is specified, that the measurements were taken a few hours after irradiation to allow for a relaxation. This explains, why the decreases quoted in Fig. 63 for a dose of $1.4 \cdot 10^{14}$ [photons \cdot mm $^{-2}$] are even less than what we initially measured after our irradiation with a dose of $7.4 \cdot 10^{13}$ [photons \cdot mm $^{-2}$]. Again for these low doses the QE enhancement in the visible range is outweighing the effect of the decrease, which could explain why we saw an enhancement at the boarder of the spot, where the dose is rapidly dropping to zero. As

mentioned above there are 2 effects: The first one is an decrease of the QE in the UV due to an excess of Cs and the second one is an enhancement in the visible range due to the lower photo ionization threshold of Cs and due to the creation of F-centers and the lower threshold of Cs. Our measurements indicate that both of these effects are not permanent as we measure an almost complete relaxation after 112 hours. In our measurements we find at first a decrease at the center of the irradiated spot. Then the response starts to improve again and 15 – 40 [h] after irradiation we even measure a quality that is higher than before irradiation. This reaches a maximum and then starts decreasing again down to the initial level from before irradiation. This effect could be explained by assuming that the QE decrease in the UV recovers faster then the relaxation of the QE enhancement in the visible range.

It should be mentioned that other measurements were carried out on different sites of the PC during the time between 40 hours and 112 hours after illumination. During these measurements on other spots, the PC was exposed to both -500 [V] and +500 [V] bias voltages for 2 minutes each and it was also heated to 60 [°C] for several hours – compare description of later illumination experiments.

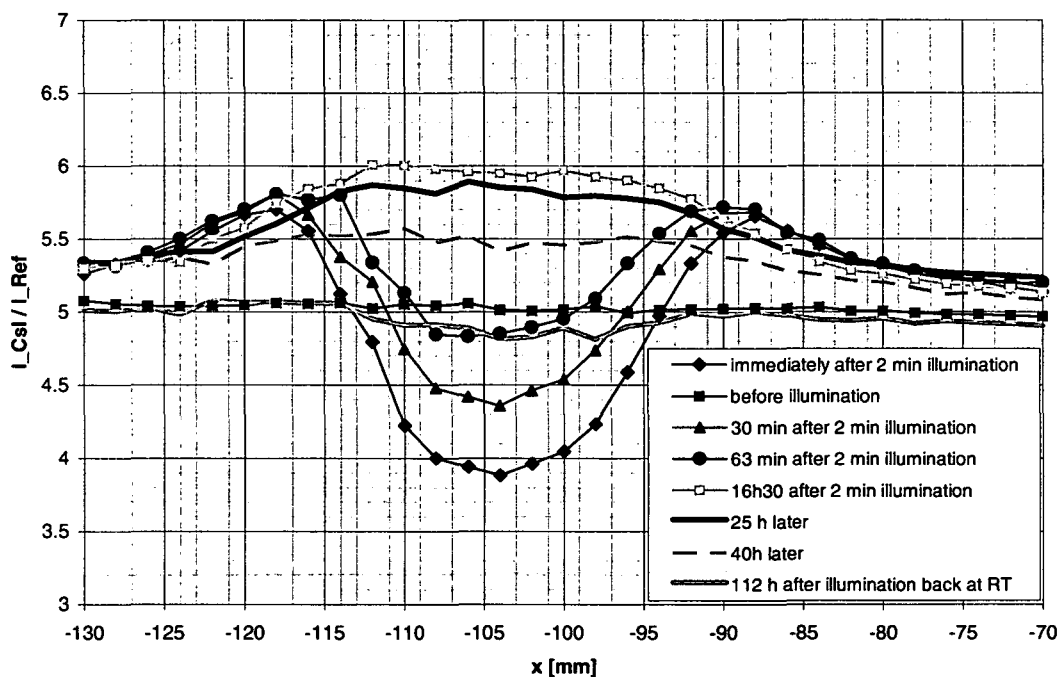


Fig. 67 Illumination for 2 min. Scans over the illuminated spot during 112 hours.

Illumination for 6 minutes

In the next test a different site of the PC was exposed to the high intensity beam for 6 minutes. This corresponds to a dose of $2.2 \cdot 10^{17}$ [photons·cm⁻²] (or $2.2 \cdot 10^{14}$ [photons·mm⁻²]). Before and during illumination the residual gas was analyzed with a quadrupole mass spectrometer to check for possible surface cleaning effects. No change in the composition (e.g. water, hydro-carbons) could be observed after the illumination was started. Scans (Fig. 68) across the illuminated spot were carried out within 90 [h] after illumination. Some tests with illumination with bias voltage were carried out 20 [h] after the 6 [min] illumination on

different sites of the PC. Immediately after illumination, a decrease of 40% can be observed at the center of the illuminated area (compared to 20% in the 2 [min] illumination). The level of the increase near the borders remains 10-15% as in the previous 2 [min] illumination. The next scans after 35 [min], 2[h]45 and 18 [h] show that the recovery time is much longer than in the test with the 2 [min] illumination: In the first test the (relative) current has fully recovered after 17 h, whereas in the case of the 6 [min] illumination, after 18 [h] the current level is still 30-35 % lower than before illumination.

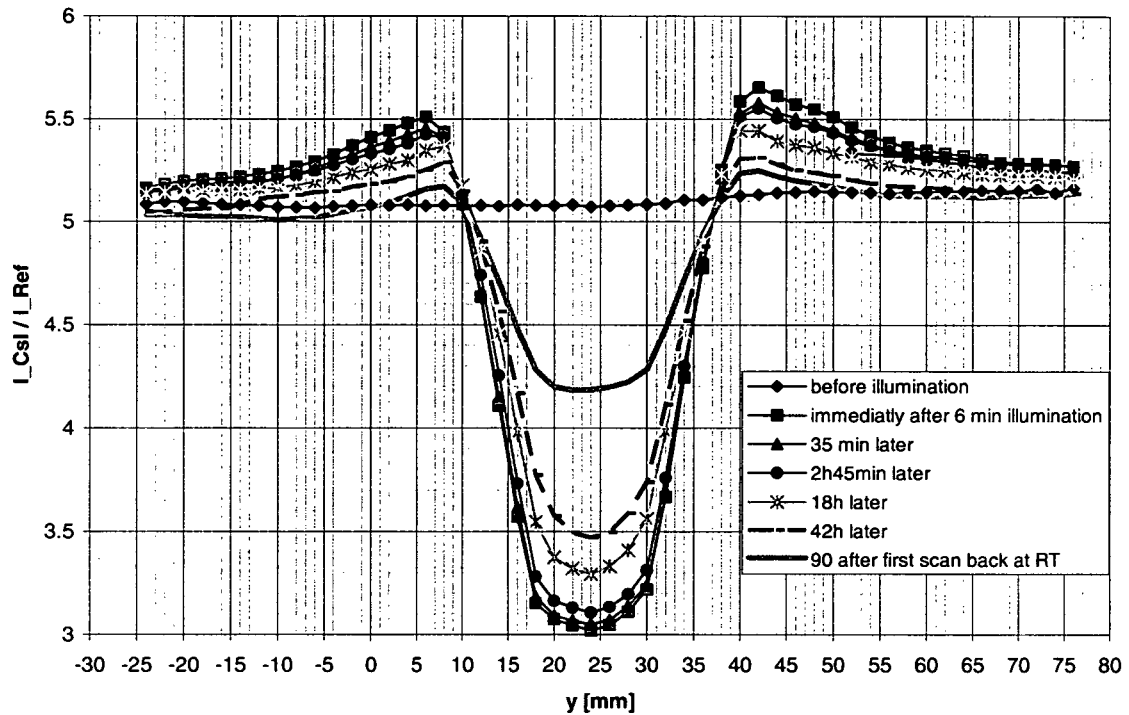


Fig. 68 Illumination for 6 minutes. The effect is increased and the recovery is slower.

To check for possible surface charging effects due to the high flux irradiation, the photocurrent was measured as a function of the voltage applied to the anode ring. The anode voltage was varied between 0 and 100 Volts and the expected plateau of the photocurrent for anode voltages >10 [V] was retrieved, which is also found in sites that were not irradiated. The voltage used in the scans is 100 [V]. So within the observed voltage range, no dependency on the extraction field could be measured.

In an additional illumination during 2 [min] at a different site on the PC, another attempt was made to measure the recovery of the photo-current by leaving the scanner at the center of the illuminated spot and take a measurement every 10-15 minutes (blue curve in Fig. 69). The plot in Fig. 69 also contains the data of the centers of the previously illuminated sites extracted from the scans in Fig. 67 and Fig. 68. The green curve shows the recovery of the 6 [min] illuminated site which is much slower and the current level is lower as mentioned before. The red and blue curve were both measured on sites that were illuminated for 2 min, nevertheless they show a different level of photo-current at the beginning and a different recovery rate. The different levels might be explained either by different positions of the spots with reference to the PC boarder, or by the fact, that the blue curve was actually recorded in one of the last tests, some time after the PC was exposed to bias

voltages, and temperature change as described below. Also the levels of the currents before illumination are different for the two sites: approximately 5.1 for the red curve and 5.3 for the blue one.

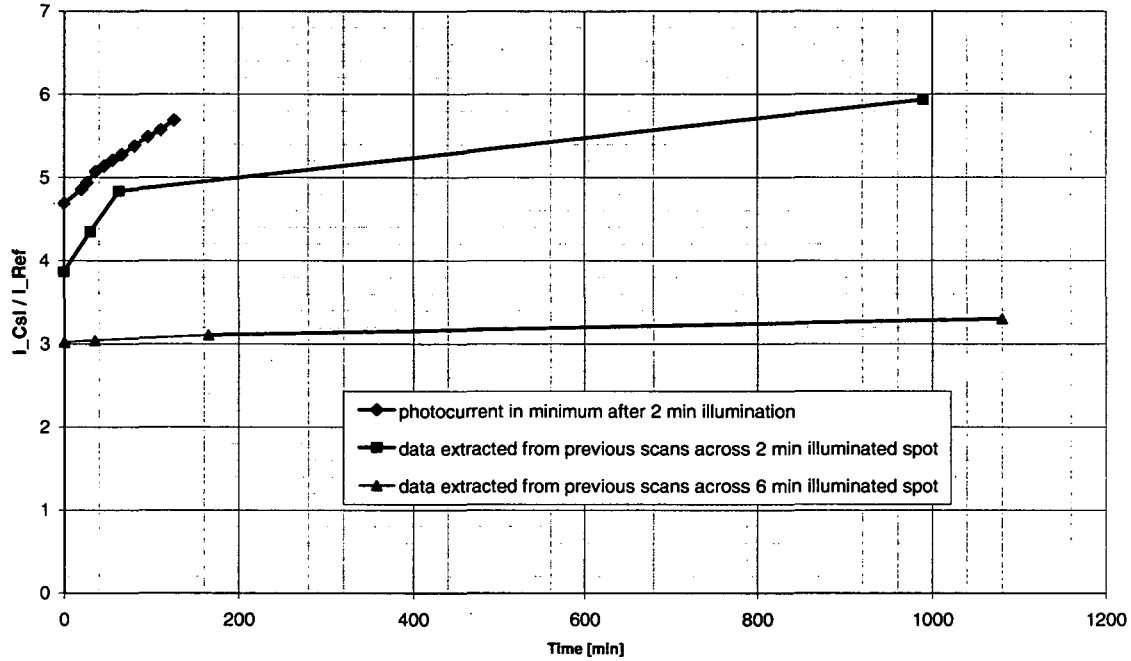


Fig. 69 Recovery of photo-currents at the center of the illuminated zone. Data for the red and green curve have been extracted from the scans given in Fig. 67 and Fig. 68. The blue curve was measured in a separate illumination test, during which the scanner was left in the center position of the spot.

Illumination for 6 minutes with biased PCs

To test the hypothesis of a charging effect in the CsI layer, 2 further illuminations were performed on the PC, one with a bias voltage of -500 [V] and another one with +500 [V] on the PC during the illumination period of 3 [min] 30 [s] and 2 [min] respectively. The following observations could be made:

- The effect of a decreased photocurrent in the illuminated zone is present also with bias voltage on the PC, the order of magnitude of the effect being the same as in the illumination tests without bias.
- In both cases an overall shift of the photocurrent could be observed independent from the illuminated area: After the illumination with +500 [V] bias the photocurrents were shifted upwards all over the PC, also in previously illuminated sites. A decrease could be observed even during the 10 minutes of the first scan immediately after illumination (red curve in Fig. 70). In the tests with negative bias (-500 [V]) a shift towards lower currents could be observed, which was rapidly increasing towards previous levels.
- It could not yet be established, if the recovery rates in the centers of the illuminated zones change with bias voltage.

These results suggest that the effect of the decreased photocurrent in the illuminated zone is independent of the bias voltage on the PC during illumination, at least within 500 [V]

(being the maximum that can be applied with the setup as it is now). However the bias voltage affects the photo-currents all over the PC.

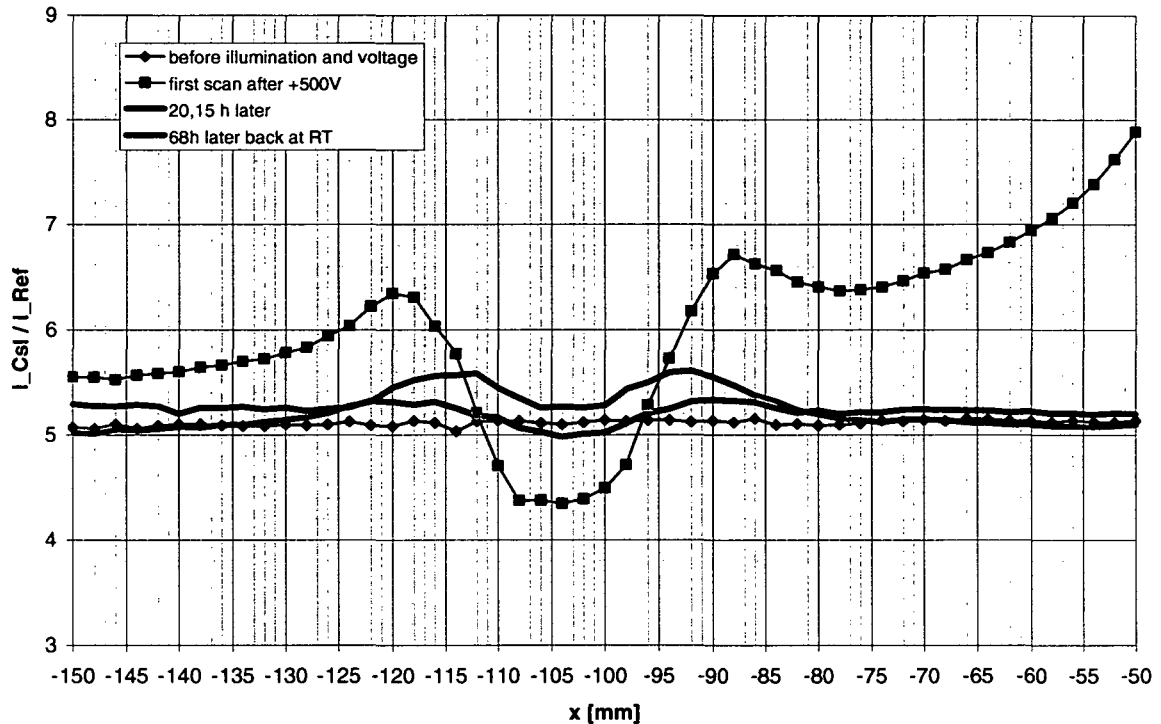


Fig. 70 Illumination for 2 [min] with +500 [V] bias voltage on the PC.

4.7.3 Negligible effect in a standard scanning procedure

The measurements presented in Section 4.7.1 show how the UV spot used in the photo current measurement can change the PC response. These measurements were performed with a D_2 source with a quartz window mounted as close as possible to the 1 [mm] entrance pinhole of the optical system. Meanwhile the system has been equipped with a lamp with a MgF_2 window to increase the wavelength range of our measurements. Due to the larger distance between the location of the discharge and the exit window in this lamp the distance between the actual source point and the entrance pinhole of our optical system was increased and consequently we lost some light intensity in our UV spot, which was compensated by a larger exit iris of the optical arm. Currently we are measuring signals in the range of 300 to 1000 [pA] and therefore we estimate the photon flux of our UV (16 [mm] diameter) spot on the PC to be approximately $2 \cdot 10^{10}$ [photons $\cdot s^{-1} \cdot cm^{-2}$]. In a standard scan the measurement of a single point takes roughly 1 minute, which includes reference and background measurements. The scanned points are usually separated by more than the spot diameter and therefore the UV spot is never longer in one position than 30 seconds. This corresponds to a dose of $60 \cdot 10^{10}$ [photons $\cdot cm^{-2}$] for a single measurement. If we compare to the initial increase of the current under continuous irradiation presented in Fig. 65, we can estimate that the effect of the irradiation during 30 seconds in a standard scan is less than 0.2 %, which is negligible, especially as these effects recover with time.

5 Post deposition enhancement

5.1 Introduction and motivation

It was already mentioned in Section 3.1 that the R&D studies of the photoemission properties of CsI photocathodes describe a heat enhancement effect of the QE of freshly evaporated PCs, i.e. an increase of QE for PCs that are either evaporated at room temperature and subsequently heated to 40-60 [°C] or evaporated already at higher temperature. These tests were mostly carried out with small samples of PCs and the results were not always consistent, as some authors even reported not to be able to measure an enhancement effect [47]. For the prototypes of the large area PCs produced at CERN for the ALICE RICH detector the chosen standard procedure was a deposition of CsI at a temperature of 60[°C] in order to speed up the enhancement process. With the recent completion of the VUV scanner it is now possible to actually measure these enhancement effects on the large area PCs produced at CERN. In order to obtain more information about the heat enhancement process and to define a standard procedure for the series production of the PCs for the ALICE HMPID detector, a series of tests was carried out.

It is important to understand the behaviour of the photocathode after evaporation in order to determine how long the PC has to stay under vacuum until the quality has stabilized. The tests also help gather valuable information as to how and when the quality evaluation measurements after evaporation are to be done in the series production, e.g. after stabilization. Furthermore it is both of practical and theoretical relevance to understand these effects and try to find correlations between the development of the quality (quantum efficiency) and other parameters like pressure, temperature and humidity.

Tests were carried out with three different types of photocathodes:

- Large area (265 x 388 [mm²]) test photocathodes evaporated and measured in the production/evaluation facility that is also used for the series production of the standard PCs for the ALICE RICH detector.
- Standard PCs during the first phase of the series production for the HMPID modules in the same setup.
- Small samples (18 x 18 [mm²]) in the R&D setup ASSET in order to reproduce the effect under different vacuum and measurement conditions.

In the following paragraphs the results of these tests are reported.

5.2 QE enhancement of large area test PCs

5.2.1 Experimental procedures

Setup

One series of enhancement tests was carried out with a 265×388 [mm²] test substrate which is identical to the standard HMPID photocathodes, except the surface is not segmented into pads and therefore there is no non-metallic interpad zone. Fig. 71 is a photo of this test substrate which is mounted on a support plate that allows an installation into the VUV scanner. Thus the same system could be used for the CsI deposition and subsequent photocurrent measurements that is also used for the series production and quality evaluation of the standard HMPID photocathodes.

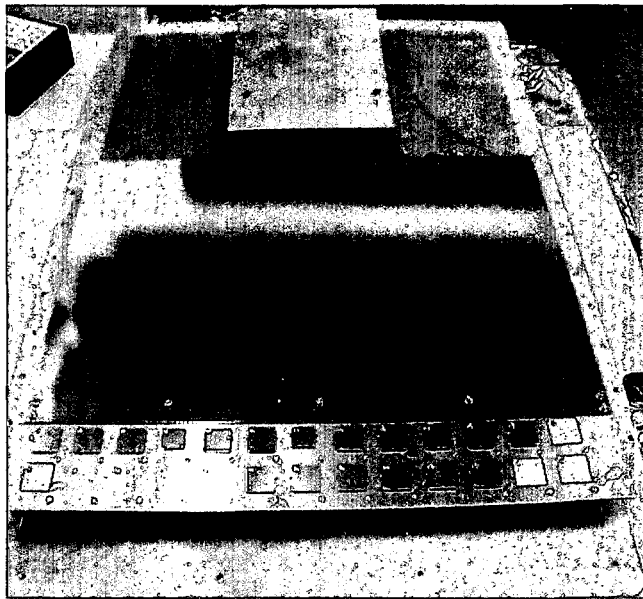


Fig. 71 Test substrate mounted on a support plate for installation into the VUV scanner.

The substrate shown in Fig. 71 was used for 8 tests in total. After an evaporation and measurement procedure the CsI was removed with demineralised water and the substrate was then cleaned with ethanol, nitrogen jet and kept at a temperature of 60 [°C] until the next test.

Procedures for enhancement measurements

The measurements were performed with a UV spot of 10 [mm] diameter after the following two procedures:

Line scans: scans across the cathode were performed at every stage of the test process (e.g. after evaporation, before and after annealing.) The scans were carried out with and without a quartz window in the optical path in order to measure the effects with different spectral composition of the UV beam and to detect possible wavelength dependencies of the effects.

Continuous scans: during these measurements the scanner was continuously moving on a rectangular path covering much of the surface of the PC during the heating or stabilization

periods. This method allows obtaining a continuous measurement of the PC response without modifying the PC due to ageing under high photon flux, as would be the case if a single spot would be measured continuously (compare Section 4.7.) A disadvantage of this method is the fact, that it includes the inhomogeneous response of the PC by measuring about 50 different positions on the PC. Fig. 72 shows the photocurrent as a function of the x/y position on the PC during one of these continuous scans. The normalized current starts at a level of approximately 2.6 before the heating period and increases to approximately 3.7 - 4 after the heat treatment. Fig. 74 shows how such data is plotted as a function of measurement time. These plots show a significant spread of the data points due to the inhomogeneities on the PC, e.g. if one side of the PC shows a systematically higher current than the other one, the plot against time shows a periodic variation in current. To make the plots clearer and a comparison of different cases possible, smoothing functions were used to average between neighbouring data points (e.g. averaging over 50 points which corresponds roughly to a full circuit on the PC, see for example Fig. 76).

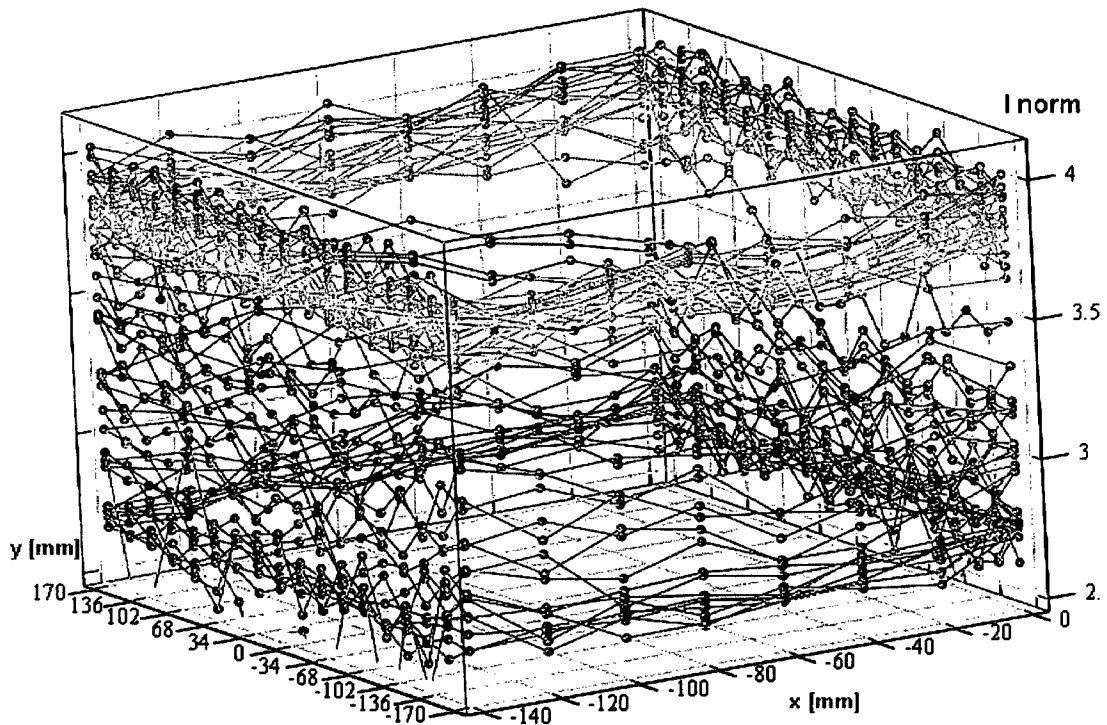


Fig. 72 Plot of the normalized photocurrent as a function of x and y coordinate during a continuous scan. The level of the normalized current increases during the heat treatment phase.

5.2.2 Summary of tests

The test substrate was used to gather experimental evidence for a post evaporation enhancement effect correlated with annealing the PCs. Both evaporations at room temperature and at 60[°C] were carried out. Table 4 summarizes all the tests that were performed. It lists parameters like pressure and temperature during the CsI deposition and a description of the heat enhancement phase, as well as the normalized photocurrents before and after the enhancement phase.

Evaporation			Initial current ratio					Heat treatment phase		Final current ratio					final level/ initial level
Nr	T _{EVAP} [°C]	P _{EVAP} [mbar]	mean value	standard deviation	stddev/ mean	nr. of samples	time after evaporation		P _{HT} [mbar] during enhancement	mean value	standard deviation	stddev/ mean	nr. of samples	time after evaporation	
T1	65	2.0E-06	3.33	0.08	0.02	200	1.8 h to 5 h	cooldown after 8h	1.50E-06	3.63	0.10	0.03	260	24h to 27h	-
T2	25	3.0E-06	2.68	0.03	0.01	260	1.2 h to 5 h	heating to 65 °C after 5h for 20h	2E-5 to 5E-5	3.94	0.12	0.03	300	70.5h to 75h	1.47
T3	25	5.0E-08	2.71	0.05	0.02	290	0.75 h to 5 h	heating to 65 °C after 5.5h for 27h	1E-7 to 5E-7	4.08	0.16	0.04	100	141.5 h to 143 h	1.51
T4	25	1.0E-05	2.67	0.04	0.02	210	2.1 h to 5 h	heating to 65 °C after 5h for 22h	5E-6 to 1.5E-6	4.21	0.16	0.04	209	190 h to 193.4 h	1.58
T5	65	1.1E-06	3.48	0.21	0.06	120	3.4 h to 5 h	cooldown after 10h	9E-7 to 2E-8	3.98	0.10	0.03	300	117.2 h to 122.5 h	-
T6	25	9.0E-07	2.69	0.10	0.04	200	4.5 h to 8.4 h	heating to 35 °C after 7h, then to 75 °C after 23h, cooldown after 32h	5.50E-07	4.04	0.08	0.02	80	117.4 h to 119 h	1.50
T7	65	1.0E-06	3.16	0.03	0.01	260	3 h to 8 h	cooldown after 25h	9.00E-06	3.35	0.07	0.02	160	312 h to 315 h	-
T8	25	1.4E-08	2.62	0.05	0.02	310	0.3 h to 6.3 h	stabilizing to 28°C after 26 h; heating to 35 °C after 66 h; heating to 70 °C after 90 h; cooldown after 169 h	< 2E-8 first 90 h	3.88	0.14	0.04	311	180 h to 185 h	1.48

Table 4: List of all test evaporations with evaporation conditions, description of heat treatment and comparison of initial and final current levels.

5.2.3 Wavelength dependent enhancement effect

One of the first results of the line scans obtained during the various tests was the fact that the heat treatment effect is wavelength dependent. The linescans were usually carried out before and after the heat treatment phase and once with and once without a quartz window in the optical path of the UV beam. Fig. 39 shows how the presence of the quartz modifies the spectral composition of the UV source. In a measurement with quartz window the long wavelength part of the spectrum is more dominant compared to the case without quartz window. The heat treatment effect, i.e. the increase of the normalized photoelectron current after the heating period, is roughly a factor of two higher if measured with quartz window than with full spectrum. Fig. 73 shows the results of linescans taken after a test evaporation at room temperature before and after a 24 [h] heating period at 64 [°C]. Therefore this effect must be more pronounced for higher wavelength and the result could indicate a shift in the photoemission threshold to higher wavelengths during the heat treatment phase. This result is in accordance with wavelength dependent measurements reported in the literature as discussed in Section 3.1 and shown in Fig. 20.

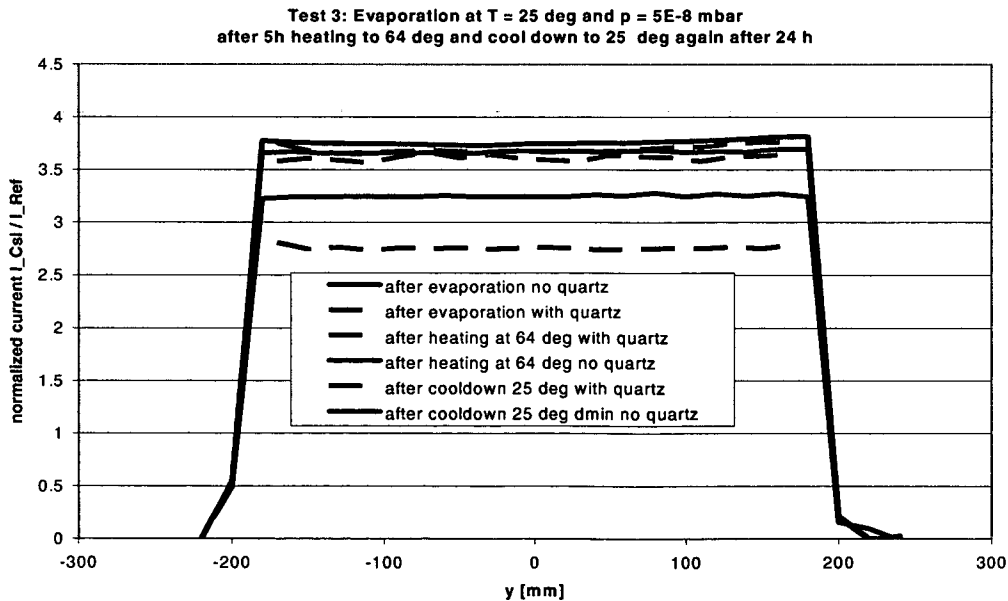


Fig. 73 Line scans before and after heat treatment with and without quartz window.

5.2.4 Influence of substrate temperature during evaporation

Before we were able to measure the enhancement effect, the established standard procedure in the photocathode production was to evaporate at a substrate temperature of approximately 60-65 [°C] and then keep the PC at this temperature for 8-12 hours before cool down to room temperature. We tested both evaporations at 65 [°C] and at room temperature. Table 4 lists all the test evaporations with evaporation conditions, annealing procedure and statistics on the development of the normalized current.

Fig. 74 shows an example for the development of the normalized current after evaporation at 25 [°C]. The PCs evaporated at 25 [°C] were heated to 65 [°C] after the first measurements and a sharp effect of the heat treatment was observed afterwards with a 50 % increase of the initial value of 2.6 of the normalized the current up to a final level of close to 4. An example for this effect is given in Fig. 74 which contains plots of the evolution of the normalized current, temperature and pressure during test T4. The plot of the evolution of the photocurrent in time in Fig. 74 was obtained from a continuous scan as described above. The spread of the data points is due to the inhomogeneity of the photocurrent on the PC surface. It is obvious from this plot, that the inhomogeneity is increasing with the enhancement, as the spread of the data points is much higher after the completion of the enhancement phase. In other words, the enhancement is not equally effective at every location on the PC. The same behavior was observed during several other enhancement measurements, e.g. the plot in Fig. 78 shows a similar increase of the spread of the photocurrent values. The summary in Table 4 shows the mean values of the current before and after enhancement together with the standard deviation of the data points as a measure for the inhomogeneity. For most of the PCs⁸ the standard deviation of the measurement values after enhancement is higher. The same effect of an increased inhomogeneity after the enhancement phase was found in the measurements on standard PCs for the detector, which will be shown in Section 5.3.

In the evaporations at 65 [°C] the normalized current starts increasing immediately after evaporation and is followed by a second phase of slower enhancement. Fig. 75 shows the development in time recorded during the tests T1, T5 and T7. In the first two of these tests the initial phase of enhancement was missed as the measurement was started too late. The measurement of the initial level is determined by the time that is required to move the PC from the evaporation position to the measurement position and start the scan. This usually takes a minimum of 10 - 15 minutes. After this initial time a level of approximately 2.6 is measured which increases up to 3.25 - 4 during the enhancement phases. The initial level is comparable to the initial levels measured after evaporations at room temperature. This behaviour was also observed in some of the standard PCs, described in 5.3.

⁸ One case in which this is not true is T5 with an evaporation at high temperature. In this case the initial level was missed as the enhancement was too fast to start the measurement in time. Consequently the data of the initial level is incorrect. The second case is T6 in which the final level was measured only on a small number of points.

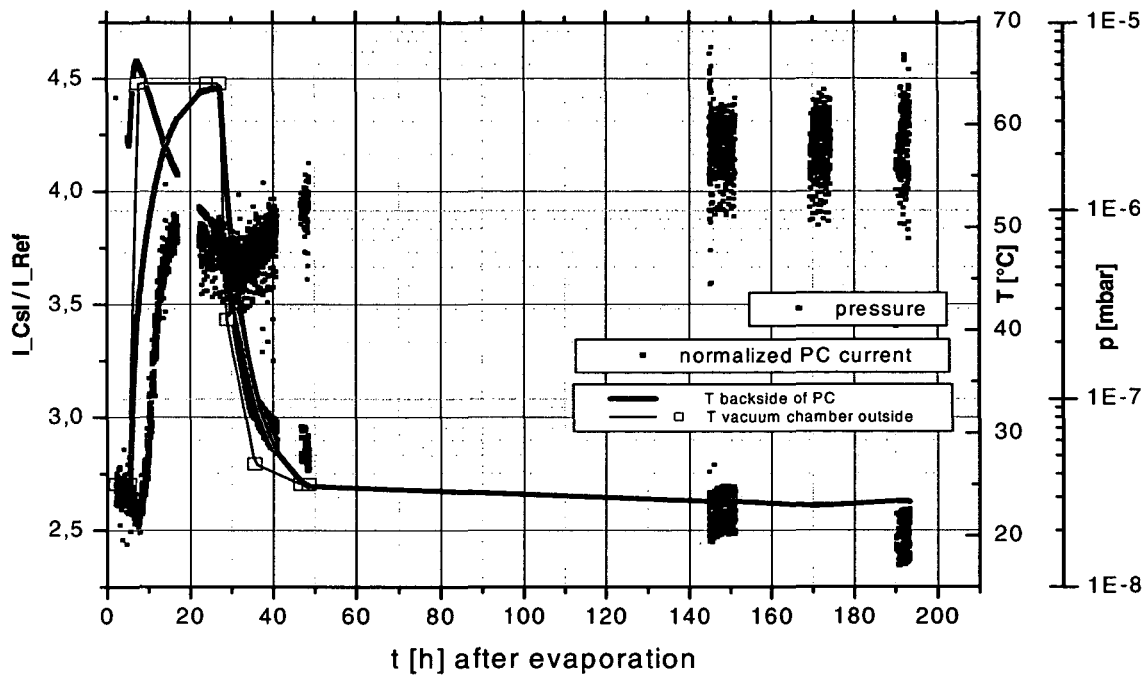


Fig. 74 Increase in normalized photo current after an evaporation at 25°C. The current starts increasing after the cathode is heated.

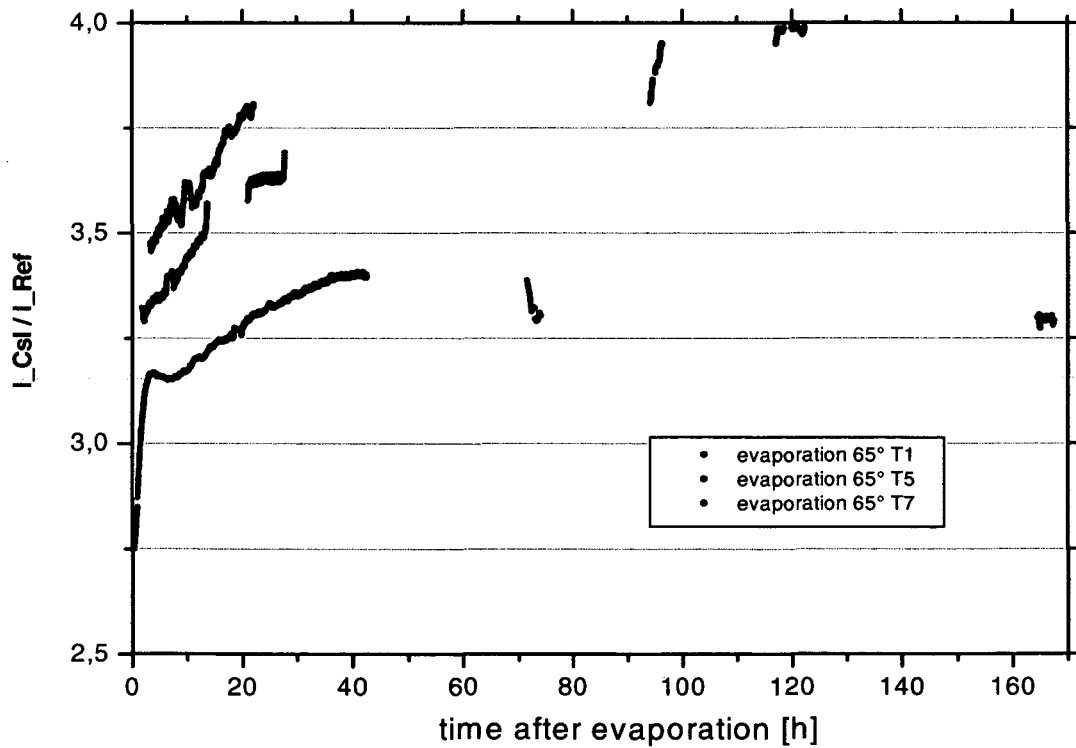


Fig. 75 Results of the continuous scans after evaporations at 65 [°C] (tests T1, T5, T7) The cooldown of the PCs to room temperature was initiated after 8 hours in T1, after 10 hours in T5 and after 25h in T7.

Both evaporations at room temperature and evaporations at 65 [°C] showed first an initial phase of fast increase of quality which is followed by a long stabilization phase, which lasts during and after the cooldown to room temperature. During this phase the current can even decrease a few percent at first and then it starts increasing again at a very slow rate. PCs re-measured after a few days usually showed a slightly higher current level than immediately after the fast increase during the heat treatment phase. This behaviour can be seen in Fig. 74 and Fig. 76.

5.2.5 Influence of pressure and temperature during the enhancement phase

In an attempt to understand, what is happening in the CsI layer during the heat treatment, a series of tests was performed to study the influence of pressure and temperature on the measured effects. As the heat enhancement phase was always rather short and difficult to measure after a high temperature evaporation with the test substrate, it was chosen to use evaporations at 25 [°C] followed by a heating phase a few hours after the evaporation for these tests. The general behavior of the QE of the CsI during such a test can be understood from the plot of Test 4 in Fig. 74: After deposition the current level is stable at first, if not even slightly decreasing. After switching on the heating (usually to 65 [°C]), there is a small time delay, during which the current was repeatedly observed to decrease⁹ slightly, before the sharp increase of the heat enhancement takes place (compare also Fig. 76). The increase is followed by a stabilization phase, during which the current level can slightly decrease before it starts to increase slowly again. The current level stays high (approximately 50% higher than the initial value) even after the substrate is cooled down to room temperature again. After cool-down the PC seems to be still improving for several days at a very slow rate. In total 5 tests like this have been performed (Tests 2, 3, 4, 6, and 8 in Table 4) In all these tests approximately the same initial and final current levels were observed, however the rate of increase during the heat enhancement phase varied considerably depending on temperature and pressure conditions (compare for example Fig. 76). In a first test series (tests T2 – T4 in Table 4) it was investigated, if the rate of increase during the enhancement phase depends on the pressure conditions during evaporation, i.e. if there is a correlation between the amount of H₂O (main constituent of the residual gas) present during evaporation and the heat enhancement. As given in Table 4 for the tests T2-T4, the evaporations were performed at $3 \cdot 10^{-6}$, $1 \cdot 10^{-5}$ and $5 \cdot 10^{-8}$ [mbar] pressure. The result was negative. Although the rate of increase was different in the 3 tests (Fig. 76), it did not correlate with the pressure during evaporation. In two further tests (T6, T8) it was investigated if the heat enhancement can be triggered by heating to less than 65 [°C]. In the first test (T6, Fig. 77) it turned out, that heating to 35 [°C] was sufficient to start the effect, however at a lower rate. A further increase of temperature towards the end of the enhancement phase accelerated the completion of the process. In the next test (T8, Fig. 78) the PC was kept at low temperature (< 26 [°C]) for more than 60 hours. The current started increasing after 30 h, however at a very slow rate. The temperature was increased twice more, which accelerated the enhancement. In a further analysis of the 5 tests, the maximum rate of increase of the current level during the heat enhancement phase was obtained, by fitting sigmoidal functions to the measurement data and taking the maxima of their derivatives. This maximum rate of enhancement was then related to the pressure in the vacuum chamber at the time of the maximum heat enhancement rate, which lead to the plot given in Fig. 79. It seems that not only the temperature, but also the pressure (or more

⁹ This could be related to outgassing effects, that take place, when the heating is started.

likely the amount of water present in the residual gas) is influencing the rate of increase during the enhancement phase.

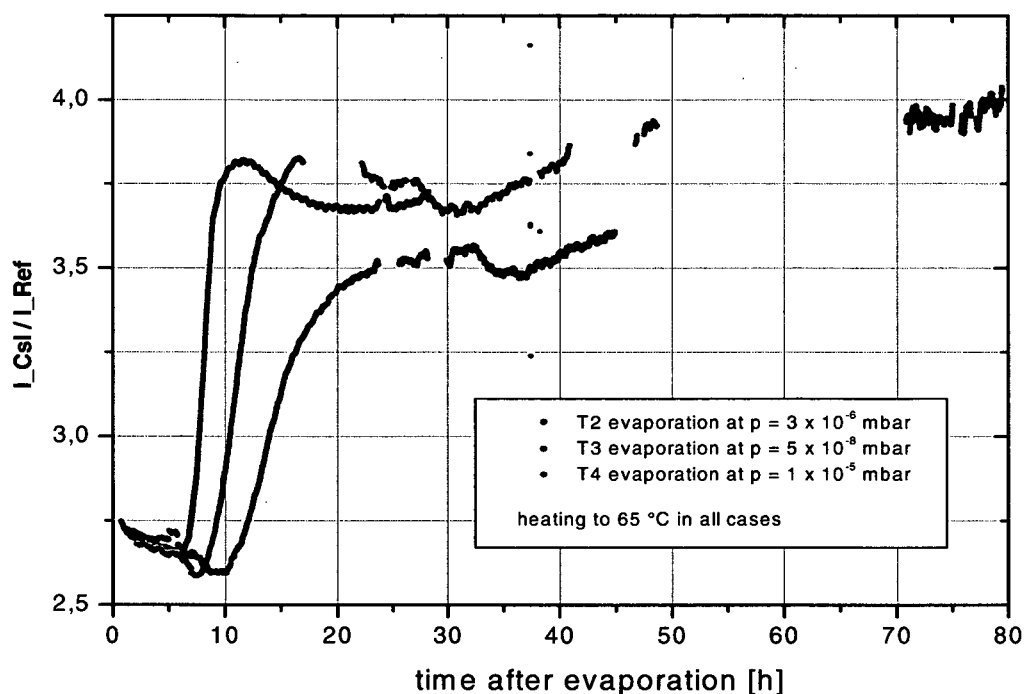


Fig. 76 Comparison of the heat enhancement for evaporations at three different pressures.

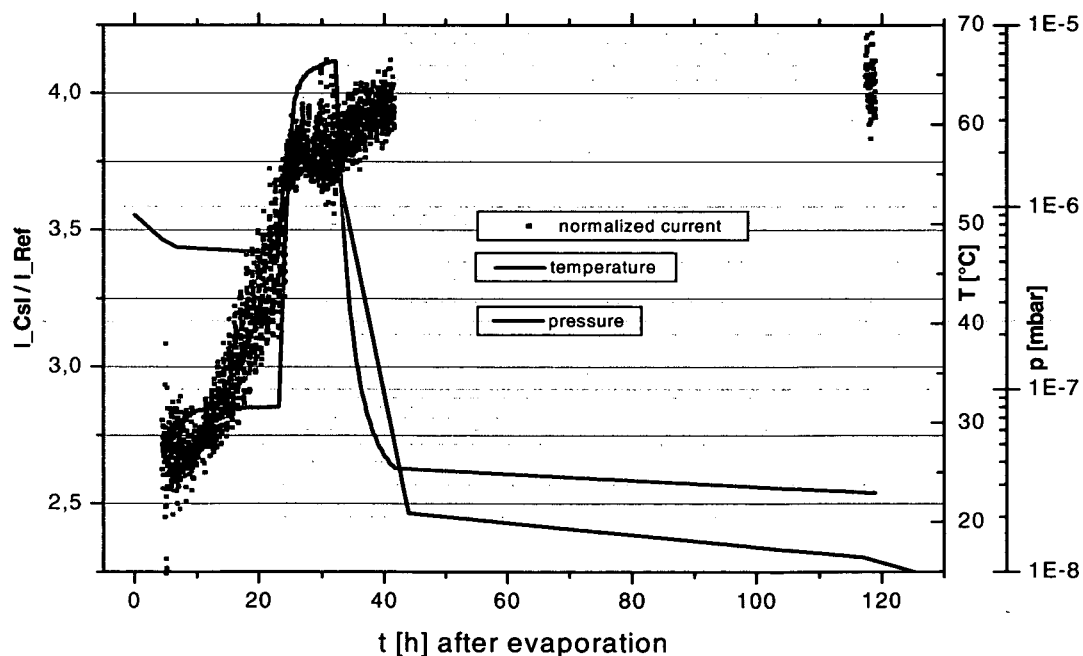


Fig. 77 Plot of current levels, pressure and temperature during test T6. In this test the PC was only heated to 35 [°C] (instead of the usual 65 [°C]) which started a slower enhancement process. A further increase of temperature towards the end of the enhancement phase accelerated the completion of the process.

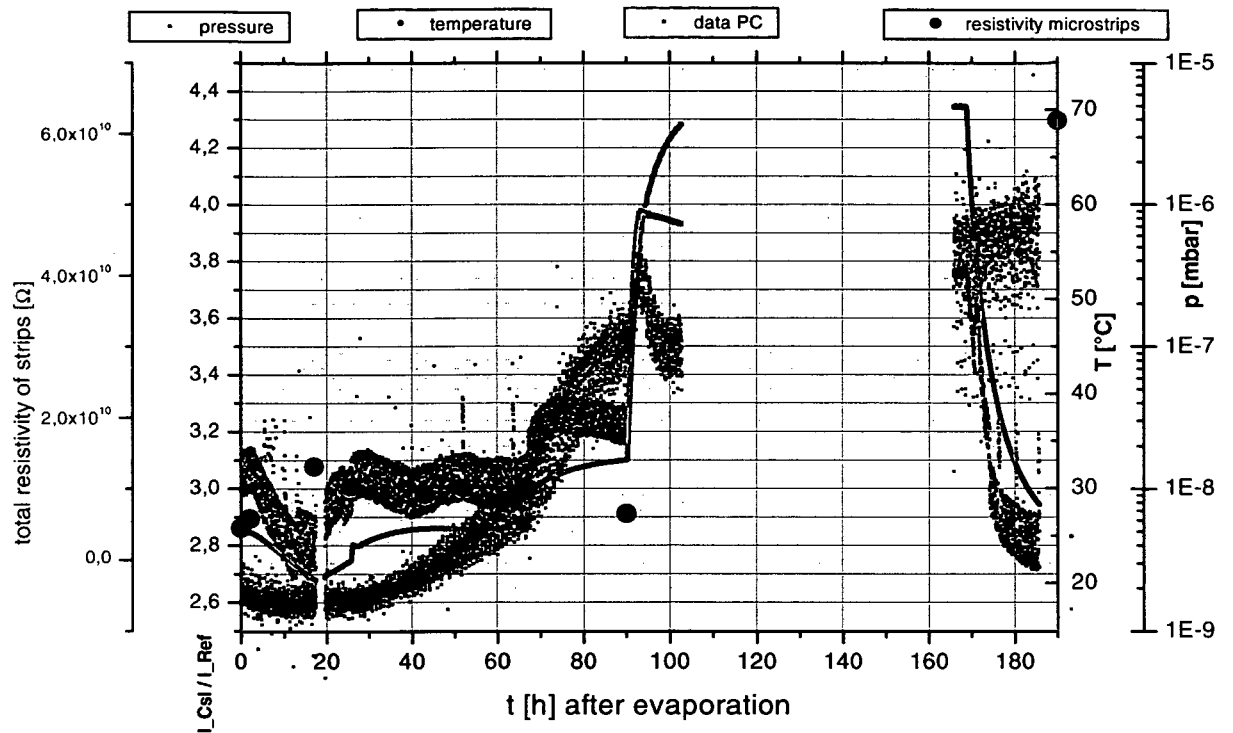


Fig. 78 Plot of current levels, pressure and temperature during test T8. Although the temperature was left at a relatively low level of < 26 [°C] up to > 60 hours after evaporation, the enhancement process starts after 30 h. Heating to 33 °C accelerates the enhancement process.

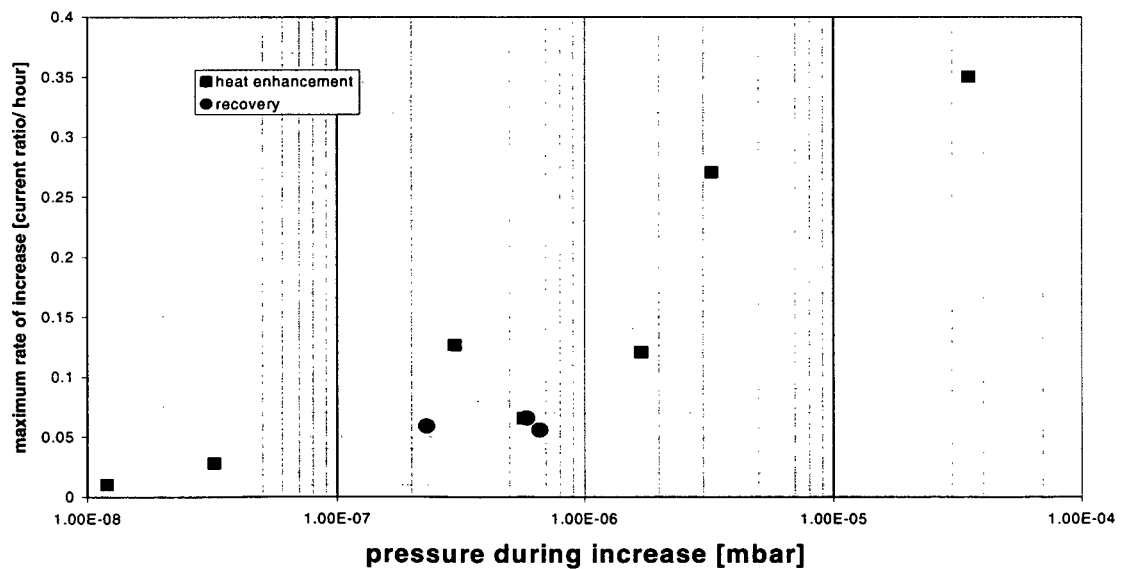


Fig. 79 Maximum rate of increase during the heat enhancement phase related to the pressure during the enhancement phase. At higher pressures the heat enhancement seems to be faster. The plot includes data from the recovery tests (Chapter 6).

5.2.6 Definition of a standard procedure for the series production of the standard PCs for the ALICE/HMPID detector

According to the results obtained from the measurements with the test PCs presented above, the PC should stay under vacuum as long as possible after evaporation to obtain the best quality. As there are many other constraints in the production process of the ALICE/HMPID modules and the maximum time allowed for the production of one PC is one week, the following procedure was established for the series production according to the test results:

The evaporation is performed at a pressure lower than 10^{-6} [mbar] at high temperature (60[°C] on the substrate, 65[°C] on the outside of the chamber) After evaporation the PC is kept at high temperature for a minimum of 12 [h] (up to 20 [h] if the schedule is not too tight) Therefore the initial fast enhancement is completed in any case. The quality control measurements are performed after cooldown and the PC is extracted on the 3rd day after evaporation, i.e. around 80 [h] after evaporation, when the PC has also stabilized during the slower 2nd enhancement phase.

5.3 QE enhancement of standard PCs in the HMPID series production

According to the procedure outlined above the series production of large area PCs for the detector was started. The main difference between the test cathodes and the standard PCs is the size and the segmentation of the substrate into 8×8 [mm²] pads. The interpad zones represent a substantial area (11% of the surface) and as this part of the surface is not metalized, additional outgassing of the substrate materials can be expected. Pressure was also the main concern during the production and sometimes we had to evaporate at pressures slightly higher than the recommended 10^{-6} [mbar]. So far 17 PCs have been produced. In addition to standard scans of the photocurrents over the PC surface before the extraction of the PCs from the production/scanning facility, measurements have been performed during the enhancement of most of the PCs. The results are given in the following Sections.

5.3.1 Summary of the results of the series production

Fig. 80 shows the behavior of 15 PCs during the QE enhancement phase. After the first few evaporations it became evident, that the observations obtained from evaporations at 65 [°C] with the test substrate presented in 5.2 and Fig. 75 were not generally true for the standard PCs. From the 3 measurements with the test cathodes a fast initial increase within the first 1-3 hours after deposition followed by a much slower stabilization phase would have been expected. Only some of the standard PCs followed this behavior (e.g. PC43, PC45 in Fig. 80) while some others showed a much longer continuous enhancement phase during 10h or even up to 15h after deposition (e.g. PC42, PC54, PC52 in Fig. 80). Particularly worrying were the cases of PCs 48¹⁰, 55, and 56 which did not show any enhancement at all (48, 55) or, as in the case of PC56, showed an initial enhancement

¹⁰ PC 48 is missing from the plot in Fig. 80 as there are no enhancement measurements available, however the level before extraction was still approximately 2.6.

followed by a decrease down to the initial level. PC 55 was a special case. It did not show any enhancement before it was extracted from the production plant. However, as will be described in Section 7.3, it performed much better than expected in the beam tests of the detector. Consequently it was transferred back to the VUV scanner approximately 120 days after the CsI deposition, to obtain a new measurement. We found an increased photocurrent in agreement with the test beam results. Therefore we assume that the enhancement phase for this PC took a very long time, weeks rather than days. The general observation after the first 17 CsI depositions was that there was both a significant spread in the rate of enhancement (varying from zero to a maximum of 0.7 units of normalized current per hour) and more importantly also a standard deviation of 12% in the final levels of normalized currents (minimum to maximum variation of 33 %).

5.3.2 Analysis of the enhancement behavior of the standard PCs

In order to find an explanation for the varying enhancement behavior of the PCs the production parameters like, pressure, residual gas composition, temperature, CsI deposition rate, CsI powder (supplier, lot) and substrate quality were carefully investigated. No correlations of the final current levels or enhancement rates were found with temperature, deposition rate or CsI powder. The main concern was the substrate quality and residual pressure before evaporation, which are possibly connected. Changes in PCB production and cleaning procedures possibly resulting in an increased outgassing of the substrates in combination with a reduced pumping capacity due to the use of a spare turbo pump during repairs of the original pump were investigated as the reason for the total lack of an enhancement phase for PCs 55 and 56. More details about the behavior of these PCs are given in the discussion of the results of the series production in Section 7.2. Fig. 81 to Fig. 84 show plots of the final levels of photocurrents and enhancement rates against the pressure before CsI deposition and against the partial pressures of water and hydrocarbons. There could be a slight correlation between the residual pressure and the final level of PCs however the result is not clear, as PC 53 was performing very well despite a relatively high pressure. The partial and total pressures from the residual gas analysis ought to be treated carefully as they depend strongly on the condition of the filament of the RGA system. An effort has been made to control this condition by regularly outgassing the filament, after this behavior was discovered.

The enhancement rate also shows no obvious correlation, neither with the pressure before evaporation nor with the pressure during the enhancement phase. Compared to the observations with the test cathodes (Fig. 79) the spread of the enhancement rate is larger, whereas the pressure during the enhancement phase varies only between $5 \cdot 10^{-7}$ and $1.6 \cdot 10^{-6}$ [mbar].

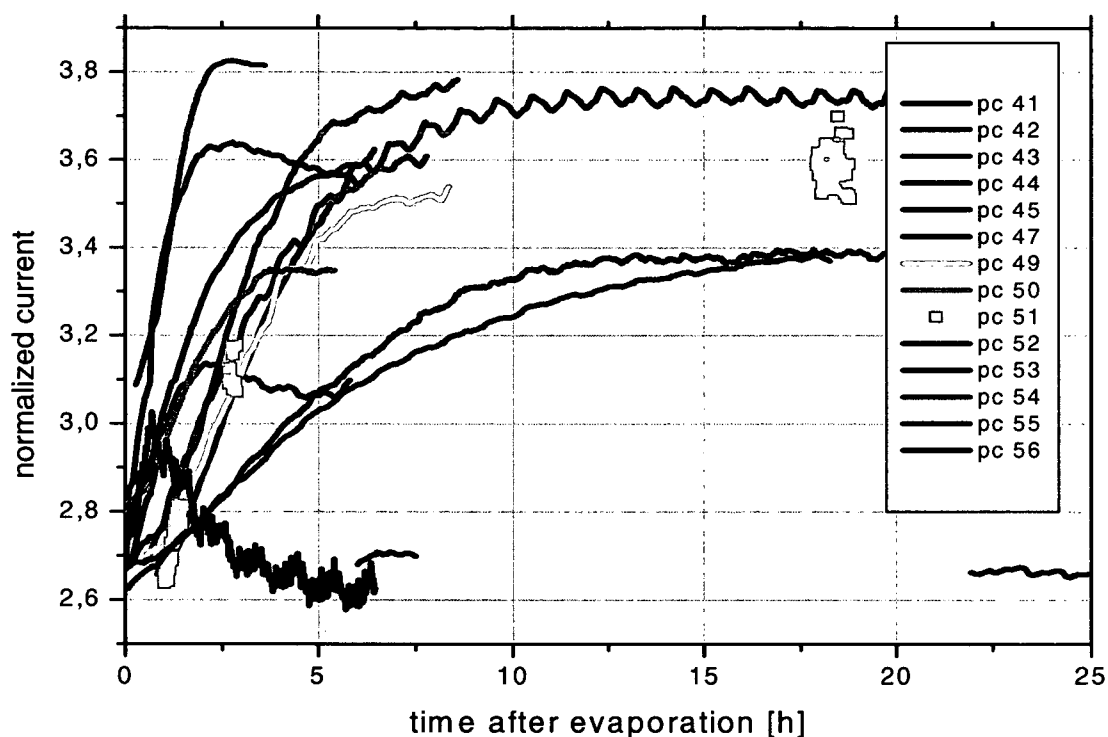


Fig. 80 Summary plot of the QE enhancement behaviour of 14 standard PCs after CsI deposition at high temperature (60 [°C]).

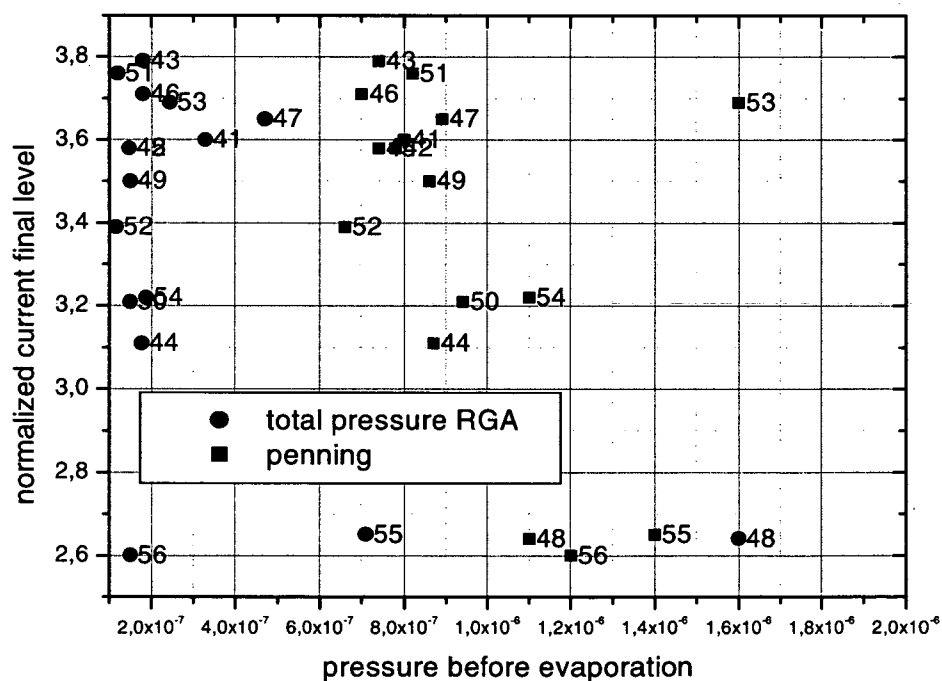


Fig. 81 Final levels of normalized photocurrent of 15 PCs plotted against the pressure before evaporation measured with a penning gauge and during RGA.

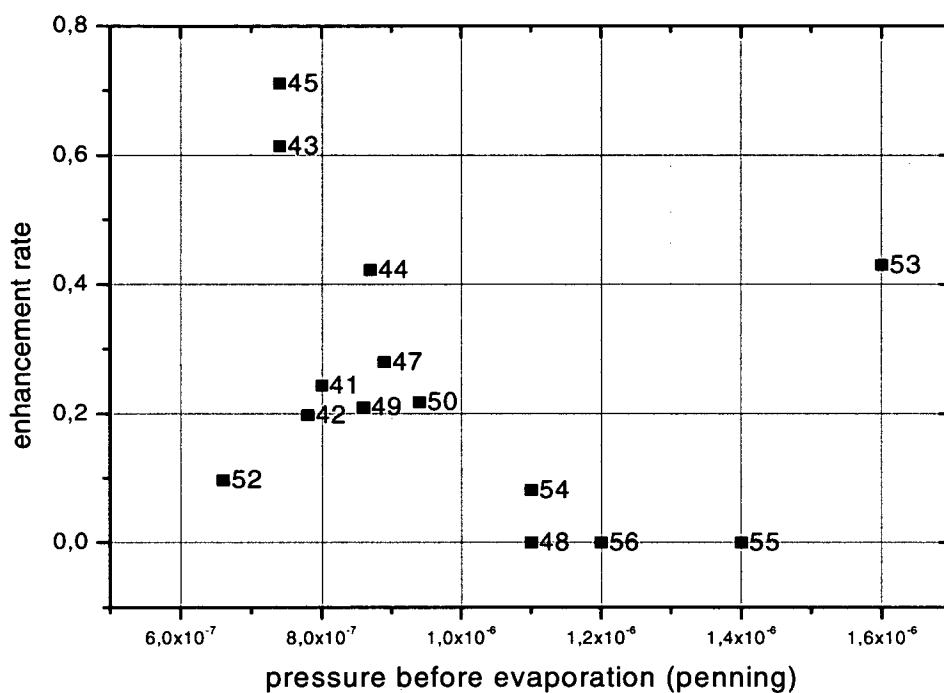


Fig. 82 Enhancement rates of normalized photocurrent of standard PCs plotted against the pressure before evaporation measured with a penning gauge.

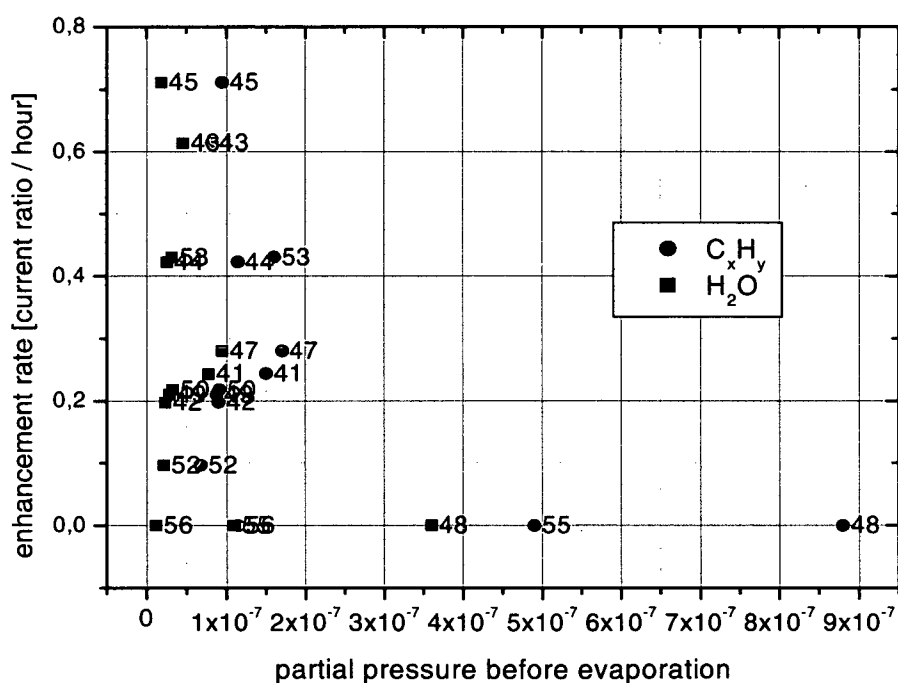


Fig. 83 Enhancement rate of photocurrent of standard PCs plotted against the partial pressures of water and hydrocarbons before evaporation.

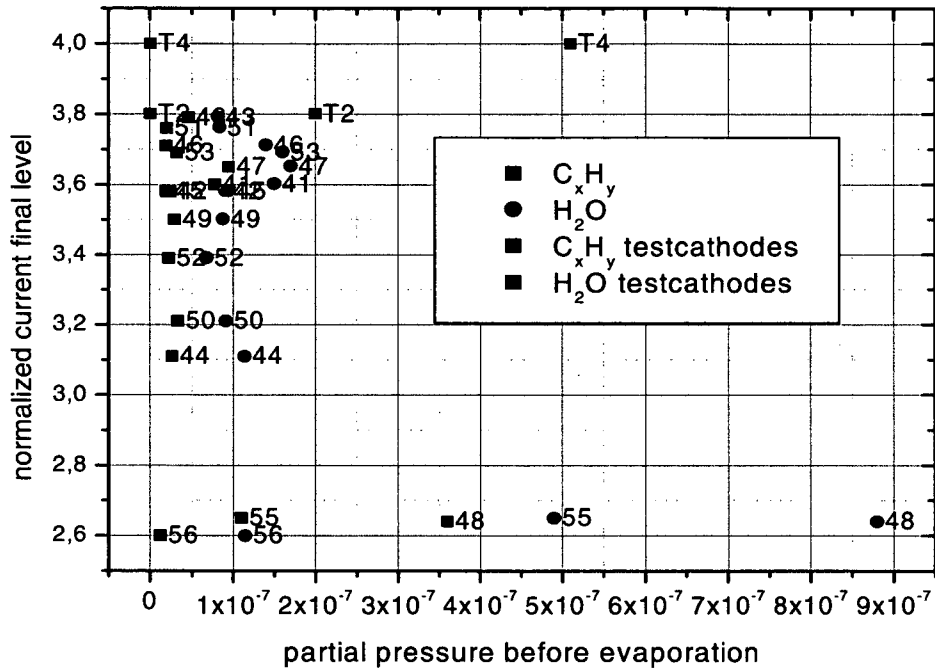


Fig. 84 Final level of photocurrent of standard PCs plotted against the partial pressures of water and hydrocarbons before evaporation.

5.4 QE enhancement of small samples

In order to reproduce the effects presented in the previous two sections under different vacuum conditions and with different VUV optics, several depositions of CsI were performed on small samples in the small sample test facility ASSET (see Section 3.2). As substrates several pieces of 18×18 [mm²] samples were cut out from a standard gold plated PCB that is used in the production of the large area PCs. The only difference to a standard substrate was the absence of the interpad zone. Evaporations were performed both at high temperature (60[°C]) and at room temperature using the same CsI powder as in the series production of large area PCs. The vacuum achieved in ASSET was roughly $5 \cdot 10^{-6}$ [mbar] and for the measurement a UV spot of 7 [mm] diameter from a deuterium source with a quartz window was used with an estimated photon flux of $5 \cdot 10^{10}$ [photons \cdot s⁻¹·cm⁻²]. The photocurrent measured on the small samples was normalized to the current measured on a Cs₂Te photomultiplier. The different spectral response of Cs₂Te leads to a different current ratio and consequently the absolute values of the normalized currents cannot be compared to the measurements obtained in the VUV scanner. The measurements were performed immediately after evaporation (5 [min]) and we found that the photocurrent on the samples was increasing rapidly during the first 40-60 [min] after evaporation regardless to the temperature of the samples. Even on samples evaporated at room temperature a sharp increase in the photocurrent could be observed without heating them. Fig. 85 shows the development of the photocurrents on 2 samples measured after evaporation at room temperature without subsequent heating.

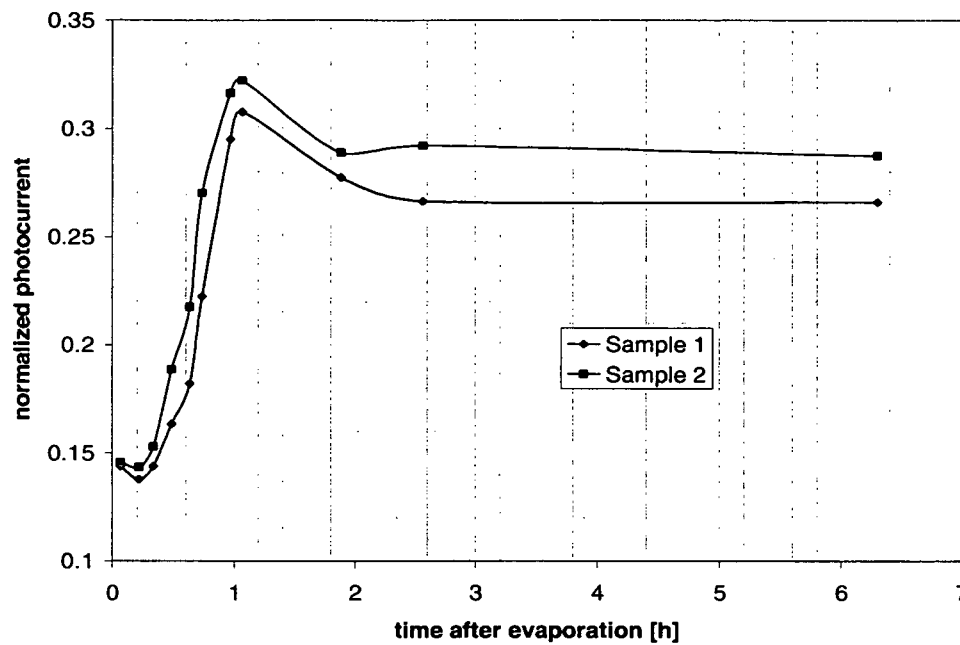


Fig. 85: Increase of the normalized photocurrent on two small samples after an evaporation at room temperature. The current increases during the first hour even though the samples are not heated.

5.5 Summary and discussion

During our studies with three different types of substrates we made the following observations about the post deposition enhancement of the CsI photoemission properties

- After deposition the photoemission from CsI is low at first and can increase up to 50 % of the initial value. This is true for both deposition on hot substrates (65 [°C]) and for depositions on cold substrates (25 [°C]) which are heated subsequently. For both methods, the same initial levels and also roughly the same final values for the photocurrent are measured. In comparisons of both methods with the same substrate the depositions on hot substrates showed a faster enhancement.
- Higher temperatures serve either as a trigger for the process or accelerate the enhancement. However temperature is only a secondary parameter, and the enhancement can take place without increasing the temperature. On the large area test cathodes we found that the enhancement starts at a very slow rate even without increasing the temperature for a deposition on a cold substrate. An increase of temperature accelerates the process. On small samples we even found a fast enhancement without heating. In the series production of large area PCs on the other hand, we also observed a few cases of depositions on hot substrates, which showed no enhancement afterwards. Two PCs (55, 56) in particular showed no enhancement in the heat treatment phase after deposition, but we could proof later with beam tests and new scans, that the enhancement had taken place during several weeks in one case and in the other case even during months after extraction from the production plant during storage inside the detector at room temperature.

These observations of very slow enhancement are consistent with reports of slow enhancement without increasing the temperature in [50].

- The rate of enhancement and the final levels observed in the series production of 17 PCs for the detector were varying strongly even though the production parameters like pressure, temperature, residual gas composition were controlled within a very narrow range, compared to the depositions on a large area test substrate. This could indicate an influence of the substrate: In the test evaporations always the same substrate has been used, and was cleaned only with demineralized water and ethanol between tests. In the series production on the other hand the substrate quality can vary due to minor changes in the production and cleaning procedures.
- The post deposition enhancement phase increases the inhomogeneity of the photoemission properties across the surface of a large area PC, i.e. it is not equally effective everywhere on the PC.
- The results of the series production also show (compare Section 7) that the variation of quality from PC to PC are largely due to the enhancement. The average photocurrent is very similar for all the PCs before the enhancement phase takes place, but it can vary strongly afterwards.

The enhancement of the photoemission properties of CsI cathodes could be connected to the presence of humidity. There is always water present during the CsI deposition, as the residual gas in the evaporation chamber is mainly (70 -80%) water. At a pressure of 10^{-6} [mbar] the impingement rate at the CsI surface is roughly equivalent to one monolayer per second. The CsI deposition rate is usually around $1 \text{ [nm}\cdot\text{s}^{-1}]$ or $\sim 2.2 \text{ [ML}\cdot\text{s}^{-1}]$. Due to the hygroscopicity of CsI, it is possible that a substantial amount of water is incorporated into the film during deposition. The enhancement afterwards could be related to a drying of the film similar as in the obvious case of the recovery of a film, which was exposed to humidity (see next chapter). The presence of water could also influence the enhancement process in a different way: if the process is related to some structural or morphological change in the CsI layer, small amounts of water could promote these changes by increasing the mobility of the CsI at the surface. Actually both processes are conceivable at the same time, as many of the enhancement measurements showed a two-fold process: a fast initial enhancement followed by a much slower increase afterwards.

The results obtained from the series production indicate, that the enhancement is both necessary to achieve a good quality but also limiting, as it leads to substantial variations of the final quality. Therefore an effort should be made to understand the nature of the process in order to control it. Also the influence of the substrate should be further investigated. It should be attempted to correlate the enhancement effect with structural or morphological changes in the CsI layer¹¹.

¹¹ It would be possible to use small samples in ASSET and investigate them in the electron microscope. However the enhancement observed on the small samples was so fast, that it was impossible to perform the transfer to the microscope in time.

6 Ageing due to exposure to humidity and recovery

Exposure to humidity or to humid air decreases the QE of a CsI photocathode – see Section 3.1. The CsI is very hygroscopic and quickly hydrated by water. Investigations of the morphology of the CsI layer with an electron microscope have shown that the grain size of a CsI film increases after exposure to humidity (Fig. 21). If the water inside the CsI film is responsible for the QE decrease, a recovery effect should be observed when the water is removed from the hydrated photocathode by annealing. In order to test this hypothesis several tests have been performed with the VUV scanner and ASSET. In both cases a decrease in QE due to exposure could be measured as well as a recovery of the QE by means of annealing under vacuum. A study of the effect on small samples in a SEM revealed the known increase in grain size after exposure, but no further changes in morphology after re-annealing the samples directly inside the microscope.

6.1 Exposure and recovery tests with a test PC in the VUV-scanner

These tests were performed in combination with the heat enhancement tests summarized in Table 4 in Chapter 5. After the measurements of the heat enhancement phase were completed, some of the test PCs were exposed to air in the laboratory for a certain amount of time by breaking the vacuum of the evaporation/scanning facility and opening the doors as specified in Table 5. After exposure the setup was pumped to vacuum again and the decrease in photocurrent was measured in the scanner revealing a quality decrease as given in Table 6 and Fig. 86. The effects were compared with the accumulated exposure to H₂O, which was calculated by converting the relative humidity measured inside the lab or chamber into [ppm H₂O] and multiplying this value with the exposure time in minutes.

Test	Exposure time [min]	Relative humidity lab RH [%]	Temperature [°C]	Concentration H ₂ O at 100% RH [%]	Absolute concentration H ₂ O [ppm]	Accumulated exposure [ppm x min]
T5	140	19	22	2.61	4959	694260
T6	250	15.1	22.1	2.61	3941.1	985275
T7	10	23	23	2.77	6371	63710
T8	53	23	24	2.95	6785	359605
T8	7050	19	22	2.61	4959	34960950

Table 5 Level of exposure during 5 exposure tests of large area test PCs to humid air.

Test	Current ratio before exposure			Current ratio after exposure			Exposure effect	Current ratio after recovery			Recovery effect
	mean value	standard deviation	stdev/mean	mean value	standard deviation	stdev/mean	exposure/before exposure	mean value	standard deviation	stdev/mean	recovery/before exposure
T5	3.98	0.10	0.03	3.34	0.22	0.06	0.84				
T6	4.04	0.08	0.02	2.73	0.10	0.04	0.68	3.75	0.21	0.06	0.93
T7	3.35	0.07	0.02	3.10	0.07	0.02	0.93	3.41	0.08	0.02	1.02
T8	3.88	0.14	0.04	3.251	0.07	0.02	0.84	3.88	0.17	0.04	1.00
T8	3.88	0.17	0.04	1.00	0.14	0.14	0.26				

Table 6 QE decrease measured after exposure tests of large area test PCs to humid air and subsequent recovery effect by re-annealing. The exposure effect and recovery effect are calculated by dividing the current level after exposure and after recovery by the current level before exposure.

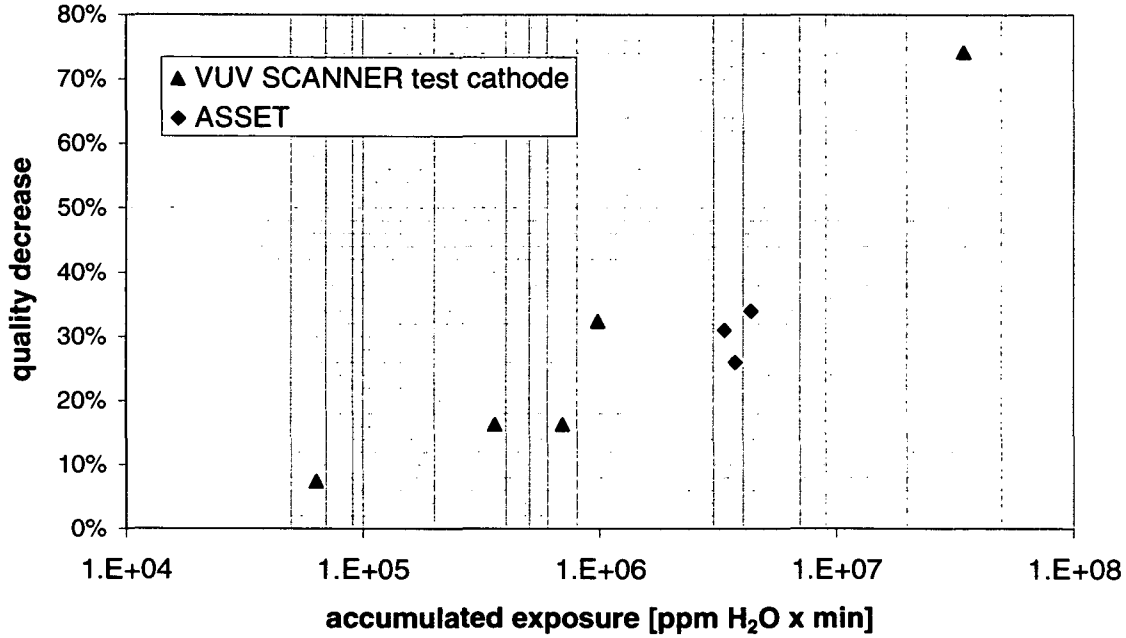


Fig. 86 Decrease in photocurrent as a function of accumulated exposure calculated from the relative humidity in the lab.

In the next step the cathodes were heated to 60-70 [°C] which triggered an enhancement phase similar to the one observed in the heat enhancement measurements presented above. Fig. 87 shows the measurement data obtained from the tests with test PC T8. The plot in Fig. 87 is an extension of Fig. 78. 186 [h] after evaporation, the PC was exposed to air with a relative humidity of 23 % at 24 [°C] for 53 [min]. After reaching a vacuum of $< 10^{-5}$ [mbar] the continuous scanning procedure was started again and revealed a 16% decrease in normalized current (averaged over a few hundred measured points) compared to the level measured before exposure. After the measurement of the decreased level the photocathode was heated to 70 [°C], which triggered at first a very slight decrease in current followed by a sharp increase up to the level before exposure. In this case the quality of the PC could be completely recovered by annealing the hydrated CsI. From Table 6 it can be seen that this recovery effect was measured for 3 different test cathodes. In 2 cases the level of current before exposure could be recovered completely, in the 3rd case a level of 93 % was achieved.

6.1.1 Increased spatial inhomogeneity of the CsI response after recovery

The normalized current of the test PC in T8 plotted in Fig. 87 is an average of 50 different positions on the PC. It does not include the spatial inhomogeneity of the photocurrent on the PC. Fig. 88 shows a plot obtained during the exposure test T6, however in this graph the actual data of the 50 different positions is plotted and not an average. The spread of data points reflects the spatial inhomogeneity of the photocurrent on the PC surface. It is an interesting observation, that this spread increases during the recovery phase after exposure, i.e. the recovery effect during the annealing phase is not homogenous on the PC surface.

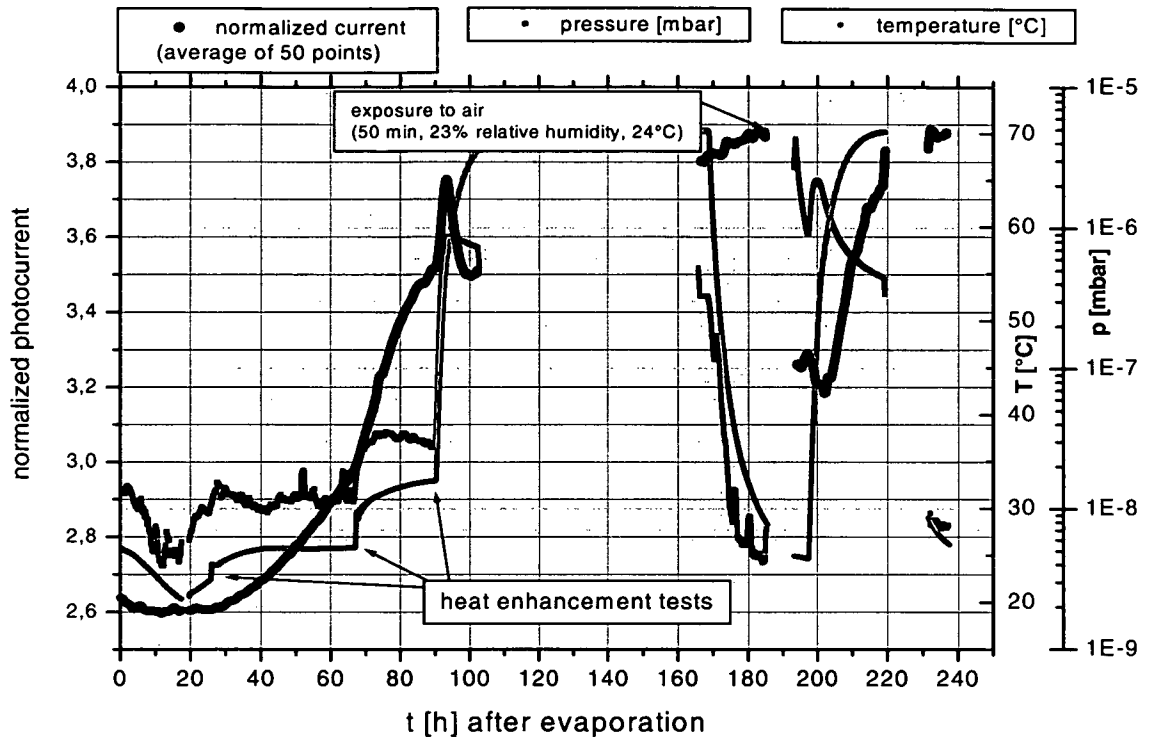


Fig. 87 Behavior of the photocurrent, temperature and pressure in T8 before and after exposure to humid air. The exposure leads to a decrease in QE which can be recovered by annealing.

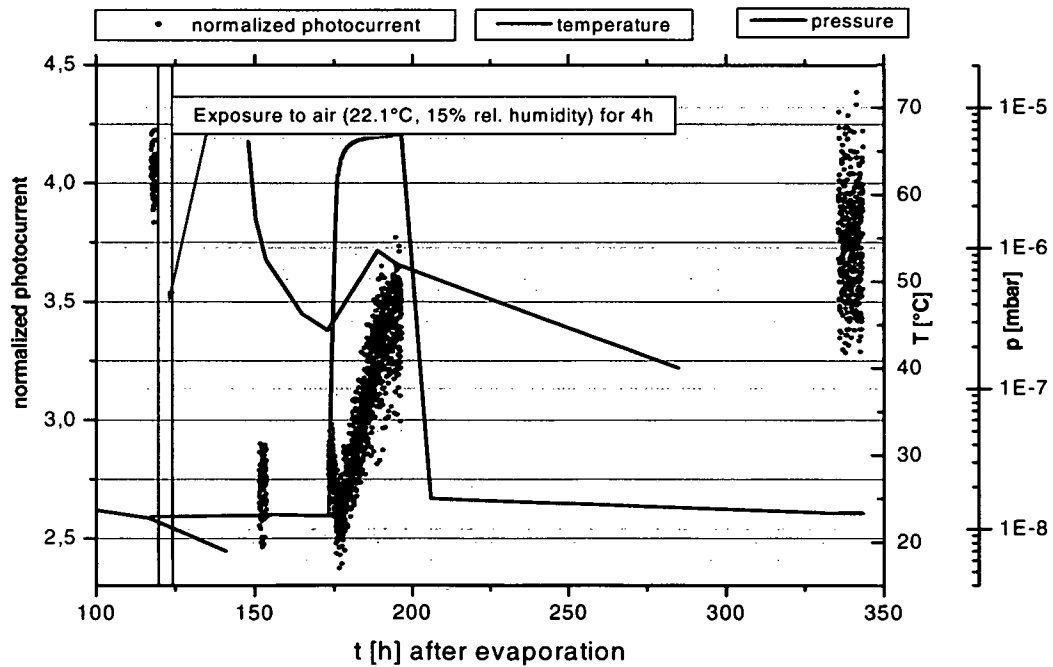


Fig. 88 Plot of temperature, pressure and photocurrent during an exposure and recovery test in T6. The spread of the data points reflects the spatial inhomogeneity of the photocurrent over 50 different positions on the PC. The spread increases during and after the recovery of the exposed PC.

The same observation was made in all exposure and recovery tests given in Table 6. The levels of the photocurrent before exposure, after exposure and after recovery given in

Table 6 were calculated as an average over a few hundred measurements on 50 different positions. The table also contains the standard deviation calculated for these levels, which are in general higher in the measurements after recovery than before.

6.2 Exposure and recovery tests with small samples in ASSET

In order to repeat the tests under different conditions, exposure tests also have been performed in ASSET. Several small samples (witness samples of the PCB substrate production, i.e. small fractions of a standard substrate) have been evaporated and used to measure the photocurrent before and after exposure, as well as during a subsequent annealing process. Table 7 summarizes the tests that were performed, and gives the calculated values for the accumulated exposure, the quality decrease measured after exposure, and the recovered level of photocurrent obtained after annealing the samples by means of the peltier elements mounted in the sample holder. Fig. 86 is a plot of the quality decrease as a function of accumulated exposure, with data points obtained from measurements with the test cathode in the VUV-scanner and with small samples in ASSET. The measurements obtained from ASSET seem to follow the trend obtained with the large area test PCs.

test description	accumulated exposure [ppm H ₂ O x min]	decrease in photocurrent	recovered level (compared to before exposure)
exposure for 4h (36.5 % RH 26 deg C), recovery by heating to 60 deg C	4362480	34%	> 90%
exposure for 6h (42 % RH 26 deg C), recovery by heating to 60 deg C	3346560	31%	> 90 %
exposure for 5h (57 % RH 20 deg C), recovery by heating to 60-70 deg C under stagnant Argon atmosphere	3730636	25%	110%

Table 7 Summary of exposure tests performed with ASSET.

The measurements in ASSET proved to be rather difficult, as the effects were superimposed over a systematic decrease in current, probably caused by bad vacuum conditions or unstable conditions in the optical system (Argon atmosphere surrounding the D₂ source.) However at least qualitatively the effects measured in the scanner could be reproduced in these quick tests. Furthermore an important conclusion can be drawn from the third test given in Table 7. In this test the quality of the samples after exposure was recovered by heating them not under vacuum but under a stagnant Argon atmosphere. This proves that the recovery can also be obtained under gas, which might be an important option in the case of an exposure accident with the detector. This test should be repeated both in the VUV scanner and by heating an exposed PC in its storage box or even inside a module.

6.3 SEM analysis of small samples before and after exposure

To find out if the annealing of exposed samples affects the morphology of the CsI layer some of the samples produced in ASSET were transferred under vacuum to a SEM. The CsI was deposited at a substrate temperature of approximately 65[°C] and after evaporation an initial increase of the photocurrent has been observed within the first 60 [min] after evaporation. Approximately 4 [h] after evaporation the samples were transferred to the SEM. The first pictures in the SEM were taken roughly 20 hours after evaporation. After taking pictures of the original CsI layer morphology (Fig. 89), the SEM chamber was opened for 5 hours at 20 [°C] and at a relative humidity of 56 % (this corresponds to an accumulated exposure of 3 900 000 [ppm H₂O · min]). Afterwards the chamber was pumped again and pictures of the CsI layer after exposure were taken (Fig. 90), which showed an increase in grain size as was expected from the tests given in Fig. 21. The samples were then heated to approximately 60 [°C] for 5 hours inside the SEM chamber by means of the peltier elements installed in the ASSET sample holder. After the annealing process and in total 19 hours after exposure the SEM revealed no further change in grain size. It can be assumed the annealing process helped to remove water from the CsI layer and resulted equally large but dry CsI grains.

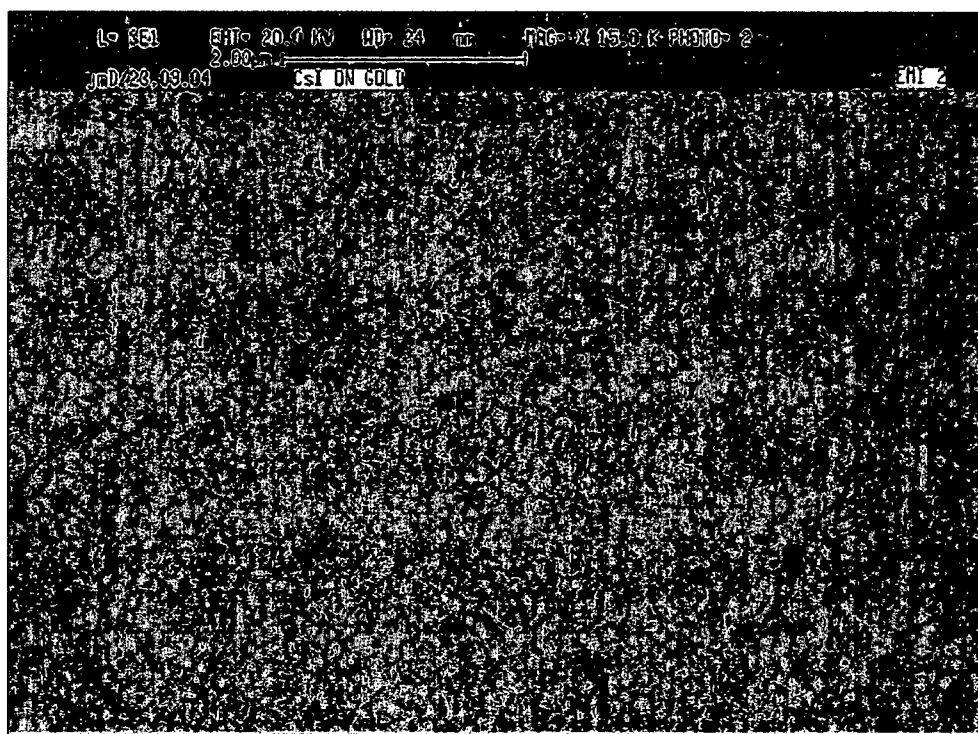


Fig. 89 Grains of the CsI layer before exposure to air.

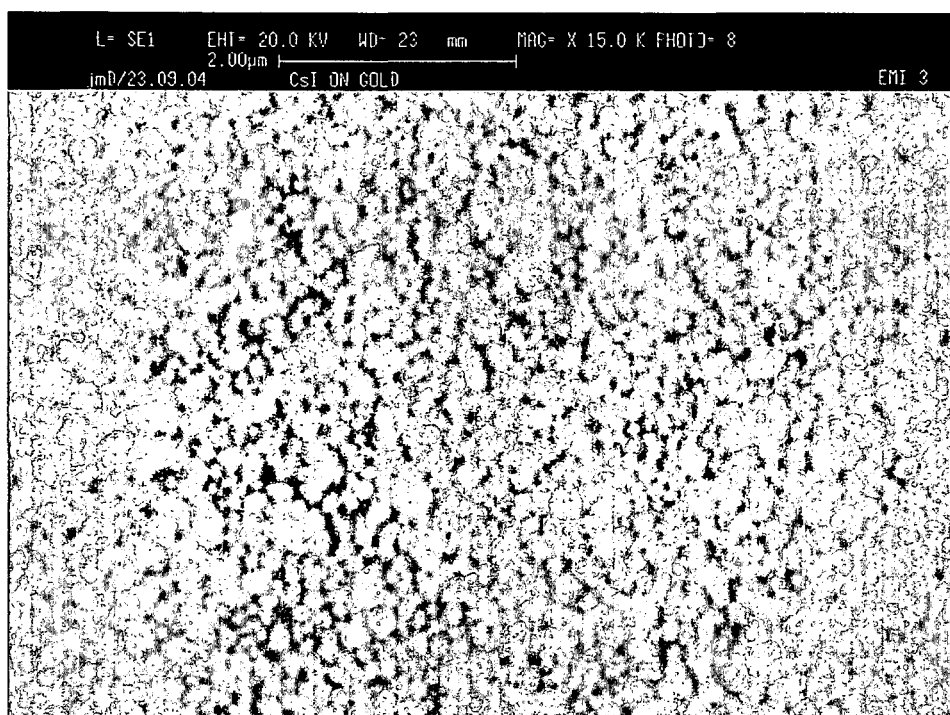


Fig. 90 Grains of the CsI layer after exposure to lab air (exposure: 5h at 20 [°C] and at a relative humidity of 56%; accumulated exposure 3 900 000 [ppm H₂O · min]). The grain size has increased up to diameters as large as the layer thickness.

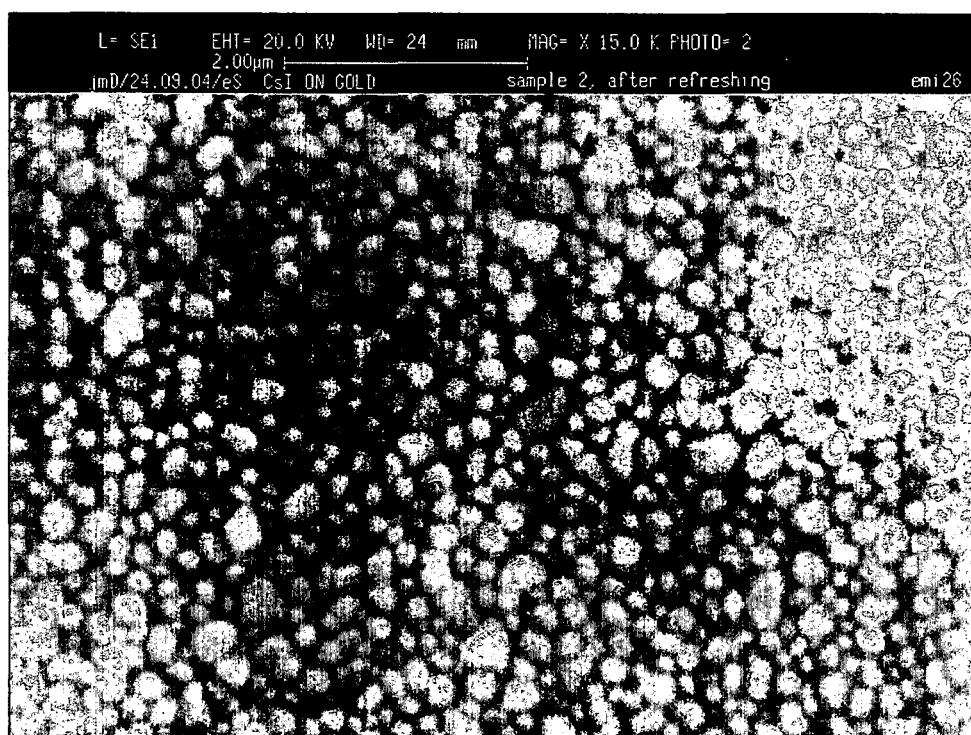


Fig. 91 Grains of the exposed CsI layer after heating at approximately 60 [°C] for 5h. The grain size has not changed again after the heating.

6.4 Conclusions and suggestions for further tests

The decreased photoemission properties of an exposed and consequently hydrated CsI layer can be improved and almost completely recovered by annealing the PC at a temperature of 60 [°C], however the spatial inhomogeneity of the CsI response increases during this process. The effect seems to be independent from the heat source, as it was measured with radiative heat conduction from the hot chamber to the PC as well as with directly heating the samples with peltier elements in the substrate holder. The recovery effect can also be obtained by annealing the PCs under a stagnant Argon atmosphere, which could eventually be used to recover an exposed PC outside the evaporation facility or even inside a detector. Further test should be done to investigate, if an exposed PC can be recovered by heating the storage box, or even by purging it with hot gas inside a detector.

7 Quality evaluation in the PC production

The CsI deposition process was already described in Section 3.4.3. The following paragraphs describe the quality evaluation measurements with the VUV scanner and give a summary about the status of the series production. A comparison between results of the photocurrent scans and the quality evaluations from beam tests is presented, which allows defining the requirements for the acceptance of a PC.

7.1 Quality evaluation scans during production

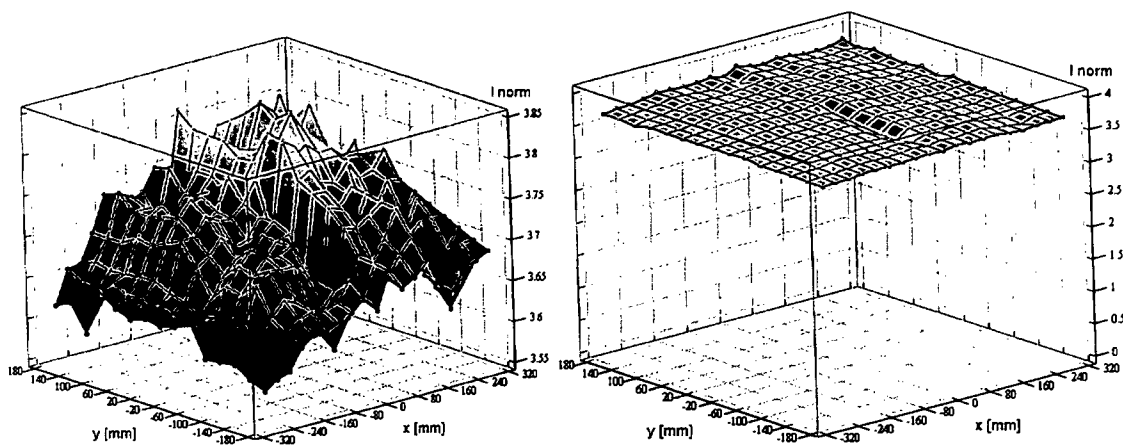


Fig. 92 3D plots of the normalized photocurrent as a function of position measured for 285 points on PC 46. The zero suppressed plot on the left side shows a slight inhomogeneity of the PC response. The mean value is 3.71 and the minimum to maximum variation is 6% in this case.

After the production of a new PC the following measurements are performed with the VUV-scanner: Immediately after CsI deposition the photocurrent from the PC is monitored in a continuous scan to check the development of the QE during the initial heat conditioning phase (compare Section 5.3). Before the PC is finally extracted from the plant, two scans covering the whole surface of the PC are performed. In the first scan 280 points on the PC are scanned using the full spectrum of the deuterium source. In the second scan the measurement is repeated for 80 points with the spectrum of the source cut by an additional quartz window in the optical path. Due to the lack of a monochromator in the optical system this is the only way to detect any changes in the shape of the QE as a function of wavelength. Compare Section 3.5 and Fig. 39. Fig. 92 shows the results of the 280 point scan with the full spectrum, obtained for PC 46 - one of our best PCs so far. The value of I_{norm} has a mean value of 3.7 and a minimum to maximum variation of 6 % of the mean value. We always measure a similar variation of I_{norm} across the PC surface, for some PCs up to 12 % of the mean value. An evaluation of the PC quality by means of test beam runs shows a similar inhomogeneity of the PC response (see Section 7.3).

7.2 Summary of production in 2004

Since May 2004 seventeen PCs have been produced and measured as described above. Fig. 93 shows the average value of I_{norm} for each of the PCs obtained from a scan 80 points spread equally over the whole PC surface. The values plotted in this table were taken from the measurements with the quartz window in order to be able to compare them with the current levels measured before the enhancement process (Section 5.3). The variation of the average photocurrent from PC to PC is substantial¹² with values from 2.7 up to 4 of $\langle I_{\text{norm}} \rangle$ which corresponds to a spread of 33%. The plot shows the level of the photocurrent before and after the post deposition enhancement phase (Section 5.3). The variations of the final levels are due to differences in the effectiveness of the enhancement process as the levels before the enhancement show much less variation. The development of the current during the enhancement phase is given in Fig. 80 and Fig. 95. Table 8 lists more details about the series production, e.g. the pressures measured during evaporation and the relative amount of hydrocarbons and water in the residual gas before evaporation. The table also contains the data for the CsI depositions on the test substrate discussed in Section 5.2.

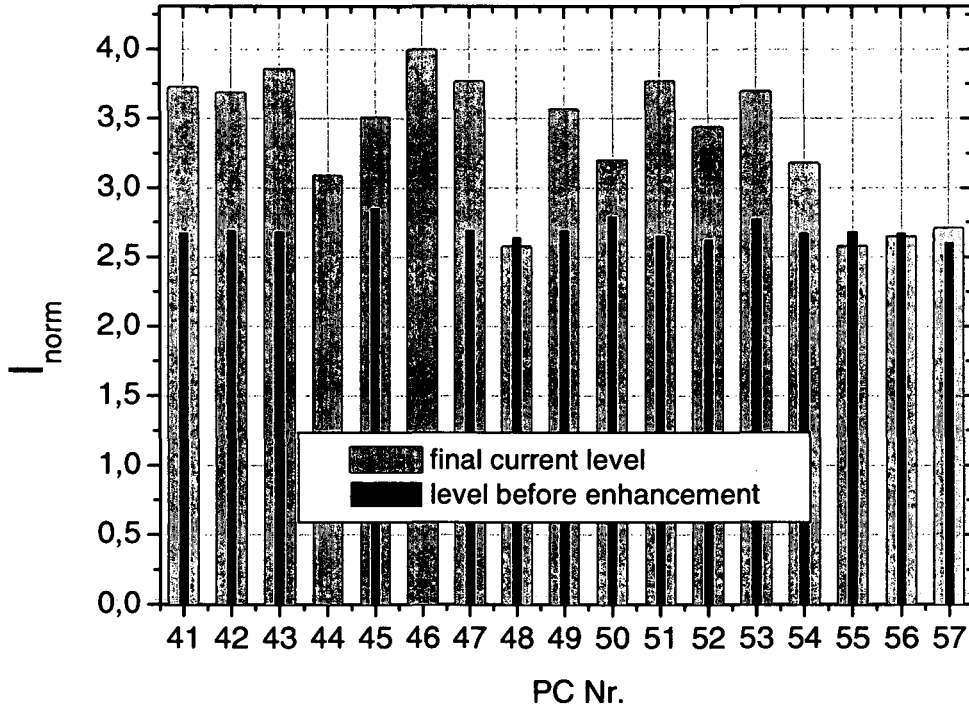


Fig. 93 Comparison of the mean values of the normalized photocurrent of PCs 41 to 57; measurements with quartz window in optics. The levels before and after heat enhancement are given.

Fig. 94 shows the mean current levels measured in the 280 point scan without quartz window and in the 80 point scan with quartz window. Furthermore a level of acceptance of $\langle I_{\text{norm}} \rangle = 3$ is given, which is derived from a comparison between scanner results and test beam results – compare Section 7.3.

¹² Variations in QE between different cathodes can also be found in commercial phototubes, and there are also discrepancies between the QE quoted by the manufacturer and re-calibration measurements as quoted in [55].

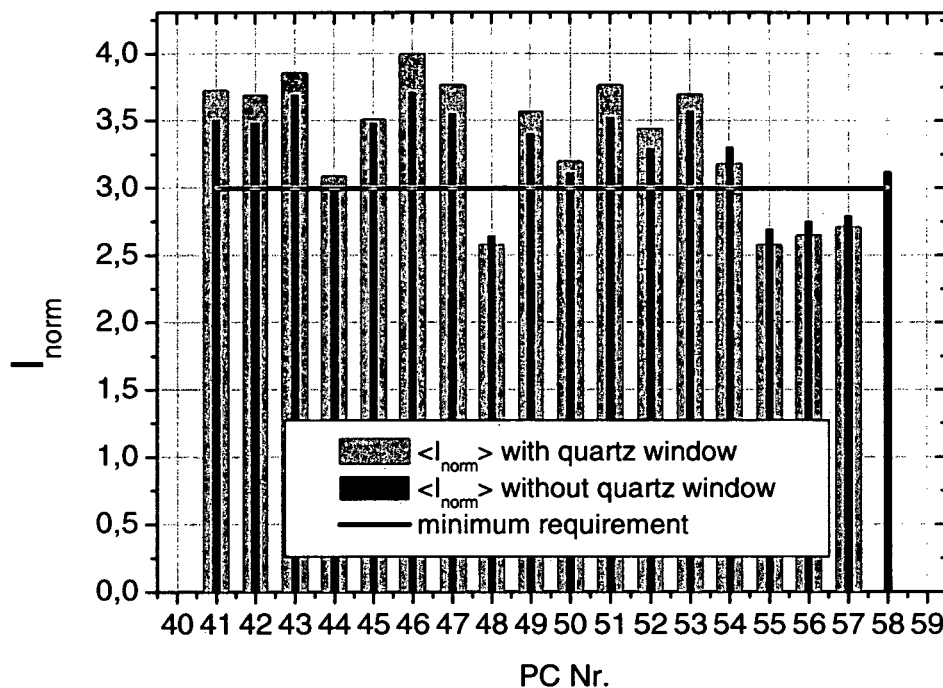


Fig. 94 Comparison of the mean values of the normalized photocurrent of PCs 41 to 58; comparison of measurements with and without quartz window in optics. The levels for the minimum requirement is given for measurements without quartz window.

PC Nr	Deposition date (week)	before Csl deposition				during deposition		measured after deposition			extraction from plant	
		P [mbar] (RGA)	[H ₂ O] %	[C _x H _y] %	T [°C]	max. depos. Voltage [V]	mean depos. rate (kronos)	I(norm) after HT without quartz	I(norm) after HT with quartz	UV spots size diameter [mm]	Enclosure Box nr	Max. ppm O ₂ in Ar gas
T7		3.90E-07	81.9	6.1	61.4	135	0.60		3.35	5		
T8		5.10E-08	66.5	11.0	25.4	175	0.84		3.88	5		
T5		4.20E-07	72.0	12.0	63.2	150	0.47		3.98	different optics		
T6		2.10E-07	89.0	1.3	23.2	140	0.61		4.04	different optics		
T4		5.60E-06	92.0	0.3	22.1	165	-		4.21	different optics		
T3		2.60E-08	79.5	1.6	26.4	160	0.25		4.08	different optics		
T2		5.50E-07	72.9	1.4	23.1	150	0.50		3.94	different optics		
T1		1.30E-06	70.0	15.4	62.0	150	0.50		3.63	different optics		
PC39v3		2.80E-07	66.0	13.5	63.0	155	0.46		3.00	15		
PC44	Mo 03/05/04	1.77E-07	81.0	8.0	59.5	140	0.37	3.00	3.08	15	6	180
PC45	Mo 10/05/04	1.47E-07	82.0	7.0	60.5	180	0.55	3.48	3.50	15	2	1600
PC43	Mo 17/05/04	1.80E-07	78.0	8.9	59.3	180	0.69	3.69	3.85	15	9	50
PC46	Mo 24/05/05	1.84E-07	77.0	9.9	60.3	170	0.94	3.71	3.99	15	10	?
PC42	Tu 01/06/04	1.47E-07	73.0	13.4	60.0	170	1.45	3.48	3.68	15	3	600
PC41	Mo 07/06/04	3.30E-07	71.0	13.0	60.5	160	0.69	3.50	3.72	15	4	300
PC47	Mo 14/06/04	4.70E-07	60.0	22.0	61.3	150	0.89	3.55	3.76	15	8	600
PC48	Mo 21/06/04	1.60E-06	55.0	22.0	62.6	180	0.60	2.64	2.57	15	7	600
PC49	Tu 29/06/04	1.50E-07	66.0	15.0	60.9	170	0.85	3.40	3.56	15	4	110
PC50	Tu 06/07/04	1.50E-07	61.0	22.0	59.7	180	0.673?	3.11	3.19	15	6	100
PC52	Tu 13/07/04	1.16E-07	58.8	19.0	59.7	170	0.75	3.29	3.43	15	3	250
PC51	Mo 19/07/04	1.27E-07	66.0	15.7	59.5		1.10	3.52	3.76	15	10	100
PC53	Mo 16/08/04	2.45E-07	65.2	13.5	63.0		0.40	3.57	3.69	15	9	100
PC55	20/09/04	7.10E-07	69.0	15.6	60.0	170	0.20	2.69	2.57	15	4	200
PC56	30/09/04	1.20E-06	77.2	8.2	60.0			2.75	2.64	15	7	400
PC57	7/10/04	7.40E-08	73.0	13.0	60.0			2.79	2.70	15		

Table 8 Summary of the production parameters and results for 17 standard PCs and 9 test depositions. As the most important parameters not only the final levels for the normalized photocurrent, but also pressure and relative amounts of water and hydrocarbons before deposition are given.

Problems with several PCs of less quality

During the production of PC 54 an accident occurred with our pumping system due to a power cut. PC 54 was exposed to air and is presumed to be damaged and will consequently

be cleaned and recoated. In the accident both the pre-vacuum pump and the turbo pumps were damaged and had to be repaired or replaced. For a while we had to run with spare pumps. Roughly at the same time some concerns arose about the substrate quality due to minor changes in the production and preparation chain and we had some indications of increased outgassing. We obtained 3 PCs with a low current level in the scanner (PCs 55-57). However the pressure achieved in the scanner during this period was still satisfactory as Table 8 and Fig. 81 - Fig. 84 show. Furthermore also the composition of the residual gas did not change significantly as can be seen as well from Table 8 and especially from Fig. 81 - Fig. 84, especially the amount of H_2O and C_xH_y was not much different from previous evaporations. PC 53 for example had been evaporated under clearly worse conditions and is still one of our best PCs. Also the test evaporations reported in Section 5.2 showed good results for much higher pressures, up to 10^{-5} [mbar], however in these cases the relative amount of hydrocarbons present in the residual gas was exceptionally low, as can be seen in Table 8. The following paragraphs describe the peculiar behavior of PCs 55 – 57.

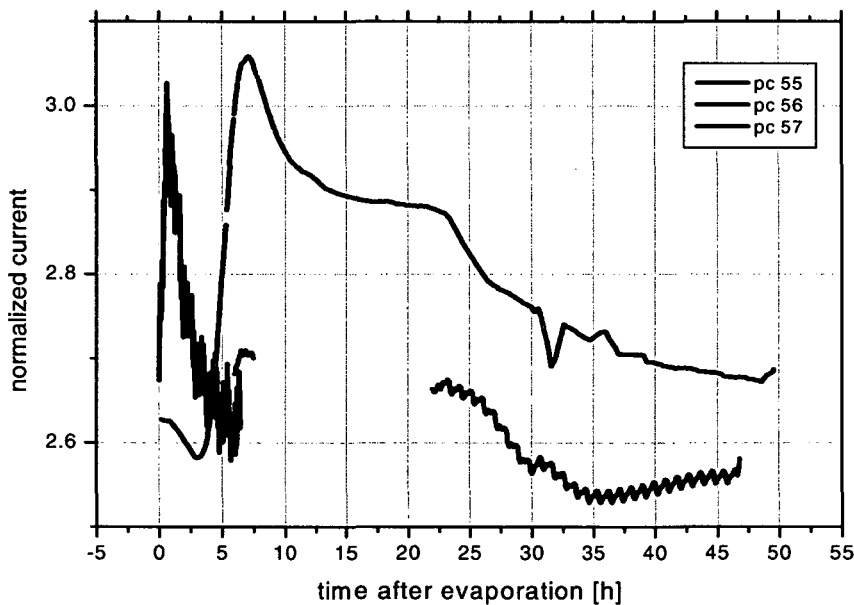


Fig. 95 Comparison of the heat enhancement behavior of PCs 55 to 57. PCs 55 was the first CsI deposition after the accident with the pumping system. PCs 55 and 56 were coated according to standard procedure, whereas PC 57 was coated at room temperature and heated afterwards.

- **PC 55:** This PC was the first one produced after the accident using spare pumps. The PC showed no heat enhancement during the first 45 hours after CsI deposition – rather a slight decrease – see Fig. 95. Afterwards in the beam tests (Section 7.3) it was performing better than expected. It was then transferred back to the scanner 120 days after the first measurements and we found an increased current level. It is assumed that the enhancement effect took a very long time in this case.
- **PC 56:** For this PC, which was produced under similar conditions as PC 55, the enhancement effect started immediately after deposition and it reached an almost acceptable level before the current started decreasing suddenly. The final level was comparable or even less than immediately after CsI deposition. In this case the test

beam confirmed the bad result. The behavior indicates some contamination either from the residual gas or even directly from the substrate which stops and even reverses the enhancement effect. The pressure during deposition was slightly higher than usual ($1.2 \cdot 10^{-6}$ [mbar]) but not significantly so. However roughly 4 months after deposition the PC was rescanned and a slight increase compared to the first measurement was observed. Renewed annealing of the PC resulted in an additional observable increase and the PC has now reached an acceptable level.

- **PC 57:** In order to check the influence of the slightly higher pressure during the depositions of PCs 55 and 56, in the production of PC 57 an evaporation at room temperature was chosen. This way the evaporation was performed at a pressure which was an order of magnitude lower. By heating it to 60 [°C] after deposition, a rather fast enhancement could be observed, which reversed into a decrease after some time, as in the case of PC 56.
- **Test PCs:** Due to the bad results with the previous PCs, a deposition was done onto the test substrate described in Section 5.2. As the test cathode also did not perform very well, the main concern shifted from the substrate to the evaporation plant and a thorough cleaning of the chamber was carried out. In the mean time we could also restore the old configuration of the pumps. In the next coating of the test substrate we observed good results.
- **PC 58:** After the successful test, the next standard substrate was coated, which lead to a negative result. The substrate was then cleaned and the CsI deposition was performed a second time. After the second coating the results were acceptable – a final level of 3.1 was observed.

From all these results it is still not clear, if the reason for the bad performance of some of the PCs is a problem with the deposition facility or the substrates. Currently the production is being started up again after an attempt to correct every conceivable problem in the plant and after checking the whole procedure from source preparation up to the measurement. The substrates are analyzed carefully as well to avoid any problems in the production chain, that might lead to contaminations or increased outgassing. The evaporation of the latest PC was successful; however the heat enhancement took a much longer time than usual. This trend follows the behavior of the PCs 55 and 56 which showed the enhancement only months after CsI deposition.

7.3 Comparison of VUV-scanner and test beam results

The PCs produced in the series production were mounted onto modules 3 to 5 of our detector and tested together with the full detector modules in a 120 [GeV/c] pion beam. The most important quantity obtained from these beam tests is the number of resolved clusters per particle track. This number depends not only on the QE of the PCs but also on several other detector parameters like radiator transmittance, chamber gain or electronics noise. Therefore this number can only be used as a first approximation in a comparison

between test beam and VUV-scanner. Also the following differences between the measurements in test beam and the VUV-scanner have to be kept in mind:

- The detector is counting single photons in the testbeam, whereas the PCs are illuminated with a flux of approximately $2 \cdot 10^{10}$ [photons·s⁻¹·cm⁻²] in the VUV scanner.
- In the detector the photoelectrons are emitted into gas, in the VUV scanner into vacuum.
- The spectrum of the Cherenkov photons is different from the spectrum of the deuterium lamp used in the scanner.

Fig. 96 shows a comparison between the number of resolved clusters and the average photocurrent measured in the VUV-scanner at the position of the Cherenkov rings in the test beam. For a given beam position a typical Cherenkov ring with a mean radius of approximately 12 [cm] and a width of 3 [cm] was defined. From the data of the 280 point scan of the photocurrent across the PC all the points lying inside this ring (≈ 20 -25) were used to calculate an average normalized current for the ring position.

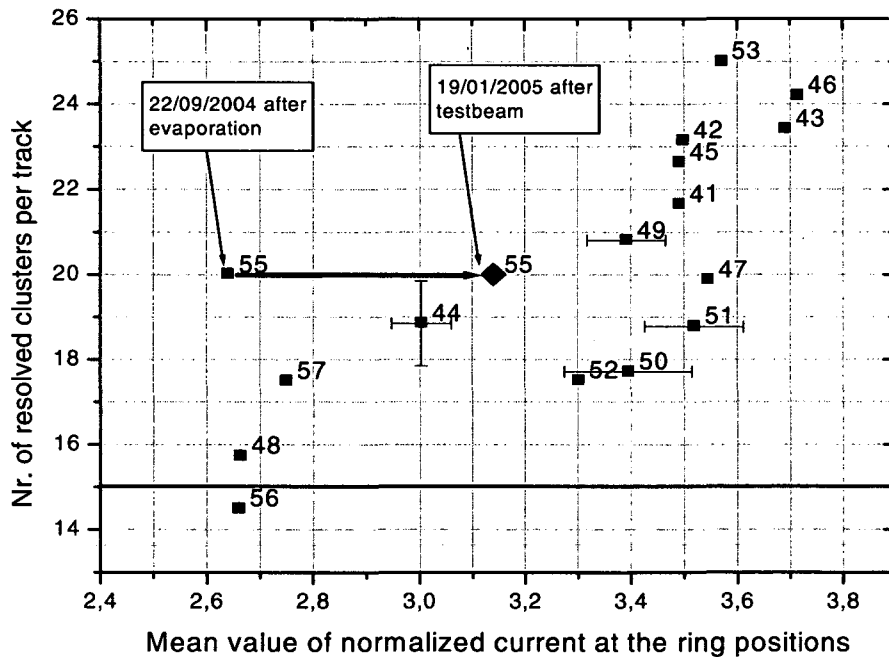


Fig. 96 Number of resolved clusters per track plotted as a function of the average normalized current measured at the position of the Cherenkov ring.

From this plot of the number of resolved clusters against the normalized photo current follows the expected trend that the PCs with a good result in the scanner also give a high number of resolved clusters in the beam. The plot also shows the minimum value of 15 resolved clusters per track which is necessary for an acceptable detector performance, i.e. to achieve the necessary Cherenkov angle resolution of 3 [mrad]. All but one cathode were higher than this limit. In the future it will be necessary to deduce a level of acceptance for the photocurrent measured in the VUV-scanner from these comparisons with test beam

data. From the first results a value of 3 for $\langle I_{\text{norm}} \rangle$ was chosen as the minimum requirement for the PCs, as all the PCs with currents higher than 3 are clearly above the limit for the number of resolved clusters in the test beam. Despite the general trend visible in Fig. 96 there are also some PCs which performed differently in the test beam than expected from the scanner results. To find out how much the other detector parameters can influence the number of resolved clusters per track, the QE was extracted from the test beam data by Monte Carlo simulation. The simulation [44] tries to reproduce the measurable quantities like the number of photoelectrons, the number of pad hits per event, the number of resolved clusters or the cluster size by varying the QE curve and taking into account variations in chamber gain, radiator transmittance, variations in the proximity gap due to mechanical limitations and many other detector parameters. With $QE(\lambda)$ obtained from these simulations and the spectrum $\Phi(\lambda)$ used in the VUV scanner measurements (see Fig. 39) it is possible to calculate a quantity proportional to the photocurrent measured in the VUV-scanner:

$$I_{\text{CsI}} \propto \int_{\lambda} \Phi(\lambda) \cdot QE(\lambda) \cdot d\lambda$$

Equation 35

The plot of this integral against the average normalized photo current is given in Fig. 97. A comparison with Fig. 96 shows that for some PCs like 51 and 47 the agreement with the overall trend is much better in this case. This indicates that the number of resolved clusters was biased due to a bad radiator transmittance or gain variations in these cases.

Still there are some PCs which also do not seem to follow the correlation between testbeam data and scanner results, even when additional chamber parameters are taken into account. It was already mentioned in the discussion of the behavior of PC 55 and it can be clearly seen in Fig. 96 that the test beam data was completely contradicting the bad performance of the PC in the scanner immediately after CsI deposition. In a later scan this could be attributed to a very slow enhancement phase of the PC. These long term stability issues might pose a problem for the construction and operation of the detector. First of all it is difficult to apply acceptance criteria in the production process, as a photocathode which is not quite acceptable in the first scans after CsI deposition might still achieve a satisfying level after some time. In principle this would only lead to a rejection of good photocathodes, which is still better than the contrary, which would be the acceptance of a photocathode which starts to degrade afterwards. So far no such case has been observed, however there are also some PCs which seem to perform worse in the test beam than expected from the scanner results, e.g. PC 52 and 50. An attempt should be made to rescan one of these PCs to determine if there is a visible decrease. In addition to the problems with the acceptance or rejection of a PC during production, the instabilities might create problems during the operation of the detector, especially for the data analysis, which might be complicated by unstable photocathode performance.

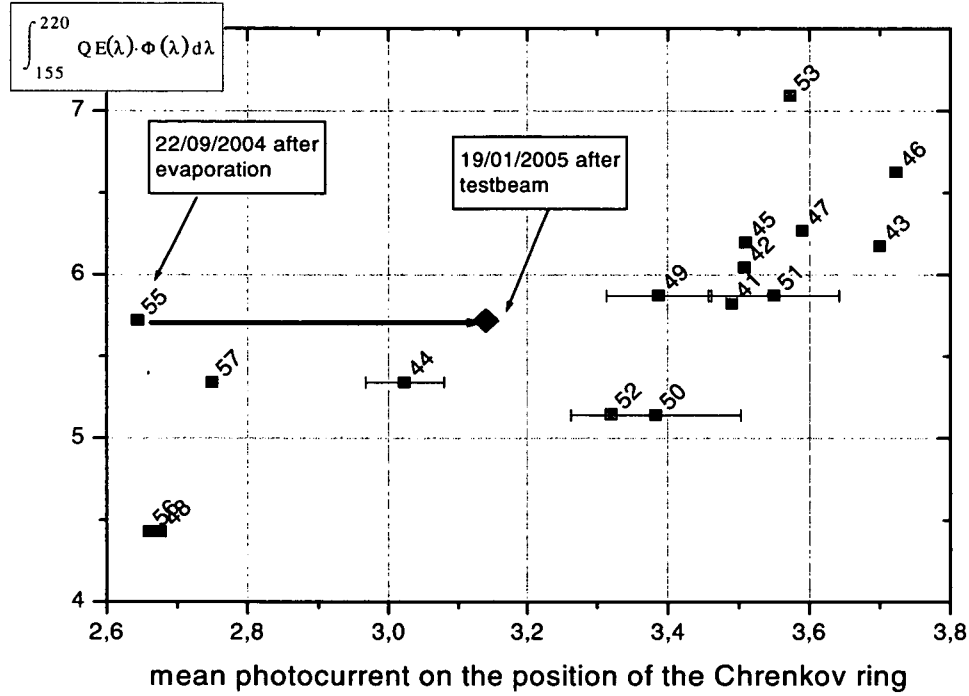


Fig. 97 Comparison of testbeam and VUV scanner: the QE extracted from test beam data was folded with the spectrum of the deuterium lamp used in the scanner. This quantity should be proportional to the photocurrent measured in the scanner.

7.3.1 Inhomogeneities in the PC response

The inhomogeneities in PC response mentioned already in Section 7.1 were confirmed in the beam tests. Fig. 98 shows a comparison between a scan of several beam positions on PC 44 and the VUV scan after CsI deposition.

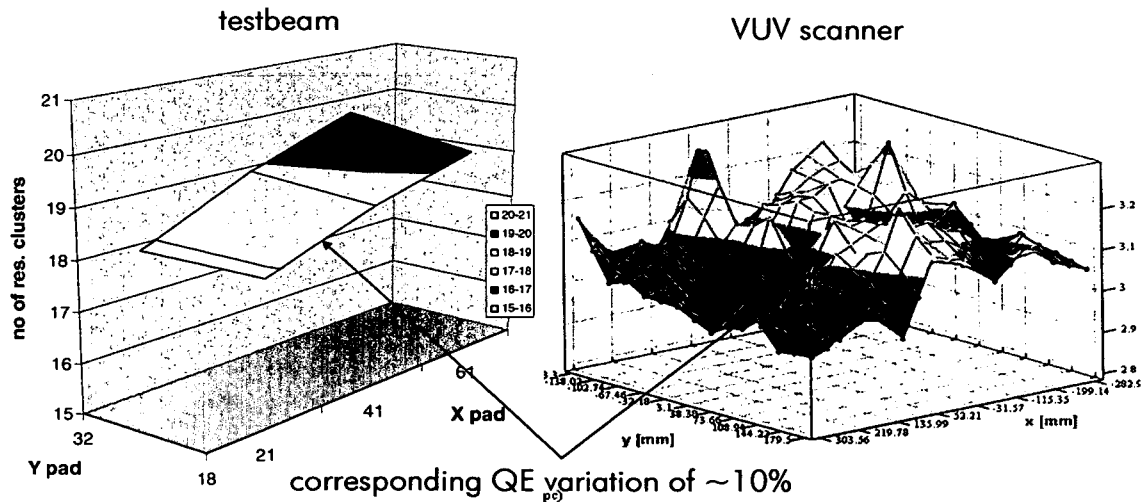


Fig. 98 Variations in PC quality measured on PC 44 both in beam tests and in the VUV scanner.

8 Ageing due to ion bombardement

8.1 Introduction

Inside a high energy physics experiment a detector is continuously exposed to high levels of irradiation with ionizing particles. In a RICH detector with proximity focusing layout these particles cause avalanche processes inside the MWPC whenever the detector is operated, i.e. whenever there is HV on the anode wires. The ions drift from the avalanche region around the wires to the PC surface where they are neutralized. Even though these ions are low energetic (~ 25 [meV]), this mechanism is known to damage the PC and can cause a decrease in QE. The problem of ageing due to the bombardment of the CsI layer with ions inside a MWPC was already mentioned in Section 3.1. A possible explanation for the effect is the dissociation of the CsI molecule during the neutralization of the arriving ion, which leads to an enrichment of Cs on the surface (“Cesiation”) – see 3.1 and Equation 23. Several lab studies [51]-[53] describe the effect measured on small CsI samples. However these studies sometimes were mixing irradiation with high UV flux and ion bombardment and most of them included transfer of samples through air, i.e. exposure to humidity. The reports on ion induced ageing of CsI under gas multiplication show a large spread of the dose necessary to obtain a 20 % efficiency drop, ranging from 1 to 100 [mC/cm²], with a high influence of the substrate and gas type. Large PCs have been exposed to low level irradiation in HEP experiments, e.g. in SPS test beams, NA44 or in STAR [35], [54] with no degradation of QE reported – see also [20].

In order to determine how much the ALICE/RICH detector in its final configuration will suffer from the irradiation inside the experiment, an ageing test was conceived, in which one of the standard photocathodes was irradiated locally with a collimated Sr 90 beta source inside a working prototype of the detector. The goal was to perform the test under conditions similar to those expected in the final experiment, i.e. using the same PC and MWPC, the same gas in the chamber, etc. In a first series of tests the PC was irradiated on three positions and subsequently investigated both in the VUV-scanner and in beam tests. The VUV-scanner proved to be very efficient in the detection of the ageing phenomena. A clear decrease in photocurrent could be observed at the irradiated locations in the scans performed after irradiation with rather high doses of up to 7 [mC/cm²]. A new effect of self-ageing was discovered in repeated measurements after the irradiation, which could be related to an interaction of the irradiated PC with residual contaminations in the Ar during storage. Results of the tests are being published in [20].

8.2 Experimental layout

For the ageing test the detector prototype “proto3” was used. This detector accepts one standard PC (PC 39 was used in the first test) and is equipped with a small C₆F₁₄ radiator for beam tests. The prototype was mechanically modified in order to accept collimated radioactive sources on three different positions. The positions were chosen so that the PC could be irradiated in three spots (32 [mm] Ø) located exactly in the fiducial zone of a Cherenkov ring for the test beam analysis. A drawing of this layout is given in Fig. 99. In

the backside view the positions of the anode wires across the PC are indicated. Only eight wires, overlapping the irradiated spots, were powered with HV during the test to achieve gain. Therefore the ageing was only effective along a 64 [cm] long and 3.5 [cm] wide region under these eight wires across each of the irradiated positions.

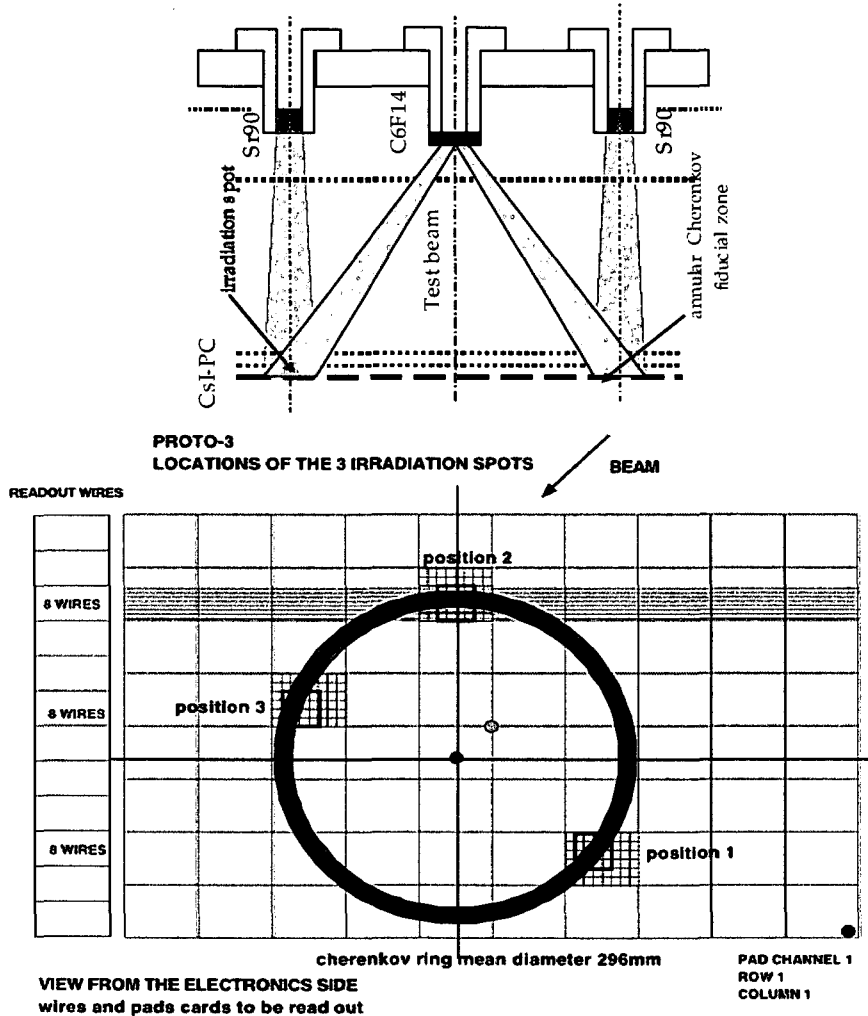


Fig. 99 Experimental layout for the ageing test. The irradiation positions were chosen to be located on a Cherenkov ring for TB analysis. Only the wires across the irradiated zones were powered with HV.

Each location was irradiated separately. During irradiation the anode current on the 8 wires was monitored to check for a possible wire ageing. No wire ageing was observed. The charge accumulated on the CsI PC was recorded by a measurement of the cathode current from the approximately 20 cathode pads which were affected by the direct irradiation cone. This way the ion charge accumulated on the CsI PC in $[\text{mC}/\text{cm}^2]$ could be measured and later be correlated with the observed QE decrease. Furthermore the charge profile on the PC could be obtained by a measurement of the charge at each pad by means of the the analog Gassiplex readout. Fig. 100 shows the charge profile measured along the wires on several pad rows (Fig. 99). Along the wire direction (x-direction of the PC), the charge profiles extends largely out of the direct irradiated area, due to the multiple scattering of the electrons in the methane and the bremsstrahlung photons emitted from the thin mylar

window in front of the source. Across the wires the profile is much narrower and restricted to the area of the pads inside the central cone, as only those wires were powered.

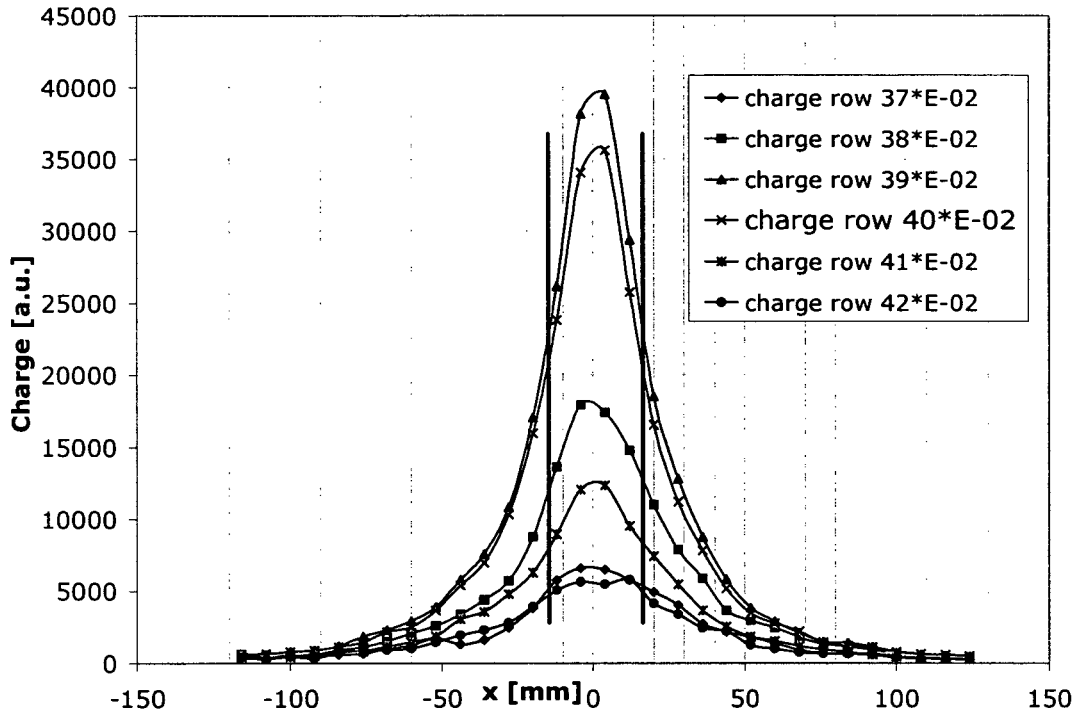


Fig. 100 Charge profile in wire direction. Each measured point corresponds to a single pad. The blue lines mark the extent of the central cone of primary radiation. Pad rows 39 and 40 are central, the others are further out and collect less charge.

8.3 Doses and dose rates

The doses and dose rates the HMPID detector will receive inside the ALICE experiment can be found in [5]. Taking into account both proton-proton and lead-lead runs, the expected dose for the detector integrated over 10 years of operation in ALICE is evaluated at 0.5 [mC/cm²]. In a first series of irradiations positions 1 – 3 were irradiated with rather high doses up to 6.8 [mC/cm²] to make sure an effect could be measured in the VUV scanner. The exact doses and rates are given in Table 9. In addition to the 3 positions irradiated in the first test series, a fourth position, which did not overlap with the regions affected by the other three positions, could be obtained for irradiation by turning the PC 180° inside the detector. The doses quoted in Table 9 correspond to the central region of the irradiated zones, as they were calculated from the charge accumulated on the central 20 pads inside the cone of primary irradiation. The dose profile for the irradiations can be obtained by scaling the dose values in Table 9 with the charge profile given in Fig. 100.

IRRADIATIONS SEQUENCE								
position	Date start	Source [MBq]	HV [V]	Duration [h]	I _{8wires} [nA]	I _{20pads} [nA]	Dose [mC/cm ²]	Dose rate [mC/cm ² /s]
1	080604	30	2167	196	661	121	6.4	9.8E-06
2	050404	260	1980	193	563	132	6.8	9.1E-06
3	090604	260	1965	48	543	122	1.57	9.1E-06
4	151104	30	2050	101			1	

Table 9 Sources, durations doses and dose rates for the irradiations of 4 positions on PC 39.

8.4 Effects measured with the VUV-scanner

8.4.1 QE decrease

After the irradiation of the first three positions the PC was dismounted from the detector under Ar atmosphere in a glove box and transferred back to the VUV-scanner under Ar. It was kept under Ar flow whenever possible and stagnant conditions were kept to a minimum during transport. The PC sees highest levels of impurities during transfer in the glove box and later just before the pumps in the VUV scanner are switched on, because the whole vacuum tank has to be purged with Ar until the purity is good enough to open the PC and start the pumps. In this procedure the oxygen concentration is measured at the output of the chamber, and the PC is opened at a level of < 500 [ppm]. Immediately afterwards the pumps are started and it takes roughly 30 minutes until the chamber is evacuated to a safe level. After PC 39 was reinstalled in the scanner in this fashion, a scan of the photocurrent across the PC immediately revealed a decreased response in the irradiated positions see Fig. 101. Especially from the contour plot in Fig. 102 it can be seen that the decreased zones are elongated in x direction, which is the direction of the wires inside the detector as indicated in Fig. 99. This is due to the fact that the irradiation profile is widened by scattered electrons and bremsstrahlung. Across the wires on the other hand the drop in QE is sharp and localized to an area of roughly 3-4 [cm] which corresponds to the 4 pads or 8 anode wires which were powered during irradiation. Therefore it can be concluded, that the QE decrease is actually due to the ion bombardement and not a consequence of the primary irradiation from the source. The quantitative decrease of efficiency will be discussed in the following sections.

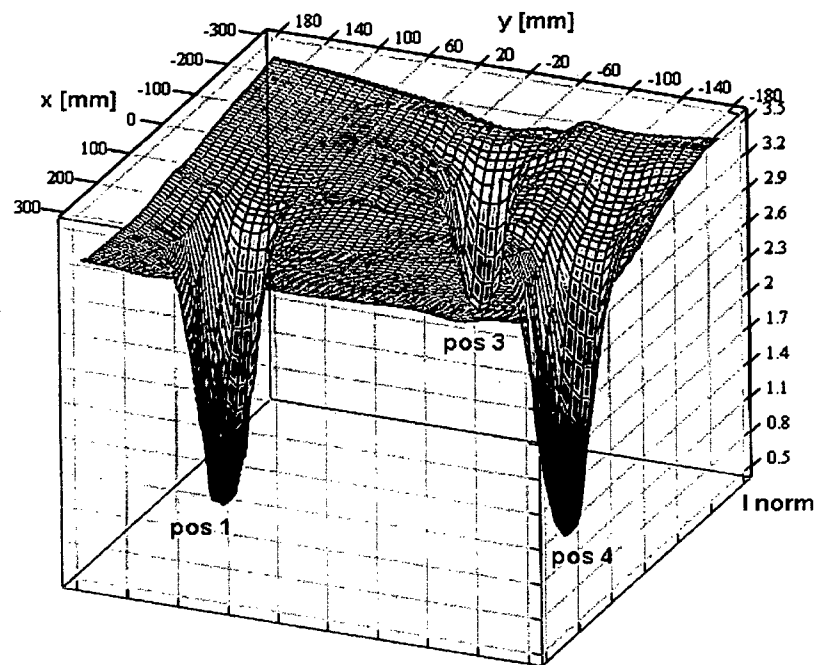


Fig. 101 Scan of PC 39 which was irradiated in three positions the ageing test.

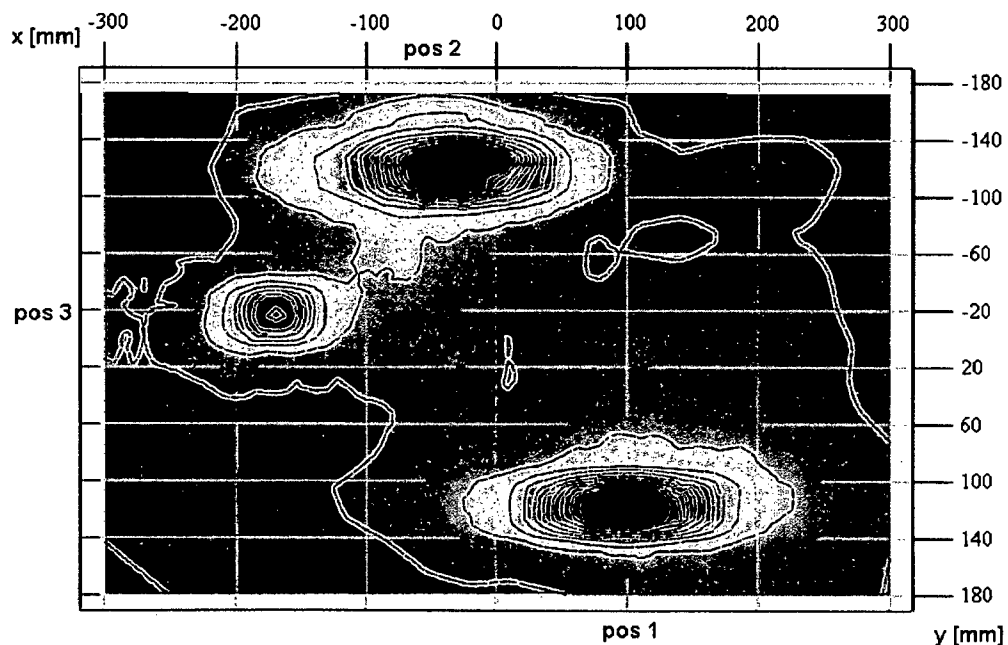


Fig. 102 Contour plot of the photocurrent on PC 39 after the irradiation of three positions. (Red level: $I_{\text{norm}} = 3.2$; blue-violet: $I_{\text{norm}} = 0.5$)

8.4.2 Time-dependent self-ageing

The actual test sequence in this ageing study was at first an irradiation of position 2, followed by a scan. Only afterwards the remaining positions were irradiated, followed by an analysis of the PC response in a beam test (Section 8.5), and further evaluations in the

VUV-scanner. When the PC was scanned the second time, it turned out that the QE drop measured in position 2 had increased, although this position had not seen any more radiation in the second series of irradiations in positions 1 and 3. Fig. 103 shows the detail scans on position 2 immediately after the irradiation and more than three months later. Obviously the effect increased in the time between the two scans. After the first measurement a decrease of roughly 40% relative to the non irradiated zones was calculated from the scan. In the next scan 110 days later, a decrease of more than 70% in the affected zone was recorded.

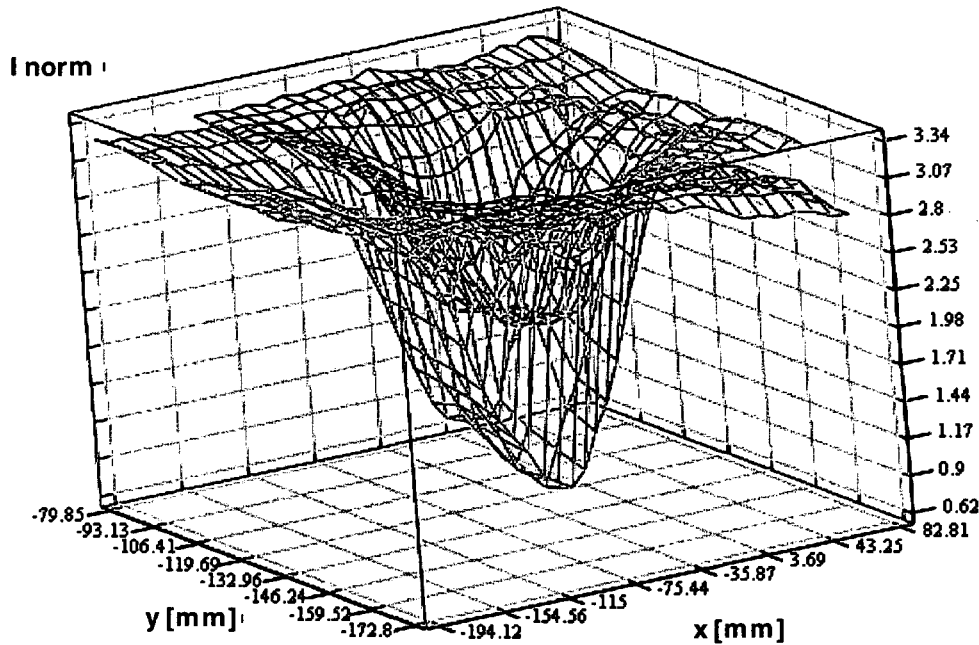


Fig. 103 Detail scans of position 2 immediately after the irradiation (black) and more than one month later (red).

After these results the PC was rescanned several times and irradiated at a fourth position as mentioned above. In total the PC was scanned 7 times over a period of 280 days from the first irradiation of position 2. The QE decrease was recorded for each of the 4 irradiated positions. The effect was always calculated in the following way:

- Inside each irradiated zone the 16 lowest values for the normalized current were taken to calculate an average. These 16 values correspond to the 16 pads in the center of the irradiation cone.
- The reference was calculated by taking an average over all the positions outside the irradiated zone, which were scanned. Usually a standard 280 point scan was performed on the whole PC to provide this reference.
- The “effect”, i.e. the drop in QE in the irradiated areas was then calculated relative to this reference. Fig. 104 shows the time-development of the decrease measured in each irradiated zone. The time- development of the reference outside the irradiated zone is given as well.

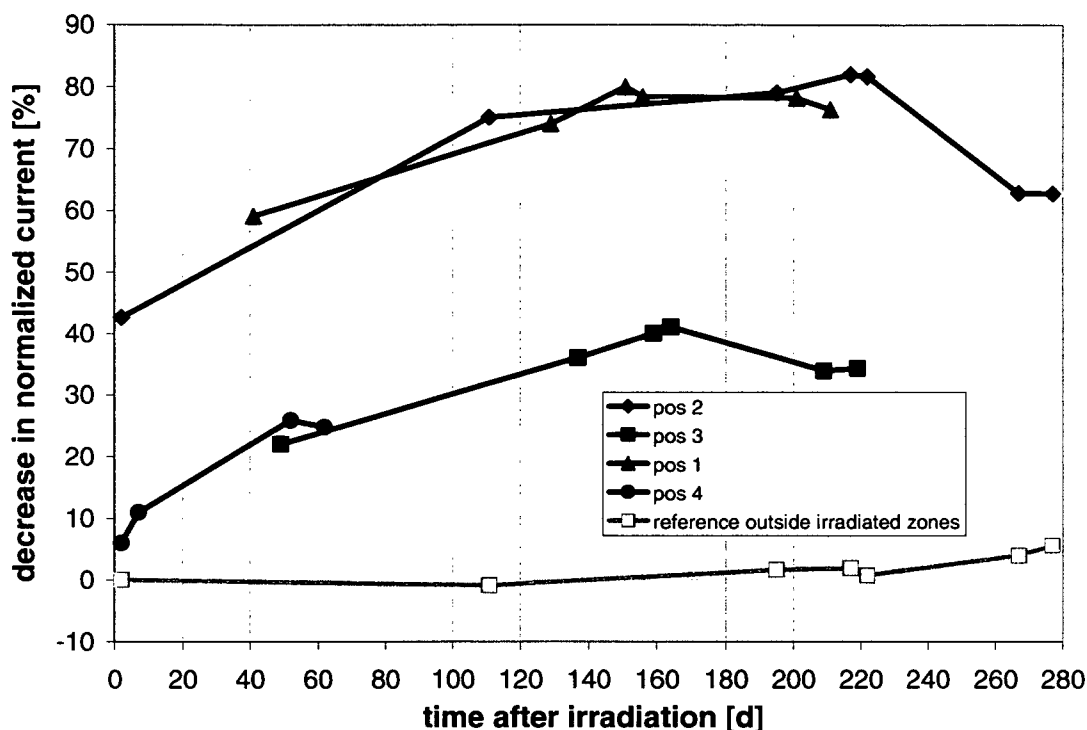


Fig. 104 Time evolution of the quality decrease measured in the 4 irradiated positions on PC 39. The decrease relative to non irradiated areas measured in the central region of the irradiated zones is plotted against the time after irradiation.

As can be seen in Fig. 104, each of the four irradiated positions showed this “self-ageing” effect. The QE drop recorded in the first measurement after the irradiation was changing in time. At first increasing fast, then after longer periods slower and finally a plateau was reached or even a recovery was observed. This self-ageing might be related to an interaction with residual contaminations in the Ar or methane during storage or operation respectively. One possible ageing mechanism is a dissociation of CsI molecules due to the bombardement of the CsI layer by avalanche ions. The desorption of the volatile I_2 from the surface could lead to an excess of Cs. The Cs is a reactive metal which will certainly be oxidized in the presence of oxygen. Compared to a Cs enriched surface the presence of Cs-oxide would decrease the QE of the overall system even more due to the electronegativity of the oxygen atoms. It is conceivable that the self ageing effect described above, i.e. the continued deterioration of the QE after the irradiation is stopped, could be related to a slow reaction of the Cs with contaminations in the argon or methane, e.g. an oxidation of the Cs. With oxygen levels of a few [ppm] during long term storage and up to a few hundred [ppm] during transfers, the PC is exposed to enough oxygen to make such a reaction possible: 1 [ppm] oxygen corresponds to a partial pressure of 10^{-3} [mbar] and the impingement rate of O_2 molecules on a surface at this partial pressure is $2.7 \cdot 10^{17}$ [$cm^{-2} \cdot s^{-1}$] compared to a surface density of CsI molecules of $4.8 \cdot 10^{14}$ [cm^{-2}]. The effect described in Fig. 104 could then be explained the following way: in the initial irradiation of the PC a certain amount of Cs is created at the surface, which decreases the QE compared to the reference outside the irradiated zones. In time the Cs reacts with oxygen or other contaminations in the gas atmosphere, which decreases the QE further. This effect continues until all the Cs that was initially present is transformed and then the effect

reaches a plateau – the QE does not decrease further. This hypothesis can be tested by keeping the PC under vacuum for a longer time, as the additional deterioration by reactions with contaminations should be dramatically reduced under vacuum. This test was performed on PC 39 during the last scans. The PC was left under vacuum for 10 days and the irradiated positions were scanned before and after. These two measurements correspond to the last two points in each curve in Fig. 104. Obviously the QE did not change further for any of the positions during this time. In a forthcoming ageing test with a new PC it is planned to transfer the PC to the scanner immediately after irradiation and monitor it there for a longer period to find out if the self-ageing also occurs under vacuum. Much more difficult to explain than the self-ageing effect is the slight recovery which was observed for positions 2 and 3. One possible recovery mechanism is slow desorption of contaminations from the surface, which would be conceivable for Cs but is not very likely for Cs oxide. In any case, more tests should be performed to investigate these phenomena. The self ageing mechanism under gas could be crucial for the use of CsI in a detector as the PC has to be operated under gas in the MWPC. If possible, tests should be carried out with smaller samples, i.e. in a miniature-wire-chamber which allows a subsequent transfer of the samples to analytical instruments capable of investigating morphology, structure or chemical composition of the aged PCs.

8.4.3 Stability of the PC performance in the reference areas

In the measurement of this time development of the PC performance it is crucial to have a stable reference, therefore the stability of the reference deserves some additional attention here. As mentioned above, the reference for the PC performance was an average of the currents scanned outside the irradiated areas. This average normalized current was approximately 3.2 in each measurement and did not change more than 5 % as can be seen from the time development of the reference given in Fig. 104. It should be stressed here that these 7 scans over a period of 280 days involved re-installing the PC in the VUV-scanner five times and mounting it several times on the detector and dismounting it again. Any of these operations involves some risk of contaminating the PC, therefore the stability of the reference level measured outside the irradiated areas can be considered exceptionally good. It proves the efficiency of the handling procedures of the PCs as well as the independence of the measurement from some minor changes in the measurement system. During the long period of these tests the UV lamp has been changed, the system needed to be realigned and the photon flux, i.e. the absolute values of the photocurrents changed several times. The fact that it was still possible to reproduce the same reference level in each measurement proves that these changes do not affect the measurement.

8.4.4 Negative result for recovery by annealing

Motivated by the measurement of a recovery effect by annealing of humidity aged PCs (Chapter 6), PC 39 was heated to 60-65 [°C] after the first irradiation of position 2. The PC was left at high temperature for several hours. During the whole time the scanner was continuously scanning 2 lines across the irradiated spot. By comparing the minima of the current inside the irradiated area with the reference points outside, the evolvement of the QE drop during this annealing test could be recorded. Fig. 105 shows that the decreased QE did not recover due to the annealing. If anything, the QE worsened slightly.

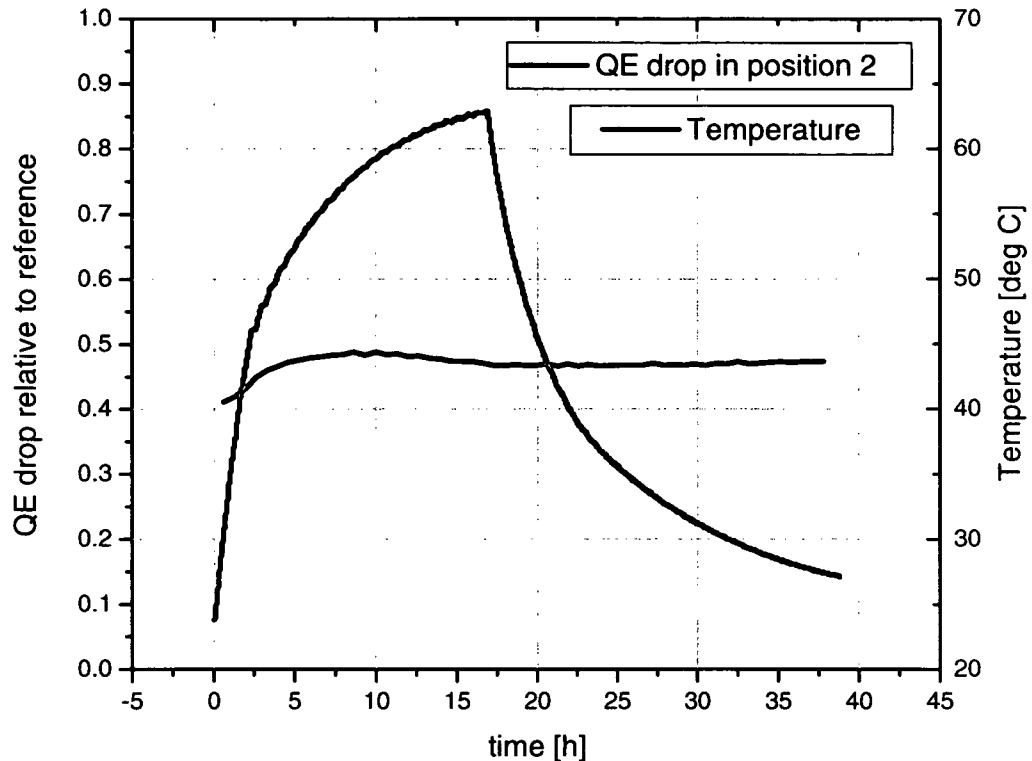


Fig. 105 Evolvement of the QE drop inside the irradiated position 2 during an annealing test.

8.4.5 Negative result for wavelength dependency of the effects

The scans of the aged PC were performed with and without a quartz window in the optical path of the UV beam, i.e. with two different spectra as given in Fig. 39. In both cases the same decrease of the irradiated zone relative to the reference zones was obtained, as given in Fig. 106. This result indicates that the QE is affected independently from the wavelength, which contradicts the hypothesis of a Cs enrichment at the irradiated surface. More Cs on the surface should change the photoemission threshold and consequently change the form of the QE curve, as discussed in 4.7. However a change in the photoemission threshold should lead to different results in the measurement with the two different UV spectra, as was observed in the measurement of the heat enhancement effect in Section 5.2.3. Nevertheless this result does not rule out the hypothesis of Cs enrichment, as the additional time evolvement has to be taken into account, which might completely modify the photoemission properties of the Cs enriched surface again.

8.5 Effects measured in test beam

After the irradiation of positions 1 – 3 the detector prototype was tested with a pion beam producing a Cherenkov ring covering the 3 irradiated positions as illustrated in Fig. 99. The display of accumulated events and the angular distribution of detected photons from these tests are given in Fig. 107. Qualitatively these results confirm the measurements obtained later in the VUV scanner and demonstrate the comparability of the VUV scanner measurements (high photon flux) and the beam tests (single photon counting).

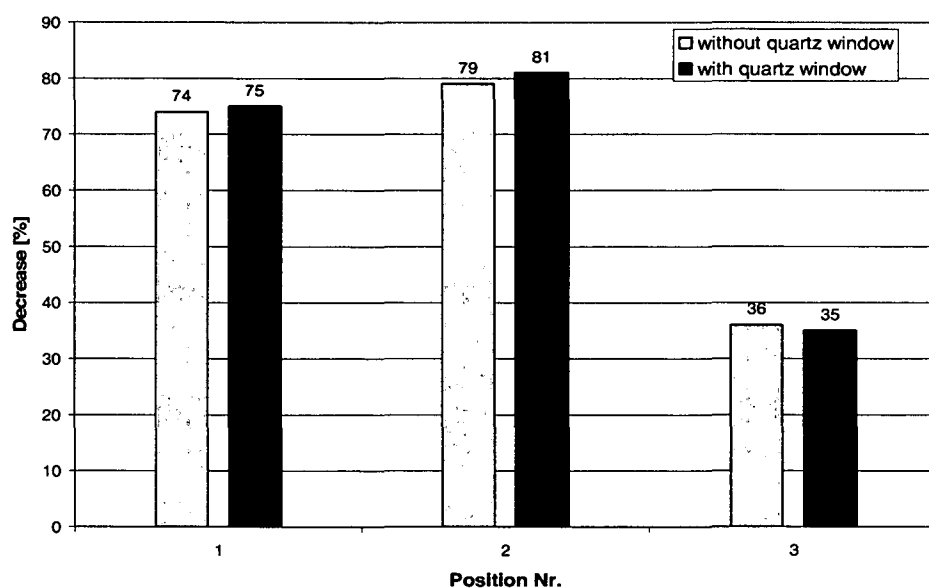


Fig. 106 Comparison of measurements of the QE drop with and without quartz window in the optical path. Both methods give the same result, which indicates the effect is not wavelength dependent.

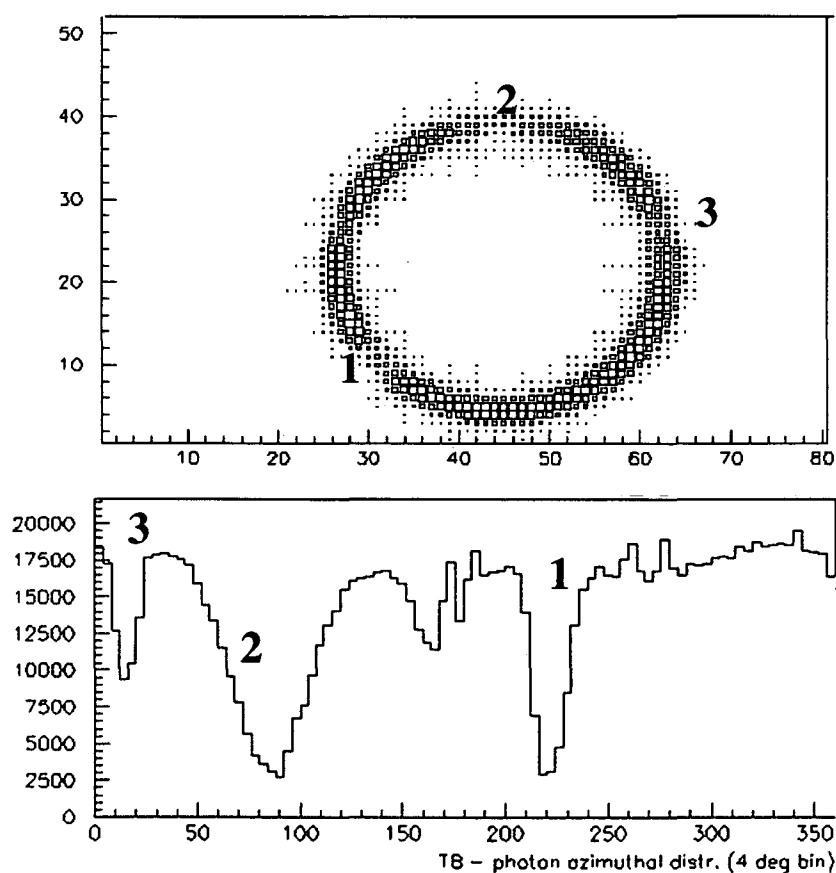


Fig. 107 Display of accumulated events (above) and angular distribution of the detected Cherenkov photons (below). In the irradiated regions photons are detected with decreased efficiency.

8.6 Dose-effect relationship

The 4 positions on PC 39 were irradiated with different doses to quantify the effect of QE loss as a function of accumulated charge on the cathode. This task is complicated due to the observation of the self-ageing effect described in **Error! Reference source not found.**. As a consequence a dose effect relationship can only be derived from measurements at the same time after the irradiation. It can be seen in Fig. 104 that for a given time after irradiations, data is not available for all positions, therefore for the other positions an interpolation has to be performed between the two measurements closest in time. Fig. 108 shows some fitted dose-effect curves obtained in this way. Each of the curves is valid for a certain time after irradiation, as the effect increases due to the self ageing.

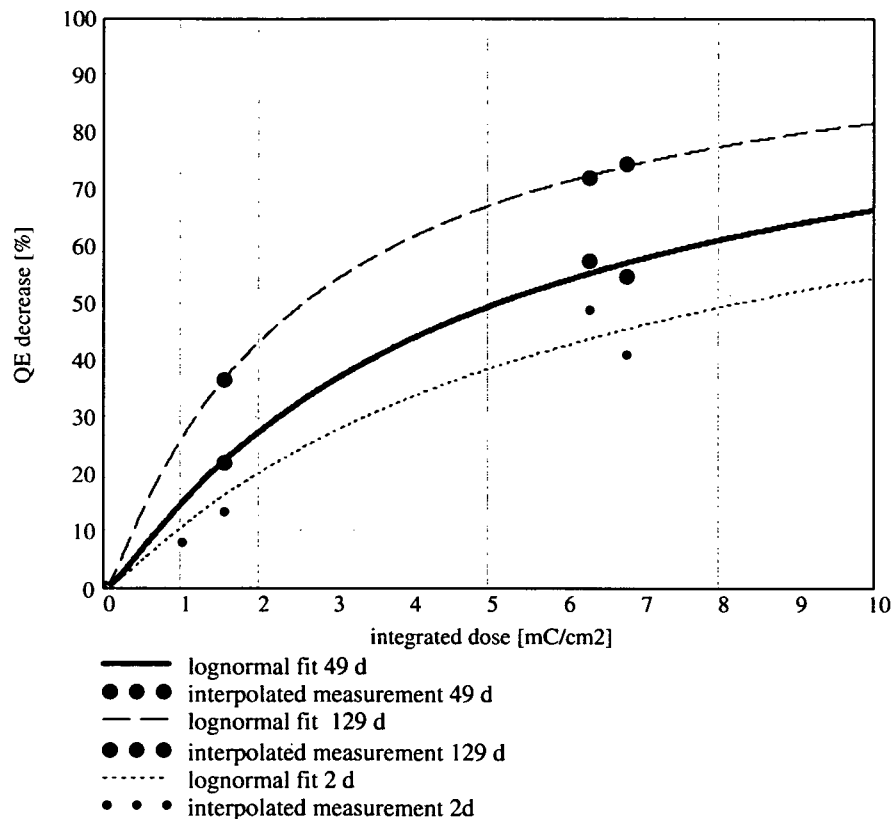


Fig. 108 Dose effect relations from measurements on the 4 positions 2, 49 and 149 days after irradiation. If no data was available for the time in question at a given point, Fig. 104 was used to interpolate between neighboring data-points.

A different method to obtain a dose-effect relationship for a given time after irradiation is to take a measurement of one position and to try to correlate the profile of the photocurrent measured across the irradiated zone (e.g. from a scan as in Fig. 101) with the charge profile measured on the cathode pads during irradiation (given in Fig. 100). This results in a dose-effect relationship as shown in Fig. 109. The plot shows the curve obtained from a measurement of the photo-current measurement profile in position 1 129 days after irradiation. For comparison a second curve is given, which was obtained using the first method described above, i.e. by taking into account the effect measured at all 4

irradiated positions and interpolating for the time effect. Both methods produce very similar results.

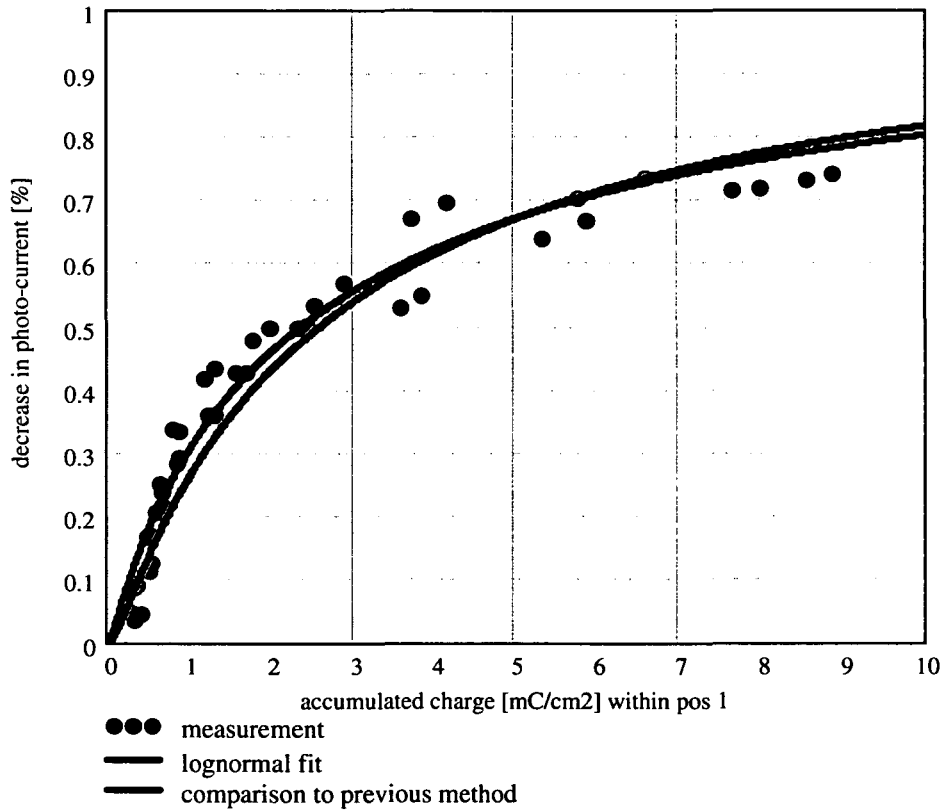


Fig. 109 Dose-effect relationship obtained from a comparison of the charge profile during irradiation of position 1 and of the photocurrent profile measured 129 days after irradiation. The plot shows the data in red and a lognormal fit in blue. For comparison the fit from Fig. 108 obtained by correlating dose and effect at from all irradiated positions is given as well. Both methods are in good agreement.

From these results it follows that the dose-effect relationship is clearly non-linear. This is not surprising for these rather high doses and can be understood with a very simple model. In this model it is assumed that an ion arriving at the CsI layer can destroy a CsI molecule. The mechanism could be the dissociation described in Equation 23 or any other mechanism which renders the site of the previously photoactive CsI molecule inactive.

- As a first approximation it can therefore be assumed a CsI molecule is an “active” site, i.e. it has the usual average QE of CsI, whereas a “destroyed”, e.g. dissociated molecule is “dead”, i.e. has no QE at all. Therefore the surface of the PC is divided into “active” and “dead” sites. This can be described with the molecular densities n_A [cm⁻²] for active sites and n_D [cm⁻²] for dead sites which add up to the total molecular surface density of CsI which can be calculated from the lattice constant: $n_A + n_D = n_T$ [cm⁻²].
- Ions are arriving at the surface with a rate r [cm⁻²·s⁻¹] and every ion has a probability p_{KILL} to eliminate an active site, which is proportional to the cross section σ of the dissociation reaction (or whatever reaction is transforming the photo-emission

properties of the surface) and the relative amount of active sites on the surface:
 $p_{KILL} = \sigma \cdot n_A / n_T$

- The number of active sites on the surface will decrease as more and more sites are destroyed, and the rate of decrease is the rate of arriving ions multiplied with their probability to kill a site:

$$\dot{n}_A(t) = -r \cdot p_{KILL} = -r \cdot \sigma \frac{n_A(t)}{n_T}$$

Equation 36

With the initial condition $n_A(t=0) = n_T$ the solution is

$$n_A(t) = n_T \cdot \exp\left(-\frac{r \cdot \sigma \cdot t}{n_T}\right)$$

Equation 37

- To come up with a dose response relation, the dose can be introduced as the number of ions arrived at the surface, i.e. $d [\text{cm}^{-2}] = r \cdot t$ and the quality decrease or the inefficiency $IE(t)$ can be expressed by means of the number of active sites:

$$IE(t) = \frac{n_D}{n_T} = 1 - \frac{n_A(t)}{n_T} = 1 - \exp\left(-\frac{r \cdot \sigma \cdot t}{n_T}\right)$$

or

$$IE(d) = 1 - \exp\left(-\frac{d \cdot \sigma}{n_T}\right)$$

Equation 38

Therefore in this simple model the inefficiency only depends on the dose of ions relative to the density of molecules at the surface and the cross-section of the reaction of the arriving ion with the surface. Fig. 110 shows this the dose response relation plotted for several hypothetical values of σ as a function of the occupation d/n_T of the surface with ions. The case of $\sigma = 1$ corresponds to the assumption that every ion arriving at an active CsI site destroys it with probability 1. The effect then only depends on the occupation d/n_T . A comparison of the experimental data shows that this is clearly unrealistic. The number of total sites can be calculated from the lattice constant of CsI and is $4.8 \cdot 10^{14} [\text{molecules} \cdot \text{cm}^{-2}]$. The total dose, e.g. in the irradiation of position 4 was $1 [\text{mC} \cdot \text{cm}^{-2}]$ which corresponds to $6.25 \cdot 10^{15} [\text{ions} \cdot \text{cm}^{-2}]$. The occupation d/n_T is therefore ~ 13 , which would mean a total loss of QE in this model with $\sigma = 1$. A comparison with the actual experimental data for the dose of $1 [\text{mC} \cdot \text{cm}^{-2}]$ in position 4, which shows a maximum of 40% decrease in efficiency taking even the self-ageing into account, allows to estimate a value of $\sigma = 0.04$. Obviously this is pushing the limitations of this simple model which can only be a rough estimation for a process which is actually two fold (initial ageing plus time evolvement). Actually the attempts to fit Equation 38 to the experimental data proved to be rather unsuccessful. Only if an additional parameter is introduced as in

$$IE(d) = A \cdot [1 - \exp(-B \cdot d)]$$

Equation 39

it is possible to reproduce the experimental data, as shown in Fig. 111. The introduction of this additional parameter is equivalent to the assumption that the maximum quality decrease is smaller than 100 %, i.e. that a “destroyed” site is not completely inactive, but has a residual QE. E.g. in the Cesium hypothesis this could be the residual QE of free Cs. However this description is clearly not accurate enough and the model should therefore be refined and maybe expanded into a Monte Carlo simulation as suggested in Section 8.7

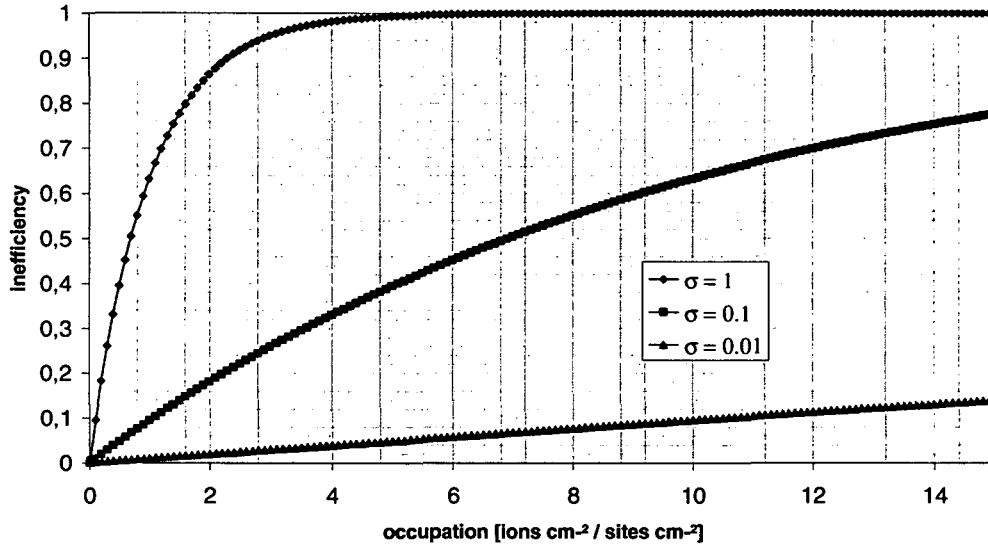


Fig. 110 Inefficiency from Equation 38 plotted as a function of the occupation d/n_T of the CsI sites with ions for three values of σ .

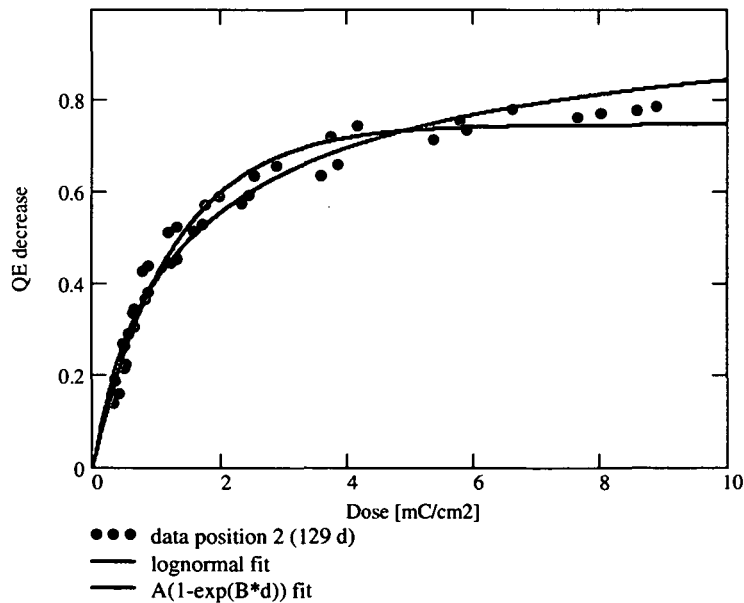


Fig. 111 Comparison of a lognormal and a $A(1-\exp(B \cdot d))$ fit for the dose-effect relation measured 129 days after irradiation in position 2.

8.7 Discussion

Even though this first series of ageing tests was dealing with doses much higher than expected for the ALICE experiment which were administered in a very short period, the results clearly show that the problem cannot be neglected and needs further investigation for two reasons: There are other experiments (e.g. COMPASS, HADES) which receive higher doses and the observation of the self-ageing effect makes the behavior with smaller doses and dose rates totally unpredictable. Experiences from detector operation under low level irradiation like in beam tests or for example in STAR¹³ have shown no ageing so far [35], [54]. The reason could be a threshold in the ageing effect which might depend on the dose rate. Such a threshold effect could be generated by a recovery mechanism on the layer surface. Within the Cesium hypothesis the recombination of Cs and I to CsI, or the desorption of Cs from the surface are possible recovery mechanisms. The following scenario is conceivable: The ions arriving at the surface are creating free Cs and I atoms. The volatile I could form I₂, desorb from the surface and leave Cs behind, which degenerates the QE. However, below a certain dose rate, the damaged sites might be so far apart, that a recombination of Cs and I to CsI is more likely than the formation of I₂ which would lead to a threshold depending on the dose rate. To test models like these the ageing tests should be continued in the following ways:

- Further irradiations with the ageing setup of proto3 and the VUV scanner should be carried out using smaller doses and dose rates which are more comparable to the actual situation to be expected inside the ALICE experiment. Such a series of irradiations is currently carried out. Two positions on a new cathode were irradiated with 0.2 [mC/cm²] corresponding to 4 years inside ALICE and a first scan 4 days after irradiation has shown no measurable decrease. After the irradiations an attempt should be made to store the PC for a long time under vacuum in order to test the hypothesis, that the self-ageing is due to interactions with contaminations in the storage gas. It is also very important that the new irradiations was carried out on a different PC, as a variation of the effect from PC to PC is thinkable.
- One should aim to understand the ageing mechanism. Therefore it would be necessary to analyze the surface chemistry of an aged sample. If possible, samples should be irradiated in a small mini-chamber and subsequently transferred under Ar or even inside a small SAS to surface analytical equipment. Additional information about possible ageing mechanisms could also be obtained from a molecular dynamics simulation of the approach of a CH₄ ion at the CsI molecule/surface, e.g. a cross section for a possible dissociation process.
- With additional information about the ageing mechanism from an analysis of the surface chemistry, models for the dose-effect relation could be obtained from a Monte Carlo simulation of the processes at the surface. In the case of the Cesium hypothesis such a MC simulation should for example include the following mechanisms:

¹³ Unfortunately there are no accurate calculations for the doses received in STAR. However in addition to the exposure in the experiment (in which the dose was very low), the detector was also tested in fixed beams at BNL and for several beam positions (MIP) on the cathodes a (probably exaggerated) upper limit of 1 [mC·cm⁻²] is quoted in [35]. No decrease was observed in these positions.

- Neutralization of the incoming ion which leads to dissociation of CsI with a certain probability.
- Desorption of neutralized CH_4 - or can it stick and form a layer?
- Surface diffusion and desorption of free Cs and I.
- Formation and desorption of I_2 .
- Reaction of free Cs with contaminations in a gas, e.g. adsorption of O_2 and oxidation of Cs – self ageing.
- The presence of Cs, CH_4 , CsO_2 etc. on the surface should be taken into account in the QE degradation by assuming changes in photon absorption, electron escape probability.

9 Summary and conclusions

This work has established the procedure of production and subsequent quality control of the HMPID photocathodes. The commissioning tests with the VUV-scanner described in Chapter 4 have shown the influence of the of a large number of parameters on the quality control measurements, e.g. photon flux, interpad zones on the PCs, pressure and pressure gauges, the alignment and robustness of the optical system, just to name a few. Nevertheless reliable and reproducible measurement procedures were successfully developed. This is best seen from the repeated measurements on PC 39, which was used in an ageing test and scanned seven times during a period of more than 9 months. The results showed only very minor changes in the response of the reference sites on the PC of less than 6% (Fig. 104). This stability is very good, considering that different optical configurations (two different UV lamps, different UV spot sizes, realignment of the optics...) were used in the measurements and even more so in view of the recent results on possible instabilities in the long term PC performance.

The post-deposition heat enhancement studies have shown that this effect is necessary to obtain a satisfactory PC quality. PCs which initially did not show an enhancement effect are just at the efficiency limit to provide the required Cherenkov angle resolution. Immediately after CsI deposition the current level on all PCs is very similar with less than 3-5% variation. The enhancement was found to be accelerated by temperature increase, and it was fastest when the CsI was deposited onto hot substrates. However the variations in the quality level after enhancement are much higher (up to 30% minimum to maximum variation). It turned out that some PCs, which did not show an enhancement after CsI deposition showed a very slow quality increase during storage (under dry argon) at room temperature within several weeks or even months. The process itself is possibly related to the presence of water at all stages. Both desorption of water originally incorporated in the film, as well as a transformation of the morphology or structure due to an increased surface mobility in the presence of water could lead to an increase in QE. To find the physical reason for the effect, additional studies on small samples should be performed which allow the use of surface analytical methods, e.g. LEED, X-ray diffraction or SEM without transfer of the CsI PCs through air. Although it might not be feasible for the completion of the ALICE/RICH, such an R&D effort is desirable for future applications. A mandatory conclusion for the HMPID project is however the necessity to monitor the long term stability of the photocathodes after production in repeated scans of selected PCs. This is important in order to provide reliable assumptions about the QE of the PCs for later data analysis in the experiment.

In the ageing tests carried out with the VUV-scanner three different mechanisms were investigated. Ageing under high photon flux was found to be a recoverable effect which can be neglected for the application of the photocurrent measurements in the VUV-scanner if the procedures are carefully chosen. Exposure to humid air up to several hours in the clean room environment (approximately 25% relative humidity at room temperature) leads to a quality decrease which can be recovered by annealing. The decrease of efficiency is correlated with an increase in grain size. Ageing under ion flux during the operation inside the MWPC was investigated for high doses and doserates in a first series of

irradiations with a radioactive source. Irradiation with 1 [mC/cm²] lead to a decrease of up to 40 % in PC response. This number is taking into account a recently discovered self-ageing effect: the degradation of an irradiated PC propagates in time possibly due to an interaction of the damaged sites with contaminations in the storage gas. In the next step of these tests a series of irradiations is being carried out involving smaller and more realistic doses and dose rates with respect to the environment inside ALICE. A first measurement on sites irradiated with 0.2 [mC/cm²] corresponding to 4 years inside ALICE has shown no initial degradation. Future measurements will show if the self-ageing effect can be observed in this case. These results also suggest further R&D efforts to clarify the physical ageing mechanisms (dissociation, reactions with O₂ or H₂O impurities), as the doses in other experiments can be higher than in the case of the ALICE/HMPID and consequently the self ageing effect is potentially dangerous.

Literature

- [1] ATLAS Collaboration: Technical Proposal for a General-Purpose pp Experiment at the Large Hadron Collider at CERN, CERN/LHCC/94-43 LHCC/P2, 15 December 1994.
- [2] LHC-B Collaboration: LHC-B Letter of Intent : A Dedicated LHC Collider Beauty Experiment for Precision Measurements of CP-Violation, CERN/LHCC 95-5 LHCC/I 8, 25 August 1995.
- [3] CMS Collaboration: The Compact Muon Solenoid Technical Proposal, CERN/LHCC/94-38 LHCC/P1, 15 December 1994.
- [4] ALICE Collaboration: Technical Proposal for A Large Ion Collider Experiment at the CERN LHC, CERN/LHCC/95-71 LHCC/P3, 15 December 1995.
- [5] ALICE collaboration, Physics Performance Report, CERN/LHCC 2003/49.
- [6] ALICE Collaboration 1998 Technical Design Report of the High-Momentum Particle Identification Detector CERN/LHCC/1998-19
- [7] ALICE Collaboration 1999 Technical Design Report of the Photon Spectrometer CERN/LHCC/1999-04
- [8] ALICE Collaboration 1999 Technical Design Report of the Zero-Degree Calorimeter CERN/LHCC/1999-05
- [9] ALICE Collaboration 1999 Technical Design Report of the Inner Tracking System CERN/LHCC/1999-12
- [10] ALICE Collaboration 1999 Technical Design Report of the Forward Muon Spectrometer CERN/LHCC/1999-22
- [11] ALICE Collaboration 2000 Technical Design Report of the Forward Muon Spectrometer Addendum-1, CERN/LHCC/2000-46
- [12] ALICE Collaboration 1999 Technical Design Report of the Photon Multiplicity Detector CERN/LHCC/1999-32
- [13] ALICE Collaboration 2003 Technical Design Report for the Photon Multiplicity Detector Addendum-1, CERN/LHCC 2003-038
- [14] ALICE Collaboration 2000 Technical Design Report of the Time-Projection Chamber CERN/LHCC/2000-01
- [15] ALICE Collaboration 2000 Technical Design Report of the Time-Of-Flight Detector CERN/LHCC/2000-12; Addendum CERN/LHCC/2002-16
- [16] ALICE Collaboration 2001 Technical Design Report of the Transition-Radiation Detector; CERN/LHCC/2001-21
- [17] ALICE Collaboration 2004 Technical Design Report of the Forward Detectors CERN/LHCC/2004-025
- [18] H. Hoedlmoser, "Quality Evaluation of CsI Photocathodes for the ALICE/HMPID Detector", submitted for publication in the Proceedings of the 5th Workshop on RICH Detectors in NIM A (2005).
- [19] A. Gallas, "Performance of the CsI-RICH for High Momentum Particle Identification in ALICE at CERN-LHC", submitted for publication in the Proceedings of the 5th Workshop on RICH Detectors in NIM A (2005).
- [20] A. Braem, G. De Cataldo, A. DiMauro, A. Franco, A. Gallas Torreira, H. Hoedlmoser, P. Martinengo, E. Nappi, F. Piuz, E. Schyns, "Ageing of Large CsI Photocathodes Exposed to Ionizing Radiation in a Gaseous RICH Detector",

- submitted for publication in the Proceedings of the 5th Workshop on RICH Detectors in NIM A (2005).
- [21] A. Di Mauro, "Status of the HMPID CsI-RICH project for ALICE at CERN/LHC", presented at the IEEE Nuclear Science Symposium, Rome 16.-22. 10. 2004.
 - [22] P.A. Cherenkov, C.R. Acad. Sci. USSR 8 (1934) 451, Doklady AN SSSR 3 (1936) 413, 14 (1937) 103, 14 (1937) 99, 20 (1938) 653, 21 (1938) 117, 21 (1938) 323 and Trudy Fizicheskogo Instituta AN SSSR 2 (1944) 4. See also Phys. Rev. 52 (1937) 378 for an English language publication of his early work.
 - [23] I.E. Tamm and I.M. Frank, Doklady AN SSSR 14 (1937) 107.
 - [24] V.L. Ginzburg, Zh. Eksperim. Teor. Fiz. 10 (1940) 589 and 608.
 - [25] Claus Grupen, Particle Detectors. – BI-Wiss.-Verl., 1993.
 - [26] E. Nappi, "RICH Detectors", CERN-EP/99-149, 1999.
 - [27] T. Ypsilantis, J. Seguinot, NIM A 343 (1994) 30.
 - [28] F. Sauli, NIM A 386 (1997) 531.
 - [29] C. W. Fabjan et al., Nucl. Instr. and Meth. A 367 (1995) 240.
 - [30] O. Chamberlain, E. Segre, C. Wiegand and T. Ypsilantis, Phys. Rev. 100 (1955) 947.
 - [31] The Proceedings of the 1st, 2nd, 3rd and 4th RICH Workshops have been published in Nucl. Instr. and Meth. A 343 (1994), A 371 (1996), A 433 (1999), A 502 (2003) respectively. The Proceedings of the 5th Workshop are to be published in 2005.
 - [32] G.R. Carruthers, Appl. Opt. 8 (1969) 633.
 - [33] P. Mine, NIM A 343 (1994) 99.
 - [34] F. Piuz, Y. Andres, A. Braem, M. Davenport, A. Di Mauro, A. Goret et al., "The CsI-based ring imaging detector for the ALICE experiment: technical description of a large prototype", Nucl. Instr. And Meth. A433 (1999), 222.
 - [35] A. Braem, M. Davenport, A. Di Mauro, P. Martinengo, E. Nappi, G. Paic, F. Piuz, E. Schyns, "Aging of large area CsI photocathodes for the ALICE HMPID prototypes", Nucl. Instr. And Meth. A 515 (2003), 307.
 - [36] E. Schyns, "Status of large area CsI photocathode developments", Nucl. Instr. And Meth. A494 (2002), 441.
 - [37] A. Braem, C. Joram, F. Piuz, E. Schyns and J. Séguinot, "Technology of photocathode production", Nucl. Instr. And Meth. A502 (2003), 205.
 - [38] Breskin, Nucl. Instr. and Meth. A 371 (1996) 116.
 - [39] D.F. Anderson, S. Kwan, V. Peskow, B. Hoeneisen, Nucl. Instr. and Meth. A 323 (1992) 626.
 - [40] A.S. Tremsin, O.H.W. Siegmund, Nucl. Instr. and Meth. A 442 (2000) 337-341.
 - [41] A.S. Tremsin, O.H.W. Siegmund, Transactions on Nuclear Science, Vol. 48, No. 3. (2001) 421.
 - [42] A. Akkerman et al., J. Appl. Phys. 76 (8) 1994.
 - [43] C. Lu, K.T. McDonald, NIM-A 343 (1994) 135.
 - [44] A. Di Mauro, D. Cozza, M. Davenport, D. Di Bari, D. Elia, P. Martinengo, A. Morsch, E. Nappi, G. Paic, F. Piuz, "Performance of large area CsI-RICH prototypes for ALICE at LHC", Nucl. Instr. And Meth. A433 (1999), 190.
 - [45] D. F. Anderson et al., NIM-A 323 (1992) 626.
 - [46] H. Brauning et al., NIM-A 327 (1993) 369.
 - [47] C. Lu, et al., Preprint Princeton/HEP/94-10.
 - [48] J. Almeida et al., NIM-A 361 (1995) 524.
 - [49] J. Almeida et al., NIM-A 367 (1995) 337.
 - [50] J. Friese et al., NIM-A 438 (1999) 86.

- [51] B.K. Singh et al., NIM-A 454 (2000) 364.
- [52] J. Va'vra et. al., NIM-A 387 (1997) 154.
- [53] P. Krizan et. al., NIM-A 364 (1995) 243.
- [54] F. Piuz, NIM-A 502 (2003) 76.
- [55] A. Breskin et. al., NIM-A 343 (1994) 159-162.

Glossary

AFM	Atomic Force Microscope
ALICE	A Large Ion Collider Experiment
ASSET	A Small Sample Evaporation Test facility
ATLAS	A Toroidal LHC ApparatuS
BNL	Berkley National Laboratory
chiral symmetry	A symmetry of the QCD lagrangian valid for massless fermions. Aproximative symmetry for practical purposes.
CMS	Compact Muon Solenoid
CNGS	Cern Neutrino beam to Grand Sasso
COMPASS	COmmon Muon and Proton Apparatus for Structure and Spectroscopy
CsI	Cesium Iodide
ESCA	Electron Spectroscopy for Chemical Analysis
FMD	Forward Multiplicity Detector
HADES	High Acceptance Di-Electron Spectrometer
HEP	High Energy Physics
HMPID	High Momentum Particle Identification
HPD	Hybride Photo Device
ITS	Inner Tracking System
LEED	Low Energy Electron Diffraction
LEP	Large Electron Positron collider
LHC	Large Hadron Collider
LINAC	LINear Accelerator
MWPC	Multi Wire Proportional Chamber
PC	Photo Cathode
PCB	Printed Circuit Board
PEEM	Photo Emission Electron Microscopy
PHOS	PHOton Spectrometer
PID	Particle IDentification
PMD	Photon Multiplicity Detector
PMT, PM	Photo Multiplier Tube, also PM
pQCD	perturbative Quantum Chromo Dynamics
PS	Proton Synchrotron
PSB	Proton Synchrotron Booster
pseudo-rapidity	see rapidity
QCD	Quantum Chromo Dynamics
QE	Quantum Efficiency
QGP	Quark Gluon Plasma
rapidity	The rapidity y is a variable frequently used to describe the behaviour of particles in inclusively measured reactions. It is defined by $\tanh(y) = p_L/E$ where y is the rapidity, p_L is the longitudinal momentum along the direction of the incident particle, E is the

	<p>energy, both defined for a given particle.</p> <p>The pseudorapidity η is a variable to approximate the rapidity if the mass and momentum of a particle are not known. It is an angular variable defined by $\eta = \log(\tan(\theta/2))$ where θ is the angle between the particle being considered and the undeflected beam.</p>
RGA	Residual Gas Analysis
RHIC	Relativistic Heavy Ion Collider
RICH	Ring Imaging Cherenkov
SEM	Scanning Electron Microscope, Secondary Electron Microscope
SPS	Super Proton Synchrotron
STAR	Solenoidal Tracker at RHIC
STM	Scanning Tunneling Microscope
TDR	Technical Design Report
TOF	Time Of Flight
TPC	Time Projection Chamber
transition radiation	<p>Transition radiation (TR) is produced when a relativistic particle traverses the boundary between materials of different dielectrical properties. The intensity of transition radiation is roughly proportional to the particle energy and TR consequently offers the possibility of particle identification at highly relativistic energies, where Cherenkov radiation or ionization measurements no longer provide useful particle discrimination. Electron/hadron discrimination is possible for momenta from about 1 [GeV/c] to 100 [GeV/c] or higher. Radiators in TR detectors consist of thin layers of different dielectrics.</p>
TRD	Transition Radiation Detector
VUV	Vacuum Ultra Violet

Curriculum Vitae

PERSONAL DATA

Date of birth: 23.12.1976

Address in Ramsau 57
Bad Ischl/Austria A-5351 Aigen-Voglhub
Austria
Tel.: 06132-2456793

Address in Segny/France: 88, Route des Anemones
F-01170 Segny
France



E-mail: herbert.hoedlmoser@cern.ch
Mobile phone: 0664-4043967

EDUCATION

1988 - 1995: Secondary school in Bad Ischl /Austria

1995: Graduation with distinction

1995 - 2001: University of Technology Vienna
Subject: Engineering Physics

Main areas of interest:

- Radiation physics, radiation protection and medical applications
- Surface physics, physics of thin films
- Computational physics and simulation (C, C++, Fortran Mathematica, Mathcad, ...)

Diploma Thesis at the Austrian Research Centers Seibersdorf

Title: Ocular Energies from Satellite Based Laser Systems
and Application to the Modelling of Human Risk

The graduation work was carried out in the course of a project of the European Space Agency. The aim of the project was the development of a mathematical model to calculate the risk of eye damage caused by exposure to radiation of space based laser systems, and the implementation of the model in a computer simulation. The thesis was written in English.

Mai 2001: Graduation with distinction

2002 – 2005 University of Technology Vienna

PhD at CERN within the ALICE/HMPID group – this document.

PUBLICATIONS

- [1] K. Schulmeister, G. Sonneck, F. Rattay, H. Hödlmoser, D. Sliney, J. Mellerio, A. Culoma, C. Preyssl: ***A probabilistic risk analysis model for receiving laser eye injury from space based lasers***, Proceedings of the 5th International Conference on Probabilistic Safety Assessment and Management, Osaka, Nov. 27th Dec. 1st 2000, Ed.: S. Kondo and K. Futura, Universal Academy Press, Tokyo, Japan, 2000, Volume 1, pages 595 – 602.
- [2] Karl Schulmeister, Herbert Hödlmoser, Helmut Schön, Volker Stübler: ***Optical Properties of Binoculars and Telescopes Relevant to Laser Safety***, Technical Digest ILSC 2001, Editor David Sliney, Laser Institute of America, March 5-8, 2001 San Diego p. 81-84.
- [3] K. Schulmeister, G. Sonneck, H. Hödlmoser, F. Rattay, J. Mellerio, D. Sliney, ***Monte Carlo Simulation of the Probability of Hazardous Human Exposure from Space Based Lasers***, Technical Digest ILSC 2001, Editor David Sliney, Laser Institute of America, March 5-8, 2001 San Diego p. 96-100.
- [4] K. Schulmeister, G. Sonneck, H. Hödlmoser, F. Rattay, J. Mellerio and D. Sliney: ***Modeling of uncertainty associated with dose-response curves as applied for probabilistic risk assessment in laser safety***, SPIE Vol. 4246, San Jose, 2001, Laser and Noncoherent Light Ocular Effects: Epidemiology, Prevention, and Treatment, Ed. B. E. Stuck and M. B. Belkin.
- [5] K. Schulmeister, D. Sliney, J. Mellerio, H. Hödlmoser, G. Sonneck: ***Model Description - Human Risk Analysis Simulator for Space Lidars***, Technical Note TN1, Austrian Research Centers Seibersdorf
OEFZS-G-0006, Vienna, September 2001.
- [6] H. Hödlmoser, Th. Auzinger, K. Schulmeister: ***Software Verification and Validation Report - Human Risk Analysis Simulator for Space Lidars***, Technical Note TN2, Austrian Research Centers
Seibersdorf
OEFZS-G-0007, Vienna, September 2001.
- [7] K. Schulmeister, H. Hödlmoser: ***Manual and Software Description - Human Risk Analysis Simulator for Space Lidars***, Austrian Research Centers Seibersdorf OEFZS-G-0008, Vienna, September 2001.
- [8] H. Hödlmoser, ***Quality Evaluation of CsI Photocathodes for the ALICE/HMPID Detector***, submitted for publication in the Proceedings of the 5th Workshop on RICH Detectors in NIM A (2005).
- [9] A. Braem, G. De Cataldo, A. DiMauro, A. Franco, A. Gallas Torreira, H. Hödlmoser, P. Martinengo, E. Nappi, F. Piuze, E. Schyns, ***Ageing of Large CsI Photocathodes Exposed to Ionizing Radiation in a Gaseous RICH Detector***, submitted for publication in the Proceedings of the 5th Workshop on RICH Detectors in NIM A (2005).

PRACTICAL EXPERIENCE

1991 – 1998 summer holidays: bank clerk at the Sparkasse Bad Ischl

2000 – 2001: Austrian Research Centers Seibersdorf

Contract with the the Austrian Research Centers Seibersdorf for half a year during graduation work. Extension of contract for 3 months after completion of graduation work.

September - October 2001: European Laboratory for Particle Physics CERN

Summer job in the experimental physics division at CERN in Geneva (ALICE/HMPID group):

research and developement of Cesium-Iodide photocathodes for use in a particle detector.

November 2001 – June 2002: Mandatory service in the Austrian Armed Forces

Participation in a **special science program** (limited number of 15-20 participants with scientific qualifications per year) of the Austrian School for NBC Defense; study on the topic of safety and possible accidents in nuclear powerplants near the Austrian boarder and possible implications for Austria.

HOBBIES

Endurance and outdoor sports: alpine climbing, ski mountaineering, triathlon. Digital imaging mostly in combination with sports activities and travelling.